Numerical Study of Debris Flight in Tornado-like Vortices

by

SHEN SHUAN RYAN HUO

A thesis submitted to the
University of Birmingham
for the degree of
DOCTOR OF PHILOSOPHY

School of Engineering
Department of Civil Engineering
College of Engineering and Physical Sciences
University of Birmingham
October 2020

UNIVERSITY OF
BIRMINGHAM

University of Birmingham Research Archive

e-theses repository

This unpublished thesis/dissertation is copyright of the author and/or third parties. The intellectual property rights of the author or third parties in respect of this work are as defined by The Copyright Designs and Patents Act 1988 or as modified by any successor legislation.

Any use made of information contained in this thesis/dissertation must be in accordance with that legislation and must be properly acknowledged. Further distribution or reproduction in any format is prohibited without the permission of the copyright holder.

Abstract

The dangers and damages caused by tornadoes and the associated flying debris have been an issue and long been recognised. Whilst the flow fields of tornadoes and debris flight under different wind conditions have been investigated comprehensively, the study on tornado-induced wind-borne debris were surprisingly sparse.

The aim of this research is to characterise tornado flows and evaluate the flying behaviour of debris in tornado flows. Two tornado-like vortices with different swirl ratios were numerically generated using Large-eddy simulation and the trajectories of five groups of compact debris with varying Tachikawa number were computed using Lagrangian particle tracking. An analysis of the simulated flow field revealed that the two tornado-like vortices have different characteristics but similar flow structure; a core with downwards flow and vortex walls with high tangential velocity and updraft flows around the core. The investigation on debris fight behaviour showed that in both of the vortices, low mass debris group with high values of Tachikawa number had the highest tendency to become wind-borne and had the longest flight duration with considerable variability observed in debris trajectories. However, the high mass debris group with low values of Tachikawa number were observed to have greater impact range despite the short flight duration; this was due to the high mass debris being ejected out of the vortex with greater inertia, while debris with a lower mass had a tendency to circulate around the vortex.

Finally, the initiation and flight altitudes of all wind-borne debris were found to be directly correlated with the updraft flows of the vortices.

Acknowledgements

Firstly, I would like to express my sincere gratitude to my first supervisor, Prof. Mark Sterling for his invaluable support and encouragement throughout my PhD. I would like to thank him for his continuous guidance, passion and enthusiasm that he expresses towards my work. His supervision had a significant impact and helped me improve as a researcher. Additionally, I would also like to thank him for helping me network as well as raising my research's visibility by means of regular Twitter posts and image display of my work in the school of engineering. I owe a debt of gratitude towards him for the trust he granted to me, and it was an immense pleasure to work alongside him.

I would also like to thank my second supervisor, Dr Hassan Hemida, for his guidance and insightful comments with respect to my work throughout the last three years. Additionally, I would also like to thank him for the various research opportunities that he provided me with.

I would like to acknowledge the financial support of the School of Engineering Scholarship, without which this research would not have been possible.

My thanks also go to all my colleagues and friends at the university, Dennis, Giulio, Anam, Şeyma, Yang, Rachel, Simon, Rafael, Frederick, Stefanie, Nagina, Gabor, Sarah, Pavel and Justyna. And particularly, I would like to express my deepest gratitude towards my housemate and dear friend, Muhammed Rassul for his emotional support and advices,

especially during the one and a half years we lived together, and the difficult pandemic times. My time at Birmingham would not have been the same without your friendship and support. I will always look back with fond memories.

It is impossible to express in words how grateful I am to my family, especially my mother Elaine, and my sister Linda, for their continuous emotional and financial support throughout the past four years. I hope to be able to repay my debt towards you.

Last but not least, I owe my deepest gratitude to my partner and best friend, Oliwia, for her affection, encouragement, understanding and patience. She supported me without any complaint and kept me emotionally intact that enabled me to complete my research.

Contents

Abstract iii
Acknowledgements v
List of Figures x
List of Tables xvii
Nomenclature xviii
1. Introduction 1
1.1. Aims and Objectives 4
1.2. Thesis layout 5
2. Literature Review 7
2.1. The Atmospheric Phenomenon of Tornadoes 8
2.1.1. Tornado flow structure 8
2.1.2. Damages caused by tornadoes 10
2.1.3. Full-scale tornado measurement 12
2.2. Modelling Tornado-like Vortices 14
2.2.1. Analytical vortex models 15
2.2.2. Physical vortex generators 23
2.2.3. Numerical vortex generators 29
2.3. Wind-borne Debris 38
2.3.1. Modelling debris flight 38
2.4. Summary of Previous Work and Research Gaps 44
3. Methodology 46

3.1. Description of Vortex Generator 47
3.1.1. Physical simulator 47
3.1.2. Numerical simulator 51
3.2. Numerical Simulation 52
3.2.1. Governing equations 53
3.2.2. Sub-grid scale modelling 54
3.3. Computational Details 56
3.3.1. Mesh generation 56
3.3.2. Boundary conditions and numerical setups 59
3.3.3. Vortex characteristics 61
3.4. Analytical Model Parameters 62
3.5. Wind-borne Debris Modelling 65
3.5.1. Tachikawa number 66
3.5.2. Analytical flight equations 66
3.5.3. Experimental setup 68
3.5.4. Numerically modelling debris motion 69
4. Tornado-like Vortices 76
4.1. Assessment of Numerical Accuracy 77
4.2. Comparison with Physically Generated Vortices 81
4.2.1. Flow field of vortex with S=0.3 82
4.2.2. Flow field of vortex with S=0.69 88
4.3. Comparison with Analytical Models 94
4.4. Tornado Flow field 99
4.4.1. Qualitative analysis of the vortex structure 99
4.4.2. Quantitative analysis of the velocity field 102
4.4.3. Vortex Wandering 110
4.4.4. An Aside 113
4.5. Summary 113
5. Wind-borne Debris 116

5.1. Validation of Debris Motion 117
5.1.1. Comparison with analytical flight equations 117
5.1.2. Comparison of aerodynamic similarity 120
5.1.3. Comparison with experimental study 124
5.2. The Impact of Varying Tachikawa Number 126
5.2.1. Debris flight in the vortex with S=0.3 127
5.2.2. Debris flight in the vortex with S=0.69 143
5.2.3. Summary relating to variations in Tachikawa number 159
5.3. The Impact of Varying Wind Fields 160
5.3.1. Debris flight behaviour 160
5.3.2. Debris impact properties 168
5.3.3. Asymptotic analysis for debris flight elevation 170
5.3.4. Summary relating to the flow field comparisons 177
6. Discussions and Recommendations for Future Work 179
6.1. Discussions 180
6.2. Recommendations for Future Work 184
Reference 188
Appendices 202
A. Debris release positions 202

List of Figures

Figure 2.1: Tornado flow structure with categorised flow regions (Wurman et al., 1996) 9
Figure 2.2: Percentage of reported tornadoes in USA in 2011. (NOAA, 2012) 10
Figure 2.3: The number of fatalities by tornado with different Fujita scales (Ashley, 2007)..... 11
Figure 2.4: The normalised radial profiles of tangential velocity of the Munhall tornado. (Lee and Wurman, 2005)..... 13
Figure 2.5: Sketch of the vortex flow observed at various vortex stages; (a) Single-celled vortex, (b) vortex breakdown stage, (c) two-celled vortex (Lugt, 1989)..... 25
Figure 2.6: Different tornado generator design (a) Ward (1972) (b) Church et al. (1977) (c) Mitsuta and Monji (1984) (d) Haan et al. (2008) (e) Refan and Hangan (2018) (f) Tang et al. (2018)..... 26
Figure 2.7: Computational domain of the Iowa State University Laboratory Tornado/Microburst Simulator. (Kuai et al., 2008)..... 31
Figure 2.8: Overview of the numerical ward type tornado simulator. (Ishihara et al., 2011)..... 33
Figure 2.9: Top view of debris trajectories released at different radial distances the tornado-like vortex at the swirl ratio of 0.7 (Bourriez et al., 2017)..... 43
Figure 3.1: Illustration of (a) The University of Birmingham Tornado Vortex Generator (Tornado generator - University of Birmingham, n.d.) (b) The dimensions of the generator (Gillmeier et al., 2017) 49
Figure 3.2: Configuration of the numerical vortex generator..... 51
Figure 3.3: (a) Isometric view of the computational domain (b) View of the mesh with the cut plane at y = 0 (c) The mesh around the guide vane region..... 58
Figure 3.4: Boundary condition setting of computational domains with the guide vanes set at (a) 50 degrees (b) 70 degrees 59

Figure 3.5: Tangential velocity component of the Rankine, Burgers-Rott, Sullivan and Baker and Sterling vortex model (a) $S_{Baker\ \&\ Sterling}$ =1.29 (b) $S_{Baker\ \&\ Sterling}$ =1.35. 64
Figure 3.6: Surface pressure coefficient of the Rankine, Burgers-Rott, Sullivan and Baker and Sterling vortex model (a) $S_{Baker\ \&\ Sterling}$ =1.29 (b) $S_{Baker\ \&\ Sterling}$ =1.35. 65
Figure 3.7: (a) An illustration of the experimental setup (b) The three-camera arrangement mounted inside of the simulator (Bourriez, 2020)..... 69
Figure 3.8: Illustration of different debris groups 70
Figure 3.9: Process diagram of numerical simulation. 74
Figure 4.1: Vertical profiles of the tangential velocity of the tornado-like vortex with S= 0.3 with different grid resolutions at the position r = 0.1, 0.15, 0.2 and 0.25. 78
Figure 4.2: Distribution of the time averaged pressure coefficient on the ground surface of the tornado-like vortex with S= 0.3 with different grid resolutions..... 78
Figure 4.3: Vertical profiles of tangential velocity of the tornado-like vortex with S= 0.69 with different grid resolutions at the position r = 0.1, 0.15, 0.2 & 0.25..... 80
Figure 4.4: Distribution of the time averaged pressure coefficient on the ground surface of the tornado-like vortex with S= 0.3 with different grid resolutions..... 80
Figure 4.5: Comparison of tangential velocity distribution from numerical simulation (CFD) and experimental results (Exp) obtained from Gillmeier et al. (2017) at the elevation of z/r_c =0.14, 1.42, 2.85 and 5.7..... 85
Figure 4.6: Comparison of radial velocity distribution from numerical simulation (CFD) and experimental results (Exp) obtained from Gillmeier et al. (2017) at the elevation of z/r_c =0.14, 1.42, 2.85 and 5.7..... 86
Figure 4.7: Comparison of vertical velocity distribution from numerical simulation (CFD) and experimental results (Exp) obtained from Gillmeier et al. (2017) at the elevation of z/r_c =0.14, 1.42, 2.85 and 5.7..... 87
Figure 4.8: Comparison of surface pressure distribution from numerical simulation (CFD) and experimental results (Exp) obtained from Gillmeier et al. (2017) 88
Figure 4.9: Comparison of tangential velocity distribution from numerical simulation (CFD) and experimental results (Exp) obtained from Gillmeier et al. (2017) at the elevation of z/r_c =0.09, 0.9, 1.8 and 3.6..... 91

Figure 4.10: Comparison of radial velocity distribution from numerical simulation (CFD) and experimental results (Exp) obtained from Gillmeier et al. (2017) at the elevation of z/r_c =0.09, 0.9, 1.8 and 3.6. 92
Figure 4.11: Comparison of vertical velocity distribution from numerical simulation (CFD) and experimental results (Exp) obtained from Gillmeier et al. (2017) at the elevation of z/r_c =0.09, 0.9, 1.8 and 3.6. 93
Figure 4.12: Comparison of surface pressure distribution from numerical simulation (CFD) and experimental results (Exp) obtained from Gillmeier et al. (2017). 94
Figure 4.13: Distribution of tangential velocity of the vortex with S=0.3 from the numerical simulation in comparison with the analytical vortex models (Rankine, Burgers-Rott, Sullivan and Baker and Sterling vortex models). 96
Figure 4.14: Distribution of tangential velocity of the vortex with S=0.69 from the numerical simulation in comparison with the analytical vortex models (Rankine, Burgers-Rott, Sullivan and Baker and Sterling vortex models). 96
Figure 4.15: Distribution of pressure coefficient on the ground surface of the tornado-like vortex with S= 0.3 in comparison with analytical vortex models (Rankine, Burgers-Rott, Sullivan and Baker and Sterling vortex models). 97
Figure 4.16: Distribution of pressure coefficient on the ground surface of the tornado-like vortex with S= 0.69 in comparison with analytical vortex models (Rankine, Burgers-Rott, Sullivan and Baker and Sterling vortex models). 98
Figure 4.17: Flow visualisation of the tornado-like vortices with the swirl ratio of 0.3 and 0.69 by injecting tracer particles from a plane source 100
Figure 4.18: (a) Contours of normalised velocity magnitude of the tornado-like vortices with the swirl ratio of 0.3 and 0.69 (b) Streamlines of the radial vertical vector of the flow fields. The length of the core radius and vortex walls are labelled as "r_c" and "r_w" respectively, and the maximum tangential velocity are marked as "x". 101
Figure 4.19: A schematic of the flow structure of the tornado-like vortices 102
Figure 4.20: (a) Horizontal profiles of normalised tangential velocity at the elevation of z/r_c=0.15, 0.3, 0.45 and 0.75 for the vortex with S=0.3 and 0.69 (b) Horizontal profiles of normalised vertical velocity at the elevation of z/r_c=0.15, 0.3, 0.45 and 0.75 for the vortex with S=0.3 and 0.69. The length of the core radius and vortex walls are labelled as "r_c" and "r_w" respectively. 104

Figure 4.21: (a) Horizontal profiles of normalised tangential velocity at the elevation of z/r_c=1, 1.5, 2 and 3 for the vortex with S=0.3 and 0.69 (b) Horizontal profiles of normalised vertical velocity at the elevation of z/r_c=1, 1.5, 2 and 3 for the vortex with S=0.3 and 0.69. The length of the core radius and vortex walls are labelled as "r_c" and "r_w" respectively. 105
Figure 4.22: Vertical profiles of normalised radial velocity at the distance of r/r_c=0.5, 1, 1.5 and 2 for the vortex with S=0.3 and 0.69. 107
Figure 4.23: Vertical profiles of normalised radial velocity at the distance of r/r_c=2.5, 3, 4 and 6 for the vortex with S=0.3 and 0.69. 107
Figure 4.24: (a) Horizontal profiles of turbulent kinetic energy at elevations of z/r_c=0.15, 0.3, 0.45 and 0.75 for the vortex with S=0.3 and 0.69. (b) Horizontal profiles of turbulent kinetic energy at elevations of z/r_c=1, 1.5, 2 and 3 for the vortex with S=0.3 and 0.69. The length of the core radius and vortex walls are labelled as "r_c" and "r_w" respectively 109
Figure 4.25: Temporal distribution of surface pressure obtained from the numerically simulated vortex with S =0.3 and 0.69 at the centre of the simulator in comparison with the experimental results obtained from Gillmeier (2019). 111
Figure 4.26: Distribution of spatial displacement of the vortex centre from the simulator centre for the (a) vortex with S =0.3 (b) vortex with S =0.69. 112
Figure 5.1: Comparison of results from numerical simulation and analytical flight equation. (a) Horizontal velocity (b) Vertical velocity (c) Dimensionless trajectories. 119
Figure 5.2: The distribution of fight duration of debris group B1, B2 and B3..... 121
Figure 5.3: Plan view of trajectories at different positions for debris group B1, B2 and B3. The grey arrow denotes the direction of debris trajectory for all debris groups.... 123
Figure 5.4: The distribution of impact radius of all wind-borne debris from debris group B1, B2 and B3. 124
Figure 5.5: Plan view of trajectories at release positions of r/r_c =1 and 2 for group B1, B2 and B3 in comparison with the experimental results from Bourriez et. al (2017).. 125
Figure 5.6: The distribution of fight duration of debris group A, B1 and C 129
Figure 5.7: (a) The percentage distribution of all wind-borne debris at the positions of r/r_c =0, 0.25, 0.5, 0.75, 1, 1.5, 2, 2.5 and 3. (b) The horizontal profiles of tangential, radial and vertical velocities of the vortex at the elevation of z/r_c =0.09. 130

Figure 5.8: Plan view of trajectories at different positions for debris A, B1 and C. The grey arrow denotes the direction of debris trajectory for all debris groups..... 131
Figure 5.9: Side view of trajectories at different positions for debris A, B1 and C. The grey arrow denotes the direction of debris trajectory for all debris groups..... 132
Figure 5.10: (a) The radial distance from the centre of the maximum debris flight altitude for debris group A, B1 and C (b) The radial position of the maximum debris flight altitude for debris group A, B1 and C..... 134
Figure 5.11: The distribution of impact radius of all released debris from debris group A, B1 and C. 135
Figure 5.12: The distribution of flight duration against impact radius of debris group A, B1 and C based on the location of debris initialisation. 137
Figure 5.13: The distribution of maximum debris flight altitude against impact radius of debris group A, B1 and C. 137
Figure 5.14: Debris flight duration against radial distance for debris group A, B1 and C. 140
Figure 5.15: Debris flight altitude against radial distance for debris group A, B1 and C. 141
Figure 5.16: Debris velocity against radial distance for debris group A, B1 and C..... 142
Figure 5.17: The distribution of fight duration of debris group A, B1 and C. 144
Figure 5.18: (a) The percentage distribution of all wind-borne debris at the positions of r/r_c =0, 0.25, 0.5, 0.75, 1, 1.5, 2, 2.5 and 3. (b) The horizontal profiles of tangential, radial and vertical velocities of the vortex at the elevation of z/r_c =0.05. 146
Figure 5.19: Plan view of trajectories at different positions for debris A, B1 and C. The grey arrow denotes the direction of debris trajectory for all debris groups..... 147
Figure 5.20: Side view of trajectories at different positions for debris A, B1 and C. The grey arrow denotes the direction of debris trajectory for all debris groups..... 148
Figure 5.21: (a) The radial distance from the centre of the maximum debris flight altitude for debris group A, B1 and C (b) The radial position of the maximum debris flight altitude for debris group A, B1 and C..... 150
Figure 5.22: The distribution of impact radius of all released debris from debris group A, B1 and C. 151

Figure 5.23: The distribution of flight duration against impact radius of debris group A, B1 and C based on the location of debris initialisation. 152
Figure 5.24: The distribution of maximum debris flight altitude against impact radius of debris group A, B1 and C. 153
Figure 5.25: Debris flight duration against radial distance for debris group A, B1 and C. 156
Figure 5.26: Debris flight altitude against radial distance for debris group A, B1 and C. 157
Figure 5.27: Debris velocity against radial distance for debris group A, B1 and C..... 158
Figure 5.28: The distribution of maximum debris flight altitude against impact radius of debris group A, B1 and C. 163
Figure 5.29: The distribution of flight duration against impact radius of debris group A, B1 and C based on the location of debris initialisation. 163
Figure 5.30: Debris flight altitude against radial distance at the position of $r/r_c=1$ for debris group (a) A (b) B1 (c) C and (d) Normalised vertical velocity profiles at different elevations. 166
Figure 5.31: (a) Debris flight altitude against radial distance for debris group A at the position of $r/r_c=1$ (b) Vertical profiles of normalised radial velocity at different radial distances..... 168
Figure 5.32: Maximum debris velocity against radial distance for debris group A, B1 and C. 169
Figure 5.33: (a) The distribution of impact velocity of debris group A, B1 and C (b) Horizontal profiles of normalised tangential velocity. 170
Figure 5.34: Flying and falling debris from numerical simulation in comparison with the parameter range calculated by Baker and Sterling (2017) 173
Figure 5.35: The radial distance from the centre of the maximum debris flight altitude for debris group A, B1 and C in comparison with the calculated asymptotic solutions. 174
Figure 5.36: comparison of the average debris flight altitude in comparison with the asymptotic solutions for debris groups A, B1 and C. 176
Figure A.1: Plan view of trajectories at different positions for debris A, B1 and C. The grey arrow denotes the direction of debris trajectory for all debris groups..... 203

Figure A.2: Plan view of trajectories at different positions for debris A, B1 and C. The grey arrow denotes the direction of debris trajectory for all debris groups..... 204
Figure A.3: Side view of trajectories at different positions for debris A, B1 and C. The grey arrow denotes the direction of debris trajectory for all debris groups..... 204
Figure A.4: Debris flight duration against radial distance for debris group A, B1 and C. 204
Figure A.5: Debris flight altitude against radial distance for debris group A, B1 and C. 205
Figure A.6: Debris velocity against radial distance for debris group A, B1 and C..... 205
Figure A.7: Plan view of trajectories at different positions for debris A, B1 and C. The grey arrow denotes the direction of debris trajectory for all debris groups..... 206
Figure A.8: Side view of trajectories at different positions for debris A, B1 and C. The grey arrow denotes the direction of debris trajectory for all debris groups..... 207
Figure A.9: Debris flight duration against radial distance for debris group A, B1 and C. 207
Figure A.10: Debris flight altitude against radial distance for debris group A, B1 and C. 208
Figure A.11: Debris velocity against radial distance for debris group A, B1 and C.... 208

List of Tables

Table 2.1: The comparison of guest wind speed between Fujita and Enhanced Fujita scale (NOAA, 2012) 10
Table 2.2: Configurations and parameters of the numerical simulators used by previous research 37
Table 3.1: Parameters used in the experimental study by Gillmeier et al. (2017)..... 49
Table 3.2: Cell number for coarse, fine and extra fine meshes 58
Table 3.3: Parameters used in the numerical simulation 61
Table 3.4: Maximum tangential velocity of all vortex models..... 64
Table 3.5: Properties of the debris groups 70
Table 3.6: Release locations of debris in the tornado-like vortices 75
Table 4.1: Characteristic parameters of the tornado-like vortices with S=0.3 and S=0.69. 102
Table 4.2: Details of the location of the vortex centre relative to the simulator centre 112
Table 5.1: The total number of wind-borne debris for debris group A, B1 and C that were initialised by the vortex with S=0.3 and S=0.69 161
Table 5.2: Details of debris flight properties for debris group A, B1 and C in the vortex with S=0.3 and S=0.69. 164
Table 5.3: Parameters obtained for debris group A, B1 and C 173
Table 5.4: Asymptotic solutions and Flight properties of debris in the vortex with $SBaker\ \&\ Sterling$ = 1.29. 175
Table 5.5: Asymptotic solutions and Flight properties of debris in the vortex with $SBaker\ \&\ Sterling$ = 1.35. 175

Nomenclature

Latin letters

a	[-]	aspect ratio
$a_{Burgers}$	[-]	constant in Burgers-Rott vortex model
C_D	[-]	spherical drag coefficient
C_P	[-]	pressure coefficient
C_S	[-]	Smagorinsky constant
d_d	[m]	diameter of debris
D_1	[m]	diameter of convection chamber
D_2	[m]	diameter of convergence chamber
D_3	[m]	diameter of exhaust outlet
F_D	[N]	drag force
f_d	[-]	van-Driest damping function
F_g	[N]	gravitational force
F_{total}	[N]	total force
g	[m/s^2]	gravitational acceleration
H_1	[m]	height of convection chamber
H_2	[m]	height of convergence chamber
K	[-]	Tachikawa number
K_{bs}	[-]	constant in Baker and Sterling vortex model
m_d	[kg]	mass of debris
n	[m]	wall normal distance of the first cell
P	[N/m^2]	pressure field
$\tilde{P}$	[N/m^2]	normalised pressure field

$\bar{P}$	[N/m^2]	filtered pressure
$\tilde{P}_0, \tilde{P}(0,0)$	[N/m^2]	pressure at the centre
$\tilde{P}_\infty$	[N/m^2]	free-stream pressure
$\tilde{P}_{Burgers}$	[-]	normalised pressure in Burgers-Rott vortex model
P_{min}	[N/m^2]	minimum pressure
Q	[m^3/s]	total volume flow rate
r	[m]	radial distance
$\tilde{r}$	[-]	normalised radial distance
r_c	[m]	radius of the vortex core
r_{rmax}	[m]	radial distance of the maximum radial velocity
r_T	[m]	radial distance of the maximum tangential velocity
Re	[-]	Reynolds number
S	[-]	swirl ratio
$S_{Baker\ \&\ Sterling}$	[-]	swirl ratio in Baker and Sterling vortex model
s_d	[m]	spatial position of debris
t^*	[-]	non-dimensional flight time of debris
t_d	[s]	flight duration of debris
$\tilde{t}_d$	[s]	dimensionless flight time of debris
t_r	[s]	time per revolution of the vortex
$\bar{U}$	[m/s]	filtered velocity field
U	[m/s]	velocity of the flow field
U^*	[m/s]	friction velocity
U_∞	[m/s]	inlet velocity/reference velocity
U_d	[m/s]	velocity of debris
U_{dx}, U_{dy}, U_{dz}	[m/s]	velocity components of the debris
$\widetilde{U}_{dx}, \widetilde{U}_{dz}$	[m/s]	dimensionless velocity components of the debris
U_t, U_r, U_v	[m/s]	tangential, radial and vertical components of velocity
$\widetilde{U}_T$	[-]	normalised tangential velocity
U_T	[m/s]	maximum tangential velocity component of the vortex
U_x, U_y, U_z	[m/s]	velocity components of the fluid flow
$\widetilde{U}_x, \widetilde{U}_y, \widetilde{U}_z$	[m/s]	dimensionless velocity components of the fluid flow

U_{rmax}	[m/s]	maximum radial velocity in Baker and Sterling vortex model
x_d, y_d, z_d	[m]	co-ordinates of debris
$\tilde{x}_d, \tilde{y}_d, \tilde{z}_d$	[m]	co-ordinates of debris
x^+, y^+, z^+	[-]	non-dimensional wall normal distance of cells
z	[m]	vertical distance
$\tilde{z}$	[-]	normalised vertical distance

Greek letters

Δ	[m]	filter width
Δt	[s]	time step size
γ	[-]	shape parameter in Baker and Sterling vortex model
μ_t	[m^2/s]	sub-grid scale eddy viscosity
ρ_a	[kg/m^3]	density of air
ρ_d	[kg/m^3]	density of debris
τ_{ij}^s	[N/m^2]	sub-grid scale stress tensor
τ_{wall}	[N/m^2]	wall shear stress
Ω	[-]	ratio of aerodynamic drag force and gravitational force
θ	[deg]	angle of guide vanes
μ	[Ns/m^2]	dynamic viscosity of air
ν	[m^2/s]	viscous dissipation
υ	[m^2/s]	kinematic viscosity of air
$\bar{\varepsilon}_{ij}$	[1/s]	filtered strain rate tensor
δ	[-]	Kronecker delta
Γ	[m^2/s]	Circulation at infinity

Acronyms

CFD	Computational Fluid Dynamics
CFL	Courant-Friedrichs-Lewy
DNS	Direct Numerical Simulation
EF	Enhanced Fujita-scale

EXP	Experiments
F	Fujita-scale
ISU	Iowa State University
LES	Large Eddy Simulation
LIDAR	Light Detection and Ranging System
NOAA	National Oceanic and Atmospheric Administration
PIV	Particle Image Velocimetry
RANS	Reynolds Averaged Navier-Stokes
ROTATE	Radar Observations of Tornadoes and Thunderstorms Experiments
RSDOW	Rapid-Scan Doppler On Wheels
RSM	Reynolds Stress Models
SGS	Sub-Grid Scales
TIV	Tornado Intercept Vehicle
TKE	Turbulent Kinetic Energy
TORUS	Targeted Observation by Radars and UAS of Supercells
TVC	Tornado Vortex Chamber
TVG	Tornado Vortex Generator
TWISTER	Tactical Weather Instrumented Sampling Tornadoes Experiment
UoB-TVG	University of Birmingham Tornado Vortex Generator
URANS	Unsteady Reynolds Averaged Navier-Stokes
VORTEX	Verification of Rotation in Tornadoes Experiment
WindEEE	Wind Engineering, Energy and Environment

1. Introduction

"When I meet God, I am going to ask him two questions: Why relativity? And why turbulence? I really believe he will have an answer for the first."

Heisenberg Werner (1996)

IND-BORNE DEBRIS is perhaps the primary cause of damage and destruction to engineering structures in severe wind events such as hurricanes and tornadoes (Lin and Vanmarcke, 2010). Objects in the environment such as tree branches, vehicles and even houses have been observed to be picked up and transported by strong tornadic events (Harms, 2019). Such debris, when reaching high velocities can significantly damage buildings, resulting in the generation of even more debris, referred to as the debris damage chain (Holmes, 2010). Accounts of individuals being buried by building wreckage and mud picked up and dropped by a tornado have also been reported (Harms, 2019). As a result, structures in hurricane and tornado regions are typically enhanced and designed to reduce damage caused by wind and debris (Ramseyer et al., 2017). Resistance against wind-borne debris is considered as a critical design factor particularly for nuclear power plants, where the failure of these structures can pose significant danger to the environment. In a study on the effects of tornado-

generated missiles, McDonald (1976) deduced that the biggest issue in a tornado resistant design of a nuclear power plant is the protection from the wind-borne missiles.

Wind-borne debris can be classified based on their geometrical properties: compact type three-dimensional (3D), plate type two-dimensional (2D) and rod type one-dimensional (1D) missiles. Tachikawa (1983) proposed a dimensionless parameter, K that represents the ratio between the inertial forces of the flow to the weight of the debris, which can be used to describe the characteristic and trajectory of debris objects of all types; since then, the research on flying debris have been conducted extensively. Baker (2007) compared the flight equations and characteristics of compact and sheet-like debris and found that the trajectories of compact debris can be accurately represented by the mathematical equations due to the simplicity in spherical configuration and axis symmetrical structure. Further investigations comparing the mechanics and aerodynamics of compact type (3D) debris (Holmes, 2004; English, 2005; Baker, 2007), plate type (2D) debris (Tachikawa, 1983; Wang and Letchford, 2003; Holmes et al., 2004) and rod type (1D) debris (Lin et al., 2007; Richards et al., 2008) have also been conducted under various different wind conditions, however, none of these studies were carried out under tornado-like flow conditions.

Tornadoes are possibly one of the most destructive weather phenomena due their violent and unpredictable nature. A tornado reported in March 2019 struck the Lee County in Alabama (USA). It was classified as an EF4 scale with wind speeds up to 275 km/h and caused catastrophic damage and claimed the lives of more than 23 people (Darrow, 2019). Tornadoes are very complex phenomena, and in the USA, more than 1,200 tornadoes are reported each year (U.S. Tornado Climatology, 2010). However, despite their frequent occurrence, surprisingly little is known about the flow structure; this is due to its

unpredictable nature and the high wind speeds, which made the near ground measurements difficult and dangerous. Therefore, the reproduction of tornadoes in laboratory scaled experiments and numerical simulation are the alternatives for researchers to study and quantify their characteristics. The earliest systematic experiment for generating laboratory scaled tornado-like vortices is frequently attributed to Ward (1972). The vortex simulator developed by Ward had an exhaust fan situated at the top to provide an updraft flow, and a number of guide vanes near the ground to generate the required angular momentum for the formation of the tornado-like vortices. The adjustment on the angle of the guide vanes allow the reproduction of vortex evolution from single-celled vortex to multi-celled vortex. However, Ward's simulator were limited to its size, and unable to reproduce some vortex characteristics due to its design. Thus, an increasing number of studies have been conducted in order to study the flow fields of tornado-like vortices (Nolan and Farrell, 1999; Hangan and Kim, 2006; Lewellen and Lewellen, 2007; Kuai et al., 2008; Hangan and Kim, 2008; Alexander and Wurman, 2005; Natarajan, 2011; Ishihara and Liu, 2014; Liu and Ishihara, 2015). Recently, several investigations on debris flight in a tornado-like wind field were undertaken; Sassa et al. (2009) studied the deposition of wind-borne debris in a simulated moving tornado. Maruyama (2011) numerically simulated a tornado-like vortex with the statistical distribution of debris velocities, Bourriez et al. (2017) studied the flight paths of debris in laboratory scaled controlled conditions and the research undertaken by Baker and Sterling (2017) provided analytical equations for the pressure and velocity fields of tornadoes and the prediction of debris flight within the tornado.

While great effort has been made to model and simulate the flow fields of tornadoes, the flight behaviour of wind-borne debris in tornado flow field is still poorly understood.

With a better understanding of tornado induced debris, the weather services can estimate where debris are likely to impact, ultimately leading to a better tornado warning system. Therefore, the motivation behind this research is to explore the behaviour of flying debris in different tornadic flows using numerical simulation.

1.1. Aims and Objectives

The aim of this research is to characterise tornado-like flow fields and evaluate the wind-borne behaviour of compact debris within those tornado flows. In order to accomplish this, Computational Fluid Dynamics (CFD) was employed to numerically simulate different types of tornado-like vortices and debris motion, and the following objectives have been devised:

Objective 1: An analysis on the numerically simulated tornado-like vortices

Two tornado-like vortices corresponding to the swirl ratio of 0.3 and 0.69 are numerically generated using Large-eddy simulation (LES). The computational domain is created based on the laboratory scaled ward-type vortex generator, University of Birmingham Tornado Vortex Generator (UoB-TVG). A mesh sensitivity test is conducted in order to ensure that the results are consistent with the variation of mesh resolution. The numerical results are then compared with the physically generated vortices and analytical vortex model for the similarities and differences.

Objective 2: Characterising the flow structure and features of the tornado-like vortices

The understanding of a tornado flow field is required in order to accurately predict and fully evaluate debris behaviour in tornado-like wind field. The numerically reproduced vortices with the swirl ratio of 0.3 and 0.69 are analysed for the flow structure and

quantitative measurements of characteristics features (i.e. vortex core, vortex walls, location of maximum velocity). The characteristic parameters of the respective vortices are determined: the radius of the vortex core, thickness of vortex walls, magnitude of maximum tangential velocity and revolution of the vortex.

Objective 3: The evaluation of the flight characteristics of different debris groups under various tornado wind fields

The trajectories of debris in two different tornado-like vortices are conducted using compact type debris with varying sizes, corresponding to the value of the Tachikawa number (K) which ranged between 0.6 and 2.5. The motion of debris are computed using Lagrangian-particle tracking. The numerically simulated debris motion are compared with analytical flight equations in order to investigate the accuracy of the numerical results. Debris are positioned and released at various radial distance throughout the flow field in order to study the process of how debris are picked up and initiated by tornadoes. The impact of Tachikawa number on debris flight are investigated, and the flight behaviour of debris in different tornado-like vortices are analysed.

1.2. Thesis layout

Following this introductory chapter, a comprehensive literature review on the numerical and experimental methods of generating tornado-like vortices, and the study on wind-borne debris are discussed and critically analysed in Chapter 2. Following the literature review, all the computational methods and numerical procedure adopted are listed in Chapter 3. The validation of the results, three-dimensional flow field, characteristics and mechanisms of the numerically reproduced tornado-like vortices are outlined in Chapter 4. The results of debris flight and analysis of debris flight behaviour in tornado-like wind-

field are reported in Chapter 5. Finally, the discussions and recommendations for future work are presented in Chapter 6.

2. Literature Review

"The biggest challenge has been simulating a tornado with wind machines and dirt and debris. Right when you walk on the set, you feel the energy of a tornado. But the hardest thing is trying to get dialogue out in all of that"

Mark-Paul Gosselaar (2013)

THE STUDY OF wind-borne debris in tornado-like wind fields involves the understanding of the tornado flow field as well as the modelling of debris flight. Therefore, in this chapter a comprehensive analysis is conducted on the current state of knowledge on both the numerical methods of generating tornado-like vortices and the simulation of flying debris. In section 2.1, the atmospheric phenomenon of naturally occurring tornadoes are reviewed. Then, the literature on analytical, laboratory and numerically generated tornado-like vortices are reviewed in section 2.2. The study on compact type debris is reviewed in section 2.3 and the summary of previous work and knowledge gaps are identified in section 2.4.

2.1. The Atmospheric Phenomenon of Tornadoes

A tornado is defined as a violently swirl of rotating air that extends from a thunderstorm to the ground surface on the earth (Huschke, 1959). Although there are many explanations to the formation of tornadoes; it is generally considered that when warm moist air and dry cold air from interacts, it creates instability in the atmosphere (NOAA, 2012). These instabilities result in condensation, and the warm rising air from the ground causes rotating columns of air within the thunderstorm. If, the conditions are right, these rotating funnels of air will touch the ground and thus a tornado is formed. Understandably, this is a gross simplification of the tornado formation process. Most of the recorded strong tornadoes are developed from large thunderstorm with well-observed radar circulation (mesocyclone), known as a super-cells (NOAA, 2012).

2.1.1. Tornado flow structure

Figure 2.1 shows an idealised representation of the flow structure associated with tornadoes based on data retrieved from full scale measurement from Doppler radar (Wurman et al., 1996). Based on Wurman et al. (1996), the flow structure can be categorised into five different flow regions: Region I is the rising out-flow region, which engulfs the tornado. Region II represents the primary core of the tornado, with high magnitude of wind velocity and low relative pressure. Region III can be described as the connection between Region II and the ground surface, where the wind speed is intensified and disrupted by the frictional interaction with the ground. Around Region IV is the surface boundary layer and Region V is where the tornado connects to the parent storm.

The violent wind speeds of a tornado are considered to be the most important parameter to study due to their damage potential. In 1971, Fujita (1971) introduced a scale to

measure the intensity of tornadoes based on the damage they inflict, known as the Fujita (F) scale. The Fujita scale can be divided into six categories in order of increasing intensity and maximum wind velocity, as shown in Table 2.1.

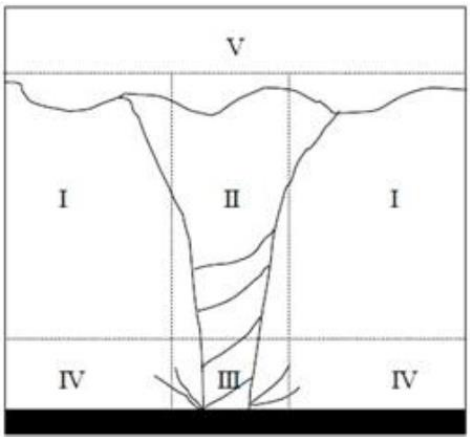

Figure 2.1: Tornado flow structure with categorised flow regions (Wurman et al., 1996)

The Fujita scale was initially widely adopted for tornado classification, but due to the overestimation of velocity (Grazulis, 1993), it was decommissioned in 2007 in favour of the Enhanced Fujita (EF) Scale, which provides a better correlation between tornado damage and maximum wind speed (NOAA, 2012). The comparison of the two scales are shown in Table 2.1.

According to the National Oceanic and Atmospheric Administration (NOAA) (2012), in 2011, 1704 tornadoes were reported in the USA, and the most common tornadoes were EF-0, EF-1 and EF-2, with 792, 631 and 197 reported tornadoes respectively, corresponding to the percentage of 46%, 37% and 12% respectively; while the severe tornadoes, EF-3, EF-4 and EF-5 only had 61, 17 and 6 reported tornadoes respectively, corresponding to the percentage of 4%, 1% and 0.35% respectively (Figure 2.2).

Table 2.1: The comparison of guest wind speed between Fujita and Enhanced Fujita scale (NOAA, 2012)

Fujita Scale		Enhanced Fujita Scale	
Fujita Scale (F)	3-second gust speed (m/s)	Enhanced Fujita Scale (EF)	3-second gust speed (km/h)
F-0	20-35	EF-0	29-38
F-1	36-53	EF-1	39-49
F-2	54-73	EF-2	50-62
F-3	74-94	EF-3	63-75
F-4	95-118	EF-4	76-90
F-5	119-142	EF-5	91-106

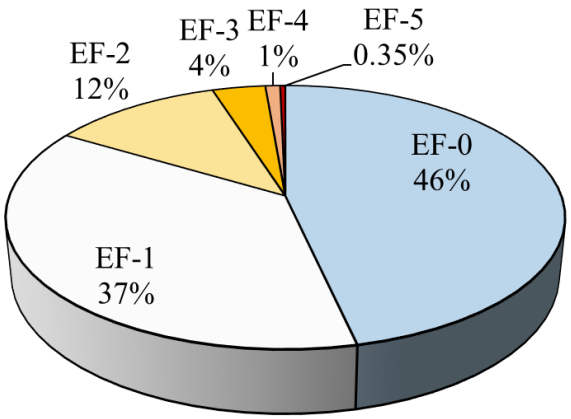

Figure 2.2: Percentage of reported tornadoes in USA in 2011. (NOAA, 2012)

2.1.2. Damages caused by tornadoes

To date, tornadoes have been reported on every continent except for Antarctica (NCEI, 2010). The most frequent and severe tornadoes tend to occur in the "plain states" of USA known as the Tornado Alley, which is generally considered to include Kansas, Dakota,

Oklahoma, Texas Panhandle, eastern South, Nebraska and eastern Colorado. The collision of contrasting air masses around these regions produce strong and violent thunderstorms (super-cells) which allows high potential of tornado development. Tornadoes can cause significant damage to properties and result in the loss of human live; the damage from tornadoes derives from the violent winds and the associated flying debris. These high winds can cause vehicles, tree branches, signboards and other (well fixed) objects to become wind-borne, turning into potentially lethal missiles. The USA in 2011, the total cost of tornado damage was approximately 28 billion dollars, and the total number of deaths due to this atmospheric disaster was 551, which was the highest in past 62 years (NOAA, 2012). Figure 2.3 shows the number of casualties due to tornadoes with different scales over the time period from 1880 to 2005. It can be observed that the severe tornadoes of more that F-4 (EF-5) results in the largest number of fatalities despite their rare occurrence (Figure 2.2); the number of casualties caused by weaker tornadoes (EF-0 to EF-2) have also been gradually increasing between the years 1960 to 1999.

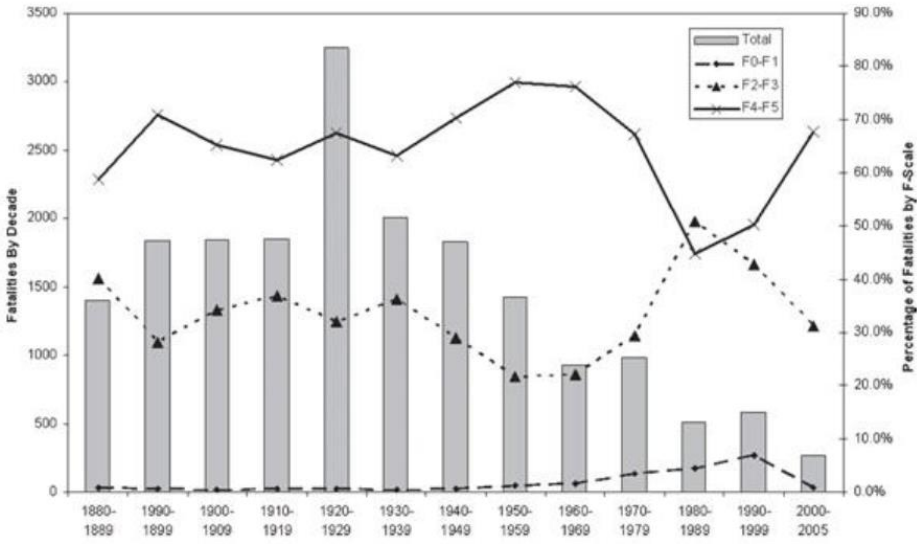

Figure 2.3: The number of fatalities by tornado with different Fujita scales (Ashley, 2007)

2.1.3. Full-scale tornado measurement

One of the primary difficulties in recording tornadoes is that a tornado, or evidence of its occurrence must have been formally recorded (NCEI, 2015). Contrary to temperature or rainfall which can be measured through a fixed instrument, tornadoes are relatively short lived and unpredictable; therefore, the chances of a tornado being documented if it occurs in a remote location where a small number of people reside is small. In recent years, with the increase in NOAA's Doppler weather radar coverage, as well as the increasing population coupled with the usage of smart phones and social media (Western University Department of Communications and Public Affairs, 2020), which were able to capture and document the occurrence of tornadoes, greater attention has been paid to tornado reporting (NCEI, 2015). Even if an actual tornado was not observed, current damage assessments are able to discern if the wind damage was caused by a tornado and provide an estimate of what the scale of that tornado may have been. Such an approach has led to an increase in the total number of tornadic events being captured particularly the smaller and weaker scaled tornadoes (EF-0, EF-1).

On 30 May 1998, Alexander and Wurman (2005) employed a mobile radar known as the Doppler on Wheels mobile radar to study the tornado that occurred in South Dakota. The utilisation of this mobile radar enabled detailed measuring of the wind speed, path and flow structure of the tornado. On 3 May 1999, an EF-5 scale tornado occurred in Oklahoma and Kansas (Lee and Wurman, 2005), the Doppler mobile radar was again deployed, providing field measurements of the tornado flow field and the horizontal profile of tangential velocity (Figure 2.4). The Doppler on Wheels mobile radar have been utilised in various different field campaigns such as the Verification of Rotation in Tornadoes Experiment (VORTEX) project, the Radar Observations of Tornadoes and

Thunderstorms Experiments (ROTATE) project, the Tactical Weather Instrumented Sampling Tornadoes Experiment (TWISTEX) and the Targeted Observation by Radars and UAS of Supercells (TORUS) project. Up to 2008, a total of 150 tornadoes have been measured using the Doppler on Wheels mobile radar (Alexander and Wurman, 2008), and has significantly improved the understanding of tornadoes.

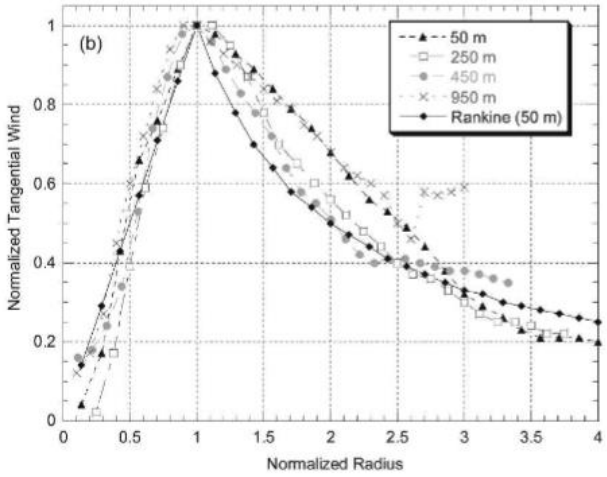

Figure 2.4: The normalised radial profiles of tangential velocity of the Munhall tornado. (Lee and Wurman, 2005)

Wurman et al. (2013) attempted to derive the data from the Doppler radar on wheels in order to obtain the three-dimensional flow field of the tornado and estimate the core radius. However, flow field measurements were only available from 50 m above the ground level, which limited its application for wind loading purposes. This was due to the flow fields being severely contaminated by ground clutter, making the near the ground radar sweeps particularly difficult, as demonstrated by Wurman et al. (2000) in a study on tornado flow field using Doppler radar on wheels. Kosiba and Wurman (2013) employed the Rapid-Scan Doppler On Wheels (RSDOW), which is radar scanning with multi-beam system that allows for fast mechanical azimuthal scanning of the environment at different

elevation angle within a shorter time period compared to the Doppler radar on wheels. The study provided a mapping of the three-dimensional structure and temporal evolution of the tornado boundary layer as low as 4 meters from the ground surface and showed that the tornado winds are significantly more intense near the ground than above. However, the Rapid-Scan Doppler On Wheels is required to be in close proximity to the tornado to be able to acquire high-resolution data.

Recently, alternative methods have been developed in order to measure the wind speeds of tornadoes; the TORUS project aims to further study the correlation between tornado genesis and severe thunderstorms (NOAA, 2019) by incorporating the use of light detection and ranging system (LIDAR) in order to acquire wind data for the investigation of the formation of tornadoes in severe thunderstorms. Wurman et al. (2007) utilised the Tornado Intercept Vehicle (TIV), an instrument mounted armoured reinforced vehicle that can within stand the strong winds of tornadoes to collect the data at the centre of an EF-2 tornado (Wurman et al. 2013). Several studies (Winn et al., 1999, Lee and Samaras, 2004, Karstens et al., 2010) have also utilised the method of deploying surface pressure probes in the path of tornadoes to obtain pressure data within tornadoes. However, this method can be difficult to set up due to the unpredictable path of the tornadoes and the inability to predict its path. Given the abovementioned difficulties observational methods, recourse is often made to models.

2.2. Modelling Tornado-like Vortices

Considering the difficulties associated with undertaking measurements from naturally occurring tornadoes, the modelling of tornadoes using analytical models, laboratory scaled experiments and numerical simulation are all alternative approaches which

researchers tend to use to study and quantify the characteristics of tornadoes. Laboratory simulations are safer for researchers due to the smaller scaled tornado-like vortices (and lower wind speeds) that are generated, while modelling vortices using CFD techniques offers the reproduction of the flow field in detail in comparison with the full-scale field measurements.

2.2.1. Analytical vortex models

The actual wind field of a tornado is very complex and can be difficult to describe; therefore, mathematical models are often used to approximate and predict the tornado flows. In recent years, much work has been carried out in order to develop analytical models to provide better understanding of the tornado wind field. Kuo (1971) developed a three-dimensional model of the boundary layer of a tornado-like vortex by solving the two nonlinear boundary-layer equations for the radial and axial distribution of velocities; the Bloor and Ingham vortex model (1987) is an exact inviscid solution of the Euler's equation in the confined conical domain; An analytical model of an inviscid tornado-like vortex was made by utilising free narrow jet solution and a modified Rankine vortex by Xu and Hangan (2009); however, it is worth noting that this is a combined model, and not an exact solution to the Navier-Stokes equations. Despite the many attempts, the Rankine vortex model, (Rankine, 1882), Burgers-Rott vortex model (Burgers, 1948; Rott, 1958) and Sullivan vortex model (Sullivan, 1959) are the most frequently used models to predict tornado flow behaviour. A recently proposed vortex model by Baker and Sterling (2017), hereafter refereed to 'Baker and Sterling vortex model' is also included in this review. A brief description and the underlying assumptions of the Rankine, Burgers-Rott, Sullivan and Baker and Sterling vortex models are outlined. The vortex models are expressed in terms of cylindrical coordinate system, where the subscripts t, r and z are

used to represent the angular position, radial distance and vertical height respectively; thus, U_t, U_r and U_z represents the tangential, radial and vertical velocity components respectively, while the subscript ˜ is used to represent the dimensionless velocity components.

Rankine vortex model

The Rankine vortex model (Rankine, 1882) is a two-dimensional vortex model that has been used to describe the distribution of tangential velocity of swirling flows such as hurricanes or tornadoes (Pan, 2013). The rotary vortex model only consists of azimuthal velocities and can be divided into two primary regions: the interior and the exterior flow field (Kilty, 2005). Giaiotti and Stel (2006) described the interior flow field of the vortex to rotate like a solid, therefore the azimuthal velocity has a linear relationship with the radial distance that reaches maximum magnitude at core radius; the velocity then decreases gradually in the exterior flow field in accordance with the radius. The Rankine vortex model is considered as one of the simplest model and has been adopted by numerous research (Church et al., 1979; Winn et al., 1999; Wurman and Gill, 2000; Mishra et al., 2008; Bech et al., 2009; Refan and Hangan, 2016; Tang et al, 2016) to model tornado-like flow pattern. The assumptions made for the derivation of this model are:

- The flow field is one dimensional
- The flow field is steady state
- The flow is inviscid
- Body forces such as gravity are neglected

The Rankine vortex model describes the tangential velocity with two separate regions, the velocity increases linearly from zero at the centre of the vortex to a maximum value, then and then decreases with the velocity component inversely proportional to the radial distance. The equation describing the distribution of velocity field is expressed in the form as followed:

$$\widetilde{U_t}(\tilde{r}) = \tilde{r}\ for\ (\tilde{r} \leq 1) \quad [2.1]$$

$$\widetilde{U_t}(\tilde{r}) = \frac{1}{\tilde{r}}\ for\ (\tilde{r} > 1) \quad [2.2]$$

where $\widetilde{U_t}(\tilde{r})$ is the normalised tangential velocity ($= U_t(r)/U_T$, where $U_t(r)$ is the tangential velocity distribution and U_T is the maximum value tangential velocity) and $\tilde{r}$ is the normalised radial distance ($= r/r_T$, where r is the radial distance and r_T is the radial distance where U_T occurs); the values of U_T and r_T are listed in Table 3.4. The normalised surface pressure distribution of the Rankine vortex model is expressed as:

$$\tilde{P}(\tilde{r}) = \widetilde{P_0} + \frac{1}{2}\tilde{r}^2\ for\ (\tilde{r} \leq 1) \quad [2.3]$$

$$\tilde{P}(\tilde{r}) = \widetilde{P_\infty} + \frac{1}{2}\left(\frac{1}{\tilde{r}}\right)^2\ for\ (\tilde{r} > 1) \quad [2.4]$$

where $\tilde{P}(\tilde{r})$ is the normalised pressure ($= P(r)/\rho {U_T}^2$, where $P(r)$ is the pressure distribution, ρ_a is the density of air and U_T is the maximum value of tangential velocity), $\widetilde{P_0}$ is the static pressure at the centre of the vortex and $\widetilde{P_\infty}$ is the free stream pressure, which is unaffected by the vortex. Details of the values for $\widetilde{P_0}$ and $\widetilde{P_\infty}$ are listed in section 3.4.

Burgers-Rott vortex model

The Burgers-Rott vortex model is a single-celled viscous vortex model created by Burgers (1948) and then extended by Rott (1958) 10 years later; it is a simplified exact solution to the Navier-Stokes equation (Kilty, 2005) that includes the pressure field, and the radial and vertical components of the vortex, thus allowing a more realistic prediction of the flow field of full-scale tornadoes (Batterson et al., 2007). The radial velocity is a function of the vortex radius and increases with radial distance, while the vertical velocity is a function of height and increases with height infinitely, as a result, both the radial and vertical velocity components are regarded as somewhat unrealistic (Refan, 2014). The Burgers-Rott vortex model has been adopted by numerous researchers (Winn et al., 1999; Brown and Wood, 2004; Lee at al., 2004; Kosiba and Wurman, 2010; Wurman et al., 2013) to model tornado-like flow pattern. The assumptions made for the derivation of this model are stated as followed:

- It is a steady state flow field
- The viscosity remains constant throughout the entire flow field
- Body forces such as gravity are neglected

The equation for the normalised tangential velocity is expressed in the form:

$$\widetilde{U_t}(\tilde{r}) = \frac{\Gamma}{2\pi\tilde{r}}\left[1 - exp\left(\frac{\tilde{r}^2 a_{Burgers} Re_\gamma}{2\Gamma}\right)\right] \qquad [2.5]$$

where $\widetilde{U_t}$ is the normalised tangential velocity ($= U_t(r)/U_T$, where $U_t(r)$ is the tangential velocity distribution and U_T is the maximum value of tangential velocity), $\tilde{r}$ is the normalised radial distance ($= r/r_T$, where r is the radial distance and r_T is the radial distance where U_T occurs), Γ is the circulation at infinity, Re_γ is the vortex Reynolds

number ($= \Gamma/\nu$, where ν is the viscous dissipation) and $a_{Burgers}$ is a constant, expressed as:

$$a_{Burgers} = \frac{2\nu}{r_T U_T} \quad [2.6]$$

The viscous dissipation, ν is responsible for removing the kinetic energy from the flow by introducing vortex stretching (the values of U_T and r_T are listed in Table 3.4 and the value for ν is listed in section 3.4). The pressure distribution of Burgers-Rott model is obtained by solving the Navier-Stokes equation using the velocity components stated above, obtaining the form of:

$$\tilde{P}(\tilde{r},\tilde{z}) = \tilde{P}(0,0) + \int_0^r \frac{\widetilde{U_t}(\tilde{r})^2}{\tilde{r}} d\tilde{r}' - \frac{a_{Burgers}^2}{2}(\tilde{r}^2 + 4\tilde{z}^2) \quad [2.7]$$

where $\tilde{P}(\tilde{r},\tilde{z})$is the normalised pressure ($= P(r,z)/\rho {U_T}^2$, where $P(r,z)$ is the pressure distribution, ρ_a is the density of air and U_T is the maximum value tangential velocity), $\tilde{z}$ is the vertical height ($= z/r_T$, where z is the vertical height) and $\tilde{P}(0,0)$ is the static pressure at the centre of the vortex. Details of the value for $\tilde{P}(0,0)$ is listed in section 3.4.

Sullivan vortex model

Similar to the Burgers-Rott vortex model, the Sullivan model (Sullivan, 1959) is also an exact solution to the Navier-Stokes equations that includes the pressure field, and the radial and vertical components of the vortex. The Sullivan model considers the stages of vortex evolution, which incorporates the single-celled vortex model and two-celled vortex model. The radial velocity component of the model increases with respect to the radial distance infinitely, i.e., it is unbounded, while the vertical velocity increases to the maximum magnitude and remains constant with the increase of radial distance (Kilty,

2005). Thus, both the radial and vertical velocity components are also regarded as somewhat unrealistic (Kilty, 2005). The Sullivan model has been adopted by several researches (Winn et al., 1999; Wood and Brown, 2011) to model tornado-like flow pattern. The assumptions made for the derivation of this model are stated as followed:

- It is a steady state flow field
- The viscosity remains constant throughout the entire flow field
- Body forces such as gravity are neglected

In order to reduce the complex mathematical definition of the formulated tangential velocity, Wood and Brown (2011) found that the velocity profile can be simplified by fitting parametric equation. As a result, the tangential velocity can be expressed as:

$$\widetilde{U_t}(\tilde{r}) = \left(\frac{\tilde{r}}{r_T}\right)^{2.4} \left[0.3 + 0.7\left(\frac{\tilde{r}}{r_T}\right)^{7.89}\right]^{-0.435} \quad [2.8]$$

where $\widetilde{U_t}$ is the normalised tangential velocity ($= U_t(r)/U_T$, where $U_t(r)$ is the tangential velocity distribution and U_T is the maximum value of tangential velocity) and $\tilde{r}$ is the normalised radial distance ($= r/r_T$, where r is the radial distance and r_T is the radial distance where U_T occurs). The values of U_T and r_T are listed in Table 3.4). The surface pressure distribution of the Sullivan vortex model is expressed as:

$$\tilde{P}(\tilde{r},\tilde{z}) = \widetilde{P_{Burgers}}(\tilde{r},\tilde{z}) - \frac{18\nu^2}{\tilde{r}^2}(1-\exp(-\tilde{r}^2))^2 \quad [2.9]$$

where $\tilde{P}(\tilde{r},\tilde{z})$is the normalised pressure ($= P(r,z)/\rho {U_T}^2$, where $P(r,z)$ is the pressure distribution, ρ_a is the density of air and U_T is the maximum value tangential velocity), $\tilde{z}$ is the vertical height ($= z/r_T$, where z is the vertical height) and $\tilde{P}_{Burgers}(\tilde{r},\tilde{z})$ is the

pressure obtained from Burgers-Rott model (equation [2.7]) and ν represents the viscous dissipation. Details of the value for ν is listed in section 3.4.

Baker and Sterling vortex model

The Baker and Sterling vortex model is an inviscid analytical vortex model created by Baker and Sterling (2017) and the exact solution to the Navier-Stokes equations. The model describes the distribution of the velocity and pressure fields of both a single and two-celled vortex, as well as the prediction of the inflow towards the tornado and the upflow in the tornado core. The radial velocity is assumed to be dependent on only the radial and vertical velocity, where it reaches a maximum magnitude and then falls to zero rather than increasing to infinity for larger radial distance; in the vertical direction, the model attempts to replicate tornado boundary-layer by assuming a maximum in the radial velocity component at a known elevation above the ground surface. The model is considered a significant improvement over other existing methods due to the radial and vertical velocity components show a more realistic behaviour and was adopted by numerous researchers (Baker and Sterling, 2018; Gillmeier, 2018) to model tornado-like flow pattern. The assumptions made for the derivation of this model are stated as followed:

- It is a steady state flow field
- The flow is inviscid
- Body forces such as gravity are neglected

Apart from the complexity of the Baker and Sterling model as compared to the other analytical models, the Baker and Sterling model utilises γ, as a shape parameter, an arbitrary number that can adjust the shape of the circumferential velocity profile. The tangential velocity is expressed as followed:

$$\widetilde{U_t}(\tilde{r},\tilde{z}) = \frac{K_{bs}\tilde{r}^{\gamma-1}[\ln(1+\tilde{z}^2)]^{\frac{\gamma}{2}}}{(1+\tilde{r}^2)^{\frac{\gamma}{2}}} \quad [2.10]$$

where $\widetilde{U_t}$ is the normalised tangential velocity ($= U_t(r)/U_T$, where $U_t(r)$ is the tangential velocity distribution and U_T is the maximum value of tangential velocity), $\tilde{r}$ is the normalised radial distance ($= r/r_T$, where r is the radial distance and r_T is the radial distance where U_T occurs), $\tilde{z}$ is the vertical height ($= z/r_T$, where z is the vertical height) γ is a shape parameter and $K_{bs}$is a constant expressed as:

$$K_{bs} = 2.88 \times S_{Baker\ \&\ Sterling} \quad [2.11]$$

where $S_{Baker\ \&\ Sterling}$ is the swirl ratio, defined the swirl ratio as ratio the between the maximum value of tangential velocity to the maximum value of the radial velocity, as:

$$S_{Baker\ \&\ Sterling} = \frac{U_T}{U_{rmax}} \quad [2.12]$$

where U_T is the maximum value tangential velocity component and U_{rmax} is the maximum value of radial velocity component (details for the values of U_T and r_T are listed in Table 3.4). The normalized surface pressure distribution of the Baker vortex model is expressed as:

$$\tilde{P}(\tilde{r},\tilde{z}) = \frac{8\tilde{r}^2\tilde{z}}{(1+\tilde{r}^2)^2(1+\tilde{z}^2)^2} - \frac{4.15S^2(\ln(1+\tilde{z}^2))^2}{(1+\tilde{r}^2)} - \frac{4\ln(1+\tilde{z}^2)\,(1-\tilde{z}^2)}{(1+\tilde{r}^2)^2(1+\tilde{z}^2)^2} \quad [2.14]$$

where $\tilde{P}(\tilde{r},\tilde{z})$is the normalised pressure ($= P(r,z)/\rho {U_T}^2$, where $P(r,z)$ is the pressure distribution, ρ_a is the density of air and U_T is the maximum value tangential velocity), $\tilde{z}$ is the vertical height ($= z/r_T$, where z is the vertical height). The study conducted by Gillmeier (2017) compared the analytical models with the flow field of a physically simulated tornado and showed that the Burgers-Rott and Sullivan vortex model are able

to provide reliable prediction of tangential velocity component, but fail to replicate the radial and vertical velocity components due to the absence of bounds in the radial and vertical direction; the Baker and Sterling vortex model shows a very good replication of flow field near the ground, but fails for greater elevation. Overall, the analytical models were able to replicate some parts of the tornado flow field such as the tangential velocity and pressure field but fails to represent the entire three-dimensional vortex flow structure. Therefore, the tangential velocity and the surface pressure distribution of the analytical models (Rankine, Burgers-Rott, Sullivan and Baker and Sterling) are used as a comparison in this study.

2.2.2. Physical vortex generators

The earliest laboratory experiment for generating tornado-like vortices can perhaps be attributed to Ward (1972); the simulator was designed with fans placed atop a convection chamber to generate an updraft flow; immediately below the convection chamber was the convergence chamber; a series of guide vanes were placed at the edge of the convergence chambers near the ground that can be adjusted at different angles (Figure 2.6 (a)). By changing the guide vane angle, the angular momentum of the inflow and the swirl ratio (details in section 3.1.1) can be altered and different vortex flow structures can be generated. A full discussion of the swirl ratio is given in Chapter 3 (section 3.1.1), but for the current purposes can simply be assumed to be the ratio of the circulation around the vortex to the updraft strength, and therefore is a measure of the amount of mass rotating around the circulation centre. The ratio between the diameter of the updraft hole and the height of the inlet is defined as the aspect ratio (further details in section 3.1.1). Jischke and Parang (1974) studied the properties of simulated tornadoes based on Ward's (1972) simulator and used the core radius of the vortex as a characteristic parameter for the

scaling of laboratory scaled model to full scale tornadoes. They also suggested three primary parameters for tornado simulation, namely the swirl ratio, aspect ratio, and vortex Reynolds number (details in section 3.1.1).

Church et al. (1977) constructed a large-scale generator based on Ward's (1972) design at Purdue University (Figure 2.6 (b)), which allows an easier control of aspect ratio, swirl ratio and vortex Reynolds number by enabling the adjustment of the height of the inflow as well as the diameter of the exhaust outlet. The study successfully reproduced the vortex evolution, from single-celled vortex stage into a four vortices configuration. Lugt (1989) describes vortex evolution with different stages; at low swirl ratio ($S \approx 0.1$), the tornado vortex is a jet-like flow known as single-celled vortex (Figure 2.5 (a)). The increase in swirl ratio ($S \approx 0.4$) results in the breakdown of the vortex core into turbulent flow (Figure 2.5 (b)). The turbulent vortex core moves downwards and touches the surface with the increase of swirl ratio ($S \approx 0.8$) resulting in the formation of two-cell vortex (Figure 2.5 (c)). A further study of vortex evolution was conducted by Church et al. (1979). Church et al. (1979) examined various different vorticies from the swirl ratio of 0 to 1 and studied the transition point in which the vortex evolves from single-celled vortex to double-celled vortex, and then from double-celled vortex to triple-celled vortex configuration. The study found that the characteristics of tornadoes can be summarised as a function of swirl ratio and vortex Reynolds number.

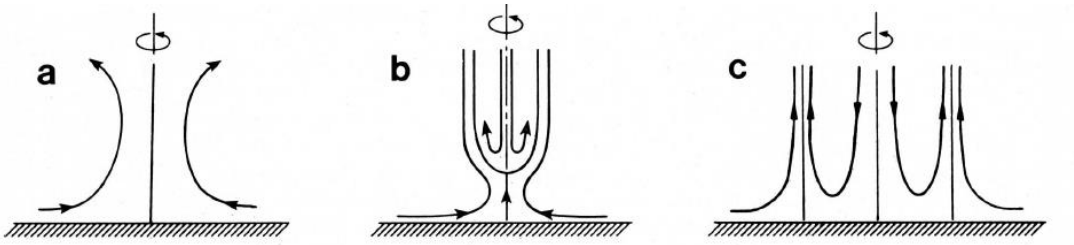

Figure 2.5: Sketch of the vortex flow observed at various vortex stages; (a) Single-celled vortex, (b) vortex breakdown stage, (c) two-celled vortex (Lugt, 1989).

Mitsuta and Monji (1984) also developed a vortex simulator by replacing the guide vanes with four small fans in the convergence chamber for the generation of angular momentum (Figure 2.6 (c)). The transition of vortex from one-cell to two-cell structure was studied, and it was found that the maximum tangential velocity occurs very close to the ground surface, and the elevation of the location of maximum tangential velocity appears to be independent of swirl ratio. Cleland (2001) simulated tornado-like vortices using the Miami University Tornado Vortex Chamber and highlights the complex flow structure of the vortex core and suggested that the instability of the position of core is dependent on the swirl ratio, in which can result in the sudden shift in diameter of the core. Tari et al. (2010) employed Particle Image Velocimetry (PIV) and measured the mean and turbulent flow fields for a range of vortices with progressing swirl ratios generated using a Ward (1972) type simulator. Tari et al. (2010) concluded that the swirl ratio is a crucial parameter that characterises the dynamics of the vortex flow, and argued that rather than the mean flow field, the instantaneous turbulent flow is responsible for most of the damage associated with tornado events close to the ground.

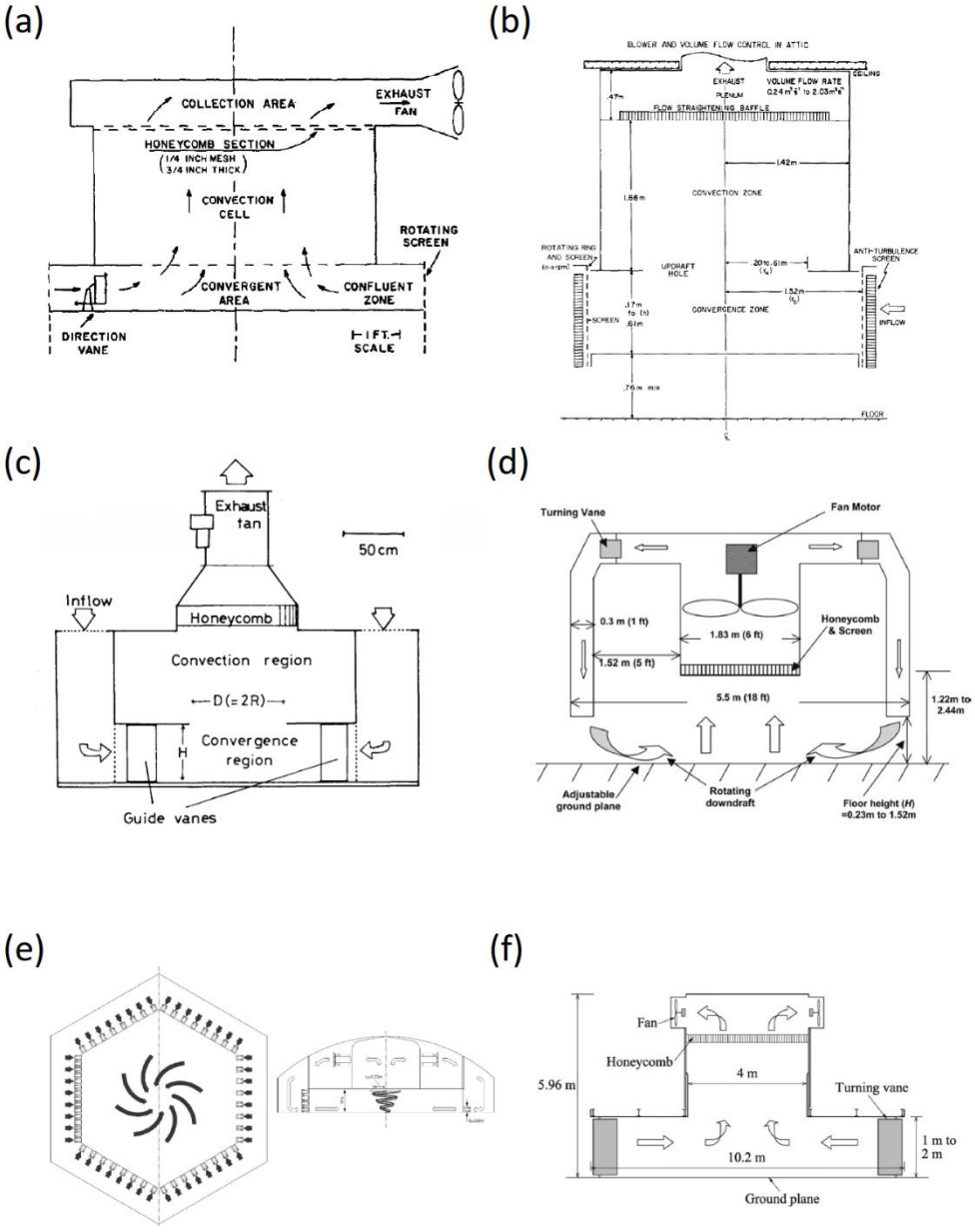

Figure 2.6: Different tornado generator design (a) Ward (1972) (b) Church et al. (1977) (c) Mitsuta and Monji (1984) (d) Haan et al. (2008) (e) Refan and Hangan (2018) (f) Tang et al. (2018).

Recently, the Iowa State University (ISU) research group developed a new tornado simulator (Figure 2.6 (d)) designed to simulate more realistic tornadoes which can accommodate larger structural models for tornado-wind engineering applications (Sarkar

et al., 2005, Haan et al., 2008). The simulator consists of a central fan that produces updraft flows, which are deflected by the guide vanes, providing the angular momentum to the flow, before being redirected downwards through a circular duct. The entire simulator is suspended on a crane off the ground in which allows the simulator to be adjustable in heigh and translated along a 10 m ground plane. The ISU simulator has shown the ability to reproduce one-celled and two-celled vortex structure (Haan et al., 2008), where the general flow structure and normalized velocity field showed excellent match with the May 1998, Spencer tornado (Wurman and Alexander, 2005) and the May 1999, Mulhall tornado (Lee and Wurman, 2005). Haan et al. (2010) examined the wind loadings of a 1:100 scale gable-roof building using the ISU simulator, and discovered that the peak values generally exceeds the recommended design loads for buildings situated in the "tornado alley" in the USA. Hu et al. (2011) further studied the tornado flow structure around the same gable-roof building using PIV and found that the wake structure around the building was different to the wake that were typically observed during severe wind events such as downbursts.

In 2011, the Wind Engineering, Energy and Environment (WindEEE) Research Institute at the University of Western Ontario in Canada, built a large-scale testing chamber that allows the generation of tornadoes (Refan and Hangan, 2018). The simulator has a hexagonal chamber that is fitted with 100 fans. For the generation of tornadoes, 8 fans at the bottom of each walls are used, where guide vanes are placed in front of every fan in order to provide the required angular momentum; a suction hole with 6 fans are situated at the top of the chamber to provide updraft (Figure 2.6 (e)). Refan et al. (2014) conducted PIV measurements for varying swirl ratios are compared the results with full-scale tornado measurements. They found that the swirl ratio of 0.1 and 1.3 appears to

correspond to the full-scale EF0 to EF3 tornadoes and suggested that the mini WindEEE dome could supposedly reproduce vortices similar to full-scale tornadoes. However, as discussed by Baker and Sterling (2019), to date, proper scaling cannot be obtained in simulators as the EF-scaling does not relate to the vortex structures as observed in the simulators. As a result, although the results presented by Refan et al. (2014) showed some similarities with the full-scale measurements, it does not fully replicate a naturally occurring tornado. Nonetheless, further investigation of tornado-like vortices using the WindEEE dome were conducted by Refan and Hangan (2016) and demonstrated that the simulator was also capable of generating vortices with one-celled and two celled structures with swirl ratios ranging from 0.1 to 1.3. Refan and Hangan (2018) examined the evolution of vortex structure using the WindEEE dome and investigated the flow field using PIV. It was found that the lower the swirl ratio of the vortex, the greater the vortex wandering. Additionally, by combining the range of radial Reynolds number tested with the mini WindEEE dome, from 1.6×10^4 to 2×10^6, it was concluded that the average pressure measurements are independent for Reynolds number greater than 4.5×10^4.

In 2009 at the Texas Tech University, a large-scale Ward type simulator, VorTECH was also developed (Tang et al., 2018). Compared to the other previous Ward type designs (Ward, 1972; Church et al., 1977; Mitsuta and Monji, 1984), the VorTECH simulator has honeycomb covering the updraft hole as well as the entire section of the convection chamber and all 64 guide vanes have a symmetric airfoil shape (Figure 2.6 (f)). Tang et al. (2018) examined the transition between the vortex structure from one cell to two celled vortex structure and matched the surface pressure of a range of swirl ratios (0.1 to 0.78) to three full-scale tornado measurement.

The studies conducted by the aforementioned researchers and others provided insight to tornado flows and demonstrated the importance of the swirl ratio, aspect ratio and vortex Reynolds number to the characteristics of tornado-like vortices. However, in view of the limitations of current observational methods, it is difficult to obtain detailed three-dimensional measurements in the boundary layer, which is thought to be an important region in tornado-like vortices. Moreover, due to the complex flow at the centre of the vortex, accurate measurements of the core often result in high experimental uncertainties. Furthermore, among all the laboratory scaled simulators, the definition of the swirl ratio can differ. Thus, modelling tornadoes using CFD techniques offers an alternative method to study the flow field.

2.2.3. Numerical vortex generators

With the recent advancement in computer technology and the development in CFD, an increasing number of studies have been conducted using numerical simulators to study tornado flows. The numerical simulation of tornado-like vortices can generally be categorized into three types; the first approach is by solving the axisymmetric Navier-Stokes equations in two-dimensional cylindrical coordinates. Rotunno (1977) numerically simulated tornado-like vortices at different swirl ratio and validated with the experimental results by Ward (1972); it was found that when the vortex core experiences breakdown, there will be expansion and tendency towards a wandering motion. Nolan and Farrell (1999) studied the flow structure and dynamics of tornado-like vortices and the effects of vortex Reynolds number; it is concluded that the flow structure of a tornado is dependent on the Reynolds number. However, these two-dimensional axisymmetric models experiences difficulties in reproducing the vortices at higher swirl ratios as the vortex flow structure experiences a wandering motion, and is no longer asymmetrical,

thus cannot be simulated with a two-dimensional axisymmetric model. (Hangan and Kim, 2006).

The second approach is to conduct full scale simulation that models the three-dimensional tornado flow structure with emphasis on the interaction between the tornado-like vortex and the ground surface. Lewellen et al. (1997) conducted LES simulation of a full-scale tornado to study the ground surface interaction and the characteristics of a tornado. It was found that the maximum tangential velocity at the near ground surface boundary layer was 60% larger than the maximum tangential velocity in the convection region. Lewellen et al. (2000) simulated a range of tornadoes with different swirl ratios in nature to study the characteristics and flow structures. The definition of a corner swirl ratio was proposed, which is the ratio between circulation per unit height in the core region and the outer region, calculated based on the maximum tangential velocity that is found closed to the ground. Lewellen and Lewellen (2007) analysed the near surface intensification in detail and concluded that the local swirl ratio determines the core flow structure in tornadoes. These full-scale simulations provide researchers with some insight to the flow structures of full scale the tornadoes, however, they are limited by the lack of data from naturally occurring tornadoes.

The final approach is to model tornado-like vortices using laboratory scaled numerical simulator. Kuai et al. (2008) conducted a series of numerical simulations using the Iowa State University (ISU) Laboratory Simulator (Figure 2.7) in comparison with full scaled tornadoes in order to verify the capabilities of a CFD model to capture the flow features and characteristics of tornadoes. Results from the simulation showed that the increase of swirl ratio results in the increase of vortex core radius but decrease in the maximum tangential velocity; it was also concluded that the flow field produced by numerical

simulators corresponds very well with physical simulators but was only able to reproduce some of the features of full scaled tornadoes.

Hangan and Kim (2008) performed unsteady Reynolds averaged Navier-Stokes (URANS) simulation to investigate the effects of swirl ratio to tornado-like vortices using a Ward type tornado-vortex chamber (TVC). The simulations showed the vortex core size to be a function of swirl ratio and confirmed that the swirl ratio describes different stages of vortex evolution; a comparison with full scale data was attempted by scaling up the radial length and the maximum tangential velocity at a selected elevation. It was found that the Fujita scale of F4 corresponds with the swirl ratio of 2. However, as only the tangential velocity component was considered in the comparison, as well as the limited full-scale data measured by Doppler radar (Wurman, 1998), the correlation between Fujita scale and swirl ratio is deemed as somewhat unrealistic.

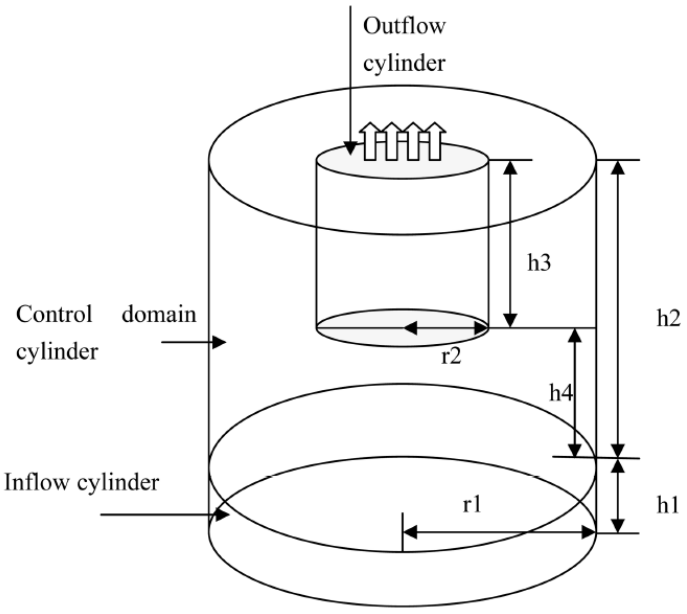

Figure 2.7: Computational domain of the Iowa State University Laboratory Tornado/Microburst Simulator. (Kuai et al., 2008)

Ishihara et al. (2011) conducted a study on the flow fields of two tornado-like vortices using numerical Ward type simulator (Figure 2.8). The numerical results were compared with experimental data obtained from laboratory simulation. It was found that single-cell type vortices have central upward flow while two-cell type vortices with downward flow at the centre. The maximum tangential velocities were observed to occur near the ground surface. Natarajan (2011) also attempted to numerically simulate different stages of a tornado with the objective of capturing the behaviour and characteristics of the evolution of the vortex. The simulated results were compared with different laboratory scaled experimental data for validation. It was found that for lower swirl ratio, the tornado flow appears to be single-celled vortex with high magnitude of vertical and radial velocity at the centre while tangential velocity appears to be maximum at the boundaries of the vortex core. As the swirl ratio increases, the intensity of the vortex core increases and the location of the maximum magnitudes of tangential, radial and vertical velocity components gradually shifts to the boundaries of the vortex core. The further increase in swirl ratio will allow the entire vortex core to penetrate to the base thus forming two-celled vortex. Overall, it was found that the LES model was able to accurately reproduce vortices at all swirl ratios, which was not the case with the Reynolds stress model (RSM).

By using LES model, Liu and Ishihara (2012) attempted to reproduce vortex evolution from single-celled vortex into a two-cell vortex configuration and analysed all vortex characteristics. It was found that the greatest magnitude of the maximum tangential velocity occurs at the vortex breakdown stage, and after which, the magnitude of maximum tangential velocity remains almost constant with the increase in swirl ratio. Phuc et al. (2012) studied the translational effects of a moving tornado-like vortex on a cube. The vortex was generated using a numerical movable tornado simulator where the

wind pressure distribution around a cube building was recorded. It was found that in a stationary tornado-like vortex, the wind pressure acting on all surfaces of the cube surface remained almost constant in time but changed drastically when the vortex was translated. This is due to the whirling wind flow generated from a moving tornado around the cube, resulting in the high-pressure difference.

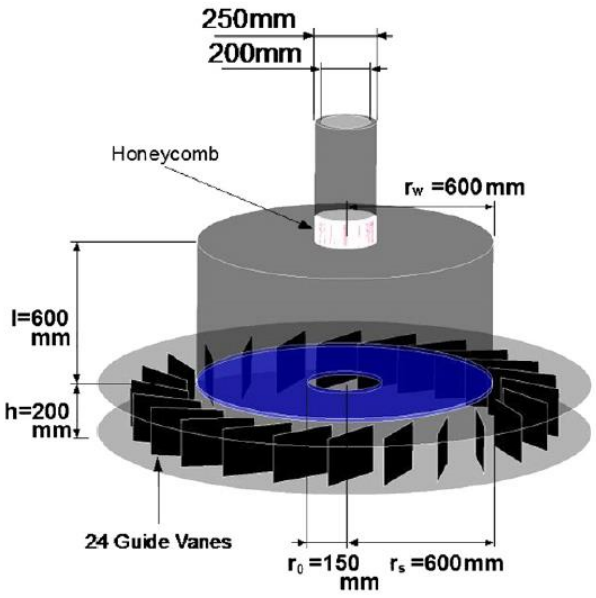

Figure 2.8: Overview of the numerical ward type tornado simulator. (Ishihara et al., 2011)

Ishihara and Liu (2014) investigated tornadoes at the vortex touch down stage with the dynamics of tornadoes and detailed description of the flow field. The mechanism of the vortex was studied, and an organised swirl of the vortex was observed; the source of the swirl was found to be the radial and tangential components of the vortex. Liu and Ishihara (2015) further investigated the characteristics of tornadoes at different stages, from laminar single-celled vortex, vortex break down, vortex touch down and multi vortex, and provided detailed information on the turbulent flow field of each vortex stages. The similarity between the numerically simulated vortices and full-scale tornadoes were

examined and suggested that the translation speed of the tornado must be taken into account in order to fully reproduce the flow field of the full-scale tornadoes. Nasir and Bitsuamlak (2016) examined the hill effects on the flow structure and ground surface pressure of the tornado-like vortex. A one-celled vortex corresponding to a naturally occurring EF-2 scale tornado was generated using a numerical Purdue tornado simulator. Two types of hills with different slopes were implemented at the centre of the simulator in order to investigate the impact of topographical changes. It was found that the maximum velocity of the vortex occurs slightly away from the peak of the hill while the overall the flow structure as well as the distribution of surface pressure were not affected by the presence of the either types of the hill. Liu et al. (2018) examined a tornado-like vortex at the sub-critical breakdown stage by using LES model and provided detailed description of the flow field. The mechanism of the vortex was revealed by examining the fluctuating components of the flow field, and it was found that the tangential fluctuation and the radial fluctuation have similar amplitude, resulting in the balance of flow structure. Spectral analysis was conducted on the velocity components at different heights in order to quantify the strength of the vortex motion, and it was observed that the offset between the instantaneous centre and the centre of the simulator is the largest at z =0.1 h; the offset decreases with the increase in elevation and the two centres intersects after the elevation of 0.5 h.

Recently, Yuan et al. (2019) attempted to numerically simulate a tornado generator that allows the translation of tornadoes. The numerical simulator was created based on the design of the tornado generator in ISU, where the entire central fan, guide vane and circular duck are suspended off the ground which allows for the ground plane to be translated; all major components including the fan, honeycomb and guide vane regions

of the tornado generator were numerically modelled. Two tornado-like vortices with the swirl ratio of 0.6 and 0.89 were generated, and the flow field were compared with the data obtained from the physical tornado simulator in ISU. It was demonstrated that the numerical simulator is capable of reproducing vortices similar to tornadoes generated the physical simulator. However, as noted by the authors, additional research is still required as the model requires further validation for tornadoes with different flow structures. Liu et al. (2020) investigated the effects of Reynolds number on the flow fields of tornado-like vortices. Two tornado-like vortices with the swirl ratio of 1.0 and 4.0 with Reynolds number ranging from ranging from 1.6×10^3 to 1.6×10^6 were systematically examined. It was found that the turbulence region near the ground for the vortex with higher swirl ratio does not vary significantly with the increase of Reynolds number. Overall, it was observed that the location of maximum radial velocity increases radially outwards with the increase in Reynolds number for vortices with all swirl ratios. Further, the radial fluctuation was found to increase linearly with Reynolds number, while organised wandering of the vortex structure was observed in all simulated cases.

Details of the configuration of the computational domains, number of cells, type of numerical simulator used to generate the tornado-like vortices, as well as the swirl ratio, vortex Reynolds number and turbulence models used in the previously mentioned studies are listed in Table 2.2. In general, the Ward type generator is the mostly used numerical simulator, while the LES was found to be the most suitable model to accurately reproduce vortices at all swirl ratios. However, among all the numerically simulated tornado-like vortices, the inclusion of guide vanes, as well as the correlation between swirl ratio and vortex stages were inconsistent as the definition of swirl ratio varies from one to another. Additionally, due to the limitations in full scale measurements, a reliable correlation

between lab scaled tornadoes and full-scale tornadoes have yet to be established. A recent study by Gairola and Bitsuamlak (2019) attempted to develop a generalised numerical tornado model that can represent several existing physical tornado simulators. The complexity of the physical simulators were reduced by simplifying physical elements such as guide vanes and ceilings, while directly using the geometric properties of physical elements as a measure of parameters required to characterize the vortex flow field. It was concluded that while the developed numerical tornado model is able to reproduce the flow-field of the original physical simulators, the inlet boundary condition and dimensions of the model varies from one to other and requires very careful specifications of characterizing parameters in order to ensure that the generated vortex flow fields are similar to the physical tornado simulators. Therefore, the numerical simulator used in current study was created with the presence of guide vanes and exact dimensions to the physical simulator in order to retain geometric similarity.

Overall, the numerical studies carried out by the abovementioned researchers and others showed that LES is the suitable model to accurately reproduce vortices and is subsequently employed for the simulation of the vortex flow field.

Table 2.2: Configurations and parameters of the numerical simulators used by previous research

Vortex generator	Simulation	Swirl ratio	Re	Domain size	Guide vanes	Number of Cells
ISU Laboratory Simulator (Kuai et al., 2008)	URANS	0.02 - 1.65	1,963,261 - 5,509,378	1.3D×1.3D×2.3D	no	25,404 - 4,432,686
Ward type TVC (Hangan and Kim, 2008)	URANS	0.1 - 2.0	N/A	1D×1D×0.5D	no	152,538
Ward type Simulator (Ishihara et al., 2011)	LES	0.31, 0.65	163,000	10D×10D×4D	yes	≈700,000
Ward type TVC (Natarajan, 2011)	RSM, LES	0.2 - 2.0	2,251,656 - 6,622,517	1D×1D×5.2D	no	150,000 1,000,000 1,750,000
Ward-type Simulator (Liu and Ishihara, 2012)	LES	0.02, 0.06, 0.23, 2.44	160,000	10D×10D×4D	yes	784,200
Ward-type Simulator (Phuc et al., 2012)	LES	0.65	133,000	5.4D×5.4D×2.7D	no	779,000
Ward-type Simulator (Ishihara and Liu, 2014)	LES	0.65	163,000	10D×10D×4D	yes	610,497
Ward-type Simulator (Liu and Ishihara, 2015)	LES	0.02, 0.06, 0.23, 2.44	160,000	10D×10D×4D	no	784,200
Ward-type Simulator (Nasir and Bitsuamlak, 2016)	RSM	0.4	N/A	1D×1D×2.6D	no	N/A
Ward-type Simulator (Liu et al., 2018)	LES	0.6	160,000	10D×10D×4D	no	780,000
ISU simulator (Yuan et al., 2019)	LES	0.47, 0.6, 0.89	5,500,000 - 6,500,000	1D×1D×0.5D	yes	89,000
Ward-type Simulator (Liu et al., 2020)	LES	1.0, 4.0	1,600 - 1,600,000	10D×10D×4D	no	8,300,000

2.3. Wind-borne Debris

Wind-borne debris can typically be referred to any loose items such as tree branches, failed building components, utility poles and vehicle parts that are being picked up and transferred by strong wind events. Flying debris have been recognised as a primary cause for the breaching of building envelope during severe wind event (Minor, 1994). While most buildings are traditionally designed to withstand wind pressure loading, breakage from impacts by wind-borne debris can lead to the failure of the building structure. According to Holmes (2010), the observational study on the wind damage caused by severe storms suggest that flying debris can cause nearly the same amount of damage as direct wind-loading on buildings in urban environments. The damage assessment of severe windstorms in the UK reported that the costliest tornado in the UK to date was the Birmingham Tornado that occurred in 2005, which caused £30 million worth of damage. The primary cause of damage in the downstream structure is by the wind-borne debris generated from the upstream structures. (Marshall and Robinson, 2006). Additionally, flying debris also poses substantial risk to human lives during strong wind events; Katsura et al. (1992) reported that among the 63 fatalities due to Typhoon Mireille that occurred in Japan in 1991, 20 were blown by wind, 19 were due to collapsed or blown structures and 15 were struck by wind-borne debris.

2.3.1. Modelling debris flight

Identifying the debris is the initial step in modelling flying debris and the damage problem. Wind-borne debris can generally be categorised into light, medium and heavy weight missiles based on the recorded damage performance (Bailey, 1984). The light-weight missiles primarily break windows, small tree branches, damage building finishes. The

medium-weight missiles can penetrate walls and fences; these include objects such as timber planks or utility poles. Heavy missiles may include vehicles or storage tanks that can cause major structural damage. Minor (1994) conducted a study on the glazing breakage of tall buildings in urban environments, and categorised wind-borne debris based on their potential impact height on buildings based on the size of the missiles. According to Wills, et al. (2002), debris can be classified based on its geometric configuration as compact type (3D), plate type (2D) and rod type (1D) missiles. Compact type debris are three dimensional and near-spherical objects that includes gravels or vehicle components; plate type debris are sheet-like objects such as roof tiles, cladding elements or roofing sheets; rod type debris are typically larger objects like timber pieces or logs. These classifications in terms of identifying the three generic debris types are widely accepted today by most researchers.

In the 1970's, numerous models for missile trajectories in tornadoes were developed based on the assumptions about debris aerodynamics; these assumptions differ with levels of complexity. The simplest missile model was developed by Simiu and Cordes (1976) that considered only the drag force on the debris to account for random tumbling. The motion of these missiles were governed exclusively by the gravitational force and drag force. Lee's model (1974) for tornado induced missiles included lift force and considered both lift and drag coefficient on the missile as constants. Twisdale et al. (1979) developed a three-dimensional model that considered lift, drag and side force that depends on the orientation of the missile with respect to the wind vector. Redmann et al. (1976) later developed a six-dimensional trajectory model that further included the pitching, yawing and rolling moments on the missile. While these studies undertaken provides insight to

the aerodynamic characteristics of tornado induced missiles, the missile models were not validated by laboratory experiments.

Tachikawa (1983) was the first to study plate aerodynamics by combining wind-tunnel experiments with numerical simulation The lift force, drag force and moment coefficients of rotating plates were measured and expressed as a function of rotational velocity and then numerically simulated; the calculated trajectories were then compared with experimental trajectories. Tachikawa also suggested the dimensionless ratio between the weight of the debris to the inertial forces of the flow, which is known today as the Tachikawa number, K, after the proposal from Holmes, et al. (2006). The Tachikawa number can be used to describe the characteristic and trajectory for a given debris type, in which a larger value of K would indicate a higher propensity to travel further and faster.

Holmes (2004) studied the trajectory of three-dimensional spherical compact debris and concluded that it is the simplest type of debris to consider as only the drag force is relevant; the flight trajectory of the compact debris were also studied under severe wind conditions. It was found that the drag resistance was significant to the vertical motion as it increases the flight duration, horizontal velocity and displacement. In the same year, Holmes et al. (2004) solved the trajectories of flat plates by utilising a quasi-steady assumption of lift, drag and moment coefficients as functions of angle of attack. In the study, the force coefficients of both compact debris and flat plate debris obtained from numerical simulations and wind-tunnel tests were compared and validated.

Baker (2007) discussed the numerical analysis of trajectories of compact and sheet type debris in dimensionless forms. The numerical trajectories were compared with experimental results from Tachikawa (1983) and Wills et al. (2002). The results for sheet

type debris were found to be more complex: the flight behaviours were sensitive to boundary conditions. Furthermore, the variety of debris and the corresponding rotation can lead to a wide spread of trajectories and velocities. On the contrary, compact debris were very well defined and the trajectories and velocities can be predicted by only considering the action of the drag force and gravitational force acting on the debris; therefore, the solutions obtained from the debris flight equations proposed by Baker (2007) are used as a comparison.

Further studies comparing the mechanics and aerodynamics of plate type debris (Tachikawa, 1983; Wang and Letchford, 2003; Holmes et al., 2004) and rod type debris (Lin et al., 2007; Richards et al., 2008) have also been conducted extensively. Overall, compact debris were found to be well defined and accurately represented by mathematical equations due to the simplicity in geometric configuration and axis symmetrical structure. While debris flight under various different wind conditions have been studied comprehensively, simulation for debris flight in tornado-like wind field were surprisingly sparse.

Recently, several investigations on debris flight in tornadoes have been conducted including Sassa et al. (2009) who studied the deposition of wind-borne debris in a simulated moving tornado. The tornado-like wind field was generated using an axial fan for updraft and rotating porous disc for angular momentum, and polystyrene particles were employed as wind-borne debris. The small-scaled tornado generator does not have any closed test chamber and can be traversed to simulate a moving tornado. The polystyrene particles of 0.8 mm in diameter and 4×10^{-6} g in weight were spread uniformly over the ground. The trajectory of the particles were also numerically calculated based on the measured flow field as comparison where the particles were assumed with drag force

and no rotation. High magnitude of tangential velocity were observed at the rear side of the traversing tornado, resulting in the concentration of debris residual around that region; both the numerical and experimental trajectories corresponds well. However, little information was provided on the vortex flow field and the swirl ratio was not specified; further, the details of flight behaviour of the wind-borne debris were insufficient.

Maruyama (2011) numerically simulated flying debris in a tornado-like vortex using LES. The flow fields of a vortex was studied, and the three-dimensional trajectories of the wind-borne debris were computed for the statistical distribution and maximum velocity. The motion of the debris were calculated with the assumption of constant drag force that is independent from the attack angle of the relative wind. Two debris groups with diameters of approximately 0.5 m and 3 m were considered in the study and positioned uniformly on a horizontal plane at the elevation of 40 m. A two-celled type vortex was simulated, and the core radius was approximately 45 m. It was found that the debris that were released around the radial distance between one and two times of the core radius have the tendency to travel at higher velocities, while debris that were released at the core have the largest deviation in trajectories. While the study provides an insight into the statistical distribution and velocities of flying debris, it failed to address the trajectory range of these debris and the behaviour of different debris sizes. Moreover, the initiation of debris were not considered as the debris were released at a high elevation.

Bourriez et al. (2017) studied the flight paths of debris in laboratory-controlled conditions. Three vortices with different swirl ratio were generated using a large-scale vortex simulator. Spherical Styrofoam beads representing compact type debris with the diameter of approximately 1.6 mm were released into the flow field at different release distance. The core radius of the generated vortices ranges between 150 mm to 300 mm, and it was

found that the largest variation in debris trajectory occurs when debris were released within the core of the tornado (Figure 2.9).

Baker and Sterling (2017) provided an analytical model describing the tornado wind wield and flight equations for the prediction of debris flight pattern in different tornado types. The analytical expression for the three-dimensional velocity field for both single-celled and two-celled vortex formulation were presented, and the debris trajectories for flying and falling cases were formulated where the swirl ratio, buoyancy parameter and inverse tornado Froude number were identified as major parameter of debris flight in tornadoes. Whilst the model presented was a significant improvement over other tornado models existed at that time, the vertical velocity component of the model was unbounded and would increase infinitely with the increase in height. In a very recent study, Baker et al. (2020) developed an improved model over the existing model in which the formulated vertical velocity component would peak at a certain elevation and then gradually decrease with the increase in height. This improved Baker and Sterling model showed a considerable difference in the wind field and provided a more realistic behaviour of tornado flow pattern.

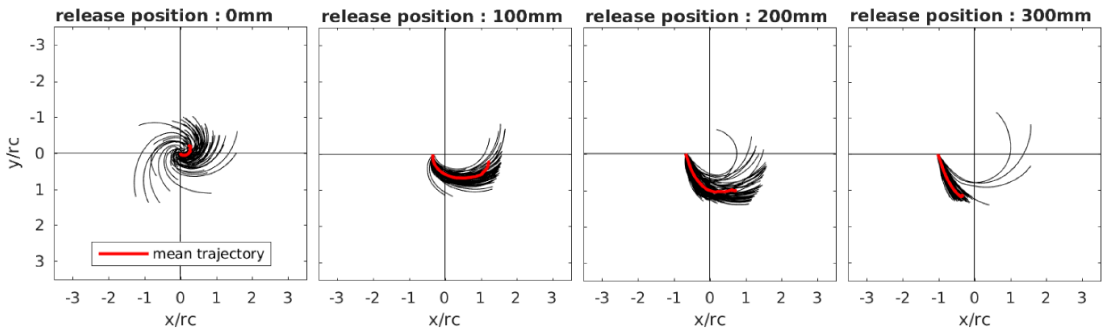

Figure 2.9: Top view of debris trajectories released at different radial distances the tornado-like vortex at the swirl ratio of 0.7 (Bourriez et al., 2017)

While these studies provide a great insight to the behaviour of tornado-induced flying debris, detailed analysis on the flight behaviour in different types of tornado wind fields are still lacking. Further, the trajectory range and impact velocities of wind-borne debris have yet to be addressed; additionally, the initiation of debris by tornadoes still remains to be investigated.

2.4. Summary of Previous Work and Research Gaps

The study of the tornado-like vortex flow fields and the modelling of debris flight have been reviewed. The formation of naturally occurring tornadoes are briefly discussed, and scales to measure the intensity of tornadoes were presented. The most reported tornadoes were the EF-0 scale. Due to the unpredictable path and high wind speeds of tornadoes, full scale measurements are undoubtedly difficult and dangerous; most of the collected data of the flow fields near the ground were severely contaminated from ground clutter and the tornado core was too small to be measured accurately by the current observational method.

Considering these associated difficulties, the modelling of tornadoes in analytical models, laboratory scaled experiments and numerical simulation were the alternatives to study the characteristics of tornadoes. The analytical models were able to represent some parts of the tornado flow field such as the tangential velocity and pressure field but fail to represent the entire three-dimensional vortex flow structures. While there are limitations with observational methods for studying tornadoes in physical simulators, laboratory experiment provides great insight to the characteristics of tornado-like vortices and demonstrated the importance of swirl ratio, aspect ratio and vortex Reynolds for vortex generation. Various different methods to numerically simulate tornado-like flows were

discussed and the Ward type vortex generator was the most common approach. The LES model was found to be able to accurately reproduce vortices at all swirl ratios.

The dangers and damages associated with wind-borne debris in severe wind events have been recognised and the most damaging type of flying debris have been identified as tornado-induced missiles. Debris can be classified based on their geometric properties, and studies on debris flight mechanics and aerodynamics have been conducted extensively. It was found that compact type debris can be accurately represented by the mathematical equations due to the simplicity in spherical configuration and axis symmetrical structure. While debris flight under different wind conditions have been investigated comprehensively, simulation under tornado-like vortex flow fields were surprisingly sparse. While Several investigations on debris flight in tornadoes have been conducted recently, the flight behaviour, impact properties and debris initiations in tornado-like vortex flow fields is still poorly understood.

Therefore, this research aims to provide further insight into the characteristic of flying behaviour of debris different tornado flow fields. Numerical methods are adopted to numerically simulate different types of tornado-like vortices and debris motion. The flow structure are analysed to reveal the characteristics of the vortices, and the trajectories of the debris are evaluated for its flight behaviour. The method of numerically simulating debris motion developed in this research will benefit the tornado research community to investigate debris flight in tornadoes further.

3. Methodology

"...the greatest disaster one can encounter on

computation is not instability or lack of convergence

but results that are simultaneously good enough to be

believable but bad enough to cause trouble"

H. Ferziger (1993)

IN THIS CHAPTER, all computational methods and numerical procedures adopted are described. The simulation of debris flight in a tornado-like vortex flow field is divided into two parts: the numerical generation of tornado-like vortices and the modelling of wind-borne debris. First, a detailed description of the physical vortex generator and the associated numerical simulation is introduced in section 3.1. The numerical approach employed is discussed in section 3.2. In section 3.3, the computational details relating to the numerical setup is given and the analytical vortex models are described in section 3.4. Finally, the simulation of debris flight is outlined in section 3.5, where the debris flight equations and the properties of various compact debris groups are specified in section 3.5.4.

3.1. Description of Vortex Generator

The model used in this current research is based on the University of Birmingham Tornado Vortex Generator (Gillmeier et al., 2017). The details of the physical simulations undertaken by Gillmeier et al. (2017) are discussed in section 3.1.1, and the computational domain of the numerical simulator is described in section 3.1.2.

3.1.1. Physical simulator

The University of Birmingham Tornado Vortex Generator (UoB-TVG) shown in Figure 3.1, is a large-scale Ward-type vortex generator based on the design of Ward's simulator (Ward, 1972). A series of exhaust fans are placed at the top of the convection chamber for the generation of updraft flows. Situated below the convection chamber is the convergence chamber, designed to draw air inwards by using a series of guide vanes that are mounted at the edge of convergence chamber. The guide vanes can be set to different angles in order to alter the angular momentum of the incoming flow. The convection chamber has a height (H_1) of 2 m and a diameter (D_1) of 3.1 m; the convergence chamber has a height (H_2) of 1 m and a diameter (D_2) of 3.6 m. A total of 30 square guide vanes of 1 m edge length and 0.01 m thickness are mounted around the edges of the convergence chamber; the centre rotation axis of the guide vanes are mounted at the radial distance of 1.68 m from the centre. The exhaust outlet with a diameter (D_3) of 1 m is located at the top of the convection chamber.

The swirl ratio is dimensionless parameter that measures the amount of mass rotating around a circulation centre, or the ratio of the circulation around the vortex to the updraft strength, which is essentially a measure of the tornado-scale helicity. Therefore, the swirl ratio can be used to describe the intensity of a vortex, where the larger the swirl ratio, the

stronger the circulation. Rotunno (1977) identified the swirl ratio as a dominant governing parameter for laboratory generated vortices, and the flow pattern of the vortices was observed to vary with swirl ratio. According to Lugt (1989) (as shown in Figure 2.5, different swirl ratios can correspond to different vortex evolution stages; at a low swirl ratio the tornado vortex is a jet-like flow known as single-celled vortex. As the swirl ratio increases, the vortex core breaks down and the turbulent core moves downwards and impinges the surface. Further increasing the swirl ratio results in the formation of a two-celled vortex. Jischke and Parang (1974) suggested three flow parameters for tornado simulation; a kinematic parameter, i.e., the swirl ratio; a geometric parameter, i.e., the aspect ratio; and a dynamic parameter, i.e., vortex Reynolds number. While various definitions for the swirl ratio (S) have been proposed it is frequently expressed as:

$$S = \frac{tan\,\theta}{2a} \qquad [3.1]$$

where θ is the angle of the guide vanes relative to the centre of the simulator, and a is the aspect ratio, the ratio between the diameter of the exhaust outlet (D_3) and the height (H_2) of the inlet, expressed as:

$$a = \frac{H_2}{D_3} \qquad [3.2]$$

Therefore, the aspect ratio of the UoB-TVG is 2, while the angles of the guide vanes (θ) are fixed at 50 degrees and 70 degrees, yielding with the swirl ratio of 0.3 and 0.69. The total volume flow rate (Q) measured at the exhaust outlet is 7.27 m^3/s and 7.42 m^3/s for the vortex with swirl ratio of 0.3 and 0.69 respectively, thus resulting in the inlet velocity (U_∞) of 0.643 m/s and 0.66 m/s respectively. The vortex Reynolds number (Re) is defined as the ratio of circulation around the vortex structure to the fluid viscosity, expressed as:

$$Re = \frac{Q}{D_3 \upsilon} \qquad [3.3]$$

where Q is the total volume flow rate, D_3 is the diameter of the exhaust outlet and υ is the kinematic viscosity of air. For the vortices with the swirl ratio of 0.3 and 0.69, the vortex Reynolds number are 497,694 and 507,963 respectively. Details of the parameters are listed in Table 3.1.

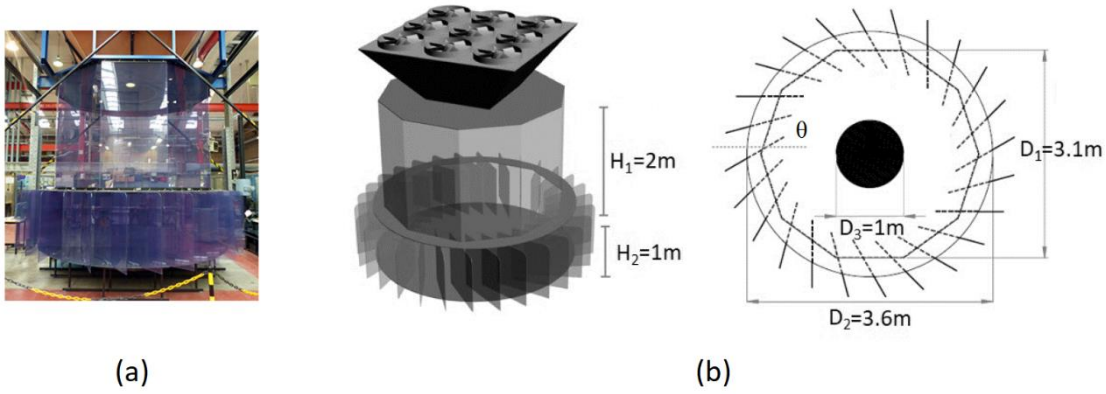

Figure 3.1: Illustration of (a) The University of Birmingham Tornado Vortex Generator (Tornado generator - University of Birmingham, n.d.) (b) The dimensions of the generator (Gillmeier et al., 2017)

Table 3.1: Parameters used in the experimental study by Gillmeier et al. (2017)

Aspect ratio, *a*	2	
Volume flow rate, *Q*	7.27 m^3/s	7.42 m^3/s
Vortex Reynolds number, *Re*	497,694	507,963
Inlet velocity, U_∞	≈0.66 m/s	0.66 m/s
Angle of guide vanes, θ	50 degrees	70 degrees
Swirl ratio, *S*	0.3	0.69

For the experimental study undertaken by Gillmeier et al. (2017), the velocity measurements of the flow field were made using a 100Hz Cobra Probe (Watkins et al.,

2002) mounted in the vortex simulator. The probe is fixed on a two axis traverse system that allows the positioning at different heights above the ground surface (0.01 m, 0.05 m, 0.10 m, 0.15 m, 0.20 m, 0.25 m, 0.30 m, 0.40 m, 0.50 m, 0.60 m) with a radial spacing of 0.025 m from the centre of the simulator to the radial distance of 0.60 m. The pressure distribution is measured on the ground surface of the vortex generator via pressure taps and recorded using pressure transducers (HCLA12X5DB). These surface pressure taps are distributed along the line with the spacing of 0.05 m from the centre up to the radial distance of 0.75 m. Different types of uncertainties in the experiments were distinguished and accounted for the measurement of the velocity flow field and surface pressure distribution in the experimental study as followed: Statistical uncertainties (which accounts for the uncertainties of measuring over a finite-time series), repeatability (which repeated measurements show same results) and device uncertainties.

The statistical uncertainty is estimated to be approximately ± 2% for tangential and vertical velocity and ±1% for radial velocity, while surface pressure is determined to be ± 0.5%. The repeatability of time-averaged velocity components is less than ± 0.5 m/s, while surface pressure is found to be low at approximately ±6 N/m^2 at the vortex core within the radial distance of 0.05 m. The device uncertainty is determined based on the measuring positions; the Cobra probe is used to measure the velocity field and are accurate within ± 0.5 m/s, but only limited to measuring velocities that are greater than 2 m/s within the cone of ± 45^o; due to these restrictions, the velocity field close to the centre of the vortex, and near the ground surface were not captured. The surface pressure taps have a typical uncertainty of approximately ± 5 N/m^2. The velocity and pressure measurements of the flow field are ensemble averages and used as a comparison for the numerical simulations (presented in Chapter 4).

3.1.2. Numerical simulator

The domain of the numerical simulator is created based on the configuration of the UoB-TVG and is shown in Figure 3.2; the size of the domain is identical to the physical simulator. The convection was simplified from decagon to a cylinder in order to reduce the corner edges of the geometry and prevent high skewness during mesh generation; since the convection is situated above the convergence chamber and does not affect the formation of the vortices, the effects of this simplification is assumed to be insignificant and can be neglected. The exhaust outlet with the diameter, D_3 of 1 m is located the top of the convection chamber.

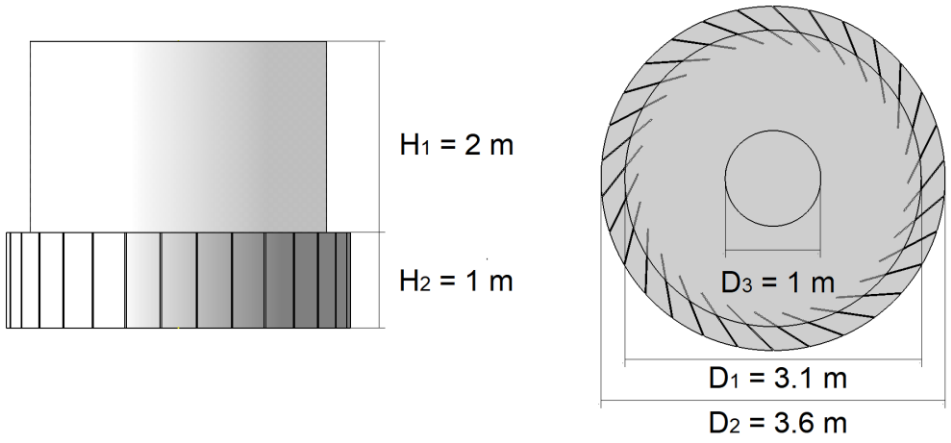

Figure 3.2: Configuration of the numerical vortex generator

Based on the domain, two different geometric configurations are generated as computational domains with the guide vanes set at 50 degrees and 70 degrees for the generation of vortex with the swirl ratio of 0.3 and 0.69 respectively (as shown in Figure 3.4). A total of 30 guide vanes of 1 m × 1 m in size and 0.01 in thickness are mounted around the edges of the convergence chamber. A Cartesian coordinate system is adopted for the generation of the computational domains, where the xy plane represents the horizontal plane with the z axis being perpendicular to the horizontal plane.

3.2. Numerical Simulation

In terms of CFD, the most accurate approach for simulating and modelling turbulent flow is using direct numerical simulation (DNS), where the full Navier-Stokes equations are directly solved using very high grid resolution to capture the eddies of all scales; as a result, simulation using DNS are computationally expensive and limited only to low Reynolds number flows and simply geometries.

In some cases, only the steady state fluid flow is concerned, thus the Reynolds Averaged Navier-Stokes (RANS) simulation is considered; the basis for the RANS approach is by solving only the averaged quantities while the effects of all turbulent motions are modelled using turbulence models. The RANS model is significantly cheaper in computational cost and has been adopted in industrial application for many years; however, the RANS model is unable to provide information about the instantaneous flow (Yang, 2015).

An alternative approach is to use a LES, initially proposed by Joseph Smagorinsky (1963). The primary concept for LES is to directly resolve the large-scale eddies of the flow, that are responsible for most of the turbulent kinetic energy in the flow, while modelling the effects of the sub-grid scales (SGS) of the turbulent flow. This approach significantly reduces the computational cost as compared to the DNS and more accurate than RANS as the large eddies contains the turbulent energies are those responsible for the momentum transfer and turbulent mixing. LES has proven to be effective in reproducing tornado-like flow fields for the study of the vortex flows without the limitations of observational methods (Natarajan, 2011, Maruyama, 2011, Ishihara et al., 2011, Ishihara and Liu, 2014). In this study, the LES is employed for the simulation of the tornado-like vortices with the

swirl ratio of 0.3 and 0.69. In section 3.2.1, the governing equations are introduced, and the sub-grid scale modelling are shown in section 3.2.2.

3.2.1. Governing equations

The Navier-Stokes equations are the governing equations and named after engineer and physicist Claude-Louis Navier and physicist and mathematician George Gabriel Stokes. The Navier-Stokes equations are derived from the fundamental conservation laws for mass, momentum and energy, which describes the correlation between the velocity, pressure, temperature, and density of a moving fluid. The flow can be regarded as incompressible if the density variations are very small, where the energy equation for incompressible flows can be completely decoupled from the Navier-Stokes equations (with the exception that the viscosity depends on the temperature).

The principal difficulty in simulating turbulent flows derives from the wide range of time and length scales; thus, applying filtering reduces the range of scales that must be resolved and decreases the computational cost for the flow simulation. The filtering operation is undertaken by applying a low-pass spatial filter to the instantaneous conservation equations, where any scales larger than the filter width is retained in the flow field and solved, while the effects of the scales smaller than the width will be modelled. The resulting filtered Navier-Stokes equations in a Newtonian incompressible flow is expressed in the conservative form as:

$$\partial_i \overline{U}_i = 0 \qquad [3.4]$$

$$\partial_t(\rho_a \overline{U}_i) + \partial_j\left(\rho_a \overline{U}_i \overline{U}_j\right) = -\partial_i \overline{P} + 2\partial_j\left(\mu \bar{\varepsilon}_{ij}\right) - \partial_j\left(\tau_{ij}^s\right) \qquad [3.5]$$

where $\overline{U}$ is the filtered velocity field, $\bar{P}$ is filtered pressure; ρ_a is density of air, μ is the dynamic viscosity of air and i, j, k denotes the x, y, z directions of the fluid element, $\bar{\varepsilon}_{ij}$ is the filtered strain rate tensor and τ_{ij}^{s} is the SGS stress tensor, expressed as:

$$\bar{\varepsilon}_{ij} = \frac{1}{2}(\partial_i \overline{U}_j + \partial_j \overline{U}_i) \quad [3.6]$$

$$\tau_{ij}^{s} = \rho_a(\overline{U_i U_j} - \overline{U}_i \overline{U}_j) \quad [3.7]$$

The filtered Navier-Stokes equations shown in equations [3.4] ad [3.5] are similar to the original Navier-Stokes equations, with an additional SGS stress tensor that arise from the filtering operation. The SGS stress tensor represents the large-scale momentum flux caused by the SGS eddies, which will be modelled using a SGS model (Smagorinsky model).

3.2.2. Sub-grid scale modelling

While there are a variety of SGS models, the most common one is the Smagorinsky model (Germano, 1991). The Smagorinsky model (Smagorinsky, 1963) is based on the concept that energy is transferred conservely from the large energy producing scales to the small dissipating scales. In which the effects of turbulence represented using eddy viscosity, is equal to the flux caused by the SGS eddies, expressed as:

$$2\mu_t \bar{\varepsilon}_{ij} = \tau_{ij}^{s} - \frac{1}{3}\delta_{ij}\tau_{kk}^{s} \quad [3.8]$$

where μ_t is the SGS eddy viscosity, δ_{ij} represents the Kronecker delta, and τ_{kk}^{s} is the isotropic part of the SGS stress. The isotropic part of the SGS stress is removed, as only the deviatoric part of the tensor is responsible for the diffusion of momentum. The SGS eddy viscosity, μ_t is expressed as:

$$\mu_t = \rho_a (f_d C_S \bar{\Delta})^2 \left\| \bar{\varepsilon}_{ij} \right\| \quad [3.9]$$

where f_d is the van Driest damping function (Van Driest, 1956), Δ is the cube root of the grid cell volume and C_S is the Smagorinsky constant (Lilly, 1967) set as C_S = 0.1, and f_d is the van Driest damping function (Van Driest, 1956) expressed as:

$$f_d = 1 + exp\left(\frac{z^+}{25}\right) \quad [3.10]$$

where the function is used to partially take the effects of the wall into account by damping the turbulence length scales; as a result, the value of C_S are reduced around the regions close to the walls to prevent over dissipation. The non-dimensional wall normal distance of each direction $x^+, y^+$and z^+ describes the relationship between friction velocity and kinematic viscosity as:

$$x^+ = y^+ = z^+ = \frac{nU^*}{\upsilon} \quad [3.11]$$

where υ is the kinematic viscosity of air, n is the normal distance between the first cell and the wall boundary in each direction, and U^* is the friction velocity, defined as:

$$U^* = \sqrt{\frac{\tau_{wall}}{\rho_a}} \quad [3.12]$$

where τ_{wall} is the wall shear stress and ρ_a is the density of air. The wall shear stress is estimated to be the value of 0.018 N/m^2. The characteristic length scale of the filter width Δ, is expressed as:

$$\Delta = (\Delta x \Delta y \Delta z)^{\frac{1}{3}} \quad [3.13]$$

where $\Delta x \Delta y \Delta z$ is the control volume spacing in each direction. The rate of the strain tensor of the resolved scales, $\|\bar{\varepsilon}_{ij}\|$ is defined as:

$$\|\bar{\varepsilon}_{ij}\| = \left(2\bar{\varepsilon}_{ij}\bar{\varepsilon}_{ij}\right)^{\frac{1}{2}} \quad [3.14]$$

applying these terms into equation [3.5] results in:

$$\partial_t(\rho_a \overline{U}_i) + \partial_j\left(\rho_a \overline{U}_i \overline{U}_j\right) = -\partial_i \bar{P} + 2\partial_j\left((\mu + \mu_t)\bar{\varepsilon}_{ij}\right) \quad [3.15]$$

The finalized form of the Navier-Stokes equations as shown in equation [3.15] are then computed explicitly. Although there are many other SGS models available, and great efforts have been made to develop more advanced SGS models, the Smagorinsky model is still used and proved surprisingly successful.

3.3. Computational Details

The two computational domains with the guide vanes set at 50 degrees and 70 degrees described in section 3.1.2 are used for mesh generation. The procedure of mesh generation for the two domains are similar, and the numerical setup for the generation of tornado-like vortices with the swirl ratio of 0.3 and 0.69 are identical.

3.3.1. Mesh generation

A total of six grids were generated for the two domains used in this study; ICEM-CFD (ICEM, 2012) mesh generator package is used to generate quadrilateral structured mesh. For each domain, three grids with different size of refinement regions were generated for the study of grid independency. Details of the grids are summarized in Table 3.2.

Piomelli (2001) stated that the required grid resolution for LES should be $x^+ \approx$ 50 - 150 and $y^+ \approx$ 15 - 40 in the stream-wise and span-wise direction and 15 layers across the

boundary layer with the first grid of $z^+ < 1$ in the vertical direction in order to resolve the wall layer. Some studies (Piomelli and Balaras, 2002; Yang, 2015; ANSYS, 2013) however, argue that the required resolution may be adjusted to $x^+ \approx$100 - 160 and $y^+ \approx$ 100 - 300 and the wall normal direction can be $z^+ \approx$1-30; it is significant to note that these obtained numbers case are specific and based on experience, therefore can only be considered as a reference. For this reason, clustered mesh with high density is adopted at the centre of the domains within the radius of 0.5 m at the convergence chamber with x^+ and $y^+ \approx$10 in the x and y directions due to the axisymmetric structure of tornado-like vortices; 15 layers of mesh were created with the wall-adjacent spatial unit of $z^+ \approx$1 for both the computational domains in order to resolve the structure of the boundary layer at the viscous sub-layers. Hyperbolic stretching is used to generate the remaining meshes to ensure a smooth transition.

Since both of the computational domains are similar and the angle of the guide vanes are the only difference, the procedure of generating the mesh were identical. The mesh resolution around the guide vanes are altered by adjusting the number of cells in the xy direction to generate three different mesh resolutions for coarse, fine and extra fine, yielding in 4.3 million, 7.5 million and 9.2 million cells respectively for the computational domain with the guide vane at 50 degrees, and 4.6 million, 7.3 million and 9.6 million cells respectively for the computational domain with the guide vane at 70 degrees The configuration of the generated mesh are shown in Figure 3.3. While effort has been made to accurately reproduce the physical simulator, there may inevitably be small differences introduced due to the meshing process; it is difficult to quantity the impact of these differences, but in what follows it is assumed that beyond a certain mesh resolution their effects are negligible (details discussed in section 4.1).

Table 3.2: Cell number for coarse, fine and extra fine meshes

Grid	Cell number	
Guide vanes	50 degrees	70 degrees
Coarse	4,348,254	4,581,849
Fine	7,451,167	7,258,561
Extra Fine	9,146,207	9,606,516

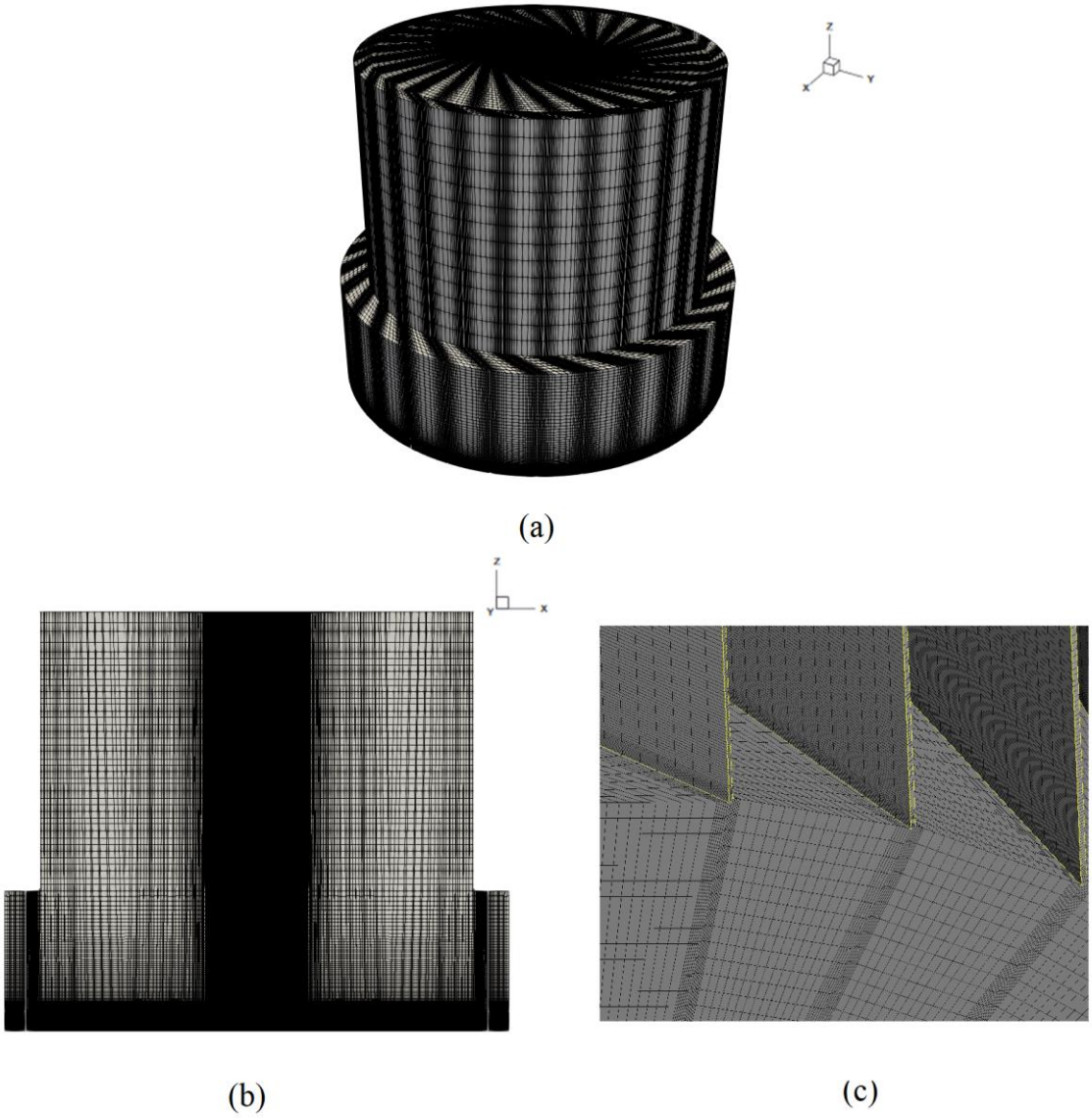

Figure 3.3: (a) Isometric view of the computational domain (b) View of the mesh with the cut plane at y = 0 (c) The mesh around the guide vane region.

3.3.2. Boundary conditions and numerical setups

The openings of the convergence chamber are set with a uniform velocity inlet, (U_∞). The exhaust outlet, D_3 is set with pressure outlet with free stream pressure P_∞=0 (shown in Figure 3.4); A no-slip boundary condition is applied to the ground surface, walls of the convection chamber and the guide vanes. The flow is considered to be incompressible and the density of air (ρ_a) is 1.225 kg/m^3 and dynamic viscosity (μ) or air is 1.81 × 10^{-5} kg/ms. Table 3.3 lists the parameters used for the boundary conditions. The reference inlet velocity for both vortex simulation are set as U_∞ = 0.66 m/s, obtained from the experimental study by Gillmeier et al. (2017), resulting in the vortex Reynolds number (*Re*) of approximately 5.1×10^5 for both the tornado-like vortices with the swirl ratio of 0.3 and 0.69.

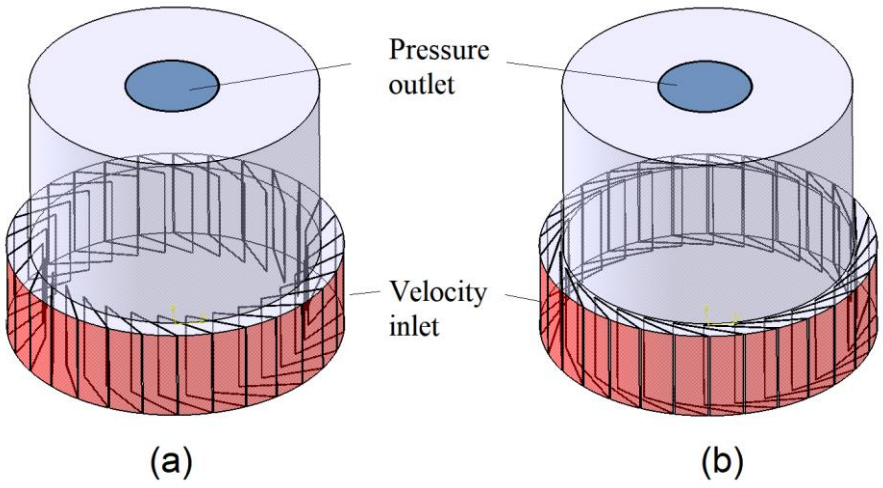

Figure 3.4: Boundary condition setting of computational domains with the guide vanes set at (a) 50 degrees (b) 70 degrees

The Courant-Friedrichs-Lewy (CFL) number (Courant et al., 1928) is a convergence condition that relates the interval lengths of spatial coordinates to the duration of the time step and the velocity that fluid in the spatial domain. The CFL number is expressed as:

$$CFL = \frac{U\Delta t}{n} \quad [3.16]$$

where n is the normal distance between the first cell and the wall boundary in each direction, Δt is the time step size and U is the velocity magnitude of the local flow field. In order to maintain the CFL number at the value of 0.5, the constant time-step of Δt = 5×10^{-4} s is determined for transient simulation of tornado-like vortices. The open source CFD program OpenFOAM (OpenFOAM, 2019) is used to perform the fluid dynamics simulation. The PISO solver (OpenFOAM, 2019) is implemented in the simulations to couple the pressure and velocity. The temporal discretization is approximated by second order implicit backward scheme; the gradients are computed with the second order central differencing scheme. A central differencing stabilised transport scheme is discretized for the convection terms; this scheme blends 75% central difference interpolation with 25% second order upwind with to stabilise the solution while maintaining second order behaviour.

The averaging of velocity and pressure field are implemented when the vortex flow is fully developed; this is ensured by monitoring the residuals of the conservation equations for convergence, where the maximum normalized residual of each equations are stable and converged to at least 10^{-4}, which ensured that the statistics did not change with time. The time-averaged results are obtained after the flow is fully developed by averaging the actual simulation time of 30 seconds, which is equivalent to approximately 460 and 300 vortex revolutions for vortex with the swirl ratio of 0.3 and 0.69 respectively. The total wall time of the LES with the extra fine mesh for the swirl ratio of 0.3 and 0.69 running at 48 processors is approximately 172 hours and 189 hours respectively.

Table 3.3: Parameters used in the numerical simulation

Angle of guide vanes, θ	50 degrees	70 degrees
Swirl ratio, S	0.3	0.69
Inlet velocity, U_∞	0.66 m/s	
Vortex Reynolds number, Re	5.1×10^5	
Time step, Δt	5×10^{-4} s	

3.3.3. Vortex characteristics

The results presented in this study are normalized using the characteristic parameters of the vortex: the radius of the vortex core (r_c), the maximum tangential velocity (U_T) and time per revolution of the vortex (t_r). The core radius, r_c measures the size of the vortex; and all spatial distances are normalised using the core radius as this provides a measurement of radial distance relative to the tornado-like vortex. The maximum tangential velocity, U_T is the maximum averaged tangential velocity component of the vortex and r_T is the radial distance at which U_T of the vortex occurs. The method of determining the location of the radius of the vortex core and maximum tangential velocity for each respective tornado-like vortices are presented in chapter 4. The time taken for the vortex to complete a single revolution, t_r is defined as:

$$t_r = \frac{2\pi r_T}{U_T} \qquad [3.17]$$

It is important to note that the vortex does not retain constant angular momentum throughout as the flow structure of the vortex consists of different regions in which the velocity varies. The quantification of the time per revolution of the vortex simply provides a measure of time at the radial distance where the vortex has the highest tangential velocity. The pressure coefficient, C_P is expressed as:

$$C_P = \frac{P - P_\infty}{0.5\rho_a {U_T}^2} \quad [3.18]$$

where P_∞ is previously defined, P is the local pressure field and $\rho_a$is the density of air.

3.4. Analytical Model Parameters

In this section, the model parameters for the Rankine vortex model, Burgers-Rott vortex model, Sullivan vortex model and Baker and Sterling vortex model are provided. The radius, r, ranging from 0 m to 12 m were used as input for the calculation of the distribution of tangential velocity.

The Burgers-Rott and Sullivan vortex model both include a viscosity parameter (ν) in the equations, which is responsible for removing the kinetic energy from the flow by introducing vortex stretching. An in-depth analysis on the effects of the viscous term and shape parameter conducted by Gillmeier et al. (2017) showed that even by increasing the viscosity parameter by several orders of magnitude, only the velocity magnitude is affected and not the structure of the vortex, therefore concluded that the viscosity parameter in both the Burgers-Rott and Sullivan vortex model is just a shape parameter. If the assumed viscosity parameter corresponds to the kinematic viscosity ($\approx 1.46\times10^{-5}$ kg/ms), the velocity components predicted by the models would be too small. Consequently, as Gillmeier et al. (2017) suggested, the viscosity is chosen with a value of ν = 2.4 kg/ms in order to ensure a meaningful comparison with the numerical results that is in the same order.

Webster and Young (2015) reported that for the Burgers-Rott vortex model, the increase in the value of Γ only increases the magnitude of maximum tangential velocity, but does not affect the structure of the vortex, therefore, the circulation of the vortex at infinity

with a value of 1 was employed. For the Baker and Sterling vortex model, the swirl ratio, $S_{Baker\ \&\ Sterling}$ with the value of 1.29 and 1.35 calculated based on the results from the numerically simulated vortices with S =0.3 and S =0.69 (details in section 4.4.4) were employed for the calculation of the constant, K_{bs}, yielding with the value of 3.72 and 3.89 respectively. According to Baker and Sterling (2017), the tangential velocity component becomes physically unrealistic if $\gamma \leq 1$, thus, in order to accurately describe the behaviour or a laboratory scaled tornado-like vortex, the recommended setting is $\gamma = 2$. Further, the height of z =0.0165 and 0.033 m (corresponding to the dimensionless height of $\tilde{z}$ (z/r_c) =0.15 and 0.3 for vortex with S =0.3 and 0.69 respectively) were employed for the calculation of tangential velocity distribution

The resulting maximum tangential velocity from all four analytical models have varying magnitudes and are listed in Table 3.4. It can be observed that both the Burgers-Rott and Sullivan vortex model estimates a considerably lower magnitude of maximum tangential velocity, while the Baker and Sterling model predicted higher magnitude of maximum tangential velocity in comparison with the Rankine vortex model. As a result, in what follows, care was been taken to normalise each vortex model by the corresponding maximum tangential velocity (U_T) and radial distance where the maximum tangential velocity component occurs (r_T) opposed to a single value, as listed in Table 3.4 in order for a meaningful comparison. The distribution of tangential velocity profiles against the radial distance of all analytical vortex models are shown in Figure 3.5, where the velocities and radial distances are represented with the normalised tangential velocity U_t/U_T ($\widetilde{U_t}$) and normalised radial distance r/r_T ($\tilde{r}$).

Table 3.4: Maximum tangential velocity of all vortex models

Vortex model	U_T, (m/s)	r_T, (m)
Rankine	1	1
Burgers-Rott	0.63	1.12
Sullivan	0.34	2.29
Baker and Sterling	1.29 (for S=0.3) & 1.35 (for S=0.69)	1

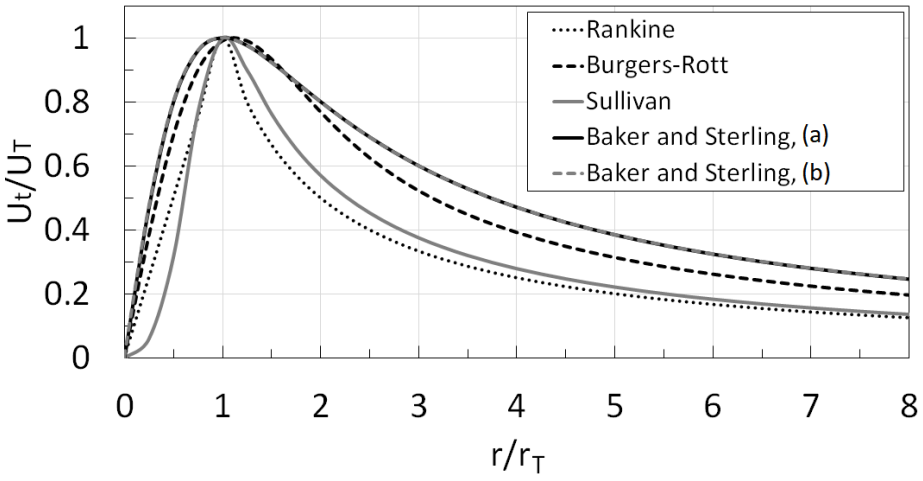

Figure 3.5: Tangential velocity component of the Rankine, Burgers-Rott, Sullivan and Baker and Sterling vortex model (a) $S_{\text{Baker \& Sterling}}$ =1.29 (b) $S_{\text{Baker \& Sterling}}$ =1.35.

The radius, r, ranging from 0 m to 8 m were used as input for the calculation of surface pressure coefficient. The static pressure at the centre were set with $\widetilde{P_0} = 1$ and $\tilde{P}(0,0) = 1$ for Rankine, Burgers-Rott and Sullivan vortex model respectively, while the free-stream pressure was set with $\widetilde{P_\infty} = 0$. In order to enable a consequential comparison, the distribution of surface pressure obtained from all vortex models were normalised by minimum pressure, P_{min} and the radial distance where the maximum tangential velocity component occurs, r_T of the respective vortex models (as shown in Figure 3.6). This

ensures that the increase in surface pressure along with the increase in radial distance of all the models are of similar order of magnitude.

All model shows that the pressure is the lowest at the centre of the vortex core. All model shows a similar trend, with the greatest difference at the slope of the distribution. From the figure, a general region of vortex core can be seen from the pressure slope.

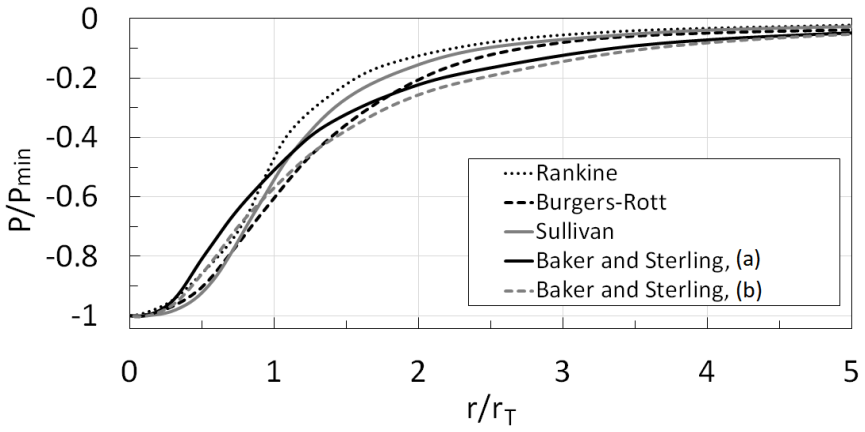

Figure 3.6: Surface pressure coefficient of the Rankine, Burgers-Rott, Sullivan and Baker and Sterling vortex model (a) $S_{\text{Baker \& Sterling}}$ =1.29 (b) $S_{\text{Baker \& Sterling}}$ =1.35.

3.5. Wind-borne Debris Modelling

This section presents a detailed description of the numerical modelling procedure that has been used for spherical compact debris. The governing dimensionless parameter (the Tachikawa number) is introduced in section 3.5.1 and the analytical flight equations are presented in section 3.5.2; the experimental study used as validation is given in section 3.5.3, the method of numerically simulating the three-dimensional motion of debris and the numerical setups are outlined in section 3.5.4. The position, time and velocity components of debris motion are denoted hereafter with subscript d.

3.5.1. Tachikawa number

After the proposal from Holmes, et al. (2006), the Tachikawa number, K, is defined as a dimensionless parameter that represents the ratio of aerodynamic forces to the gravitational force acting on the wind-borne debris. The Tachikawa number can also be used to determine the trajectories of debris objects of all types; in which a larger value of K would indicate a higher propensity to travel further and faster under wind action. The Tachikawa number (Tachikawa, 1983) used in the current research is defined as:

$$K = \frac{\rho_a {U_\infty}^2 {d_d}^2}{2 m_d g} \quad [3.19]$$

where ρ_a is the density of the air, U_∞ is the reference velocity, d_d is the diameter of the debris (see Table 3.5), m_d is the mass of the debris and g is the acceleration due to gravity.

3.5.2. Analytical flight equations

In this section, the analytical flight equations for compact type debris introduced by Baker (2007) are discussed. The two-dimensional equations of motion that describes debris flight are presented in a generalised form, where the lift and moment coefficients are assumed to be zero and the accelerations of debris in the x and z direction in a steady horizontal wind are expressed in the dimensionless form as:

$$\frac{d^2 \tilde{x}_d}{d\tilde{t_d}^2} = \frac{d\widetilde{U}_{dx}}{d\tilde{t_d}} = \left(\widetilde{U}_x - \widetilde{U}_{dx}\right)\left(\left(\widetilde{U}_x - \widetilde{U}_{dx}\right)^2 + {\widetilde{U}_{dz}}^2\right)^{0.5} \quad [3.20]$$

$$\frac{d^2 \tilde{z}_d}{d\tilde{t_d}^2} = \frac{d\widetilde{U}_{dz}}{d\tilde{t_d}} = \left(C_D\left(-\widetilde{U}_{dz}\right)\left(\left(U_x - \widetilde{U}_{dx}\right)^2 + {\widetilde{U}_{dz}}^2\right)^{0.5} - \frac{1}{K}\right) \quad [3.21]$$

where $\tilde{x}_d$ and $\tilde{z}_d$ are the non-dimensional spatial positions of the debris, $\widetilde{U}_x$ is the non-dimensional horizontal velocity of the fluid flow, $\widetilde{U}_{dx}$ and $\widetilde{U}_{dz}$ are the velocity of the

debris in the x and z directions and C_D is the spherical drag coefficient. The dimensionless parameters are defined by Baker (2007) as:

$$\widetilde{U}_x = U_x/U_\infty \quad [3.22]$$

$$\widetilde{U}_{dx} = U_{dx}/U_\infty \quad [3.23]$$

$$\widetilde{U}_{dz} = U_{dz}/U_\infty \quad [3.24]$$

$$\tilde{x}_d = \frac{x_d}{d_d}\left(\frac{0.5\rho_a A_d d_d}{m_d}\right) \quad [3.25]$$

$$\tilde{z}_d = \frac{z_d}{d_d}\left(\frac{0.5\rho_a A_d d_d}{m_d}\right) \quad [3.26]$$

$$\tilde{t}_d = \frac{t_d U_\infty}{d_d}\left(\frac{0.5\rho_a A_d d_d}{m_d}\right) \quad [3.27]$$

where U_∞ is the reference velocity, U_{dx} and U_{dz} are the velocity of the debris in the x and z direction, x_d and z_d are the spatial positions of the debris d_d is the diameter of the debris, ρ_a is the density of the air, A_d is the spherical cross section of the debris, m_d is the mass of the debris and t_d is the flight time. According to Baker (2007), the comparison of analytical flight equations with experimental results showed that the trajectories and velocities compact debris can be appropriately predicted by only considering the action of the aerodynamic drag force and gravitational force acting on the debris, which is essentially a function of K (represented as Ω by Baker (2007), where $\Omega = \frac{1}{K}$). As the flight equations do not have an exact solution, the velocities and displacements are numerically solved over a range of time, where the horizontal velocities of the fluid flow, U_x are used as input to the equations. In order to ensure a meaningful comparison

with the numerical results, the parameters for debris A, B1 and C (see Table 3.5) are employed for the calculations.

3.5.3. Experimental setup

A series of physical simulations were undertaken by Bourriez et al. (2017) and are used as a comparison for the numerical simulated debris trajectory. The experimental study investigates the flight motion of wind-borne debris in tornado flow fields; the tornado-like vortex is generated using the University of Birmingham Tornado Vortex Generator. Spherical polystyrene beads were employed in the experiments to represent compact type debris. The diameter and density of the beads varies between 1.5 - 1.7 mm and 24 - 28 kg/m^3 respectively. 100 bead particles were released at 4 locations from the centre of the tornado, and the motion of the debris were tracked using the 3D-PTV technique (Maas et al., 1993; Malik et al., 1993). Three high speed digital cameras, Sony NEX-FS700RH were positioned in the simulator (shown in Figure 3.7) and setup to record videos at 480 fps at the shutter speed of 1/2000s with the resolution of 1920 x 1080 pixels. The images were pre-processed in order to enhance particle detection using the threshold of intensity of 25%.

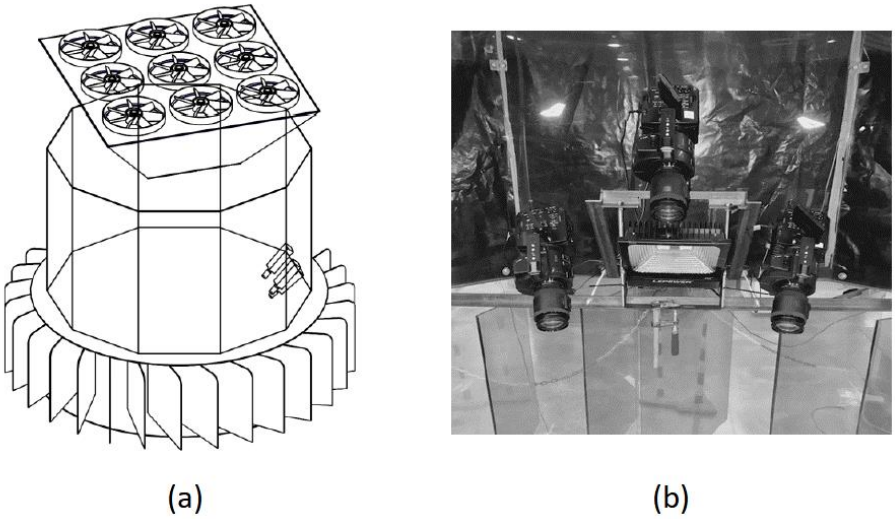

Figure 3.7: (a) An illustration of the experimental setup (b) The three-camera arrangement mounted inside of the simulator (Bourriez, 2020)

Uncertainties and limitations in the results were taken into account; the experimental setup was unable to capture the entire trajectory of some particles which left the tracking window and/or fell to the ground (confines of the tracking window not specified); some variations in trajectory paths may be attributed to the inconsistent size of the beads used and the considerable changes on the local field of the vortex due to the wandering motion or turbulent fluctuations (turbulence intensities not specified). The results in the experiments are used as a comparison for the numerical simulations (presented in chapter 5).

3.5.4. Numerically modelling debris motion

A series of debris groups with varying diameter and densities corresponding to the Tachikawa number which ranged between 0.6 and 2.5 are considered (illustrated in Figure 3.8). Debris group B1, B2 and B3 are chosen for the study of aerodynamic similarity and have identical value of Tachikawa number of K=1.2 but different mass, where debris

group B1 corresponds to the polystyrene beads employed in the experiments (Bourriez et al., 2017); debris group A, B1 and C with the value of Tachikawa number of 2.5, 1.2 and 0.6 respectively, are chosen for the study of impact of Tachikawa number on the flight characteristics and impact properties of debris. The corresponding Reynolds number of the debris based on the Tachikawa number, and the properties of all debris groups are listed in Table 3.5.

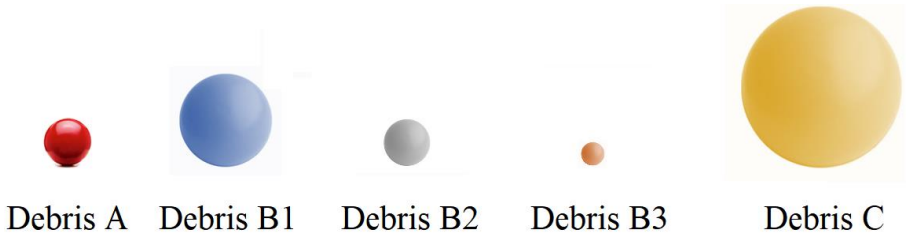

Figure 3.8: Illustration of different debris groups

Table 3.5: Properties of the debris groups

Debris group	Diameter, d_d (m)	Density, ρ_d (kg/m3)	Mass, m_d (kg)	Reynolds number, Re_d	Tachikawa number, K
A	0.00075	28.1	6×10^{-9}	34	2.5
B1	0.0015	28.1	50×10^{-9}	68	1.2
B2	0.00075	56.2	12×10^{-9}	34	1.2
B3	0.00037	112.4	3×10^{-9}	17	1.2
C	0.003	28.1	397×10^{-9}	136	0.6

The three-dimensional motion of the debris in the tornado-like vortex flow field is numerically simulated in order to determine the trajectories and velocities. Similar to Baker's (2007) approach, the motion of each individual debris were computed by considering only the aerodynamic drag force and gravitational force acting on the debris, with no rotation assumed. The general form is expressed as:

$$F_{total} = F_D + F_g \quad [3.28]$$

where F_D is the drag force, F_g is the gravitational force and F_{total} is the sum of all forces acting on the debris, expressed as:

$$F_{total} = m_d \frac{dU_d}{dt} \quad [3.29]$$

$$U_d = \frac{ds_d}{dt} \quad [3.30]$$

where m_d is the mass of debris, U_d is the velocity magnitude of debris and s_d is the spatial position of the debris. The drag force, F_D is expressed as:

$$F_D = \frac{3}{4}\frac{\rho_a}{\rho_d}\frac{m_d}{d_d} \cdot C_D(U - U_d)|U - U_d| \quad [3.31]$$

and the gravitational force and buoyancy force are combined as a single force as, F_g as:

$$F_g = m_d g\left(1 - \frac{\rho_a}{\rho_d}\right) \quad [3.32]$$

where ρ_a is the density of the air, ρ_d is the density of the debris, d_d is the diameter of debris, U is the velocity of the local flow field and C_D is the spherical drag coefficient. The drag coefficient of debris is computed based on the debris Reynolds number computed based on the local flow field, using the Schiller-Nauman drag model (Putnam, 1961) expressed as:

$$C_D = \begin{cases} \frac{24}{Re_d}(1 + \frac{1}{6}Re_d^{\frac{2}{3}}), & Re_d \leq 1000 \\ 0.424, & Re_d > 1000 \end{cases} \quad [3.33]$$

and the debris Reynolds number as:

$$Re_d = \frac{\rho_a U d_d}{\mu} \quad [3.34]$$

where the viscosity of air is μ = 1.81 × 10^{-5} kg/ms. It should be noted that other forces such as centrifugal forces and lift force caused by magnus effects were neglected due to low magnitude in comparison with the total force (drag and gravitational forces) considered in this study. By inspecting the vortex flow fields (as presented in section 4.4), the centrifugal force of debris around regions with higher tangential velocity (between r/r_c=1 to 2.5) were estimated to be approximately 1.1 ×10^{-6} N, 8.8×10^{-6} N and 7.1×10^{-5} N for debris A, B1 and C respectively. While the majority of the other regions further away (r/r_c=3 to 12) the tangential velocities are significantly lower, resulting in the low magnitude of centrifugal force of approximately 2.7×10^{-7} N, 2.2×10^{-6} N and 1.8×10^{-5} N for debris A, B1 and C respectively. At the regions close to the ground where the vorticity of the flow field are high (between r/r_c=1 to 1.5), the magnitude of the lift force caused by the rotation of debris (magnus effect) were estimated to only be approximately 2.8×10^{-7} N, 2.3×10^{-6} N and 1.8×10^{-5} N for debris A, B1 and C respectively. In comparison with the total forces (drag and gravitational forces), which ranges from approximately 1.2 ×10^{-4} N, 4.7×10^{-4} N and 1.9×10^{-3} N for debris A, B1 and C respectively at regions with higher tangential velocity (between r/r_c=1 to 2.5), to 2.6 ×10^{-5} N, 1.0×10^{-4} N and 4.2×10^{-4} N for debris A, B1 and C respectively, at regions further away (r/r_c=3 to 12), the combination of both the centrifugal and lift forces at the maximum magnitude are approximately 9.4 ×10^{-3}, 1.9×10^{-2} and 3.7×10^{-2} times lower than the total forces for debris A, B1 and C respectively, and are therefore neglected in this study.

However, it should be stressed that while the magnitudes of centrifugal force and lift force are low and difficult to quantify, the effects of these forces, coupled with the instantaneous

changes of the flow field may, to some extend lead to some differences in the overall trajectories. As a result, further research on the incorporation of these forces should be conducted in the future in order to quantify these differences. Additionally, since the size of the largest debris considered, debris group C, is approximately 1×10^{8} times smaller than the convergence chamber of the UoB-TVG, the effects of debris on the flow is considered to be negligible; thus, one-way coupling is assumed to be sufficient where the interaction between the debris and the flow are ignored in the calculation.

The motion of debris is computed using the Lagrangian particle tracking method with the transient solver icoUncoupledKinematicParcelFoam (OpenFOAM, 2019). The calculation process of debris motion is shown in Figure 3.9. Initially, the Reynolds number of each individual debris are calculated based equation [3.34] using the initial conditions or the velocity of the debris from the previous time-step. Then, taking account of the effects of the local wind field, the drag coefficients of the debris are determined using Schiller-Nauman drag model (equation [3.33]). The force balance equations as specified in equation [3.28] are then solved, where the velocity and spatial position for the current time-step are updated. The entire process is repeated over time in order to obtain the trajectories of the debris. According to the recommendations of OpenFOAM (2019), in order to maintain the CFL number (equation [3.17]) at the value of 0.5, the constant time-step of $\Delta t = 5\times10^{-4}$ s is employed for the simulation of particle motion.

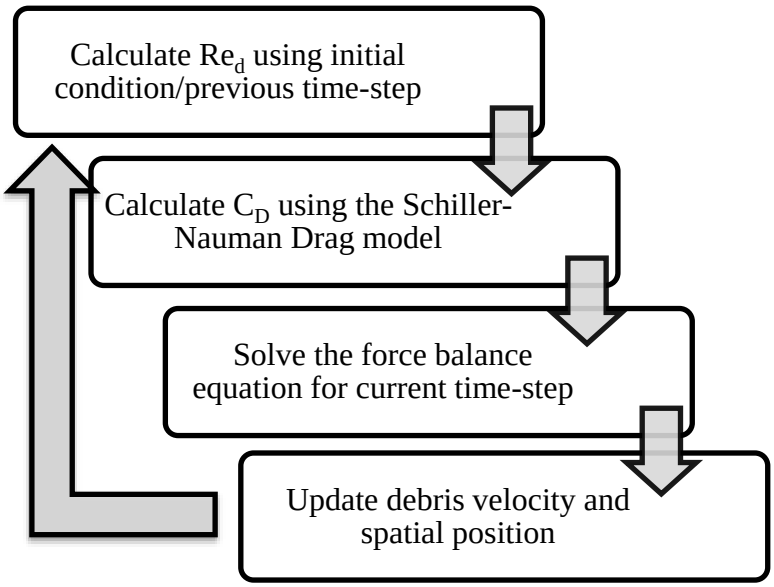

Figure 3.9: Process diagram of numerical simulation.

Debris group A, B1 and C are released in the tornado-like vortex with S = 0.3, and group B1, B2 and B3 and group A, B1 and C are released in the tornado-like vortex of S = 0.69. Each debris group are released at 50 time selected instances of the vortex flow in order to obtain converged distribution of statistics; the release times are chosen at every quarter revolution of the vortex from the time, t = 65 s for both of the vortex flow field. 450 individual debris of each debris group are released and a total of 3600 individual debris are released in the two tornado-like vortices.

The initial velocity of debris are zero and are released near the ground surface at the elevation of z =0.006 m (corresponding to z/r_c =0.09 and z/r_c =0.05 for tornado-like vortex with S = 0.3 and S = 0.69 respectively); the debris are positioned along 9 different radial distances in the two tornado-like vortices; with 5 locations within the core of the vortex at r/r_c =0, 0.25, 0.5, 0.75 and 4 locations away from the core at r/r_c =1.5, 2, 2.5 and 3. The release locations of debris in the two tornado-like vortices are outlined in Table 3.6.

Table 3.6: Release locations of debris in the tornado-like vortices

	Radial Distance (m)								
r/r_c	0	0.25	0.5	0.75	1	1.5	2	2.5	3
S =0.3	0	0.0175	0.035	0.0525	0.07	0.105	0.14	0.175	0.21
S =0.69	0	0.0275	0.055	0.0825	0.11	0.165	0.22	0.275	0.33

4. Tornado-like Vortices

"There are three rules to follow when parallelizing large codes. Unfortunately, no one knows what these rules are"

W. Somerset Maugham & Gary Montry (2012)

AN IN-DEPTH COMPREHENSION of the flow field is required in order to accurately predict and evaluate debris flight behaviour in tornado-like wind fields. Hence, two tornado-like vortices corresponding to swirl ratios of 0.3 and 0.69 are numerically generated and the flow fields are presented, followed by a comparison between the CFD simulations, analytical vortex models and experimental measurements described in chapter 3. First, an investigation on the impact of grid resolution is performed in section 4.1, then, a comparison with the experimental data is carried out in section 4.2. The numerical results are compared with the analytical vortex models in section 4.3 and an in-depth analysis of the flow patterns of the vortex structure and the method of determining the characteristic parameters are discussed in section 4.4, followed by a summary in section 4.5. Due to the axis-symmetrical structure of vortices, results

presented henceforth are expressed in terms of radial distance, r, from the centre of the numerical simulator while the velocity components are represented by tangential, radial and vertical velocities with U_t, U_r and U_v respectively.

4.1. Assessment of Numerical Accuracy

In order to investigate the impact of grid resolution on the numerical results, a series of simulations are performed on the coarse, fine and extra fine mesh to verify that flow patterns and certain flow parameters are stable under variations of the grid resolutions; the tangential velocity component and the surface pressure distribution of the tornado-like vortices with S =0.3 and S =0.69 are discussed and compared individually. The finalized results are used for further comparison with analytical models and experimental data.

Figure 4.1 shows the time averaged tangential velocity of the tornado-like vortex with the S=0.3 with different grid resolution along four vertical lines at various radial distances from the centre of the simulator respectively at 0.1 m, 0.15 m, 0.2 m and 0.25 m. A general agreement can be observed where all three meshes predicted similar and consistent magnitude of tangential velocity from the elevation above z = 0.1 m and the velocity profile at radial distance of r = 0.25 m. However, a noticeable difference can be found on the velocity profile distribution at the near ground region predicted by the coarse mesh, compared to the fine and extra fine mesh which predicted very similar results; the difference is attributed to the lower grid resolution near the guide vanes for the coarse mesh, in which inevitably lead to the variation of velocity profile. The maximum tangential velocities obtained from the three meshes are 11.04, 11.62 and 11.70 m/s for

coarse, fine and extra fine mesh respectively, which yields the difference of 5% from coarse to fine mesh and 0.69% from fine to extra fine mesh.

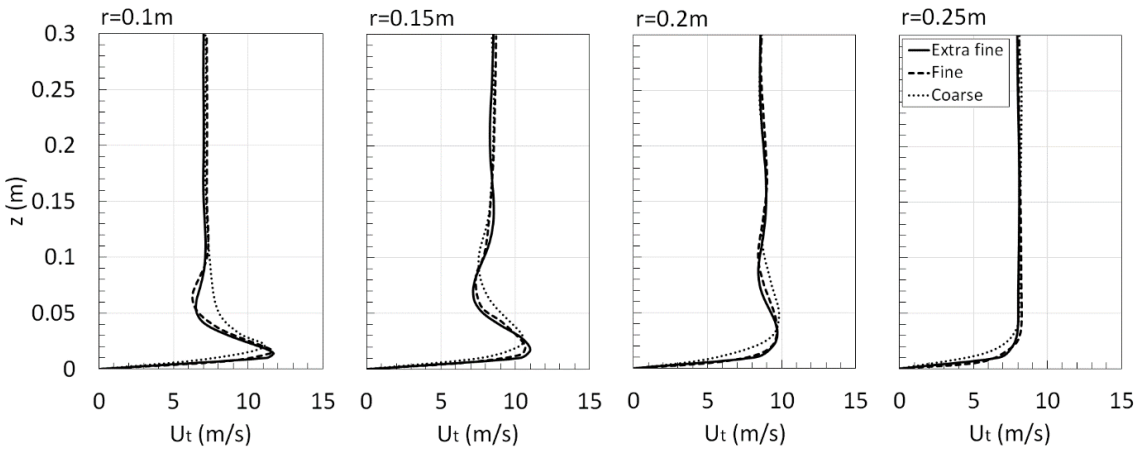

Figure 4.1: Vertical profiles of the tangential velocity of the tornado-like vortex with S= 0.3 with different grid resolutions at the position r = 0.1, 0.15, 0.2 and 0.25.

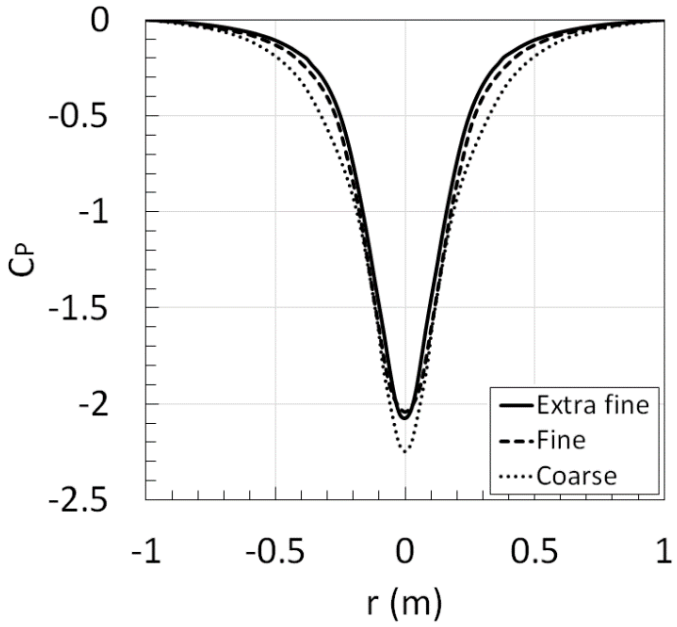

Figure 4.2: Distribution of the time averaged pressure coefficient on the ground surface of the tornado-like vortex with S= 0.3 with different grid resolutions.

Figure 4.2 illustrates the horizontal distribution of pressure coefficient at the ground surface of the simulator with different grid resolution; all simulations predicted the lowest magnitude of pressure coefficient at the centre of the simulator of -2.5, -2.07 and -2.04 for coarse, fine and extra fine mesh respectively, resulting in the difference of 17.2% from coarse to fine mesh and 1.2% from fine to extra fine mesh. The surface pressure increases with the increase in radial distance, where a similar trend can be observed for the results from the fine and extra mesh, while the coarse mesh shows the highest discrepancy and predicted the lowest magnitude in comparison.

The time averaged tangential velocity of the tornado-like vortex with S =0.69 with different grid resolution along four vertical lines at the radial distance of 0.1 m, 0.15 m, 0.2 m and 0.25 m from the centre of the simulator is shown in Figure 4.3. While a similar trend can be observed where all three meshes predicted consistent magnitude of tangential velocity from the elevation above z = 0.1 m, a notable difference can be observed where the thickness of the boundary layer predicted by the coarse mesh is greater in comparison with the fine and extra fine mesh, which predicted very similar results. Since the method of generating mesh is similar for both computational domains, these differences are attributed to the lower grid resolution near the guide vanes. The maximum tangential velocities obtained from the three meshes are 11.53, 12.64 and 12.71 m/s coarse, fine and extra fine mesh respectively, which yields the difference of 9.6% from coarse to fine mesh and 0.61% from fine to extra fine mesh.

Figure 4.4 shows the horizontal distribution of pressure coefficient at the ground surface of the simulator with different grid resolution. Similarly, the results from the coarse mesh predicted the lowest magnitude of pressure coefficient at the centre of the simulator of -2.73, -2.61 and -2.58 for coarse, fine and extra fine mesh respectively, resulting in the

difference of 4.4% from coarse to fine mesh and 1.1% from fine to extra fine mesh. The highest discrepancy can be observed around the radial distance of 0.5 m for the results predicted by coarse mesh, while the fine and extra mesh shows very similar trend of pressure distribution.

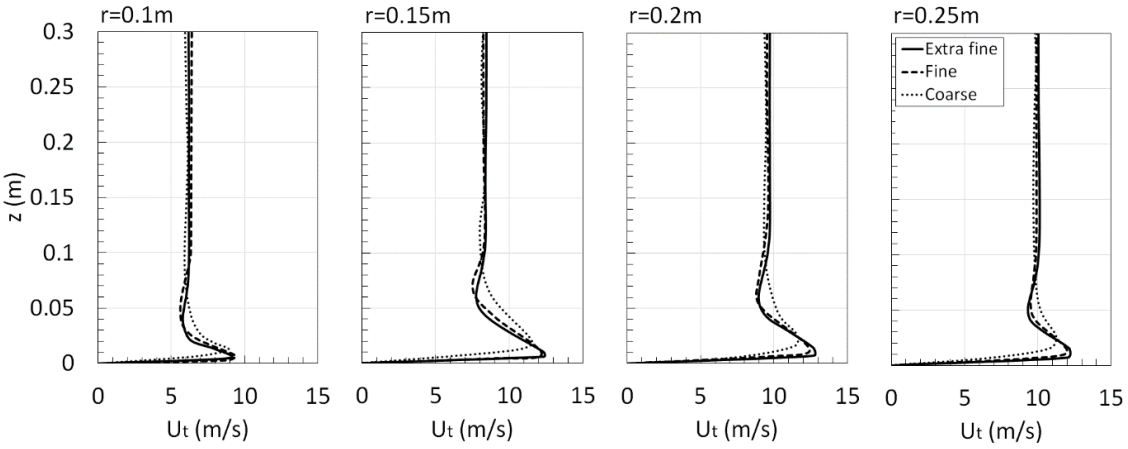

Figure 4.3: Vertical profiles of tangential velocity of the tornado-like vortex with S= 0.69 with different grid resolutions at the position r = 0.1, 0.15, 0.2 & 0.25.

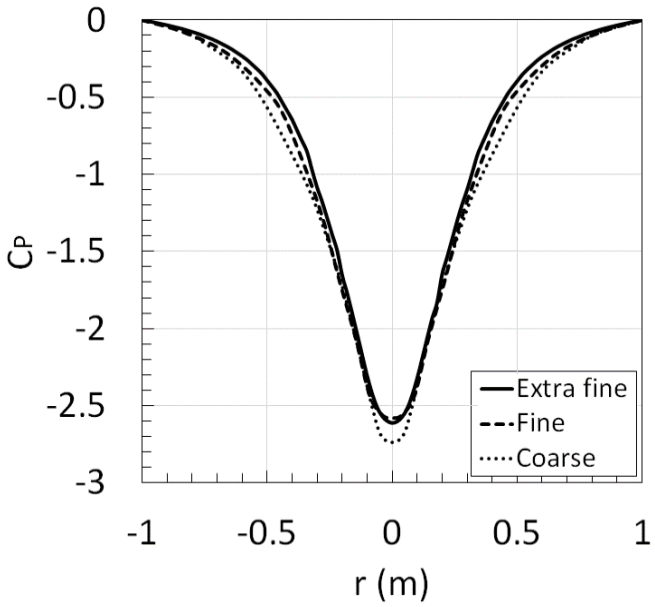

Figure 4.4: Distribution of the time averaged pressure coefficient on the ground surface of the tornado-like vortex with S= 0.3 with different grid resolutions.

Generally, the increase in grid resolution near the guide vanes shows a convergence in the results produced by the coarse and fine mesh; further refinement of grid resolution shows a difference of less than 1% in the velocity field and approximately 1.2% difference for pressure distribution predicted by fine and extra fine for both vortices. The refinement of grid resolution from coarse mesh to fine mesh shows the collapse of results, but only minor changes in the flow field from fine and extra fine mesh. Understandably, LES directly resolves the large-scale eddies of the flow while filtering out the sub-grid scales (SGS) of the flow, any eddies that are larger than the filter width are retained in the flow field and solved; as the filter width is dependent on the mesh size, finer grid resolution generally results in the higher range of vortices in the flow field to be resolved. However, as the vortex flow field was stable under the variation of grid resolutions, the differences of further refining the grid resolution are inevitably small and can be neglected. Henceforth, the results from the simulation with extra fine mesh are used for further analysis and comparisons, and are normalized using the characteristic parameters of radius of the vortex core (r_c) and the maximum tangential velocity (U_T) of the respective vortices (details of the vortex characteristics discussed in section 4.4).

4.2. Comparison with Physically Generated Vortices

In this section, numerical simulations are compared with the physically generated tornado-like vortices from the experiments conducted by Gillmeier et al. (2017). The comparison of the velocity components and surface pressure distribution for the tornado-like vortices with S =0.3 and S =0.69 are presented in section 4.2.1 and section 4.2.2 respectively. The velocity measurements that are used as a comparison are obtained at the

elevation of z = 0.01 m, 0.1 m, 0.2 m and 0.4 m[1]; however, it should be noted that the velocity measurements close to the vortex centre at the radial positions of r =0 m and 0.025 m were not used as a comparison due to the large experimental measurement uncertainties and poor data quality (of less than 80%) at those positions, where the data quality is calculated based on the percentage of velocity samples measured over time which exceeds the limitation of the Cobra probe (velocities that are lower than 2 m/s and have an angle of attack of greater than the cone of 45°).

4.2.1. Flow field of vortex with S=0.3

The flow field of the vortex with S =0.3 obtained from the physically generated tornado-like vortex are compared with the results from the numerical simulation. The velocity measurements at elevations of z = 0.01 m, 0.1 m, 0.2 m and 0.4 m correspond to the normalised elevations of z/r_c=0.14, 1.42, 2.85 and 5.7 respectively. The comparison of horizontal profiles of tangential, radial and vertical velocity components are illustrated in Figure 4.5, Figure 4.6 and Figure 4.7 respectively, while the surface pressure distribution is shown in Figure 4.8.

Figure 4.5 shows the comparison of tangential velocity from numerical simulation and experimental results at different elevation. Generally, it can be observed that the distribution of tangential velocity predicted by the numerical simulation and results from the experiments shows similar trend and corresponds relatively well, particularly around the near ground region at the elevation of z/r_c=0.14; both the vortices shows the increase of low velocity at the centre of the vortex to a maximum and then gradually decreases as the radial distance increases. however, some differences can be found at the elevation of

[1] Normalised equivalent values given in the following subsections since r_c is a function of swirl ratio.

z/r_c=2.85 and 5.7, where the velocity distribution obtained from numerical simulation shows very distinguishable peaks of maximum tangential velocity, while the experimental results shows lower magnitude of tangential velocity. A noticeable difference can also be found around the vortex centre at the radial position of r/r_c=0.7 at the elevations of z/r_c=1.42, 2.85 and 5.7 where the numerical simulation predicted a lower magnitude of tangential velocity which exceed the range of experimental uncertainties.

The comparison of radial velocity from numerical simulation and experimental results at different elevation are shown in Figure 4.6. The distribution of radial velocity predicted by the numerical simulation and results from the experiments around the near ground region at the elevation of z/r_c=0.14 predicted very similar trend of distribution. However, noticeable difference can be found at the elevation of z/r_c=1.42 around the radial location of r/r_c=3, where the experimental result shows higher trend of outflow, as well as the elevation of z/r_c=0.14 at the radial location of r/r_c=0.7, where the numerical simulation predicted a lower magnitude of radial inflow. At higher elevations z/r_c=2.85 and 5.7, the numerical results show slightly higher magnitudes of radial velocity than the experiments around the radial distance of r/r_c=1 to 3.

Figure 4.7 shows the comparison of vertical velocity from numerical simulation and experimental results at different elevation. Both the numerical simulation and results from the experiments shows very similar trend of vertical velocity distribution. However, some difference can be observed at the elevation of z/r_c=5.7 at the far away region (z/r_c>4), where the experimental results shows the higher distribution of velocity magnitude in comparison. It should be pointed out that while both methods show very similar results, the experimental results do not clearly indicate downwards flow at the vortex centre; this

can perhaps be attributed to the lack of fine scaled data around this region, thus making further comparisons around the vortex centre difficult.

Figure 4.8 shows the comparison of pressure coefficient on the ground surface obtained from numerical simulation and experimental results. Both the numerical simulation and experimental results corresponds well and indicate similar distribution of pressure coefficient in both trend and magnitude, where the numerical simulation predicted a lower minimum pressure at the centre of the vortex in comparison with the experimental results.

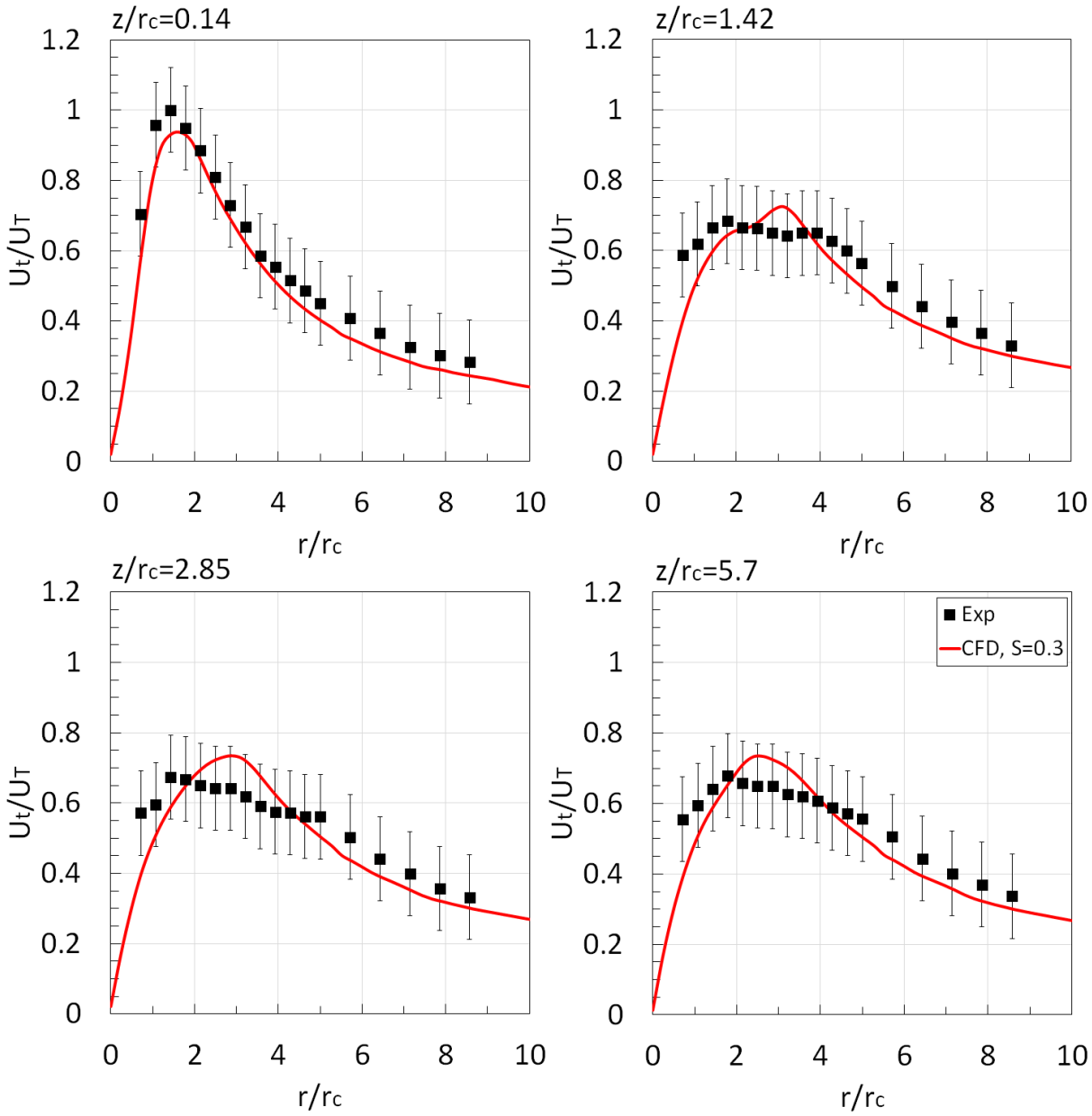

Figure 4.5: Comparison of tangential velocity distribution from numerical simulation (CFD) and experimental results (Exp) obtained from Gillmeier et al. (2017) at the elevation of z/r_c =0.14, 1.42, 2.85 and 5.7

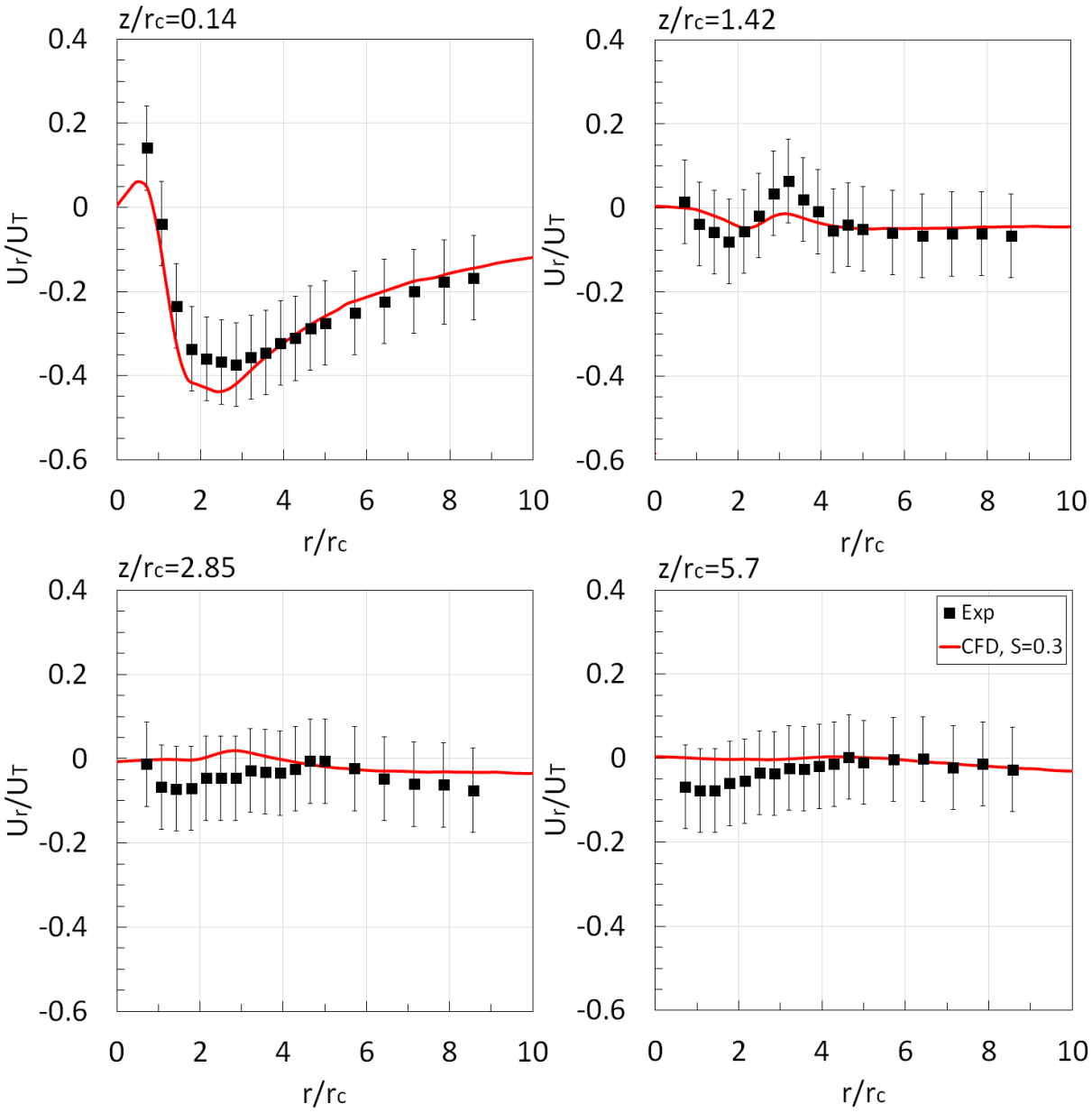

Figure 4.6: Comparison of radial velocity distribution from numerical simulation (CFD) and experimental results (Exp) obtained from Gillmeier et al. (2017) at the elevation of z/r_c =0.14, 1.42, 2.85 and 5.7.

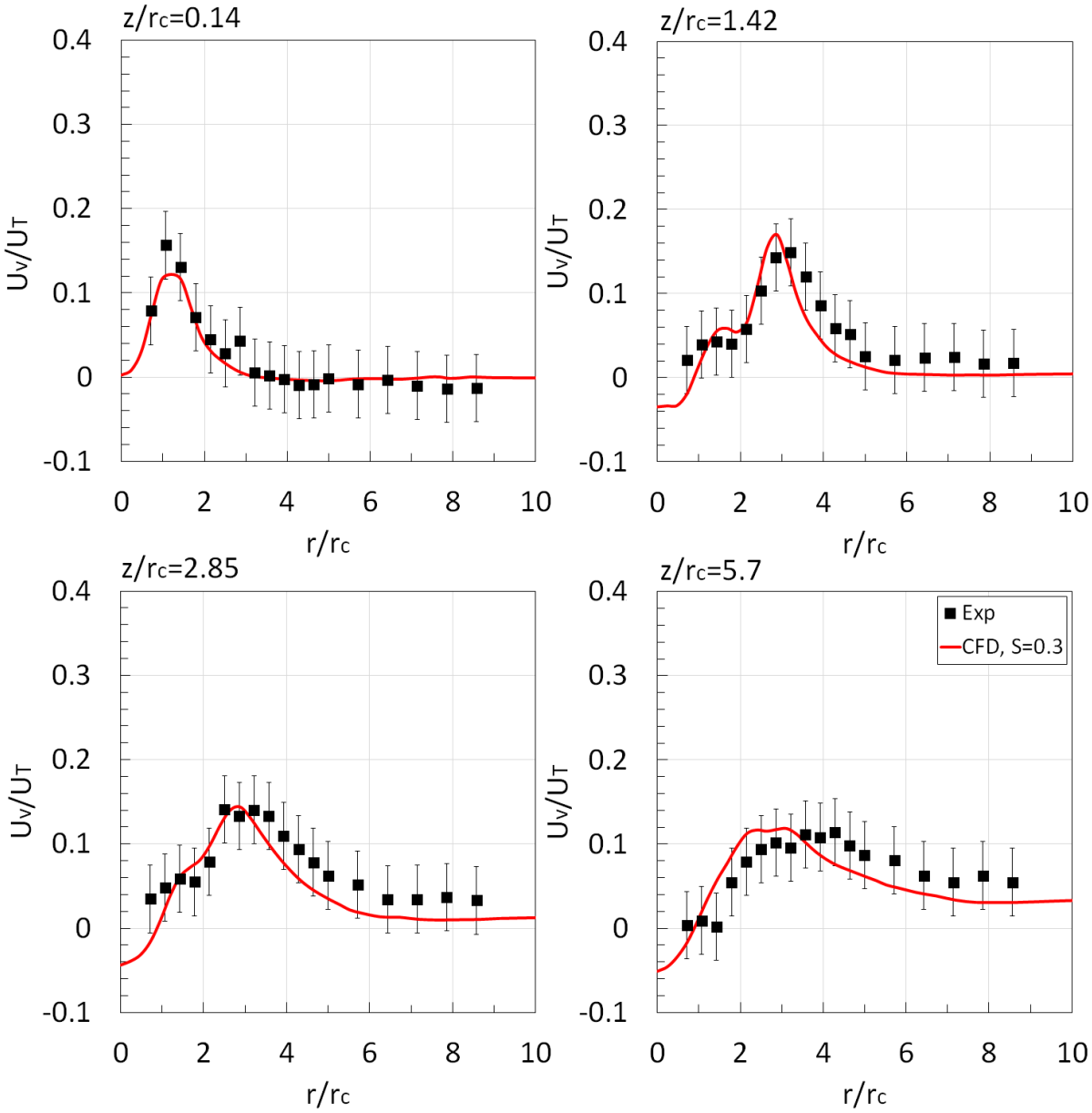

Figure 4.7: Comparison of vertical velocity distribution from numerical simulation (CFD) and experimental results (Exp) obtained from Gillmeier et al. (2017) at the elevation of z/r_c =0.14, 1.42, 2.85 and 5.7.

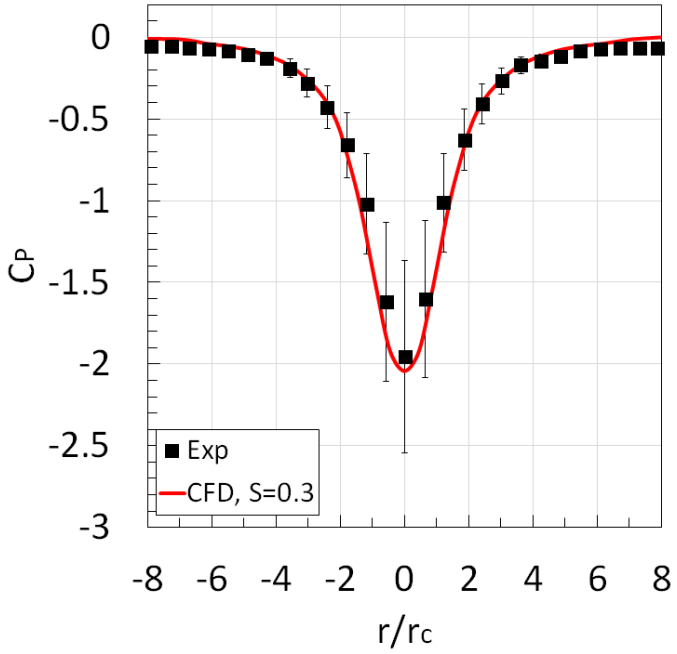

Figure 4.8: Comparison of surface pressure distribution from numerical simulation (CFD) and experimental results (Exp) obtained from Gillmeier et al. (2017)

4.2.2. Flow field of vortex with S=0.69

In this section, the flow field of the vortex with S =0.69 obtained from numerical simulation and physically generated tornado-like vortex are compared. The horizontal profiles of tangential, radial and vertical velocity components are illustrated in Figure 4.9, Figure 4.10 and Figure 4.11 respectively, while the surface pressure distribution is shown in Figure 4.12. The elevation of the velocity measurements at elevations of z = 0.01 m, 0.1 m, 0.2 m and 0.4 m correspond to the normalised elevation of z/r_c=0.09, 0.9, 1.8 and 3.6 respectively.

Figure 4.9 shows the tangential velocity distribution for the vortex with S =0.69. Both the numerical simulation and experimental results show low magnitude of tangential velocity at the centre, and then increases to a maximum while gradually decreases as the radial distance increases. Some differences can be observed around the vortex centre at

r/r_c=0.45, as well as regions further away at r/r_c>3 around the near ground region at the elevation of z/r_c =0.09, where numerical simulation appears to predict lower tangential velocity distribution than the experimental results. At higher elevations, z/r_c=0.9, 1.8 and 3.6, the numerical simulation shows a faster increase of tangential velocity with the increase of radial distance around the radial distance from r/r_c=0.7 to 2.8.

The comparison of radial velocity from numerical simulation and experimental results at different elevation are shown in Figure 4.10. Around the near ground at the elevation of z/r_c=0.09, both results shows similar characteristic; outflow can be observed around the radial distance from r/r_c =0 to approximately r/r_c =1, and inflow from the radial distance of r/r_c=1 to r/r_c=8, with the experimental results predicting lower magnitude of both inflow and outflow in comparison. At the elevation, z/r_c=0.9, the experimental results show slightly higher magnitude of radial velocity in comparison with numerical simulation, while at other heights (z/r_c=1.8 and 3.6), both results shows very similar trend.

Figure 4.11 shows the comparison of the vertical velocity component. Around the near ground at the elevation of z/r_c=0.09, both the numerical simulation and results from the experiments shows updraft flows from the radial distance of r/r_c<45 onwards, where the results from the experiments shows larger region of vertical flows than the numerical simulations. The distribution of vertical velocities at higher elevations, z/r_c=0.9, 1.8 and 3.6 shows consistent behaviour and similar trend, where the experiments predicted lower magnitude of updraft flows. Similar to the comparison of results for the vortex with S =0.3, it is worth noting that while the results from the experiments and numerical simulation shows similar vortex flow patterns, the numerical simulation predicted considerably higher magnitude of downdraft flow at the centre of the vortex at higher

elevations z/r_c =0.9, 1.8 and 3.6, while the experimental results does not indicate downwards flow at that region. As a result, a comparison between numerical simulation and experimentally obtained results at the vortex centre is difficult due to the lack of good experimental data.

The comparison of pressure coefficient on the ground surface obtained from numerical simulation and experimental results are shown in Figure 4.12. Both the numerical simulation and experimental results shows a similar distribution of pressure coefficient, where the numerical simulation predicted lower minimum pressure at the centre of the vortex in comparison with the experimental results, as well as a faster increase of pressure coefficient with the increase of radial distance.

In general, the comparison of numerically and physically generated tornado-like vortices from the experiments corresponds well and shows similar flow patterns and characteristics. However, both the numerical simulation and experimental methods are not without their limitations; whilst every effort has been made in numerical modelling in order to accurately reproduce the physical vortex generator, there are inevitably small differences introduced due to the numerical process. Although it is difficult to quantity the impact of these differences, these differences are generally well within the experimental uncertainties, thus considered suitable for the purposes of this work.

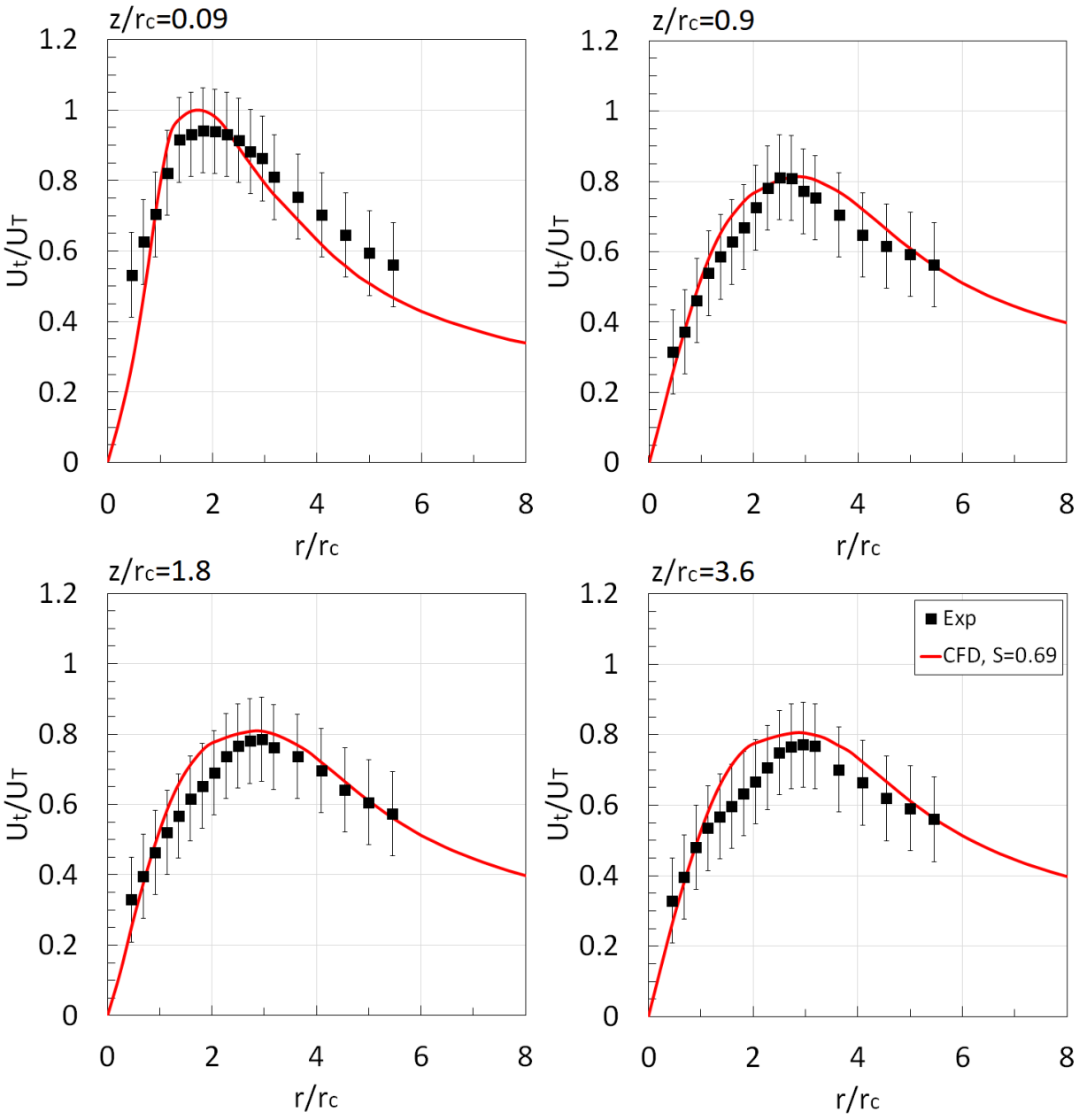

Figure 4.9: Comparison of tangential velocity distribution from numerical simulation (CFD) and experimental results (Exp) obtained from Gillmeier et al. (2017) at the elevation of z/r_c =0.09, 0.9, 1.8 and 3.6.

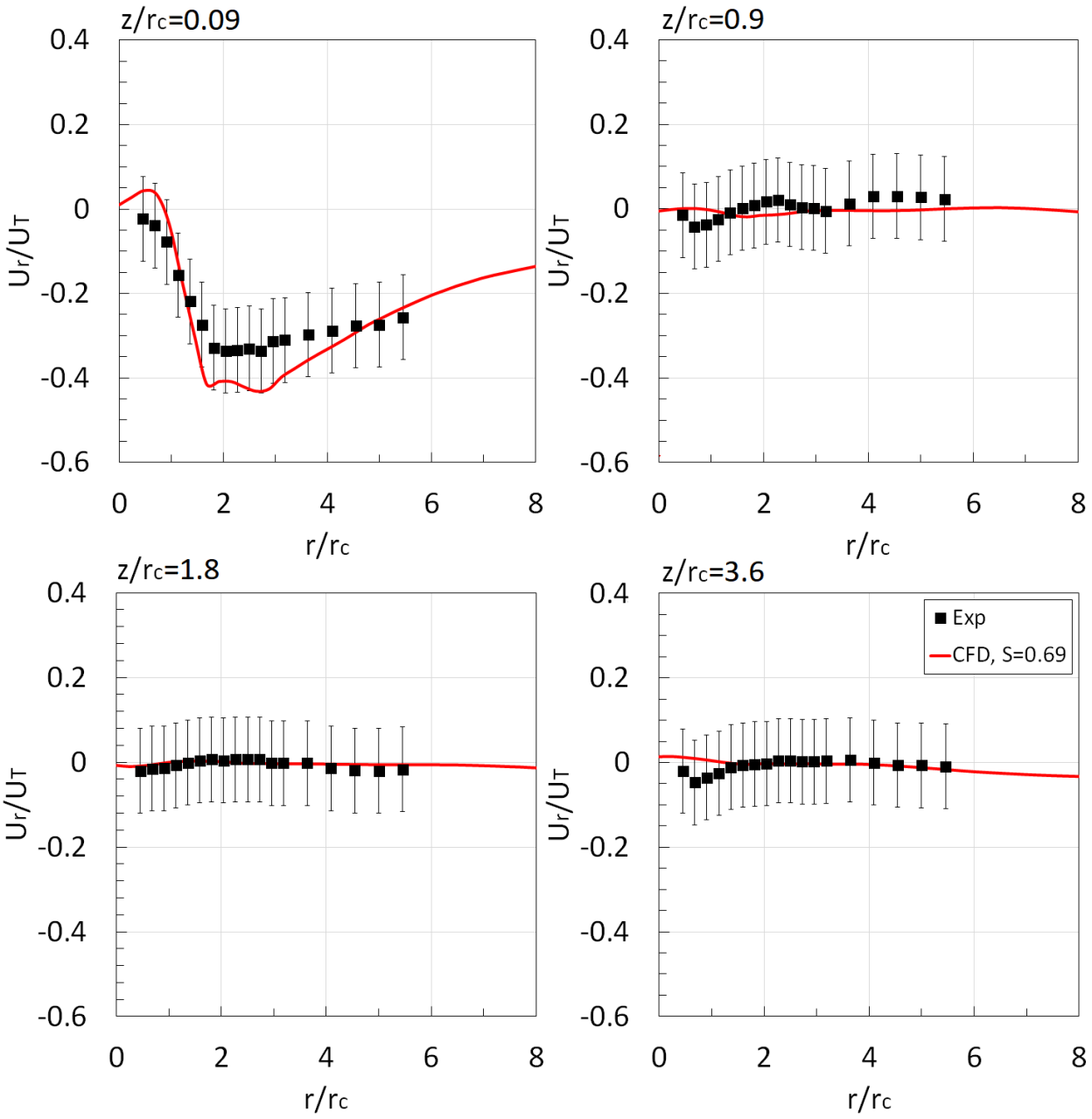

Figure 4.10: Comparison of radial velocity distribution from numerical simulation (CFD) and experimental results (Exp) obtained from Gillmeier et al. (2017) at the elevation of z/r_c =0.09, 0.9, 1.8 and 3.6.

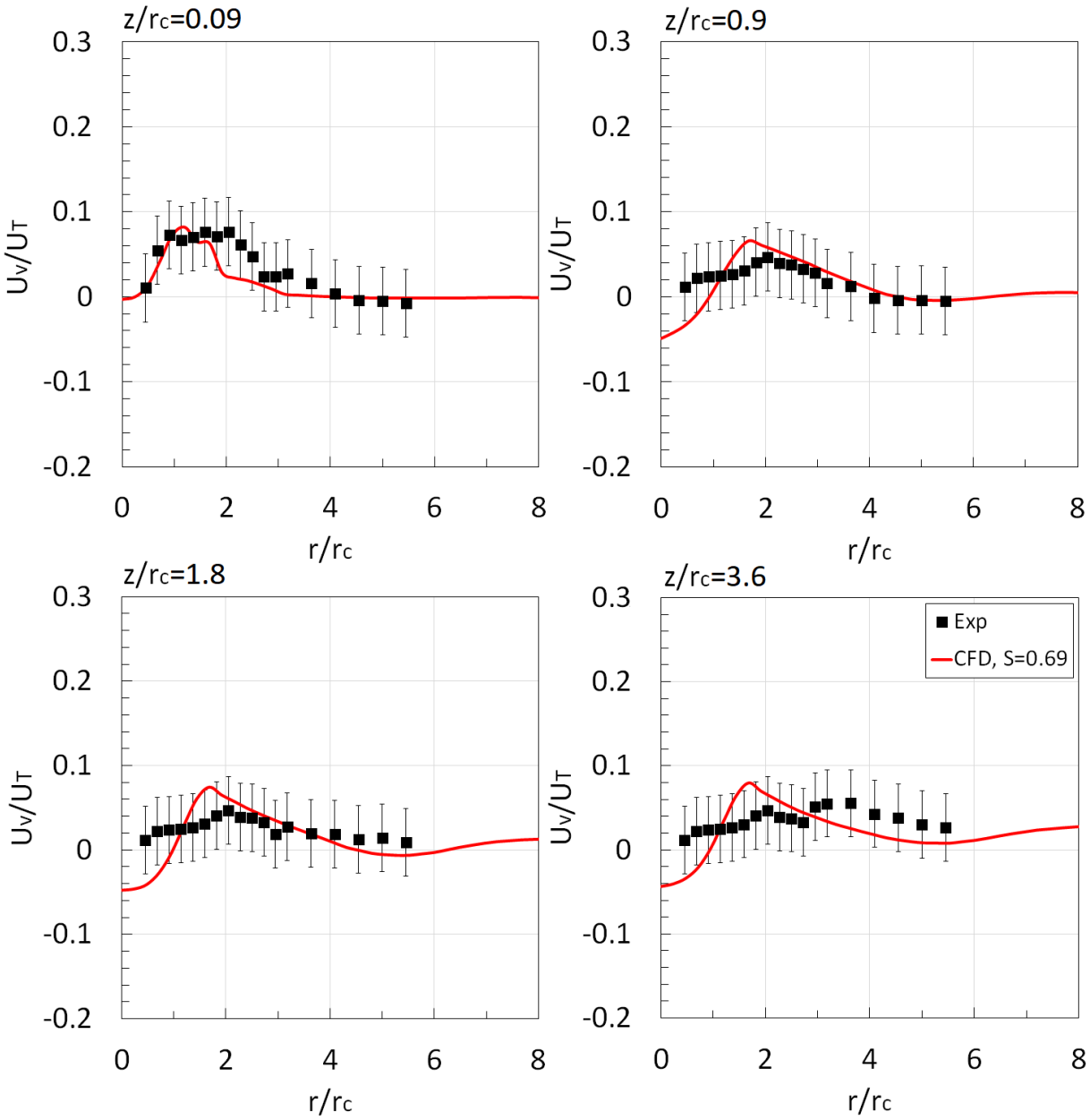

Figure 4.11: Comparison of vertical velocity distribution from numerical simulation (CFD) and experimental results (Exp) obtained from Gillmeier et al. (2017) at the elevation of z/r_c =0.09, 0.9, 1.8 and 3.6.

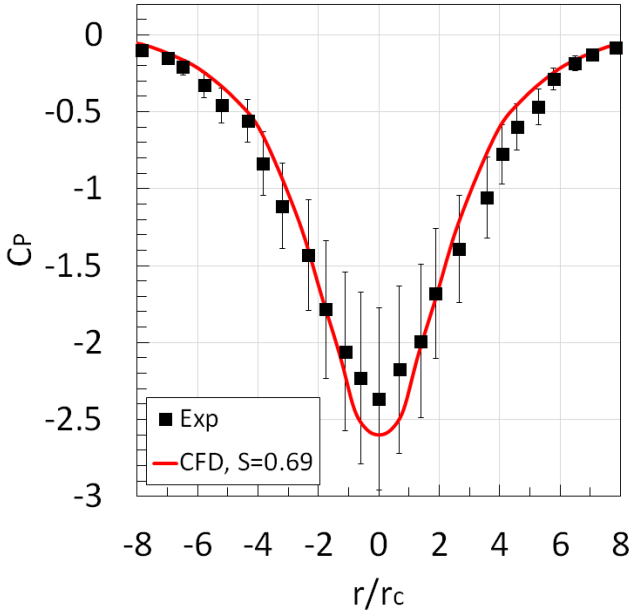

Figure 4.12: Comparison of surface pressure distribution from numerical simulation (CFD) and experimental results (Exp) obtained from Gillmeier et al. (2017).

4.3. Comparison with Analytical Models

In this section, results from the numerical simulations are compared with the Rankine vortex model, Burgers-Rott vortex model, Sullivan vortex model and Baker and Sterling vortex model. The tangential velocity profiles and the surface pressure distribution of the analytical vortex models are compared with the tornado-like vortices with S =0.3 and S =0.69. It should be pointed out that the core radius (r_c) presented in this study is the radial distance which separates the updraft and downwards flow, opposed to the radial distance of the maximum tangential velocity (r_T). This is due to the fact that the core radius distinguishes the flow structure of the vortex by separating the flow patterns, therefore contrasting the effects of debris flight behaviour in relation with the vortex flow pattern (details of debris flight in Chapter 5). Hence, the results for the analytical models presented are normalized by the respective vortex characteristic lengths, where the core

radii are 0.07 m and 0.11 m for the vortices with S =0.3 and S =0.69 respectively. The pressure distribution are normalised based on the minimum pressure at the centre of the vortices of approximately C_p =2.6 and C_p =2 for the vortex with S =0.3 and S =0.69 respectively. The tangential velocity components of Rankine, Burgers-Rott and Sullivan vortex models are not a function of height, therefore, only the elevation where the maximum tangential velocity occurs from the respective vortices are compared (z/r_c=0.15 and 0.3 for vortex with S =0.3 and 0.69 respectively).

Figure 4.13 shows the distribution of tangential velocity at an elevation of z/r_c = 0.3 for the vortex with S =0.3 from the numerical simulation in comparison with the analytical vortex models. Around the radial distance of r/r_c =0 to 1, the Rankine and Sullivan vortex models appear to underestimate the magnitude of tangential velocity, while Burgers-Rott model matches the numerical results well. At regions further away r/r_c >2, the Rankine and Sullivan vortex models failed to capture the distribution while the Burgers-Rott and Baker and Sterling model represents the trend reasonably well.

Figure 4.14 shows the distribution of tangential velocity at the elevation of z/r_c ≈0.15 for the vortex with S =0.69 from the numerical simulation are compared with the analytical vortex models. All analytical models failed to accurately capture the distribution of tangential velocity at the region around the radial distance of r/r_c =0 to 1. At regions further away (r/r_c >2), both the Rankine and Sullivan vortex models again failed to predict the distribution while the Burgers-Rott and Baker and Sterling vortex model are able to closer represent the trend.

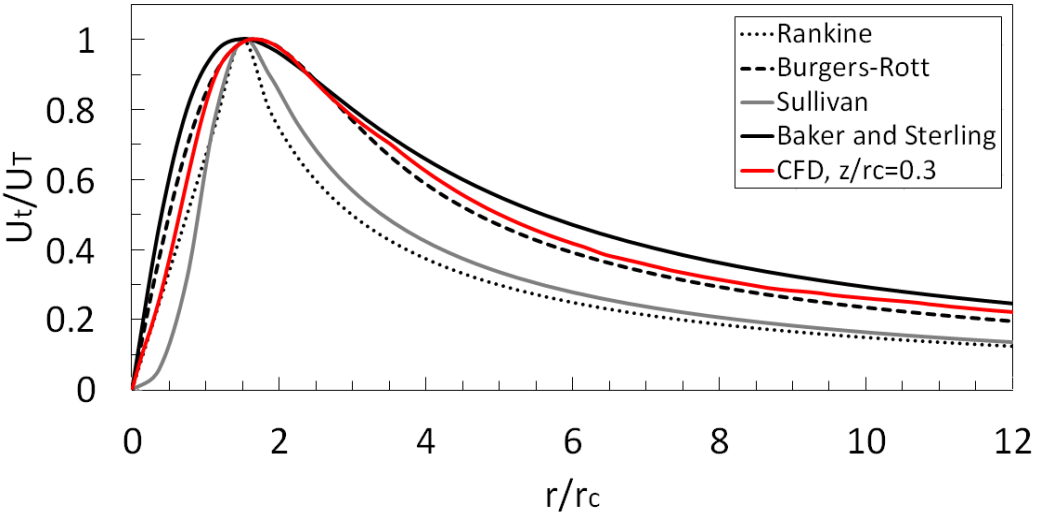

Figure 4.13: Distribution of tangential velocity of the vortex with S=0.3 from the numerical simulation in comparison with the analytical vortex models (Rankine, Burgers-Rott, Sullivan and Baker and Sterling vortex models).

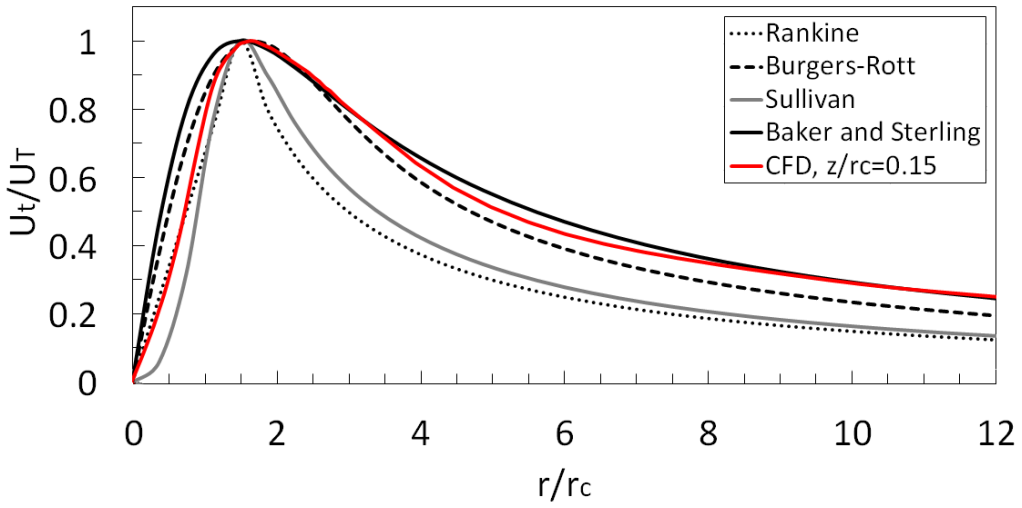

Figure 4.14: Distribution of tangential velocity of the vortex with S=0.69 from the numerical simulation in comparison with the analytical vortex models (Rankine, Burgers-Rott, Sullivan and Baker and Sterling vortex models).

Figure 4.15 and Figure 4.16 shows the surface distribution of pressure coefficient for vortex with S =0.3 and S =0.69 respectively, in comparison with the analytical vortex

models. The distribution of pressure coefficient predicted by the Baker and Sterling vortex model shows good agreement with the numerically simulated vortex with S =0.3 in comparison with all other vortex models, where the largest difference is found between the radial distance of approximately r/r_c =1.5 to 4. A similar trend can be observed for the distribution of pressure coefficient predicted by the analytical vortex models for the vortex with S =0.69, where the Baker and Sterling vortex model is able to represent the surface pressure distribution while all other vortex models overestimated the increase of pressure around the radial distance of approximately r/r_c =1.5 to 6.

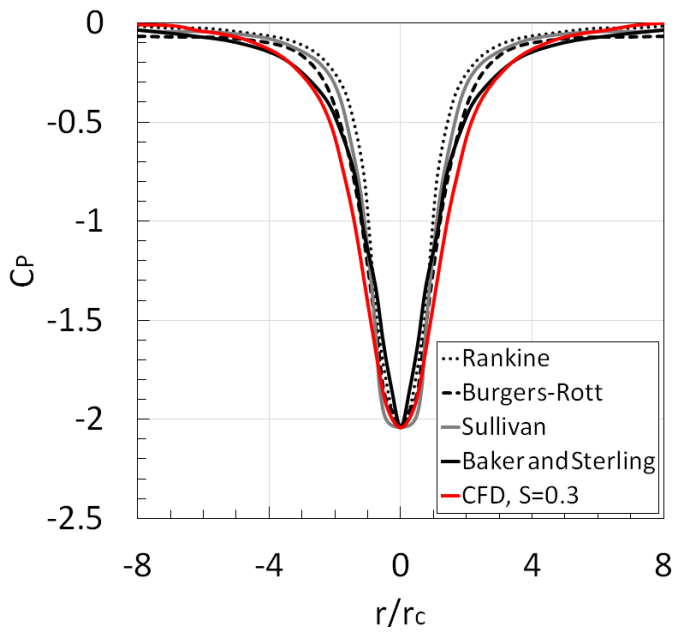

Figure 4.15: Distribution of pressure coefficient on the ground surface of the tornado-like vortex with S= 0.3 in comparison with analytical vortex models (Rankine, Burgers-Rott, Sullivan and Baker and Sterling vortex models).

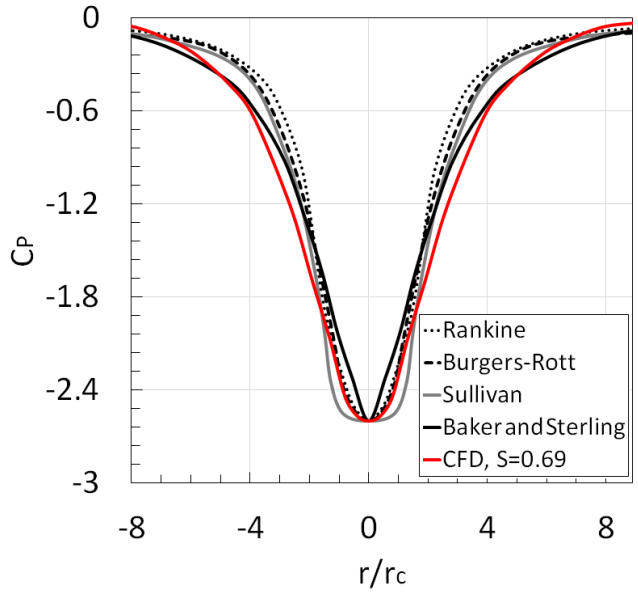

Figure 4.16: Distribution of pressure coefficient on the ground surface of the tornado-like vortex with S= 0.69 in comparison with analytical vortex models (Rankine, Burgers-Rott, Sullivan and Baker and Sterling vortex models).

In general, the Rankine and Sullivan vortex models failed to represent the tangential velocity and surface pressure distribution of the vortices with both swirl ratios, while the Burgers-Rott and Baker and Sterling vortex model is able to represent the velocity field of the vortex with S =0.3 and S =0.69 well. The Burgers-Rott vortex model failed to predict the surface pressure and the flow pattern of the vortex with S =0.69, while the Baker and Sterling vortex model shows reasonable agreement with the numerical results for the prediction of pressure field and for both the vortices. Understandably, none of these presented analytical models can be used to fully represent the entire three-dimensional flow field tornado-like vortices due to the assumptions made during the derivations. The numerically generated vortices capture the transient effects of the flow field while the analytical vortex models assume steady state. As Gillmeier et al. (2017) noted, the time-dependent flow characteristics of physically generated vortices were

found to significantly influence the instantaneous pressure field of the vortices. With that being said, the Burgers-Rott and Baker and Sterling vortex models, although simple, are able to represent some parts of the tornado flow field such as the tangential velocity and pressure distribution relatively well.

4.4. Tornado Flow field

A detailed analysis of the vortex structure and the flow patterns of the vortex with the swirl ratio of 0.3 and 0.69 are presented in section 4.4.1 and velocity flow fields of the vortices are analysed and the method of determining the radius of the core and vortex wall thickness are discussed in section 4.4.2.

4.4.1. Qualitative analysis of the vortex structure

Figure 4.17 illustrates the flow field of the tornado-like vortices with S =0.3 and S =0.69 by injecting tracer particles from a plane source parallel to the ground surface. It can be observed that the core structure of the vortex with S =0.69 appears to occur very close the ground surface, while the vortex with S =0.3 occurs considerably further above the ground. The contours of normalised velocity magnitude of the tornado-like vortices with S =0.3 and S =0.69 on the radial vertical plane are illustrated in Figure 4.18 (a), where U_{mag} denotes the velocity magnitude of the flow field. Both of the vortices consist of two main features, a vortex core and thick vortex walls; the core is situated at the centre of the vortex while the wall surrounds the core and gives an outline to the structure of the vortex. Low velocities are observed at the core while high magnitude of velocities can be found near the ground regions for both of the vortices.

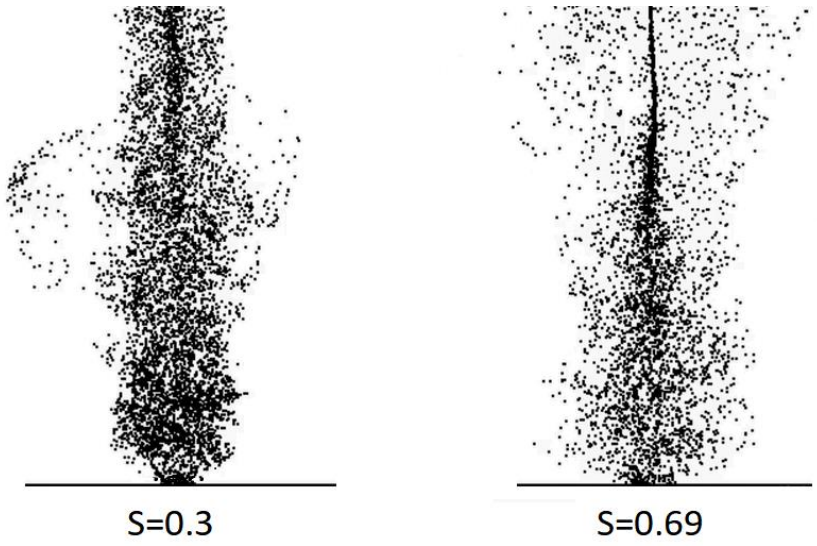

Figure 4.17: Flow visualisation of the tornado-like vortices with the swirl ratio of 0.3 and 0.69 by injecting tracer particles from a plane source

Figure 4.18 (b) shows the streamlines of the radial vertical vector of the vortex flow fields. Based on the streamlines, downwards flows are found at the centre for both of the vortices; a region of inflow can be observed towards the centre, and then redirected towards the vertical direction. The radial distance in which separates the updraft and downwards flow are identified as the core radius, marked as "r_c", while the vortex wall region, marked as "r_w", consists of the redirected vertical flows close to the vortex core and high magnitudes of tangential velocity. The core of the vortex with S=0.69 is comparably larger and closer to the ground surface; a recirculation ring can be observed situated outside of the vortex wall with the radius of approximately r/r_c=0.5 around the radial distance of r/r_c=6 at the height of z/r_c=1.2. A general schematic of the overall flow structure of both the vortices are illustrated in Figure 4.19.

The maximum tangential velocity U_T, at the radial location r_T, is marked as "x" in red. For the vortex with S =0.3, the maximum averaged tangential velocity is 11.7 m/s occurring at the radial distance of 0.12 m at the elevation of approximately 0.0165 m, and

the radius of the vortex core and wall thickness are 0.07 m and 0.32 m respectively; for the vortex with S =0.69, the maximum averaged tangential velocity is 12.71 m/s occurring at the radial distance of 0.2 m at the elevation of approximately 0.021 m, and the radius of the vortex core and wall thickness are 0.11 m and 0.54 m respectively. As a result, the time per revolution of the vortices are 0.065 s and 0.1 s for S = 0.3 and S =0.69 respectively. Details of the parameters are listed in Table 4.1. According to Lugt's (1989) description of vortex evolution, the flow pattern observed for the vortex with S=0.3 can be identified to closely resemble to the vortex break down stage, where the core of the vortex broke down from laminar flow to turbulent flow; while the vortex with S =0.69 is vortex touch down stage, where the vortex core is observed to touch the ground surface.

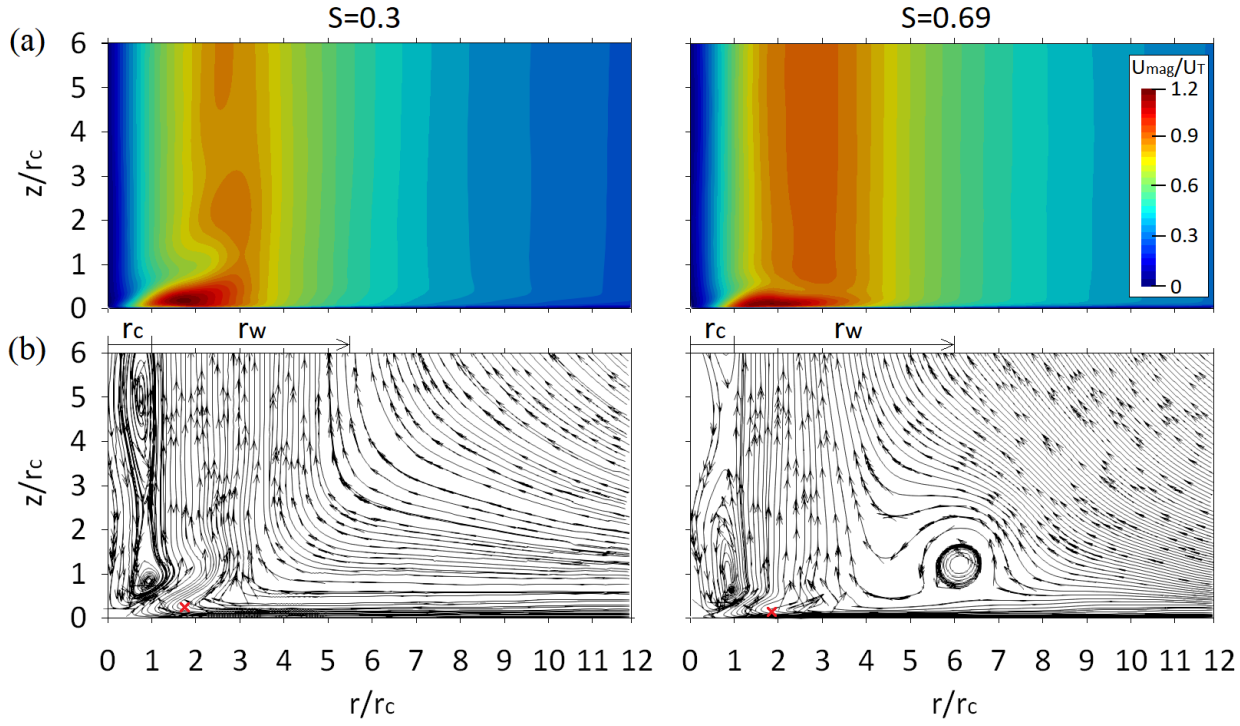

Figure 4.18: (a) Contours of normalised velocity magnitude of the tornado-like vortices with the swirl ratio of 0.3 and 0.69 (b) Streamlines of the radial vertical vector of the flow fields. The length of the core radius and vortex walls are labelled as "r_c" and "r_w" respectively, and the maximum tangential velocity are marked as "x".

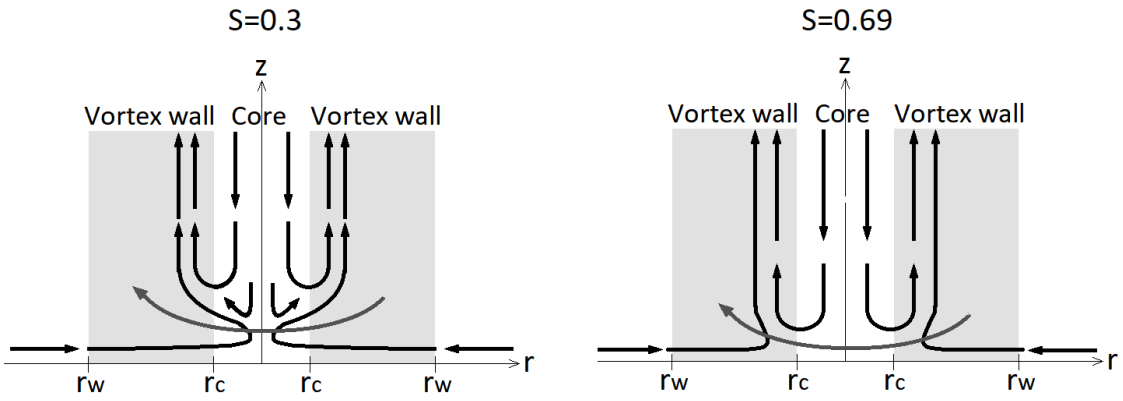

Figure 4.19: A schematic of the flow structure of the tornado-like vortices

Table 4.1: Characteristic parameters of the tornado-like vortices with S=0.3 and S=0.69.

Swirl ratio, S	0.3	0.69
Vortex stage	Vortex breakdown	Vortex touchdown
Maximum tangential velocity, U_T	11.7 m/s	12.71 m/s
Location of U_T, r_T	0.12 m	0.2 m
Vortex core radius, r_c	0.07 m	0.11 m
Vortex wall thickness, r_w	0.32 m	0.54 m
Revolution time, t_r	0.065s	0.1 s

4.4.2. Quantitative analysis of the velocity field

In this section, the velocity field of the vortices are analysed and the method of determining the vortex core and vortex walls are discussed. The horizontal profiles of tangential and vertical velocity components of the vortex with S =0.3 and 0.69 are illustrated in Figure 4.20 and Figure 4.21, where Figure 4.20 shows the profiles at the elevation of z/r_c=0.15, 0.3, 0.45 and 0.75 and Figure 4.21 shows the profiles at the elevation of z/r_c=1, 1.5, 2 and 3. In Figure 4.20 (a), it can be observed that the tangential velocity for both of the vortices increases from zero at the centre of the vortex to a

maximum around the vortex wall region, and then gradually decreases as the radial distance increases. For vortex with S =0.3, the tangential velocity distribution shows very distinguishable peaks with the highest magnitude occurring at the height of z/r_c=0.3, and then gradually decreases with the increase of elevation. For the vortex with S =0.69, the highest magnitude of tangential velocity distribution occurs very close to the ground surface at z/r_c=0.15, while the distribution tangential velocity at higher elevation shows very similar trend. According to the distribution of vertical velocity profiles shown in Figure 4.20 (b), the vortex with S =0.3 has comparably higher downwards flow at the centre and significantly greater magnitude of updraft flows. The peak of the vertical velocity increases radially outwards with the increase of height, while the highest magnitude of vertical velocity can be observed at the elevation of z/r_c=0.3. For the vortex with S =0.69, the vertical velocity profiles show a similar distribution at all elevations with the highest magnitude of vertical velocity observed to be closer to the ground, at the elevation of z/r_c=0.15.

A general behaviour of the vertical velocity is observed for both of the vortices where the flow changes direction from downwards flow to updraft flows as the radius increases; the radial distance in which the velocity magnitude gradually reduces to zero is identified as the core radius, r_c, obtained from the mean radial distance of zero vertical velocity over all elevations. As a result, the core radius is identified as the radius which separates the updraft and downwards flow. The mean maximum tangential velocity over all elevations at the core radius (r_c) corresponds to U_t/U_T≈0.43 and U_t/U_T≈0.51 for S =0.3 and S =0.69 respectively; the magnitude of these velocities are used to mark the boundaries for the determination of the vortex wall thickness, resulting in the wall thickness for the

vortex with S =0.3 of r_w=0.32 m or r/r_c=4.5, and wall thickness for the vortex with S =0.69 of r_w=0.54 m or r/r_c=5.

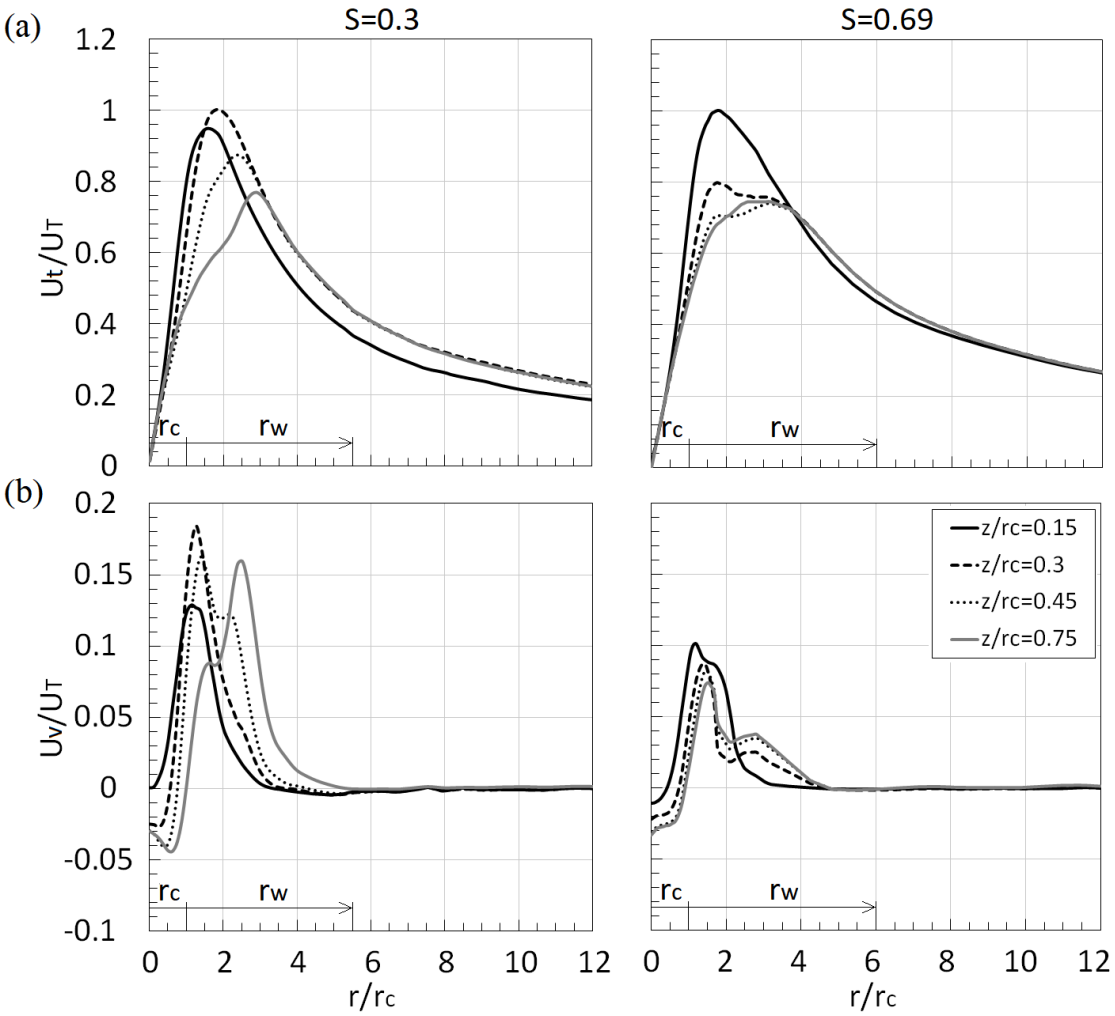

Figure 4.20: (a) Horizontal profiles of normalised tangential velocity at the elevation of z/r_c=0.15, 0.3, 0.45 and 0.75 for the vortex with S=0.3 and 0.69 (b) Horizontal profiles of normalised vertical velocity at the elevation of z/r_c=0.15, 0.3, 0.45 and 0.75 for the vortex with S=0.3 and 0.69. The length of the core radius and vortex walls are labelled as "r_c" and "r_w" respectively.

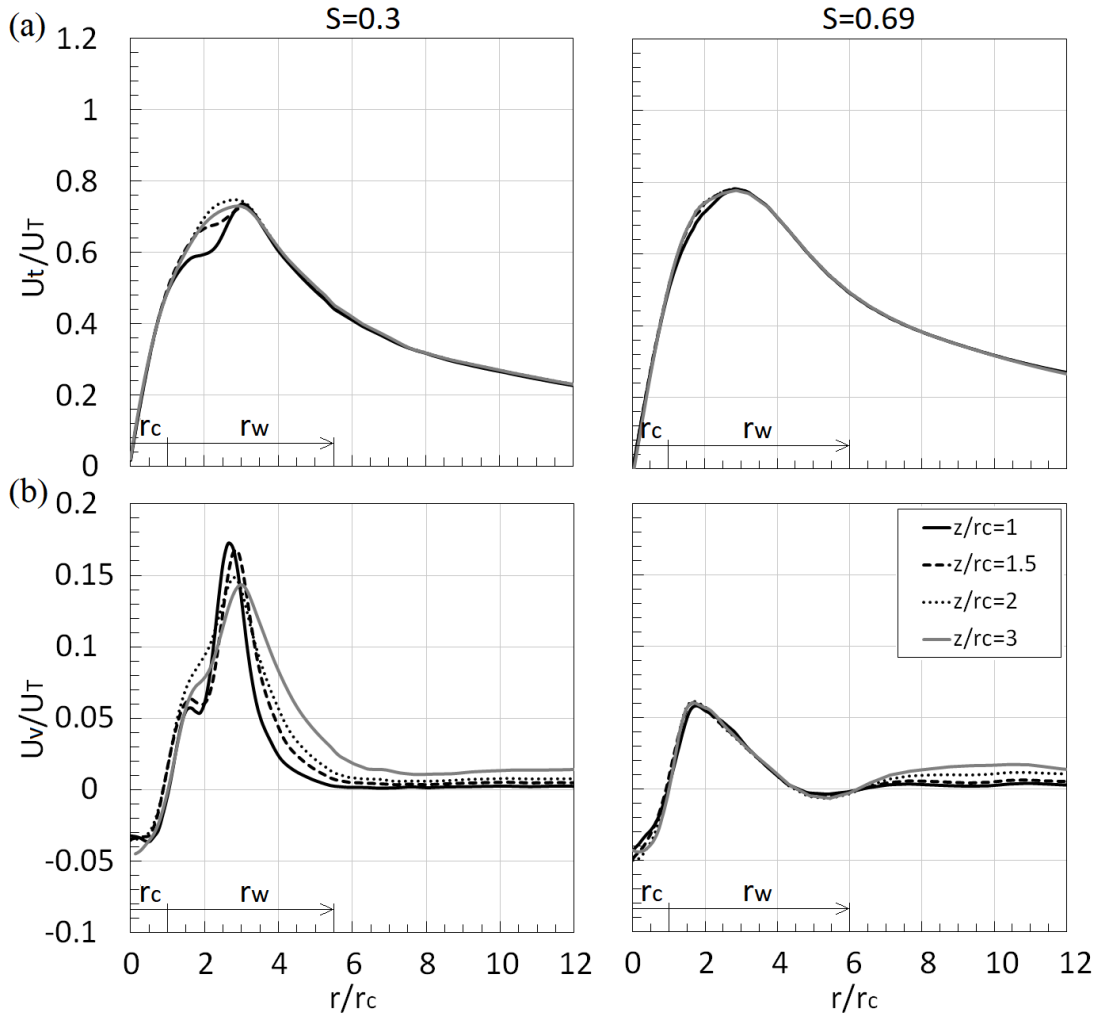

Figure 4.21: (a) Horizontal profiles of normalised tangential velocity at the elevation of z/r_c=1, 1.5, 2 and 3 for the vortex with S=0.3 and 0.69 (b) Horizontal profiles of normalised vertical velocity at the elevation of z/r_c=1, 1.5, 2 and 3 for the vortex with S=0.3 and 0.69. The length of the core radius and vortex walls are labelled as "r_c" and "r_w" respectively.

The tangential velocity profiles at greater elevations shown in Figure 4.21 (a) illustrate similar and consistent distribution for both of the vortices, where the velocity increases from zero at the centre to a maximum and then gradually decreases with the increase in radial distance. Similar distribution at all elevations can be observed for the vertical

velocities as shown in Figure 4.21 (b) where both of the vortices shows very distinguishable peaks of high vertical velocity within the vortex wall region.

The vertical profiles of radial velocity components of the vortex with S =0.3 and 0.69 are illustrated in Figure 4.22 and Figure 4.23, where Figure 4.22 shows the profiles at the radial distance of z/r_c=0.5, 1, 1.5 and 2 and Figure 4.23 shows the profiles at the radial distance of z/r_c=2.5, 3, 4 and 6; the negative values of radial velocity denotes inwards flow, while positive value denotes outwards flow. Different outflow heights can be observed for the vortices as shown in Figure 4.22, where the vortex with S =0.3 has an outflow that spans up to the elevation of approximately z/r_c=1, while the height of the outflow for vortex with S =0.69 is closer to the ground spanning only up the elevation of approximately z/r_c=0.57, suggesting that the vortex core occurs closer to the ground. For vortex with S =0.3, low magnitude of radial outflow are found in the vortex core; the magnitude of outflow increases gradually with the increase in radial distance where the highest outflow can be found at the radial location of r/r_c=1.5 and 2, within the vortex wall region. For vortex with S =0.69, the magnitude of outflow is comparably lower, with the maximum outflow occurring at the radial location of r/r_c=1.5. The maximum radial velocity of U_{rmax} (U_r/U_T) = 0.34 and 0.74 occurs at the radial distance of r_{rmax} = 1.1 and 2 respectively, for the vortex with S =0.3 and 0.69 respectively.

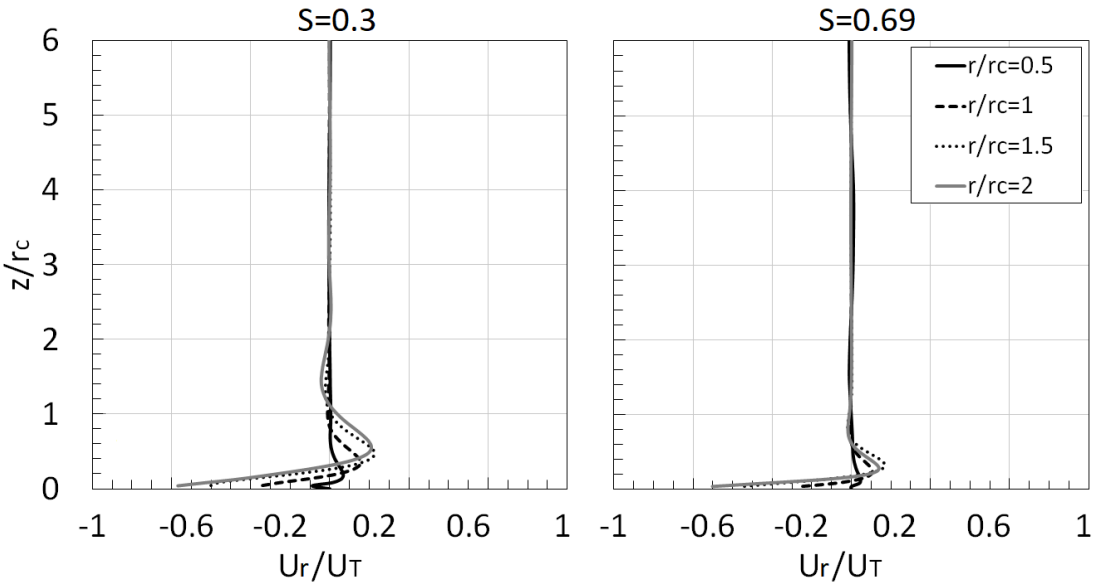

Figure 4.22: Vertical profiles of normalised radial velocity at the distance of r/r_c=0.5, 1, 1.5 and 2 for the vortex with S=0.3 and 0.69.

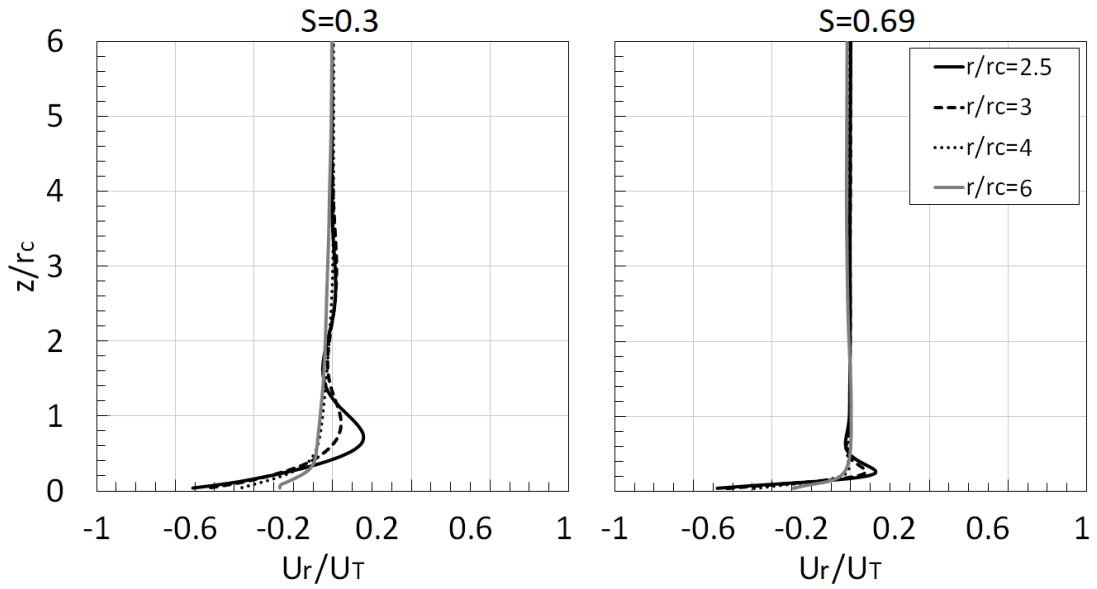

Figure 4.23: Vertical profiles of normalised radial velocity at the distance of r/r_c=2.5, 3, 4 and 6 for the vortex with S=0.3 and 0.69.

In Figure 4.23, low outflow magnitudes can be observed at the radial location of r/r_c=2.5 and 3, and inflow at regions further away at r/r_c=4 and 6 for the vortex with S =0.3. In

comparison, the height of the outflow is significantly lower for vortex with S =0.69 and inwards flows are observed at regions further away at r/r_c =4 and 6. Figure 4.24, illustrates the horizontal profiles of turbulent kinetic energy (TKE) of the vortex with S =0.3 and 0.69, where Figure 4.24 (a) shows the profiles at the elevation of z/r_c=0.15, 0.3, 0.45 and 0.75 and Figure 4.24 (b) shows the profiles at the elevation of z/r_c=1, 1.5, 2 and 3. For both of the vortices, regions of high TKE generally occurs around the edge of the vortex core in the vicinity of the vortex walls, where the vortex with S =0.3 has comparably higher magnitudes of TKE than the vortex with S =0.69. The high magnitude of TKE are attributed to the tangential velocity components and the updraft flows at that region, where the highest TKE is observed to occur at the elevation of z/r_c=0.15 and then decreases with the increase in height for both of the vortices. The turbulence kinetic energy measures of the energy content of eddies in turbulent flows, thus, the high regions of TKE at low elevation indicates a turbulence region near the ground surface. It is observed that the rate of decrease of TKE with height for the vortex with S =0.3 is lower compared to vortex with S =0.69, suggesting a greater region of turbulent flows near the ground surface; further, the magnitude of TKE at the centre of the core for both of the vortices are considerably lower in comparison with the near ground region and all other regions.

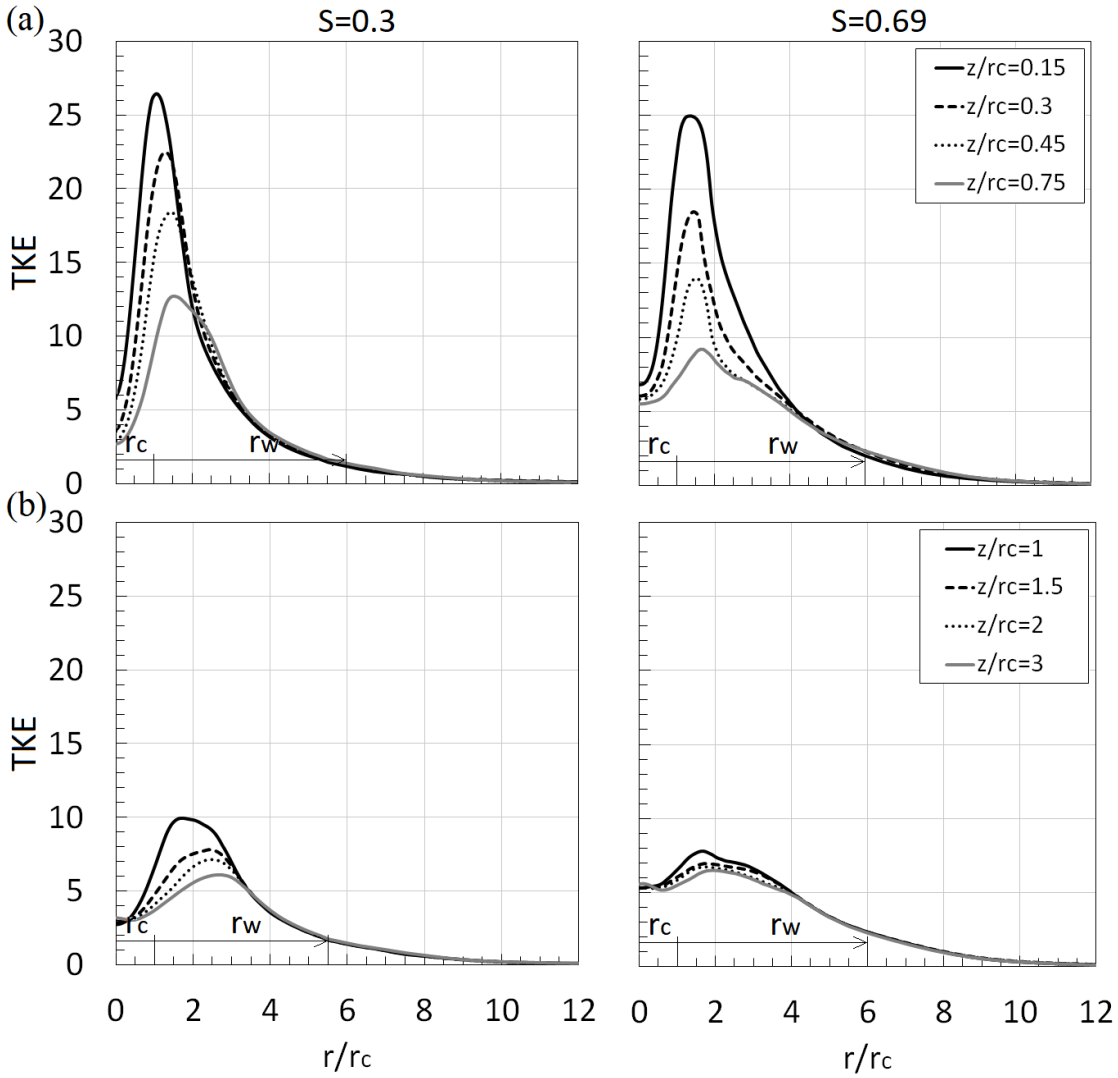

Figure 4.24: (a) Horizontal profiles of turbulent kinetic energy at elevations of z/r_c=0.15, 0.3, 0.45 and 0.75 for the vortex with S=0.3 and 0.69. (b) Horizontal profiles of turbulent kinetic energy at elevations of z/r_c=1, 1.5, 2 and 3 for the vortex with S=0.3 and 0.69. The length of the core radius and vortex walls are labelled as "r_c" and "r_w" respectively

4.4.3. Vortex Wandering

An analysis was conducted in order to examine for the wandering motion of the vortex with time, as the understanding of the transient behaviour of vortex may have potential effects on the debris initialisation process. Surface pressure were obtained for both the vortices with S =0.3 and S =0.69 in order to investigate the transient behaviour of vortices and to quantify the magnitude of spatial displacement of vortex wandering.

Figure 4.25 shows the temporal distribution of surface pressure at the centre of the numerical simulator in the form of a box and whisker plot. The instantaneous pressure are normalised with the corresponding time-averaged minimum pressure (P_{min}), which is -171 N/m^2 and -248 N/m^2 (C_P =-2.05 and -2.58) for the vortex with S =0.3 and S =0.69 respectively (as presented in section 4.1). The centre horizontal line of the box plot represents the median, the top and bottom of the box represents the first and third quartile, the mean value is represented by and "×"and the "whiskers" represents the remaining sample points of the corresponding surface pressure distribution. The numerical results (represented in grey) are compared with the experimental measurements (represented in white) by Gillmeier (2019).

The pressure fluctuation at the centre of the simulator for both of the vortices were observed to have low fluctuation with the standard deviation of approximately 0.2 and 0.17 for the vortex with S =0.3 and S =0.69 respectively. In comparison with the experimentally measured surface pressure, it can be observed that the fluctuations in pressure predicted by the numerical simulation are considerably lower. The mean surface pressure of the numerically simulated flow field are 1.06 and 1.21 for the vortex with S =0.3 and S =0.69 respectively, which is approximately 11% and 23% lower that the

experimentally obtained measurements. In general, the low surface pressure fluctuations for both the vortex with S =0.3 and S =0.69 suggest that the vortex structure have small instantaneous variability in time around the centre of the simulator. According to Gillmeier (2019), a similar behaviour was also observed for vortices with higher swirl ratio (S =0.3 and S =0.69), while high surface pressure fluctuation appears to only occur at low swirl ratio of S =0.14.

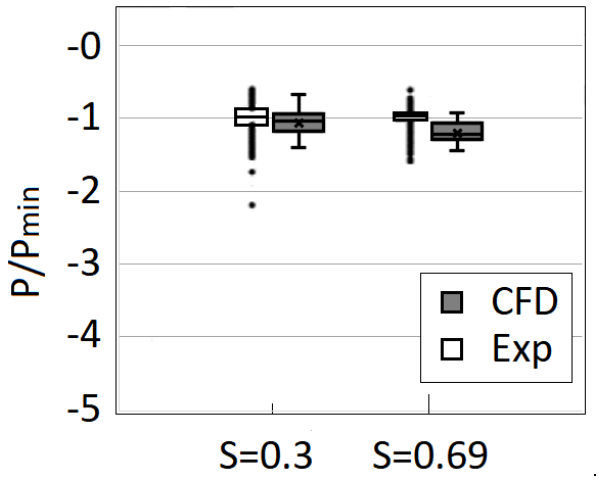

Figure 4.25: Temporal distribution of surface pressure obtained from the numerically simulated vortex with S =0.3 and 0.69 at the centre of the simulator in comparison with the experimental results obtained from Gillmeier (2019).

Additionally, the minimum surface pressure of the vortex at any time was identified in order to examine the non-stationary movement of the vortex centre and to quantify the magnitude of spatial displacement of vortex wandering. Figure 4.26 illustrates the distribution of spatial displacement of the vortex centre for the vortex with S =0.3 and S =0.69, expressed in terms of the percentage of occurrence against the radial distance where the minimum surface pressure occurs from the centre. The radial distance are normalised with the corresponding core radius for the vortex with S =0.3 and S =0.69

respectively (as listed in Table 4.1). Generally, the vortex centre of both of the vortices generally have majority of the duration at the centre of the simulator, with the average spatial displacement of only r/r_c =0.02 and 0.01 for the vortex with S =0.3 and S =0.69 respectively, and the low standard deviation of 0.085 and 0.068 for the vortex with S =0.3 and S =0.69 respectively. The vortex with S =0.3 shows a higher shift in vortex centre with the maximum displacement of r/r_c =0.19 in comparison with S =0.69 with the maximum displacement of r/r_c =0.15. Detailed information regarding the location of the corresponding vortex centre are listed in Table 4.2.

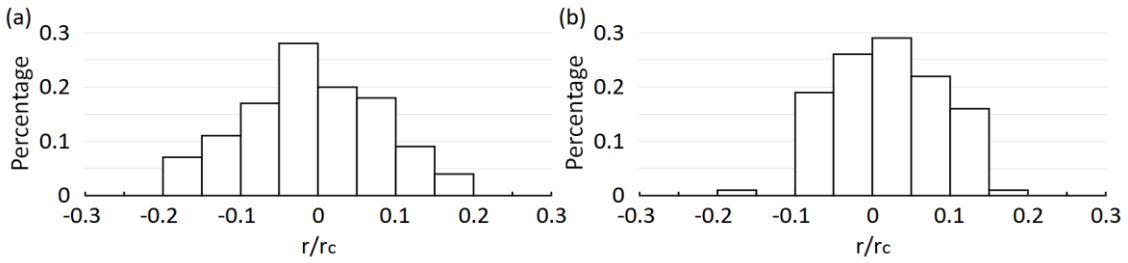

Figure 4.26: Distribution of spatial displacement of the vortex centre from the simulator centre for the (a) vortex with S =0.3 (b) vortex with S =0.69.

Table 4.2: Details of the location of the vortex centre relative to the simulator centre

Radial Distance	r/r_c	
Swirl ratio, S	0.3	0.69
Mean	0.02	0.01
Standard deviation	0.085	0.068
Max	0.19	0.15

Overall, while both the numerically and physically generated vortices shows similar magnitude of minimum pressure at the centre of the vortices, the numerically simulated vortices shows lower magnitude of pressure fluctuation in comparison with the experimentally measured surface pressure. The examination of the spatial displacement

of the vortex centre further showed that the wandering motion only has an average displacement of approximately r/r_c =0.02, with the maximum displacement less than r/r_c =0.2 for both of the vortices. The transient behaviour of vortex in time and space presented in this section is possibly be due to the transient vortex intensifying and weakening in time, resulting in the non-stationary movement and wandering of vortex centre. However, due to the low overall displacement in vortex centre, it is postulated that the wandering motion will not have significant effects on the debris initialisation process.

4.4.4. An Aside

In chapter 2, it was noted that the definition of the swirl ratio varies between physical simulators (section 2.2.2). Baker and Sterling's analytical model was also discussed (section 2.2.1) in which the swirl ratio is defined as ratio between the maximum value of tangential velocity to the maximum value of the radial velocity, as specified in equation 2.12. If equation 2.12 is applied to the current results as presented in section 4.4.2, the swirl ratio transforms from 0.3 and 0.69 to 1.29 and 1.35 respectively. In the following chapter, the $S_{Baker\ \&\ Sterling}$ will be employed in the Baker and Sterling's model when the results corresponding to the maximum flight altitude of the debris trajectories are examined.

4.5. Summary

In this chapter, the numerically simulated tornado-like vortices with the swirl ratio of 0.3 and 0.69 were discussed. Initially, a grid independence study was conducted to investigate the impact of grid resolution on the numerical results; then, the numerical results were compared with the analytical vortex models and experimental measurements. Finally, an

in-depth analysis of the flow fields of the vortices were conducted. The following summary can be made:

- The study on the impact of grid resolution demonstrated that the extra fine mesh was able to provide adequate and consistent results for the generation of tornado-like vortex with S =0.3 and S =0.69, as the refinement of grid resolution from coarse mesh to fine mesh shows the collapse of results, but only minor changes in the flow field from fine and extra fine mesh.
- The overall characteristics of the vortex with S =0.3 predicted by numerical simulation and experimental results are similar; both results correspond well and shows similar trend of velocity distribution at the near ground region and higher elevation while the highest discrepancies are observed around the vortex centre. Similarly, for the vortex with S =0.69, the flow field predicted from both the numerical simulation and experimental results shows similar flow patterns and characteristics with the highest differences around the vortex centre region.
- The comparison with analytical models showed that the Burger-Rott and Baker and Sterling vortex models, although simple, are able to represent some parts of the tornado-flow field such as the tangential velocity and pressure distribution relatively well.
- The analysis showed that the flow structure of both of the vortices consists of two main features; a core that consists of primarily downwards flow that are determined based on the radial distance that separates the updraft and downwards flow, and the vortex wall outlines the vortex core with high tangential velocity and updraft flows.

- The flow pattern for the vortex with S=0.3 is identified to resemble the vortex break down stage, where the vortex core is further away from the ground surface; in which a region of radial outflow and turbulence region between the vortex and the ground surface can be observed. Both the vortex core and vortex walls of the vortex with S=0.3 are smaller but the vertical velocity component is considerably greater in comparison with the vortex with S=0.69.
- The flow pattern for the vortex with S=0.69, on the contrary, is identified as the vortex touch down stage, where the vortex core is observed to occur very close to ground surface, thus resulting in a smaller turbulence region. The magnitude of tangential velocity is higher, and the vortex core and walls are larger; a recirculation ring can be observed in the streamlines (shown in Figure 4.18), however, the velocity at that region is low therefore have very minor effects to the overall vortex structure.
- The examination of the spatial displacement of the vortex centre further showed that the wandering motion only has an average displacement of approximately r/r_c =0.02, with the maximum displacement less than r/r_c =0.2 for both of the vortices. Due to the low overall displacement in vortex centre, it is concluded that this wandering motion will not have significant effects on the debris initialisation process.

5. Wind-borne Debris

"No amount of experimentation can ever prove me right; a single experiment can prove me wrong"

Albert Einstein (1926)

THIS CHAPTER PRESENTS the study on the flight characteristics and impact properties of various debris groups under different tornado-like flow fields; debris groups with varying sizes corresponding to the Tachikawa number which ranged between 0.6 and 2.5 are employed for the simulation of debris motion. Initially, an investigation on the accuracy of the numerically simulated debris motion is conducted in section 5.1, where the numerical results are then compared with the experimental results as described in chapter 3. Then, the study on the impact of Tachikawa number on debris flight is investigated in section 5.2. The analysis on the flight behaviour of debris in different tornado-like vortices are presented in section 5.3. Certain sections of this chapter borrow heavily from the following paper for which the author can claim a considerable intellectual input: Numerical Study of Debris Flight in a Tornado-like Vortex (Huo et al., 2020).

5.1. Validation of Debris Motion

In this section, a comparative study is carried out in order to investigate the accuracy of the numerical results. In section 5.1.1, the numerically simulated debris trajectories in a uniform flow field are compared with the analytical solutions obtained from flight equations introduced by Baker (2007) as presented in section 3.5.2. Then, a series of numerical simulations with debris group B1, B2 and B3 with identical Tachikawa number (K =1.2) were released in a tornado flow field for the comparison of aerodynamic similarity by verifying that debris motion are consistent under variations of diameter and density. In section 5.1.3, the results from the series of numerical simulations with debris group B1, B2 and B3 are compared and contrasted with the debris trajectories obtained from the physical simulations undertaken by Bourriez et al. (2017) as described in chapter 3.

5.1.1. Comparison with analytical flight equations

A series of simulations are conducted with Debris A, B1 and C, where the three-dimensional motion of debris are numerically simulated in a uniform flow field in a 50 m × 1 m × 50 m computational domain. The boundary conditions of the computational domain are set with uniform velocity inlet for the inlet surface, pressure outlet for the outlet, and symmetry for all other surfaces. The domain is initialised with the reference inlet velocity of U_∞ = 0.66 m/s and the free stream pressure P_∞ = 0. The reference velocity is calculated based on the Tachikawa numbers of 2.5, 1.2 and 0.6 for debris A, B1 and C respectively. The initial debris velocities were set to zero and are released at the top of the computational domain, at the location of 0.1 m × 0.5 m × 49.9 m; the simulation was

conducted with the constant time step Δt = 0.01 s and terminated once the debris left the computational domain.

For the analytical flight equations, the reference inlet velocity with the horizontal velocity of U_x= 0.66 m/s and vertical velocity of U_z= 0 m/s as used as input for the calculation for the trajectory and velocity of debris group A, B1 and C. The spherical drag coefficients (C_D) of the debris are 1.9, 1.34 and 0.96 for debris A, B1 and C respectively, calculated based on the debris Reynolds number as specified in equation 3.34 at the reference velocity of 0.66 m/s. The initial position of the debris are situated at the horizontal position of x = 0.1 m and vertical height of z = 49.5 m. The equations are numerically solved over the time of 10 s with the time step of 0.01 s for all three debris groups.

The debris motion obtained from both numerical simulation and analytical flight equations are compared and discussed, where the horizontal and vertical velocities are shown in Figure 5.1 (a) and (b) respectively, and the trajectories are shown in Figure 5.1 (c). The results are normalised using the non-dimensional parameters as shown in equations [3.22] to [2.28]. The comparison of horizontal velocity of debris groups A, B1 and C showed that the larger and heavier debris C shows higher acceleration and requires the least time to reach terminal velocity in comparison with debris A and B1. This is expected as Tachikawa number is a ratio of aerodynamic forces to gravitational force; therefore, gravitational force will have greater effects on heavy debris with high mass (low values of K).

Generally, the results obtained from both the numerical simulation and analytical flight equations corresponds very well, particularly the horizontal velocity, $\widetilde{U}_{dx}$ and the trajectories. Some very minor difference can be observed for the distribution of vertical

velocity, where the debris velocities predicted by numerical simulation shows lower rate of acceleration and lower terminal velocity: this can perhaps to attributed to the underlying assumptions of the numerical method; as buoyancy forces were included together with gravitational forces as a term, the buoyancy forces although small, may have some minor effects on the debris motion. Further, the debris motion were simulated in a three-dimensional flow field, while the analytical equations assumes a two-dimensional flow field. With that being said, the overall good agreement between the numerical results and analytical flight equations has proven that the current numerical method is effective and able to predict debris motion relatively well.

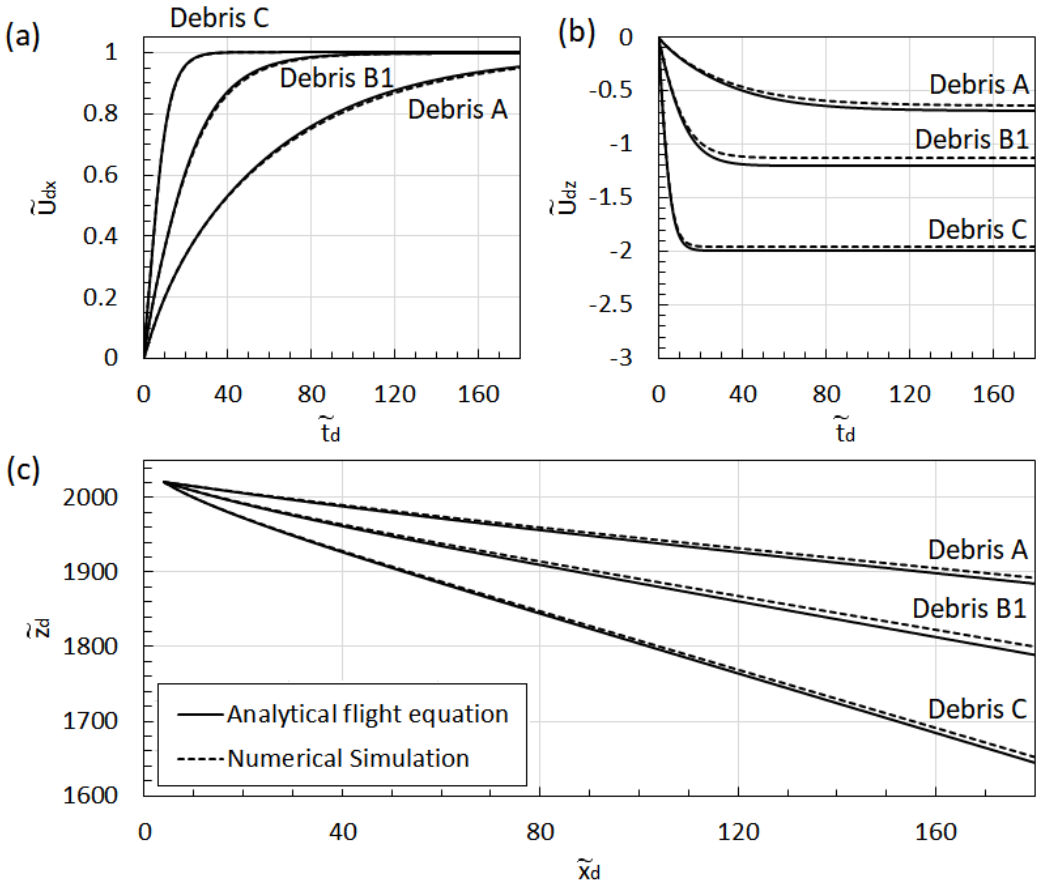

Figure 5.1: Comparison of results from numerical simulation and analytical flight equation. (a) Horizontal velocity (b) Vertical velocity (c) Dimensionless trajectories.

5.1.2. Comparison of aerodynamic similarity

A series of numerical simulations with debris group B1, B2 and B3 with identical Tachikawa number (K =1.2) were simulated in the tornado flow field as outlined in section 4.4 (S = 0.69) and 450 individual debris of each debris group were released at 50 time selected instances of the vortex flow at every quarter revolution of the vortex from the time t = 65 s; the debris were released near the ground surface (z/r_c =0.05) at nine different radial positions (r/r_c =0, 0.25, 0.5, 0.75, 1, 1.5, 2, 2.5 and 3). The results are normalised using characteristic parameters of the vortex with S=0.69; the radius of the vortex core (r_c), the maximum tangential velocity (U_T) and the time per revolution of the vortex (t_r).

The flight duration of each individual debris, t_d, is calculated based on the total airtime of the debris from initialisation to the impact on the ground surface; a debris is considered to be initialised, (hereby referred to as wind-borne) if the spatial distance (s_d). of the debris from the original release position is greater than zero (s_d>0). Debris that are not initialised or have flight duration of less than one single revolution of the vortex (i.e., t_d/t_r<1) are not considered as wind-borne in the current analysis since the velocity of the debris examined (and therefore the corresponding momentum) are too low to be considered as potentially damaging. However, it should be noted that the actual impact force and velocity of debris is dependent of the size of the debris, in which is correlated in the scale of the tornado-like vortex. As the scales of the vortices are not discussed in this study, it is reasonable to assume that the corresponding momentum of debris with short flight duration results in lower damage potential.

The distribution of normalised flight duration of wind-borne debris from all three debris groups, B1, B2 and B3 are shown in Figure 5.2. The mean flight duration is denoted by a "×" while the maximum and minimum flight durations are represented by the whiskers on the box plots. The mean flight duration of debris groups B1, B2 and B3 are 3.51, 3.61 and 3.48 respectively, where all three debris groups shows similar interquartile range with positive skew. The total number of wind-borne debris are 90, 82 and 86 for debris group B1, B2 and B3 respectively, yielding in the percentage of debris becoming wind-borne of 20%, 18% and 19% for debris groups B1, B2 and B3 respectively. It is worth pointing out that this low percentage is not too surprising as this study only considers the flow field of stationary tornadoes where the translation effects of the tornadoes are ignored; research has shown tornado translation speeds can range from 0.05 U_T to 0.7 U_T (Kosiba et al., 2014; Matsui et al., 2008; Phuc et al., 2012). Understandably, the translating movement of a naturally occurring tornado may potentially result in a higher percentage of debris becoming wind-borne.

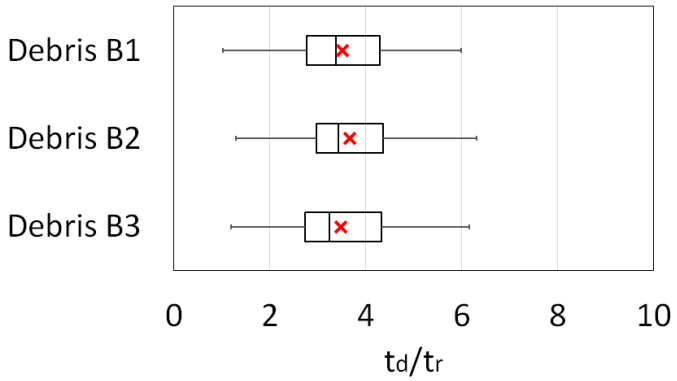

Figure 5.2: The distribution of fight duration of debris group B1, B2 and B3.

Figure 5.3 illustrates the plan view of wind-borne debris trajectories for debris group B1, B2 and B3 from the positions of r/r_c =0.5, 0.75, 1, 1.5 and 2 the debris trajectories are represented with a grey arrow as all debris travel in clockwise direction. Data pertaining

to the positions of r/r_c =0, 0.25, 2.5 and 3 are excluded from Figure 5.3 and shown in Figure A.1 separately since debris initialised from these positions was found to be infrequent. This is primarily due to the downwards flow around the regions of r/r_c =0 and 0.25 at the centre of the vortex region as well as the absence of updraft flow at regions further from the core around r/r_c =2.5 and 3, resulting in the low number of debris initialised. Generally, it can be observed that the position of r/r_c =0.75 and 1, all three debris groups shows the highest number of debris becoming wind-borne, while the position of r/r_c =0.5 shows the least. All debris initialised from the position of r/r_c =1 tends to show a greater of variation in trajectory path. Overall, the trajectories of the debris group B1, B2 and B3 show a very similar distribution at all positions.

The distribution of impact radius of all wind-borne debris from group B1, B2 and B3 are shown in Figure 5.4, where the normal distribution is represented with the curve (red line), expressed in terms of the percentage of impact occurrence against the impact radius. The percentage of impact occurrence is calculated based on the number of occurrence of debris that impacts at that respective radial distance, while the impact radius is the distance between the impact locations and the vortex centre, as this provides a measurement of damage range of the tornado-like vortex. In general, all three debris groups show a similar distribution of impact range and similar standard deviation, where the mean impact radius for debris group B1, B2, and B3 are 7.5, 7.47 and 7.12 respectively. The series of numerical simulations with debris group B1, B2 and B3 in a tornado- like flow field showed that the numerically modelled debris motion are consistent under the variations of diameter and density, where all three debris groups exhibits the propensity to travel with very similar flight duration and trajectories due to the identical Tachikawa number of K =1.2.

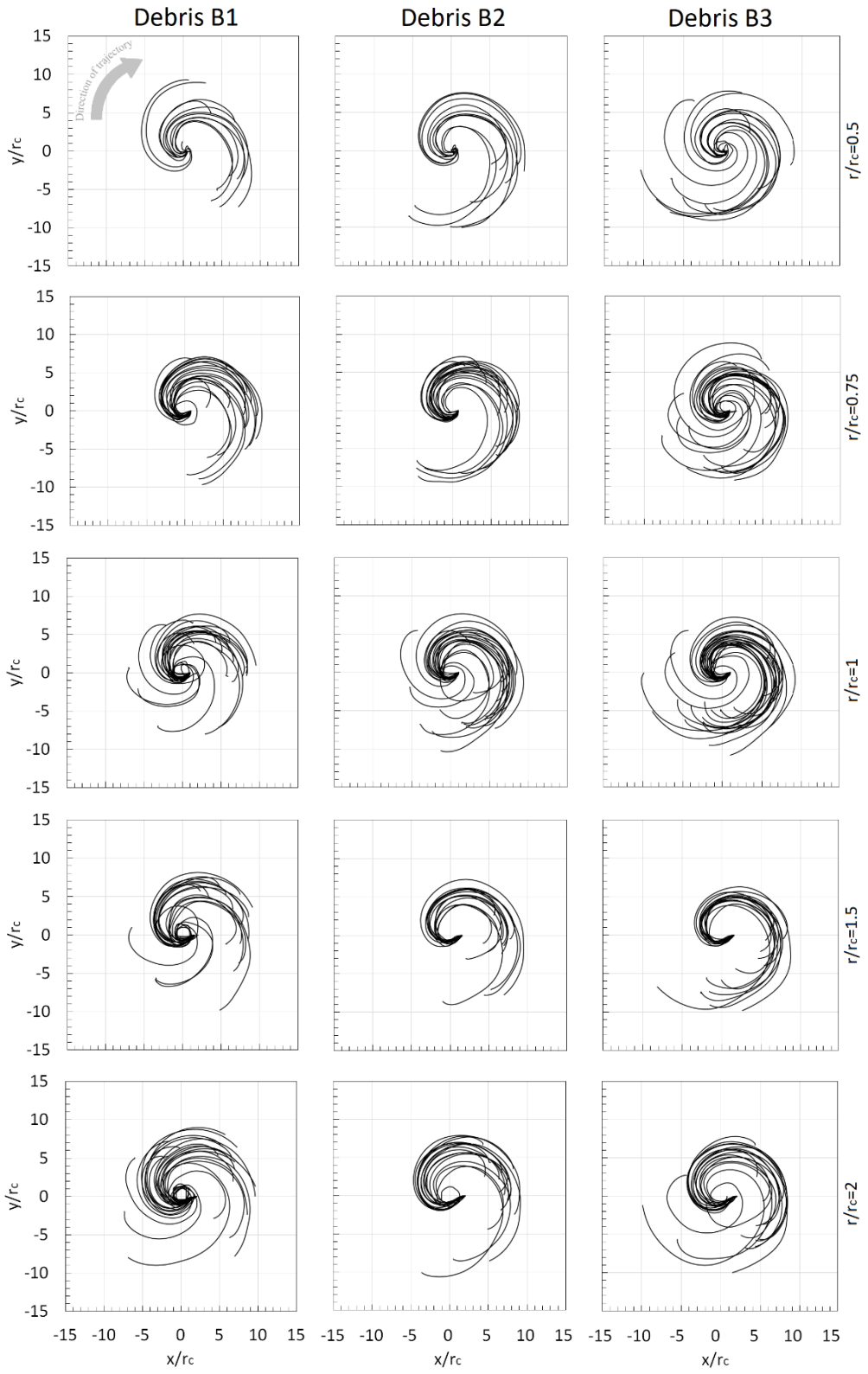

Figure 5.3: Plan view of trajectories at different positions for debris group B1, B2 and B3. The grey arrow denotes the direction of debris trajectory for all debris groups.

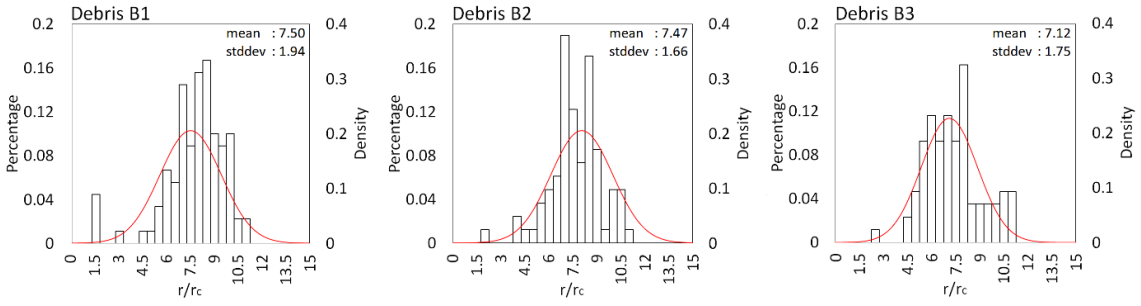

Figure 5.4: The distribution of impact radius of all wind-borne debris from debris group B1, B2 and B3.

5.1.3. Comparison with experimental study

In this section, the results from the series of numerical simulations with debris group B1, B2 and B3 are compared and contrasted with the debris trajectories obtained from the physical simulations undertaken by Bourriez et al. (2017). The diameter of the spherical polystyrene beads employed in the experiments varies between 1.5 to 1.7 mm which corresponds to the Tachikawa number of approximately 1.1 to 1.2. The comparison of debris trajectories from numerical simulation and experimental results are shown in Figure 5.5, where the positions of r/r_c =1 and 2 corresponds to the closest release positions from the experiments of r/r_c≈0.9 (100 mm) and r/r_c≈1.8 (200 mm). The results from the numerical simulations are represented in black solid lines and the experiments are represented in grey lines; the red solid lines represent the mean trajectory of the numerical simulation while the red dashed lines represent the mean trajectory of the experimental results. The debris trajectories from the experimental results shows shorter trajectories in comparison with the numerical simulation, where all three debris groups show similar distribution; this is due to the debris leaving the tracking window in the experimental setup where the entire trajectories were not captured.

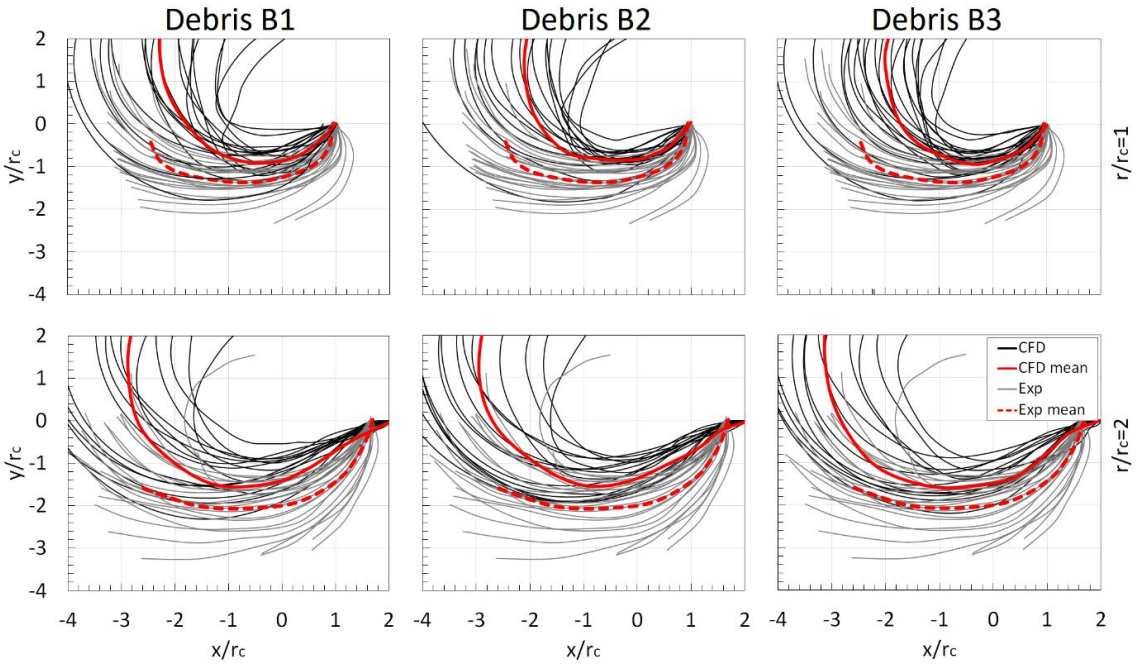

Figure 5.5: Plan view of trajectories at release positions of r/rc =1 and 2 for group B1, B2 and B3 in comparison with the experimental results from Bourriez et. al (2017).

Generally, both the numerical and experimental results shows similar behaviour of debris trajectories; the region of overlap for both results at the position r/r_c =1 is approximately 78%, whereas at the location of r/r_c =2, the overlapping trajectory path is lower at approximately 61%; the larger and wider variation of trajectory paths shown in the experiments is likely due to the variation of Tachikawa number of the debris employed, which resulted in the discrepancy of aerodynamic behaviour. While the mean trajectories of both the numerical simulation and experiments shows very similar curvature with the average distance of approximately r/r_c =0.3 apart, the experiment shows trajectories that are slightly further from the core in comparison to the numerical simulation that predicted trajectories that are closer to the vortex core.

Overall, the prediction of debris trajectories corresponds well for both the numerical simulation and experiments results with some differences observed. These differences

can perhaps be attributed to the different release position and inconsistent size of the debris employed in the experiments, as well as the considerable changes on the vortex flow field due to the turbulent fluctuations or wandering motions of the vortex. On the contrary, it should be noted that the numerically modelled debris motion is computed on top of the simulated flow field (at recorded time steps); while this method provides a good prediction of the statistical distribution of debris flight, the effects of continuous changing local flow field may be dismissed. It should also be noted that the lack of turbulence data associated with the physical measurements further results in the uncertainty of the flow simulation in this region and is probably the main cause of the small differences observed. Notwithstanding this, the numerically simulated debris motions are consistent with experimental results and are able to predict the entire trajectory of debris flight, consequently, provide a better understanding of the impact distribution and extend the results of the physical simulation.

5.2. The Impact of Varying Tachikawa Number

A series of numerical simulations are carried out with debris group A, B1 and C corresponding to the Tachikawa number of K =2.5, 1.2 and 0.6 respectively, in order to investigate the behaviour of wind-borne debris in tornado like flow field with varying Tachikawa number. Results for debris flight in the tornado-like vortex with S =0.3 and S =0.69 are discussed in section 5.2.1 and 5.2.2 respectively. The process of debris initialisation are reported and the correlation of Tachikawa number and debris flight behaviour are investigated. All results presented in this section are normalised using characteristic parameters of the vortices as appropriate.

5.2.1. Debris flight in the vortex with S=0.3

Results for debris flight in the tornado-like vortex with S = 0.3 are presented in this section. Figure 5.6 shows the distribution of flight duration of all three debris groups A, B1 and C, expressed in terms of the flight duration of each individual debris, t_d, normalized by the revolution of the vortex, t_r of the vortex. Similar to previously defined, t_d, is calculated based on the total airtime of each individual debris from initialisation to the impact on the ground surface; debris that are not initialised or have flight duration of less than one single revolution of the vortex (i.e., t_d/t_r <1) are not considered as wind-borne in the current analysis for the reasons given above. The total number of wind-borne debris for debris group A, B1 and C are 118, 99 and 56 respectively; as a result, the percentage of debris becoming wind-borne are 26%, 22% and 12% for debris group A, B1 and C respectively. The mean flight duration (denoted by a red "×") of debris groups A, B1 and C are 9.07, 6.08 and 4.44 respectively. The distribution of flight duration for debris group A can be observed to show considerably higher dispersion in comparison with debris group B1 and C. The smaller and lighter debris group A has significantly longer flight duration than the heavier and larger debris group C; this is perhaps not too surprising as the debris Tachikawa number is the ratio of aerodynamic forces to the gravitational force, thus, low mass debris with high values of K will have the tendency to stay airborne for longer.

The percentage of wind-borne debris that are initialised by the vortex at the 9 release positions are shown in Figure 5.7 (a); the percentage is calculated based on the number of debris that are initialised by the vortex at that position with respect to the total number of wind-borne debris (118, 99 and 56 debris for debris group A, B1 and C respectively). Subsequently, at the position r/r_c =1, 41 individual debris from group A are initialised,

yielding 35%, while 41 individual debris from debris group B1 are initialised, yielding 41% and 24 individual debris from debris group C are initialised, yielding 43%. Figure 5.7 (b) shows the horizontal profiles of tangential, radial and vertical velocity components that corresponds to the debris release elevation. The scales of the normalized tangential and radial velocities are shown on the right vertical axis while the normalized vertical velocity is shown on the left vertical axis; the difference in scale has been used to highlight the trend in vertical velocity.

According to the figure, it can be observed that debris initialisation based on the release position closely resembles with the distribution of vertical velocity profile, and all three debris groups shows very similar trend of distribution. As previously reported, the centre of the vortex with S =0.3 primarily consists of downwards flow, while high magnitudes of updraft flows are observed surrounding the vortex core $r/r_c \leq 1$. As a result, debris are initialised in accordance to the presence of vertical velocity which provided upwards lift, where the highest percentage of debris initialised can be observed at the position of r/r_c =1 for all three debris groups, while no debris are initialised around the centre of the vortex at r/r_c =0 and 0.25 due to the downwards flows. At regions further away at r/r_c <2, debris are observed to have very low percentage of initiation by the flow despite the high magnitudes of tangential and radial velocities. The general shape of the curves in Figure 5.7 (a) illustrate that it is the flow pattern which dominates debris flight initiation whilst the Tachikawa number governs the extent of the flight path; although the latter does also play a role in initiation, in the current case it is of secondary importance to flow patterns (over the range of Tachikawa numbers investigated).

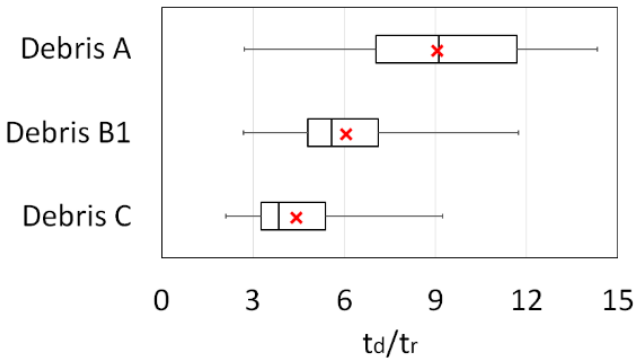

Figure 5.6: The distribution of fight duration of debris group A, B1 and C

In order to generate debris flight, the debris were place at a height (z/r_c =0.05) above the ground; this was a requirement of the simulation in order to generate debris flight - interestingly, the physical simulation conducted by Hann et al. (2017) adopted a similar approach. It is perhaps unrealistic that debris are placed at an elevation from the ground surface for the investigation of debris initialisation. However, as noted above, it is the flow field and in particular the presence of vertical velocity component which is of importance in terms of flight initiation and it is not unreasonable to assume that for lighter, smaller objectives they would become airborne if they were located on the ground. Finally, it is also worth pointing out that despite the different total number of debris considered as wind-borne, all three debris groups shows similar percentage at the position of vortex core radius r/r_c =1.

Figure 5.8 and Figure 5.9 illustrates the plan view and side views respectively, of the trajectories of all wind-borne debris for debris group A, B1 and C at the positions of r/r_c =0.5, 0.75, 1, 1.5 and 2; the debris trajectories are represented with a grey arrow as all debris travel in clockwise direction. Data pertaining to the positions of r/r_c =0, 0.25, 2.5 and 3 are excluded from Figure 5.8 and Figure 5.9 and are shown in Figure A.2 and Figure

A.3 respectively since debris initialised from these positions are infrequent. The height of the debris above the ground during flight is henceforth referred to as debris flight altitude.

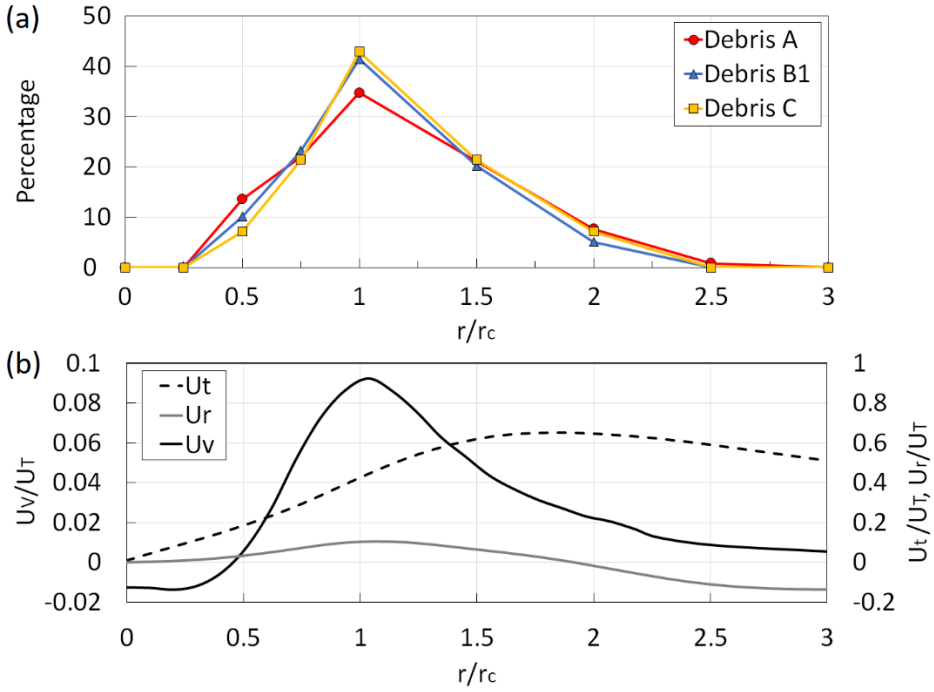

Figure 5.7: (a) The percentage distribution of all wind-borne debris at the positions of r/r_c =0, 0.25, 0.5, 0.75, 1, 1.5, 2, 2.5 and 3. (b) The horizontal profiles of tangential, radial and vertical velocities of the vortex at the elevation of z/r_c =0.09.

In Figure 5.8, debris group A with lower mass are observed to have significantly longer flight trajectories that circulates around the centre with the swirl of the vortex flow, while the trajectories of debris group B1 are shorter in comparison but resembles the trajectories of debris group A; debris group C, shows the overall shortest trajectories with the tendency to travel away from the vortex centre. All three debris groups show the highest number of wind-borne debris at the release position r/r_c =1. Debris group A and B1 shows similar distribution of trajectories at every positions, where the variation of trajectory path for debris B1 are low and consistent at every positions; for debris group C, higher variation of trajectory path can be observed at the position r/r_c =1.

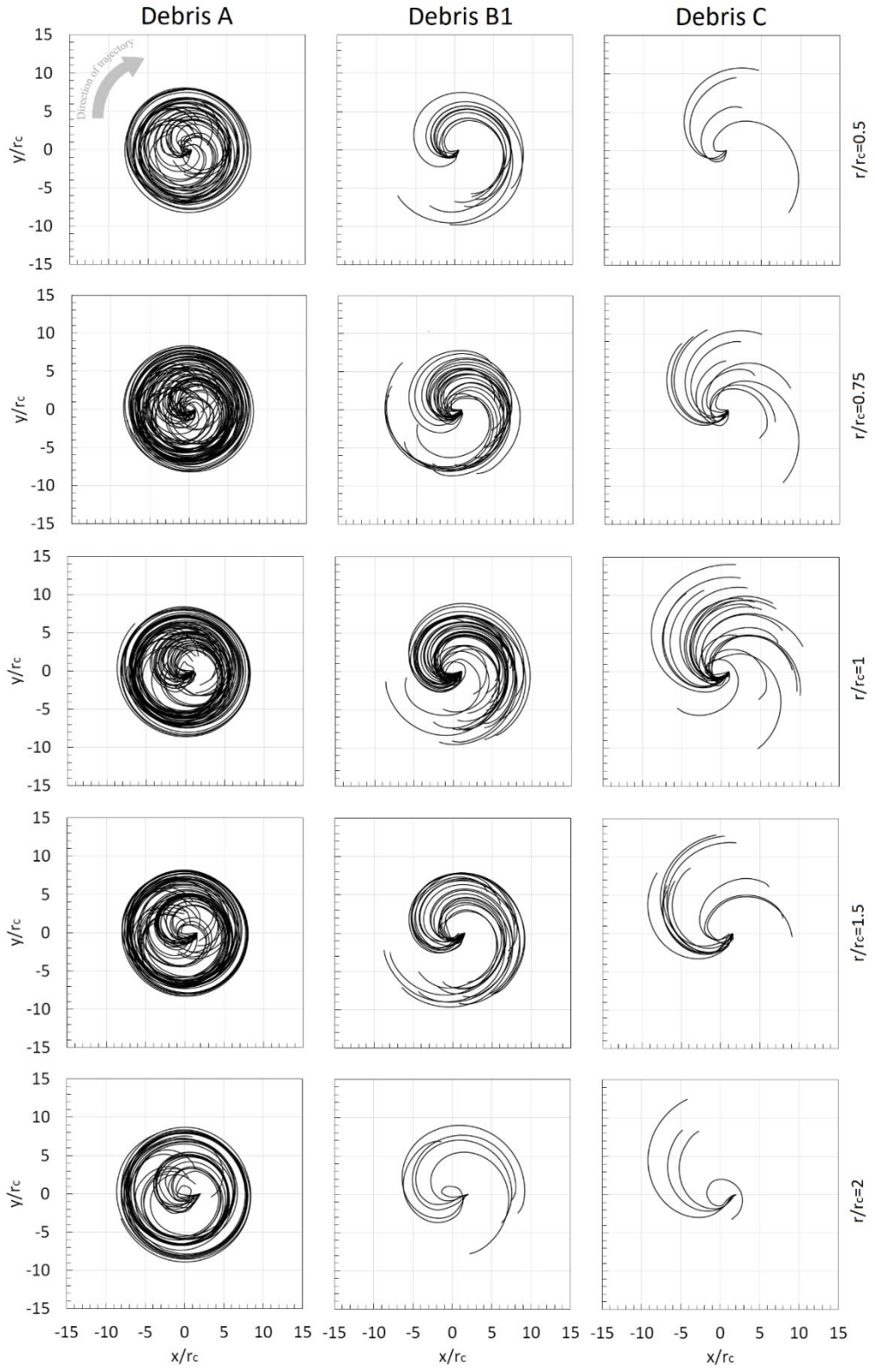

Figure 5.8: Plan view of trajectories at different positions for debris A, B1 and C. The grey arrow denotes the direction of debris trajectory for all debris groups.

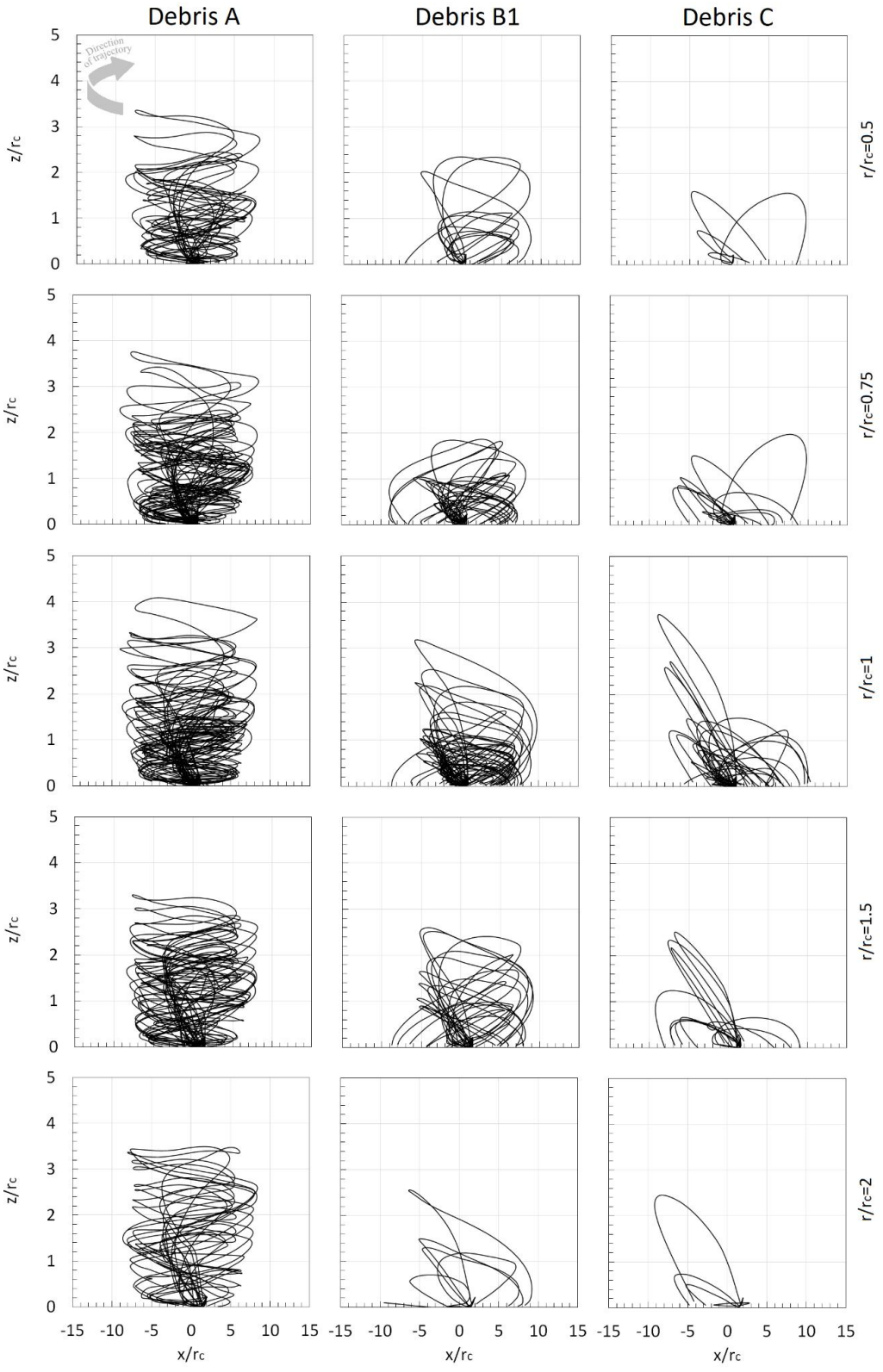

Figure 5.9: Side view of trajectories at different positions for debris A, B1 and C. The grey arrow denotes the direction of debris trajectory for all debris groups.

In Figure 5.9, all three debris groups are observed to gain altitude around the vortex core region (r/r_c >1). Debris group A with longer trajectories can be observed to reach significantly higher altitude and circulates around the vortex centre; the trajectories of debris group B1 are shorter and with lower height, while debris group C shows short parabolic trajectories and lower altitude with higher impact range in comparison. It is significant to point out that while debris group A shows similar distribution of trajectories at all positions, the maximum altitude of the trajectories for debris group B1 and C occurs at the position of r/r_c =1; this is due to the high magnitude of vertical velocity of the vortex flow field around that region, in which also resulted in the higher variation of trajectory path for debris group C position of r/r_c =1.

Figure 5.10 shows maximum flight altitude against the corresponding radial distance for debris group A, B1 and C. The vortex core of the vortex with S = 0.3 is outlined at the centre with the radius of r/r_c =1, while the grey shaded area (similarly in Figure 5.12, Figure 5.13, Figure 5.14, Figure 5.15 and Figure 5.16) highlights the vortex wall region from the radial distance of r/r_c =1 to 5.5. The vortex core is outlined at the centre with the radius of r/r_c=1, while the grey shaded area highlights the vortex wall region. It can be observed that debris group A with the lowest mass obtains the highest flight altitude, while debris group C with greater mass has the lowest altitude; the average maximum flight altitude for debris group A, B1 and C are 2.01, 1.19 and 1.03 respectively. For debris group A, the distribution of maximum flight altitude can be found to occur generally around the mean radial distance of r/r_c =5.88, while the distribution for debris group B1 occurs around the mean radial distance of r/r_c =5.54. The flight altitude for debris group C is observed to increase with the radial distance with the mean radial distance of r/r_c =6.12, showing that the debris trajectories are directed away from the

vortex centre. It is worth pointing out that debris in the same group has the tendency to fall on a specific region around the vortex (for example, debris group A are observed to cluster around the bottom side of the vortex as shown in Figure 5.10 (b)). This is because debris with identical mass has similar momentum and are likely to fall at a specific region under similar conditions.

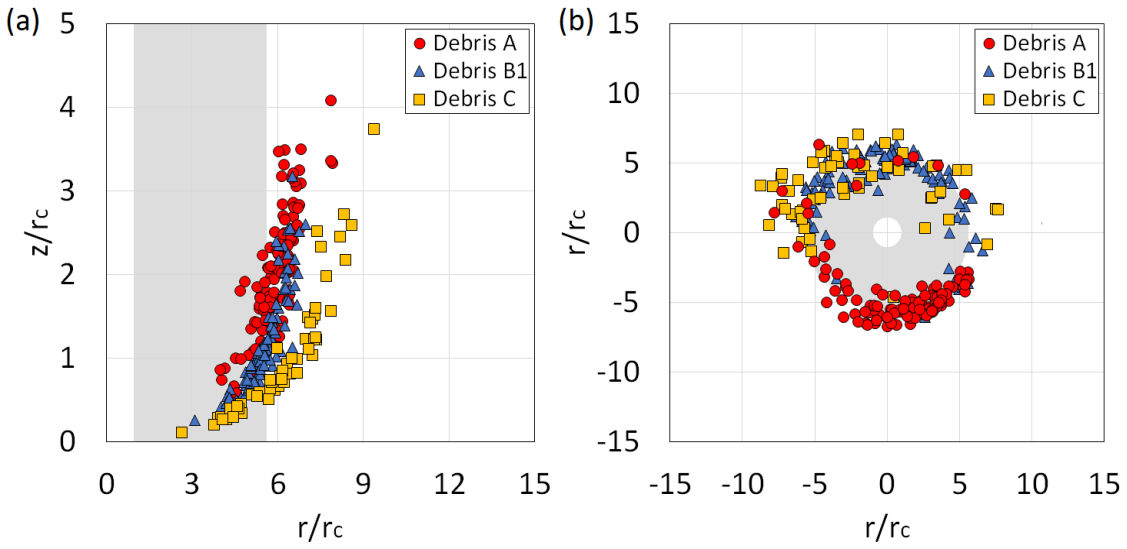

Figure 5.10: (a) The radial distance from the centre of the maximum debris flight altitude for debris group A, B1 and C (b) The radial position of the maximum debris flight altitude for debris group A, B1 and C.

The distribution of impact radius of all wind-borne debris from group A, B1 and C are illustrated in Figure 5.11; the normal distribution is represented with the curve (red line), expressed in terms of the percentage of impact occurrence against the impact radius. The percentage of impact occurrence is calculated based on the number of occurrence of debris that impacts at that respective radial distance, while the impact radius is the distance between the impact locations and the vortex centre. The mean impact radius for debris groups A, B1 and C are 3.17, 7.34 and 9.6 respectively, where debris group A shows the shortest mean impact radius while debris group C has the furthest impact radius.

Concurrently, debris groups C exhibits the highest impact potential with a maximum value of approximately r/r_c =14.6, whereas debris group A and B1 shows comparable maximum impact radii of r/r_c =6.1 and 10.3. The distribution of impact range suggests similar variation for debris group A and B1 with the standard deviation of 1.18 and 1.28 respectively, while debris group C shows a comparatively higher variation of impact distribution with the standard deviation of 2.2.

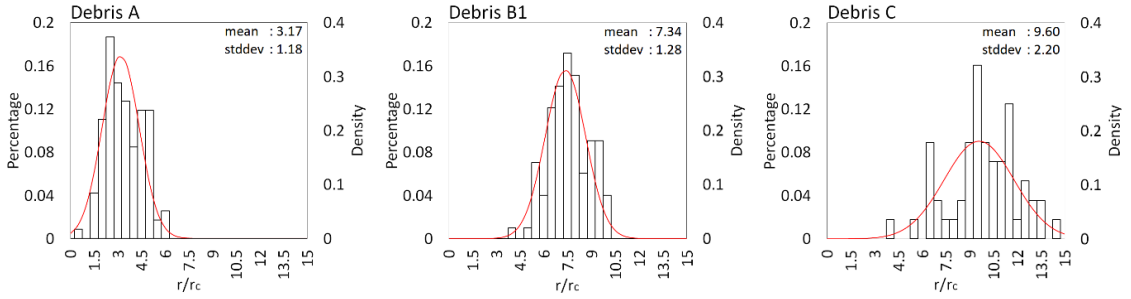

Figure 5.11: The distribution of impact radius of all released debris from debris group A, B1 and C.

Figure 5.12 shows the correlation between the flight duration and impact range of debris group A, B1 and C; the position in which debris are initialisation are represented by different markers in the figure legend, in general the regions within the core radius, r/r_c ≤1 are a darker shade while regions outside of the core radius r/r_c >1 are a lighter shade (of the relative colour representing the debris group). The mean flight duration (as presented in Figure 5.6) of debris groups A, B1 and C are 9.07, 6.08 and 4.44 respectively, while the mean impact radius (as presented in Figure 5.11) for debris groups A, B1 and C are 3.17, 7.34 and 9.6 respectively. An approximately linear relationship between flight duration and impact radius can be observed for both debris group B1 and C; in general, the longer the flight duration (within a particular group) the greater the impact range. The gradient of the two trends can be observed to differ between B1 and C. Interestingly,

although group A (the lower mass particles) have considerably longer flight duration, they do not impact at greater radial distance. The distribution of impact radius for debris group A are observed to cluster only within the vortex wall region between the radius of r/r_c =1 to 6 (this phenomenon will be further discussed and shown in Figure 5.14, but can be inferred from Figure 5.9). In general, the position of initialisation only effects the possibility of debris becoming wind-borne and appears to have no direct correlation with the flight duration or impact radius, thus again highlighting the important role that the vertical velocity component plays in debris flight initiation (Figure 5.7 (b)).

Figure 5.13 outlines the correlation between the maximum debris flight altitude and impact range of debris group A, B1 and C. The average maximum flight altitude (as presented in Figure 5.10) for debris group A, B1 and C are 2.01, 1.19 and 1.03 respectively, while the average impact radius for debris groups A, B1 and C are 3.17, 7.34 and 9.6 respectively. Debris group B1 are observed to somewhat resemble a linear relationship between maximum flight altitude and impact radius where the higher the flight altitude, the greater the impact range; debris group C appears to show a parabolic relationship that impacts at greater radial distance under the same flight altitude in comparison with debris group B1 but showing an asymptotic behaviour after the radius of approximately r/r_c <10. On the contrary, debris group A is observed to cluster around the radial distance of r/r_c =1 to 6 around the vortex wall region regardless of the flight altitude.

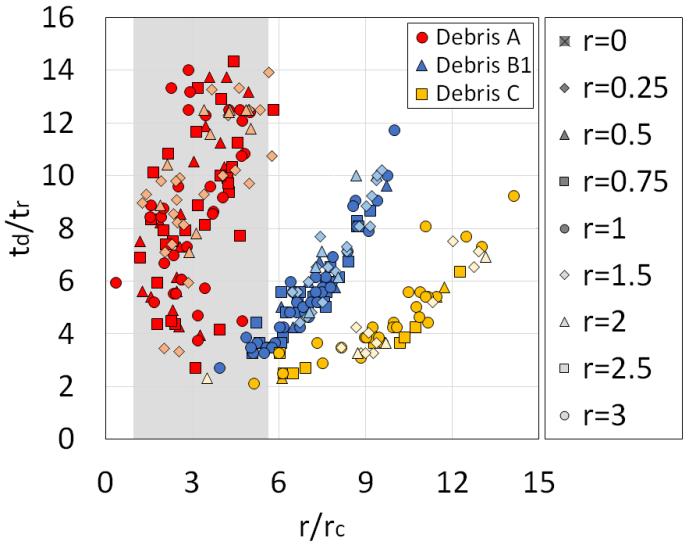

Figure 5.12: The distribution of flight duration against impact radius of debris group A, B1 and C based on the location of debris initialisation.

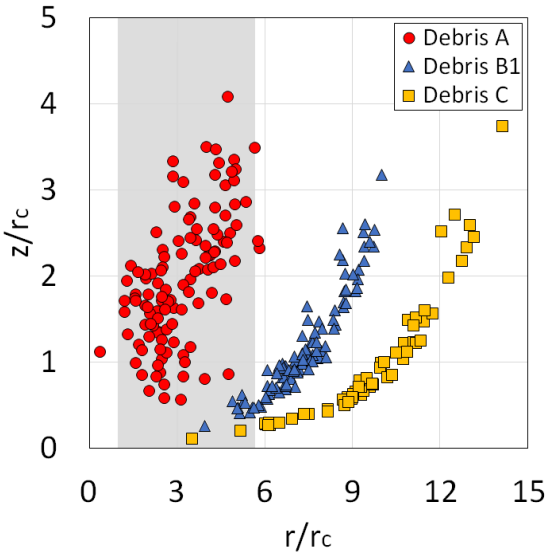

Figure 5.13: The distribution of maximum debris flight altitude against impact radius of debris group A, B1 and C.

Figure 5.14 shows the total flight duration of each individual wind-borne debris from initialisation to the impact on the ground at the positions of r/r_c =0.5, 0.75, 1, 1.5 and 2, expressed in terms of the radial distance from the centre of the vortex (positions of r/r_c

=0, 0.25, 2.5 and 3 are shown in Figure A.4); thereby providing an insight to the debris trajectories in relation to the regions of the vortex whilst characterising the wind-borne behaviour of different debris groups. All three debris groups have similar trend of distribution at every release position and show a reduction in radial distance once initialised, indicating the tendency to travel radially inwards before the flight duration of t_d/t_r <0.6; then, all debris are observed to travel away from the centre with the rapid increase of radial distance after the flight time of t_d/t_r >0.6. For debris group A, after the rapid increase of radial distance, majority of the debris are observed to maintain at a consistent radial distance (r/r_c =5~8) from the centre for a considerable duration of flight time, indicating the debris circulation around the vortex flow. Towards the end of the flight duration, a decrease in radial distance is observed as the debris are drawn towards the centre due to the radial inflow before impacting on the ground, resulting in the clustered impact locations within the vortex wall region (r/r_c =1~6). On the contrary, the radial distance of debris group C is observed to constantly increase throughout the flight duration travelling further away from the centre due to the inertia of the debris. The trajectories of debris group B resembles debris group C with shorter impact range; a small number of debris can also be seen travelling towards the centre before impacting on the ground surface.

Figure 5.15 shows the flight altitude against the radial distance from the centre of the vortex throughout the entire flight duration of each individual wind-borne debris at the positions of r/r_c =0.5, 0.75, 1, 1.5 and 2 (positions of r/r_c =0, 0.25, 2.5 and 3 are shown in Figure A.5). All three debris groups have similar trend of distribution and are observed to gain flight altitude within the vortex walls, where debris reaches a maximum flight altitude, then descends towards the ground surface. Generally, group A are observed to

reach a significantly greater flight altitude than group B1 and C, then maintains at a consistent radial distance of approximately r/r_c =5 to 8 while descending; around z/r_c =0.4, debris are drawn radially inwards due to the radial inflow close to the ground before impacting on the ground surface. In contrast, the trajectories of debris group C resemble a parabolic trajectory with the constant increase in radial distance, travelling further away from the vortex centre until the impact on the ground. While the trajectories of debris group B resemble the trajectories of group C, debris group B can be noticed travelling towards the centre at the elevation of z/r_c =0.2 before impacting on the ground surface.

The wind-borne velocity of each individual debris against the radial distance from the centre of the vortex throughout the debris flight at the positions of r/r_c =0.5, 0.75, 1, 1.5 and 2 are shown in Figure 5.16 (positions of r/r_c =0, 0.25, 2.5 and 3 are shown in Figure A.6). All three debris groups show similar behaviour, where debris show a reduction in radial distance once wind-borne while rapidly gaining flight velocity. All debris are observed to obtain their maximum velocity magnitude within the vortex wall region, then gradually decreases while travelling further away from the vortex centre; an immediate decrease in velocity magnitude are noticed for all debris before the impact on the ground surface. The average maximum velocity for debris group A, B1 and C are U_d/U_T =0.93, 0.85 and 0.72 respectively, occurring around the average radial distance of r/r_c =2.06, 2.34 and 2.62 for debris group A, B1 and C respectively; debris group A has the highest overall maximum velocity that occurs closer to the vortex, while debris group C has comparably lower maximum velocity that occurs further away from the vortex. As a result, it is significant to note that despite the differences in Tachikawa number, all wind-borne debris generally have the greatest damage potential around the vortex wall region between the radial distance of r/r_c =2 to 3 as debris are at the highest velocity magnitude.

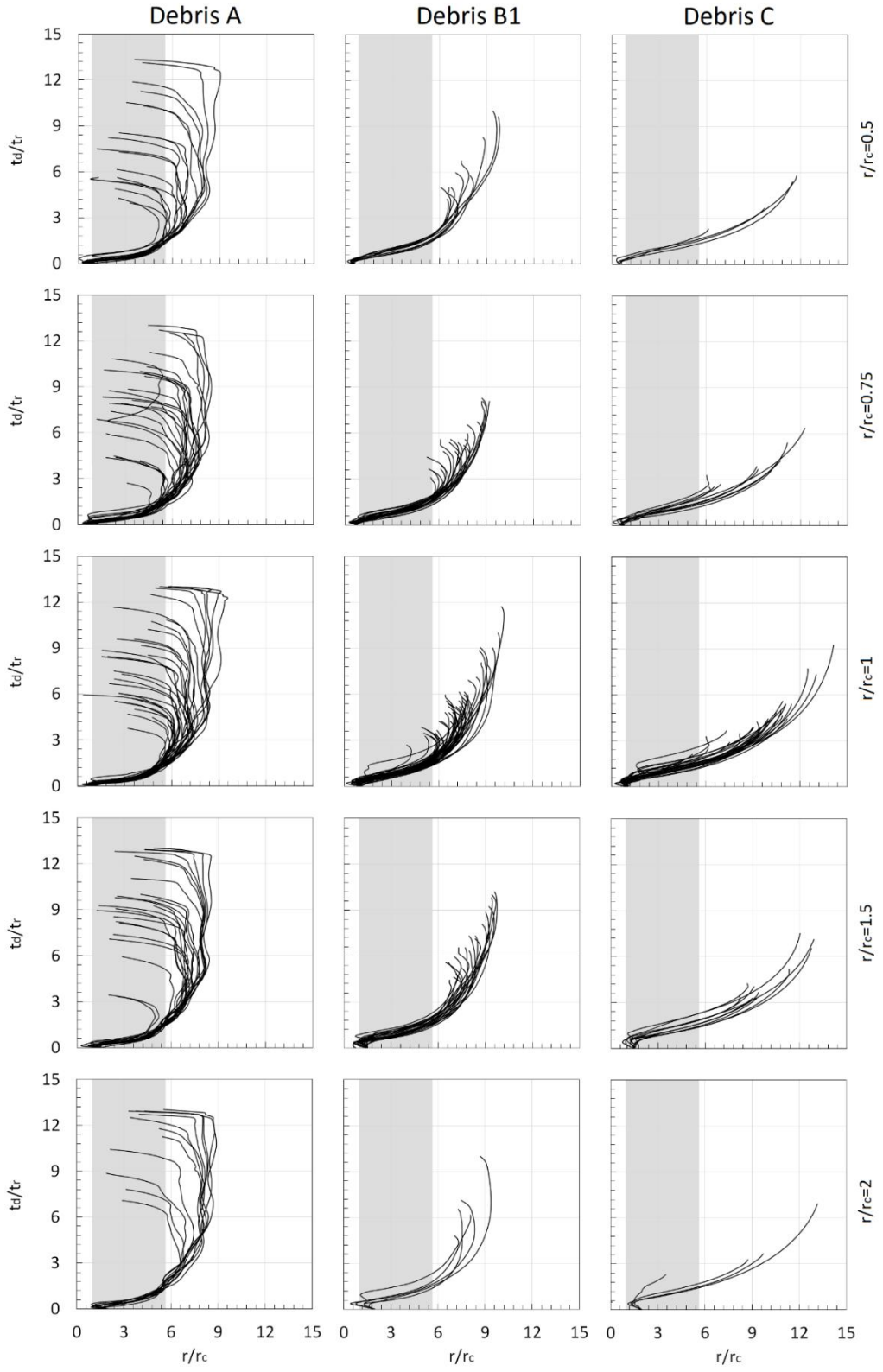

Figure 5.14: Debris flight duration against radial distance for debris group A, B1 and C.

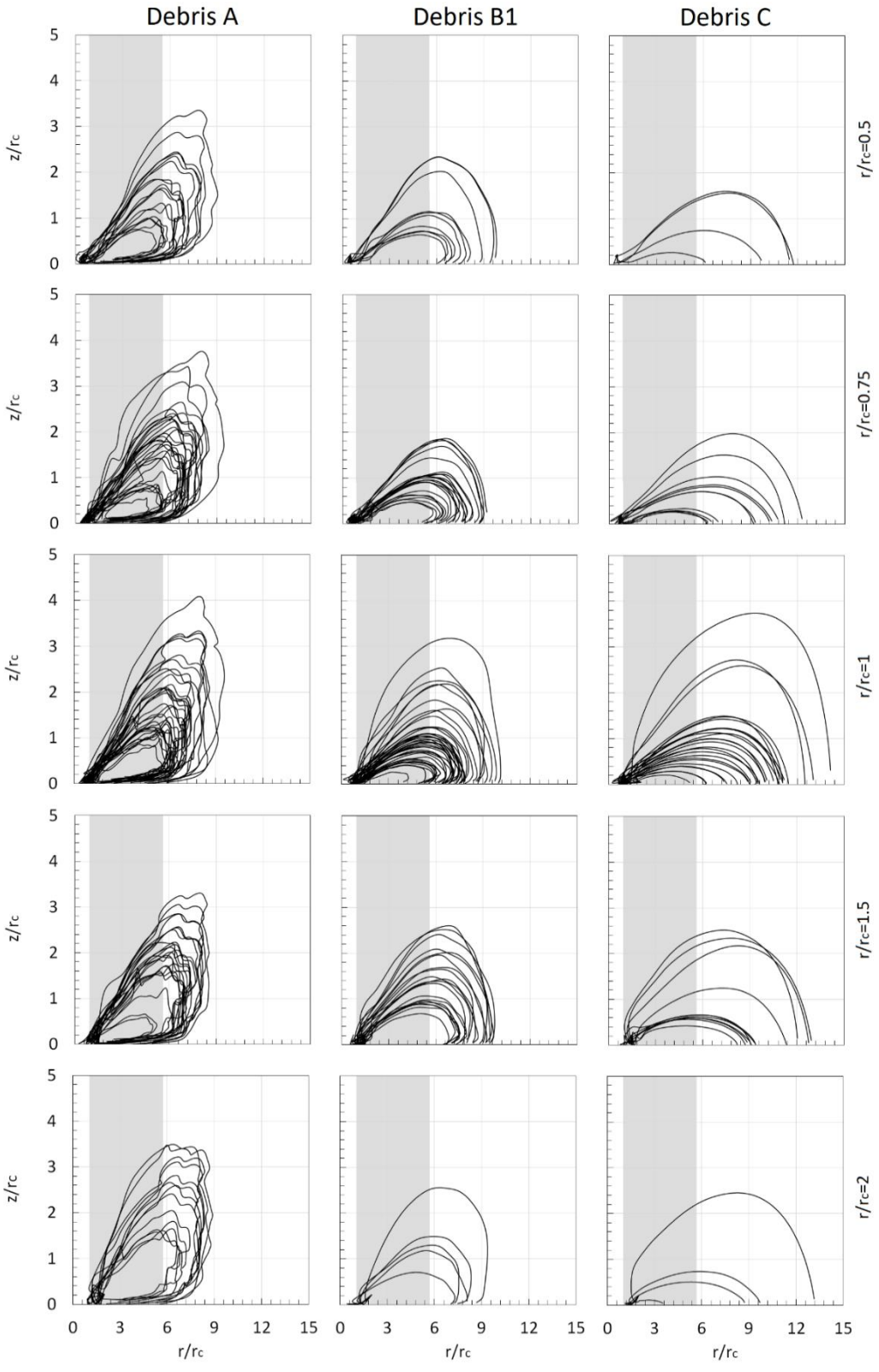

Figure 5.15: Debris flight altitude against radial distance for debris group A, B1 and C.

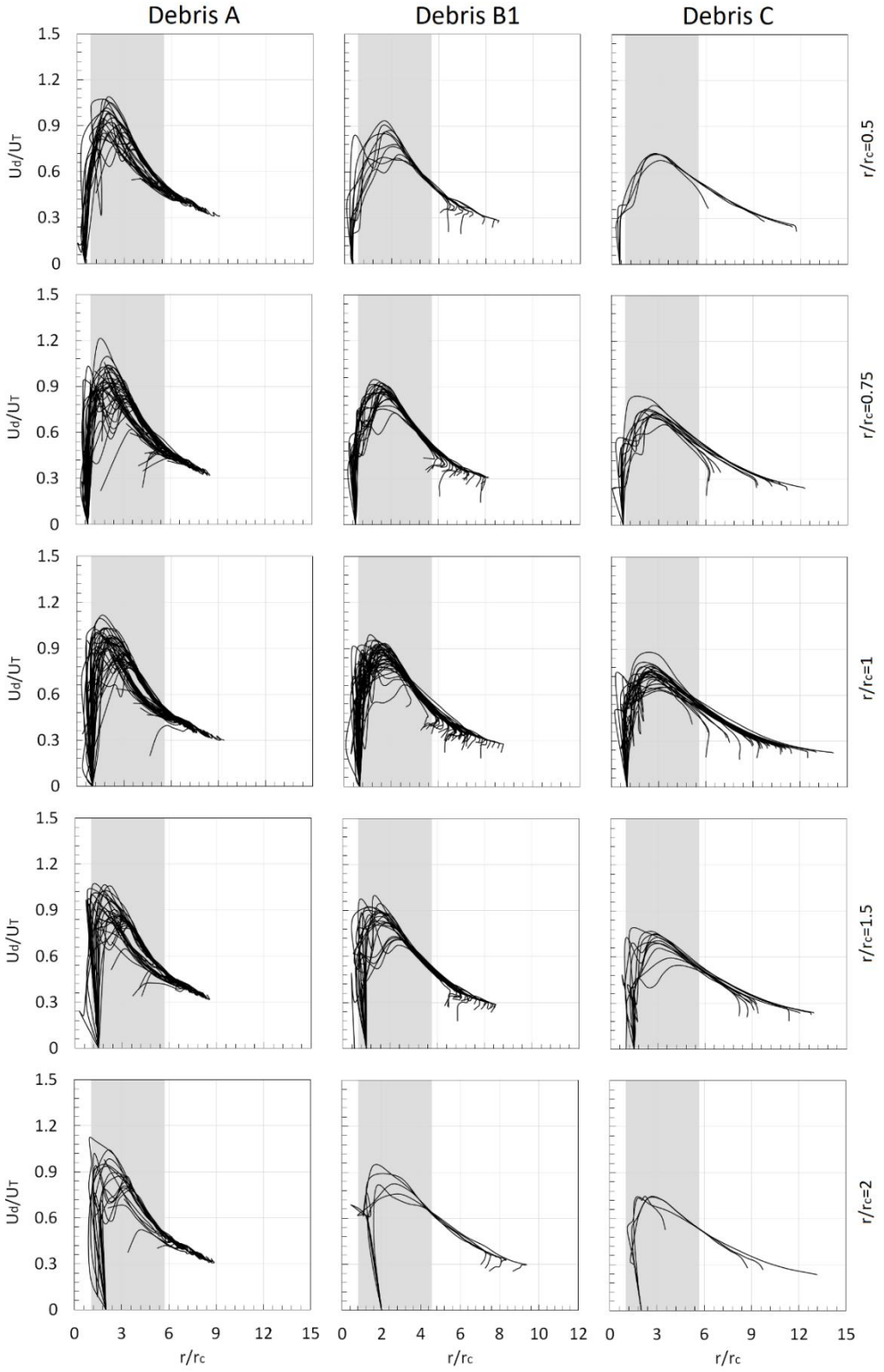

Figure 5.16: Debris velocity against radial distance for debris group A, B1 and C.

5.2.2. Debris flight in the vortex with S=0.69

Results for debris flight in the tornado-like vortex with S =0.69 are presented in this section. The distribution of flight duration for all three debris groups A, B1 and C are shown in Figure 5.17. The normalisation process outlined in the previous section has been adopted and in keeping with the above, only debris that have flight durations greater than one revolution of the vortex are considered. The total number of wind-borne debris are 104, 101 and 52 for debris group A, B1 and C respectively, yielding the percentage of debris becoming wind-borne of 23%, 22% and 12% for debris group A, B1 and C respectively. The mean flight duration (denoted by "×") of debris groups A, B1 and C are 5.46, 3.51 and 2.79 respectively. Debris group A is observed to have significantly longer flight duration and negative skew in the distribution of flight duration, while debris group B1 and C have comparably lower flight duration and shows positive skew. Debris groups B1 and C shows similar minimum and maximum range of flight duration, of approximately t_d/t_r =1 and 6.5, while debris group A has a moderately greater range of approximately t_d/t_r =1.5 and 7. Since Tachikawa number is the ratio of aerodynamic forces to the gravitational force, low mass debris with high values of K shows the tendency to stay airborne for longer, while debris with low values of K and greater mass have shorter flight duration.

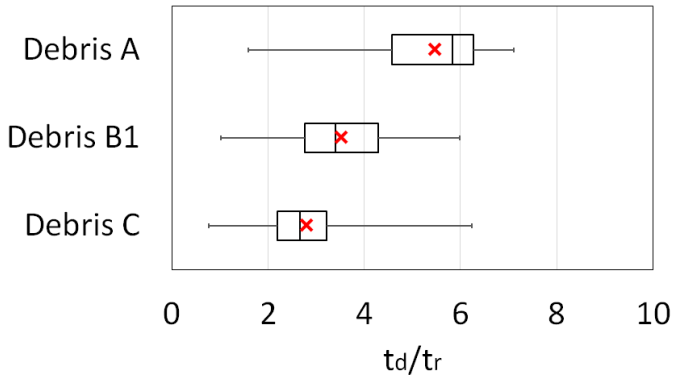

Figure 5.17: The distribution of fight duration of debris group A, B1 and C.

Figure 5.18 (a) shows the distribution of percentage of wind-borne debris that are initialised by the vortex at the 9 release positions; the percentage is calculated based on the number of debris that are initialised by the vortex at that position with respect to the total number of wind-borne debris (104, 101 and 52 debris for debris group A, B1 and C respectively). Consequently, at the position r/r_c =1, 27, 24 and 20 individual debris are initialised for groups A, B1 and C respectively. These figures correspond to 26%, 24% and 25% of the overall particles for groups A, B1 and C respectively. Figure 5.18 (b) shows the horizontal profiles of tangential, radial and vertical velocity components that corresponds to the debris release elevation (in keeping with the approach used for Figure 5.7, the velocities are normalised and different axis and scales are used to enable the key flow features to be understood).

Based on the figure, it can be observed that debris initialisation at different release positions shows a good correlation with the vertical velocity profile; debris group A and B1 shows very similar trend of distribution, while some minor differences in the percentage can be observed at the location of r/r_c=0.75 and 1.5 for debris group C. However, in general the overall trends are similar which again suggests that the flight

initiation is governed more by the flow than the weight of the particles (over the range examined).

As noted in chapter 4, the centre of the vortex with S =0.69 was found to primarily consists of downwards flow and occurs very close to ground surface, while updraft flows are observed surrounding the vortex core. The largely positive vertical velocity for r/r_c=0.5 to 2 ensures that this region is responsible for the majority of the particles which become airborne; as a consequence, debris positioned around these regions are approximately 10% more likely to be initialised, with the highest percentage of debris initialised at the position of r/r_c =1 for all three debris groups. Understandably, the upwards lift provided by the vertical velocity provides (in conjunction with the pressure distribution in this region) the input required for debris to become wind-borne. For r/r_c > 2.5, it can be observed that there is very little debris flight initiated despite the relatively large magnitudes of the tangential and radial velocities. Similarly, for r/r_c < 0.25 relatively few particles become airborne due not only to the flow patterns in this location and the impact that vortex wandering of the tornado is likely to have, i.e., the small magnitudes of the vertical velocity component are likely to extend over a relatively larger region than that shown in Figure 5.18 due to the motion of the parent vortex (even though the actual magnitude of the wandering is small, its relative impact on the velocities in this location is higher in this location than say other locations). Overall, debris initialisation are found to be correlated to the presence of vertical velocity. All three debris groups show a similar trend in distribution (and percentage initiated) at the position of vortex core radius r/r_c =1, despite the different total number of debris considered as wind-borne.

Figure 5.19 and Figure 5.20 illustrates the plan view and side views respectively, of the trajectories of all wind-borne debris for the debris group A, B1 and C at the positions of

r/r_c =0.5, 0.75, 1, 1.5 and 2; the debris trajectories are represented with a grey arrow as all debris travel in clockwise direction. Data pertaining to the positions of r/r_c =0, 0.25, 2.5 and 3 are excluded from Figure 5.19 and Figure 5.20 and are shown in Figure A.7 and Figure A.8 respectively since debris initialised from these positions are infrequent.

The findings of Figure 5.19 are similar to the findings outlined in Figure 5.8 corresponding to S = 0.3: debris group A particles are observed to have long scattered trajectory paths that circulates around the centre the vortex whilst the trajectories for the larger debris group C have low curvature and the tendency to travel away from the vortex centre; while the trajectories of debris group B1 the trajectories of debris group C with slightly longer trajectories. In general, the distribution of trajectories for all three debris groups shows similar variation at every position.

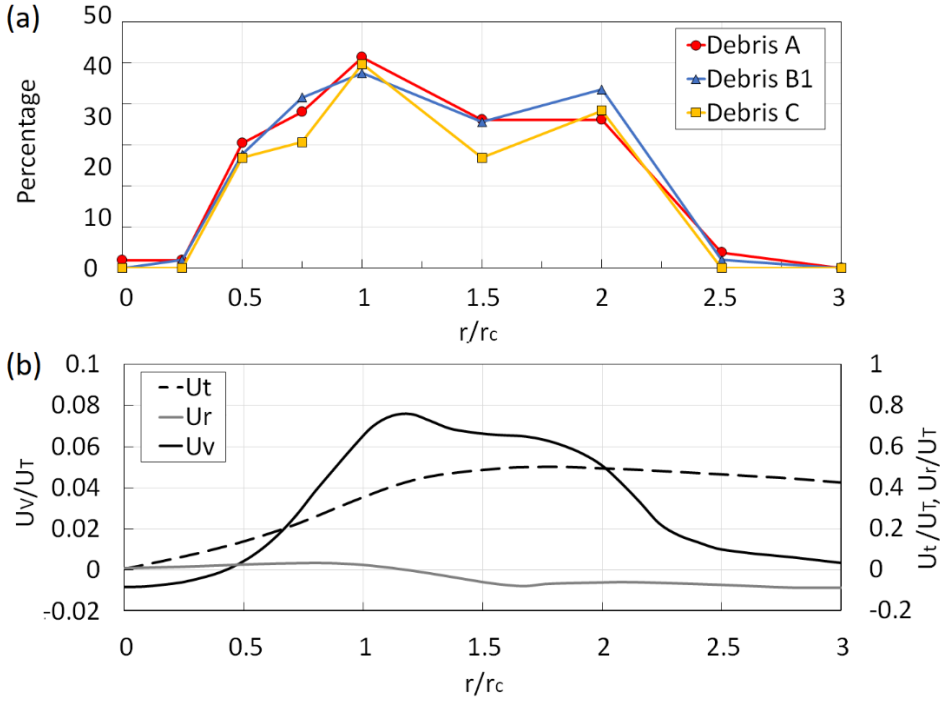

Figure 5.18: (a) The percentage distribution of all wind-borne debris at the positions of r/r_c =0, 0.25, 0.5, 0.75, 1, 1.5, 2, 2.5 and 3. (b) The horizontal profiles of tangential, radial and vertical velocities of the vortex at the elevation of z/r_c =0.05.

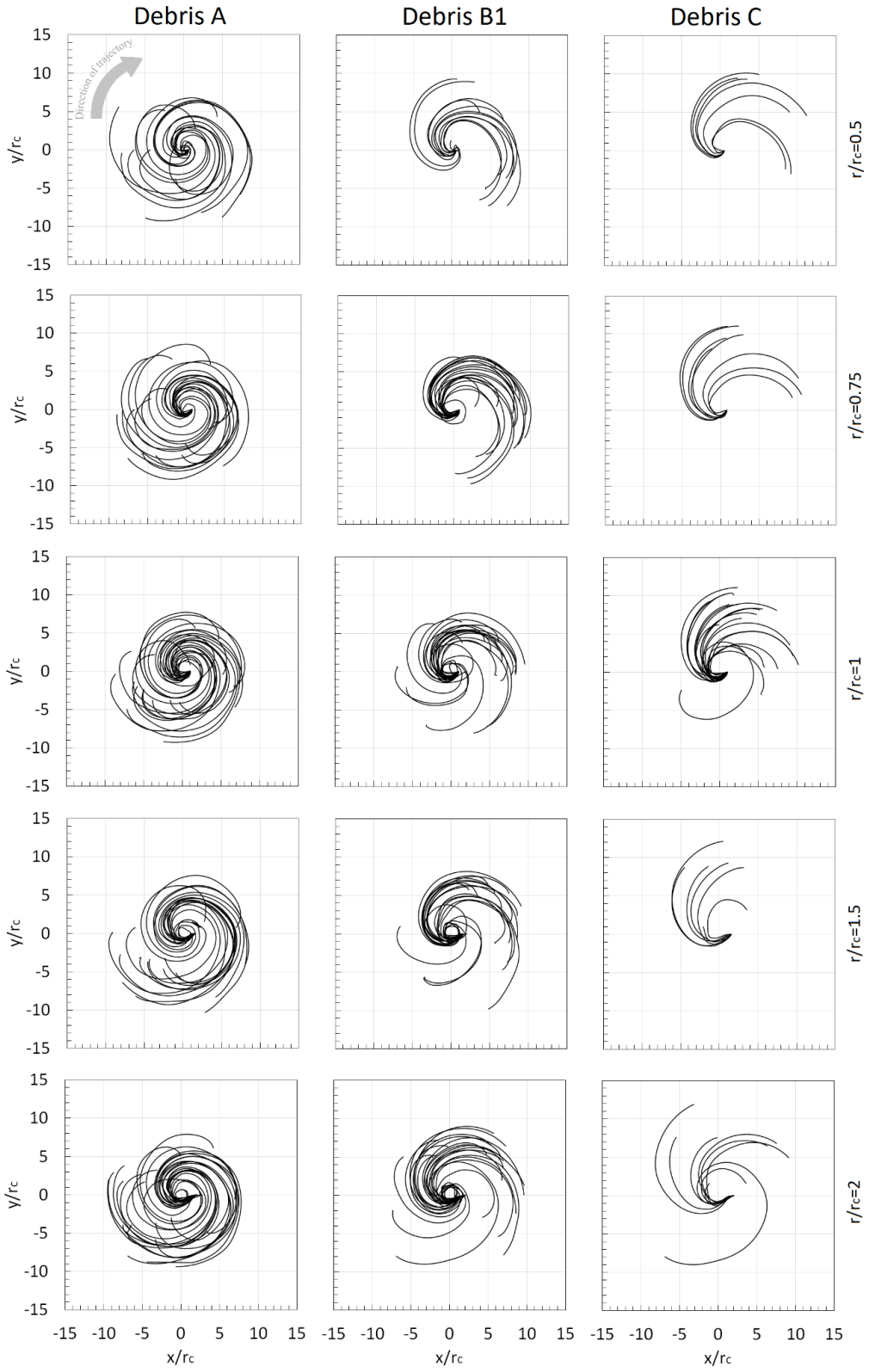

Figure 5.19: Plan view of trajectories at different positions for debris A, B1 and C. The grey arrow denotes the direction of debris trajectory for all debris groups.

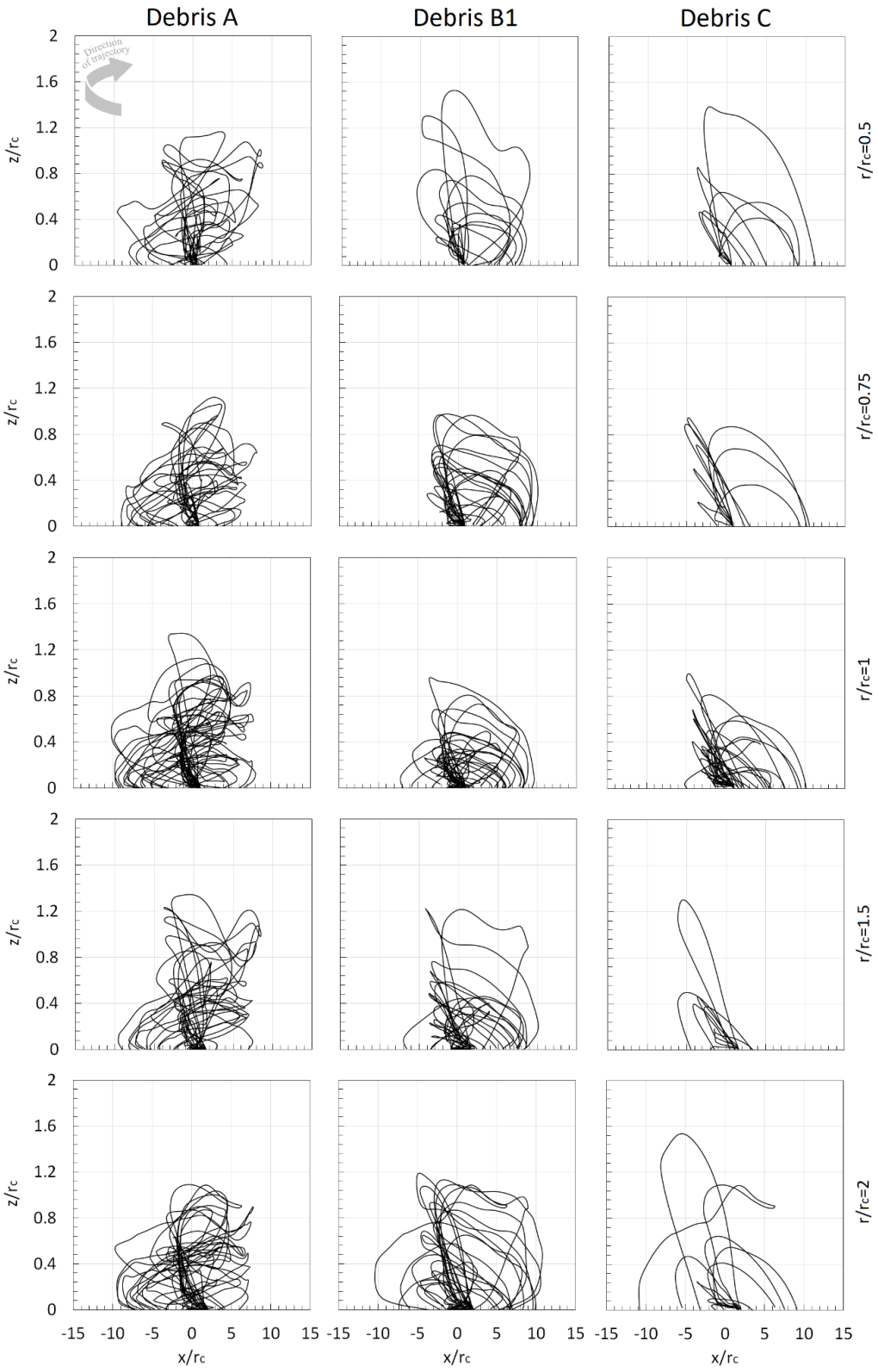

Figure 5.20: Side view of trajectories at different positions for debris A, B1 and C. The grey arrow denotes the direction of debris trajectory for all debris groups.

In Figure 5.20, all three debris groups are observed to gain altitude around the vortex core region (r/r_c >1); despite the varying masses, all three debris groups show similar flight altitude behaviour. Debris group A with longer trajectories can be observed to circulate around the vortex centre with the decrease in altitude, while debris group C shows short almost parabolic trajectories with greater impact range. All three debris groups show similar distribution of trajectories at all positions.

Similar to Figure 5.10, Figure 5.21 shows maximum flight altitude against the corresponding radial distance for debris group A, B1 and C. The vortex core of the vortex with S =0.69 is outlined at the centre with the radius of r/r_c =1, while the grey shaded area (similarly in Figure 5.23, Figure 5.24, Figure 5.25, Figure 5.26 and Figure 5.27) highlights the vortex wall region from the radial distance of r/r_c =1 to 6. The vortex core is outlined at the centre with the radius of r/r_c=1, while the grey shaded area highlights the vortex wall region. The average maximum flight altitude for debris group A, B1 and C are 0.69, 0.54 and 0.51 respectively. For debris group A, the distribution of maximum flight altitude can be found to occur generally around the mean radial distance of r/r_c =4.01, while the distribution for debris group B1 occurs around the mean radial distance of r/r_c =4.19. The flight altitude for debris group C is observed to increase with the radial distance with the mean radial distance of r/r_c =4.88. In general, debris group A with the lowest mass obtains slightly higher flight altitude that occurs closer to the vortex in comparison with the greater mass debris group C, with lower flight altitude that occurs further away from the vortex, showing that the debris trajectories are directed away from the vortex centre.

Figure 5.22 shows the distribution of impact radius of all wind-borne debris from group A, B1 and C. The normal distribution is represented with the curve (red line), expressed

in terms of the percentage of impact occurrence against the impact radius. The percentage of impact occurrence is calculated based on the number of occurrence of debris that impacts at that respective radial distance, while the impact radius is the distance between the impact locations and the vortex centre. As a result, the mean impact radius for debris groups A, B1 and C are 6.87, 8.05 and 9.81 respectively, where debris group A shows the lowest mean impact radius while debris group C has the highest impact radius. Debris groups C exhibits the highest impact potential with a maximum value of approximately r/r_c =12.7, whereas debris group A and B1 shows similar maximum impact radius of r/r_c =11.

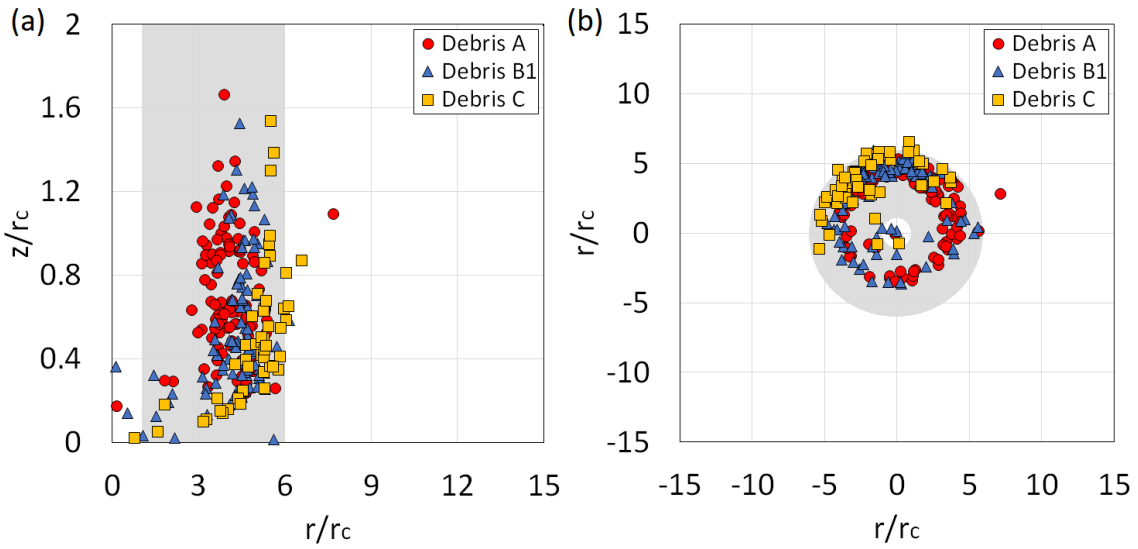

Figure 5.21: (a) The radial distance from the centre of the maximum debris flight altitude for debris group A, B1 and C (b) The radial position of the maximum debris flight altitude for debris group A, B1 and C.

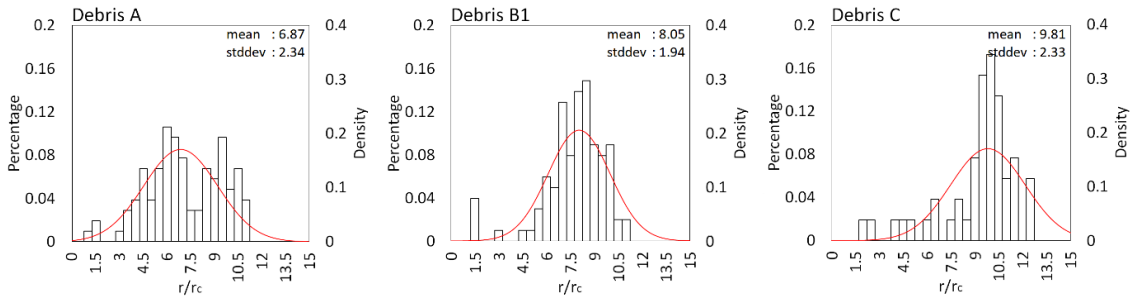

Figure 5.22: The distribution of impact radius of all released debris from debris group A, B1 and C.

The correlation between the flight duration and impact range of debris group A, B1 and C are illustrated in Figure 5.23. The position in which debris are initialisation are represented by different markers; the regions within the core radius, $r/r_c \leq 1$ are in a darker shade while regions outside of the core radius $r/r_c > 1$ are in a lighter shade of their respective colours. The mean flight duration (as presented in Figure 5.17) of debris groups A, B1 and C are 5.46, 3.51 and 2.79 respectively, while the mean impact radius (as presented in Figure 5.22) for debris groups A, B1 and C are 6.87, 8.05 and 9.81 respectively. The correlation between flight duration and impact radius for both debris group B1 and C resembles a linear relationship, where longer flight duration results in greater impact range; in comparison, debris group C shows a lower gradient that impacts at greater radial distance under shorter flight duration. Debris group A shows considerably longer flight duration and a cluster of debris impact around the radial distance of r/r_c =4 to 10 (this phenomenon will be further shown and discussed in Figure 5.25). In general, the position of initialisation appears to have no correlation with the flight duration or impact radius and only effects the possibility of debris becoming wind-borne (as discussed in Figure 5.18).

The correlation between the maximum debris flight altitude and impact range of debris group A, B1 and C are illustrated in Figure 5.24. The average maximum flight altitude (as presented in Figure 5.21) for debris group A, B1 and C are 0.69, 0.54 and 0.51 respectively, while the average impact radius for debris groups A, B1 and C are 6.87, 8.05 and 9.81 respectively. Both debris group B1 and C are observed to somewhat resemble parabolic relationship and shows an asymptotic behaviour after the radius of approximately r/r_c <8 and 10 for debris group B1 and C respectively. In contrast the distribution of debris group A are scattered with the majority of debris impact around the radial distance of r/r_c =4 to 10.

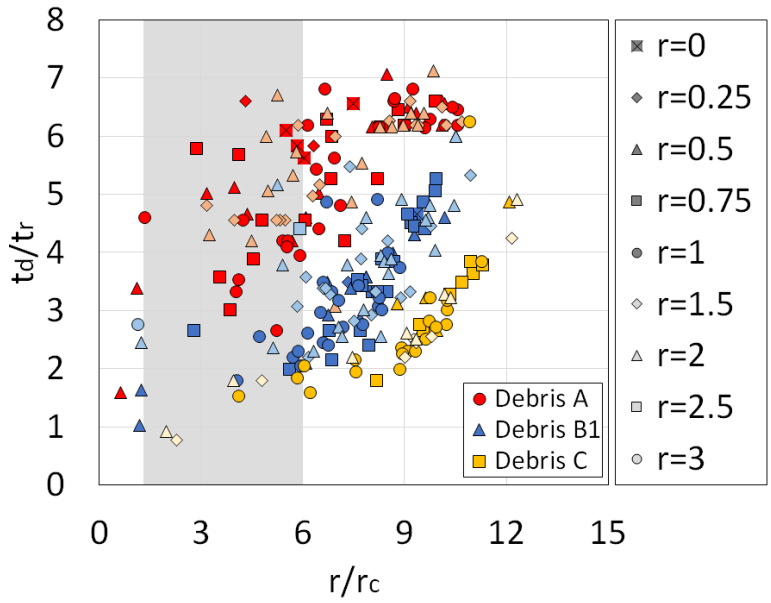

Figure 5.23: The distribution of flight duration against impact radius of debris group A, B1 and C based on the location of debris initialisation.

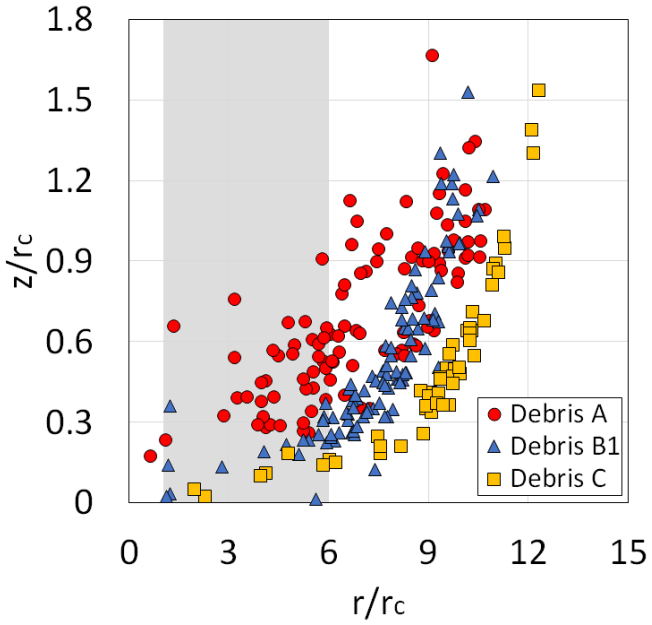

Figure 5.24: The distribution of maximum debris flight altitude against impact radius of debris group A, B1 and C.

Figure 5.25 shows the total flight duration of each individual wind-borne debris from initialisation to the impact on the ground at the positions of r/r_c =0.5, 0.75, 1, 1.5 and 2, (positions of r/r_c =0, 0.25, 2.5 and 3 are shown in Figure A.9), expressed in terms of the radial distance from the centre of the vortex. All three debris groups show similar trend of distribution at every release positions. Generally, all three debris groups show a reduction in radial distance once initialised, indicating the tendency to travel radially inwards before the flight duration of t_d/t_r <0.4; then all wind-borne debris are observed to travel away from the centre with the rapid increase of radial distance after the flight time of t_d/t_r >0.4. For debris group A, after the rapid increase of radial distance, a number of debris are ejected outwards with the radial distance of more than r/r_c =8, while the other debris are observed to maintain at a consistent radial distance of r/r_c =6 to 8 from the centre, indicating the circulation around the vortex. Towards the end of the flight duration, a decrease in radial distance is observed as the debris are drawn towards the

vortex centre due to the radial inflow before impacting on the ground surface. This results in the cluster of impact locations around the region between the radius of r/r_c =4 to 10. For debris group C, the radial distance of the debris trajectories is observed to increase constantly throughout the flight duration due to the inertia of the debris, travelling further away from the centre until the impact on the ground. While the trajectories of debris group B resemble the trend of debris group C with shorter impact range in comparison, and a low number of debris circulating within the vortex wall region.

Figure 5.26 shows the flight altitude against the radial distance from the centre of the vortex throughout the entire flight duration of each individual wind-borne debris at the positions of r/r_c =0.5, 0.75, 1, 1.5 and 2 (positions of r/r_c =0, 0.25, 2.5 and 3 are shown in Figure A.10). All three debris groups show similar trend of distribution at every release positions and are observed to gain flight altitude around the vortex wall region, where debris obtains the maximum flight altitude before descending towards the ground. Debris group A are observed to travel radially outwards around the distance of r/r_c =6 after obtaining maximum flight altitude; this is due to the recirculation ring with the circulation centre situated at the location of r/r_c=6 at the height of z/r_c=1.2 outside of the vortex wall. The anti-clockwise rotation resulted in the reduction of debris flight altitude and the increase in radial distance. The wind-borne debris then maintains at a consistent radial distance of approximately r/r_c =7 to 11, indicating that debris are circulating around the vortex swirl. All debris are drawn towards the vortex centre due to the radial inflow before impacting on the ground surface. Due to the low velocity magnitude of the recirculation ring, the recirculation appears to have no apparent effects on the trajectories of debris group B1 and C. Debris group C resembles a parabolic trajectory with the constant increase in radial distance, travelling further away from the vortex centre until the impact

on the ground, while the trajectories of debris group B resembles the trajectories of debris group C with shorter impact range. Before the impact on the ground surface, debris group B can be noticed travelling towards the centre at the elevation of z/r_c =0.2.

Figure 5.27 shows the wind-borne velocity of each individual debris against the radial distance from the centre of the vortex throughout the debris flight at the positions of r/r_c =0.5, 0.75, 1, 1.5 and 2 (positions of r/r_c =0, 0.25, 2.5 and 3 are shown in Figure A.11). All three debris groups show similar behaviour at all positions, where debris gains a rapid increase flight velocity within the vortex walls due to the high tangential velocity around that region, then gradually decreases while travelling further away from the vortex centre. An immediate decrease in velocity magnitude are noticed for the debris before the impact on the ground surface. Due to the low velocity magnitude of the recirculation ring, the recirculation appears to have no apparent effects on the velocity magnitude for all three debris groups. The average maximum velocity for debris group A, B1 and C are U_d/U_T =1.07, 0.96 and 0.85 respectively, occurring around the average radial distance of r/r_c =1.69, 1.95 and 2.44 for debris group A, B1 and C respectively; debris group A has the highest overall maximum velocity that occurs closer to the vortex, while debris group C has comparably lower maximum velocity that occurs further away from the vortex. As a result, it is significant to note that despite the differences in Tachikawa number, all wind-borne debris generally have the greatest damage potential around the vortex wall region between the radial distance of r/r_c =1.5 to 2.5 as debris are at the highest velocity magnitude.

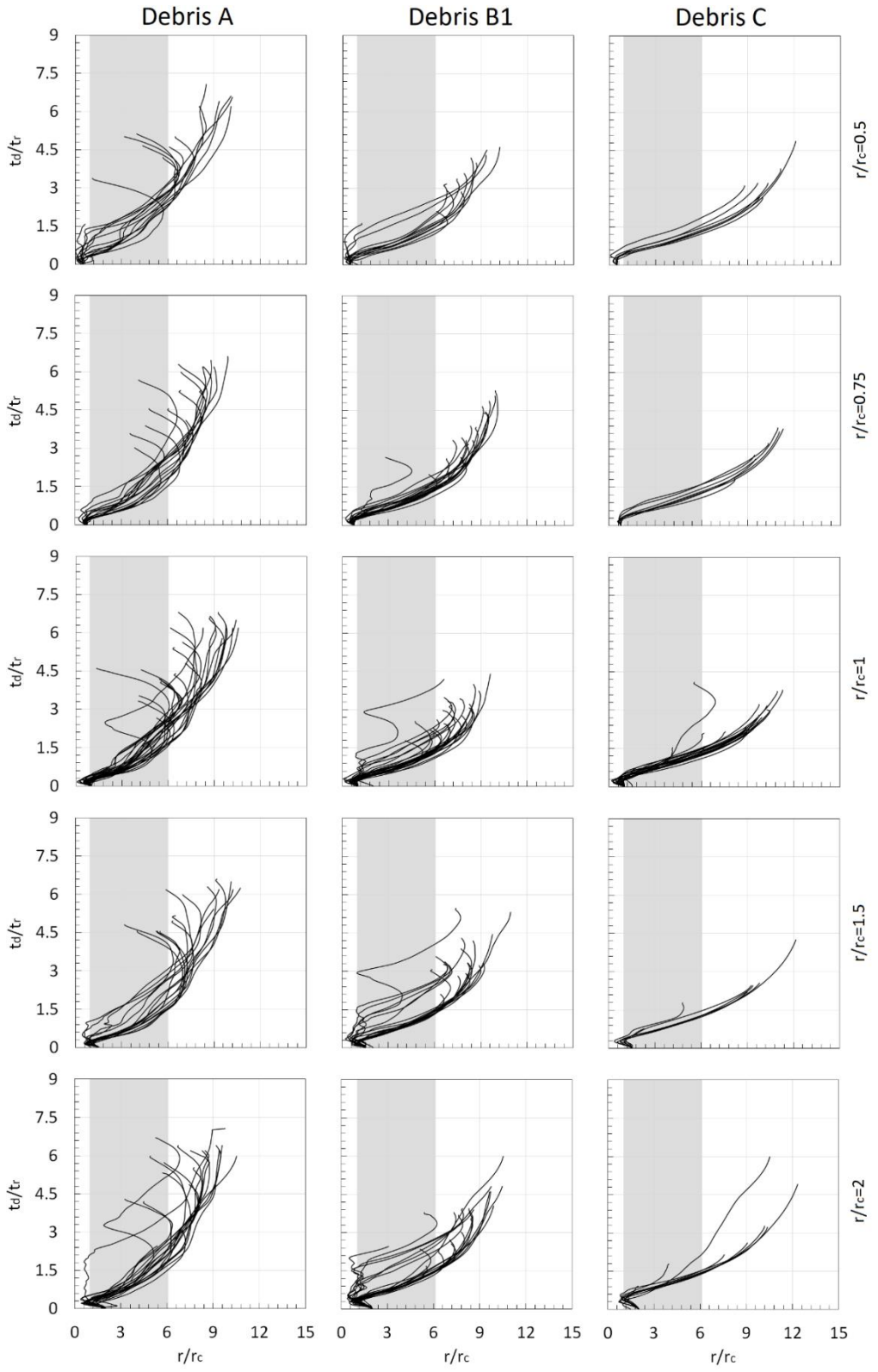

Figure 5.25: Debris flight duration against radial distance for debris group A, B1 and C.

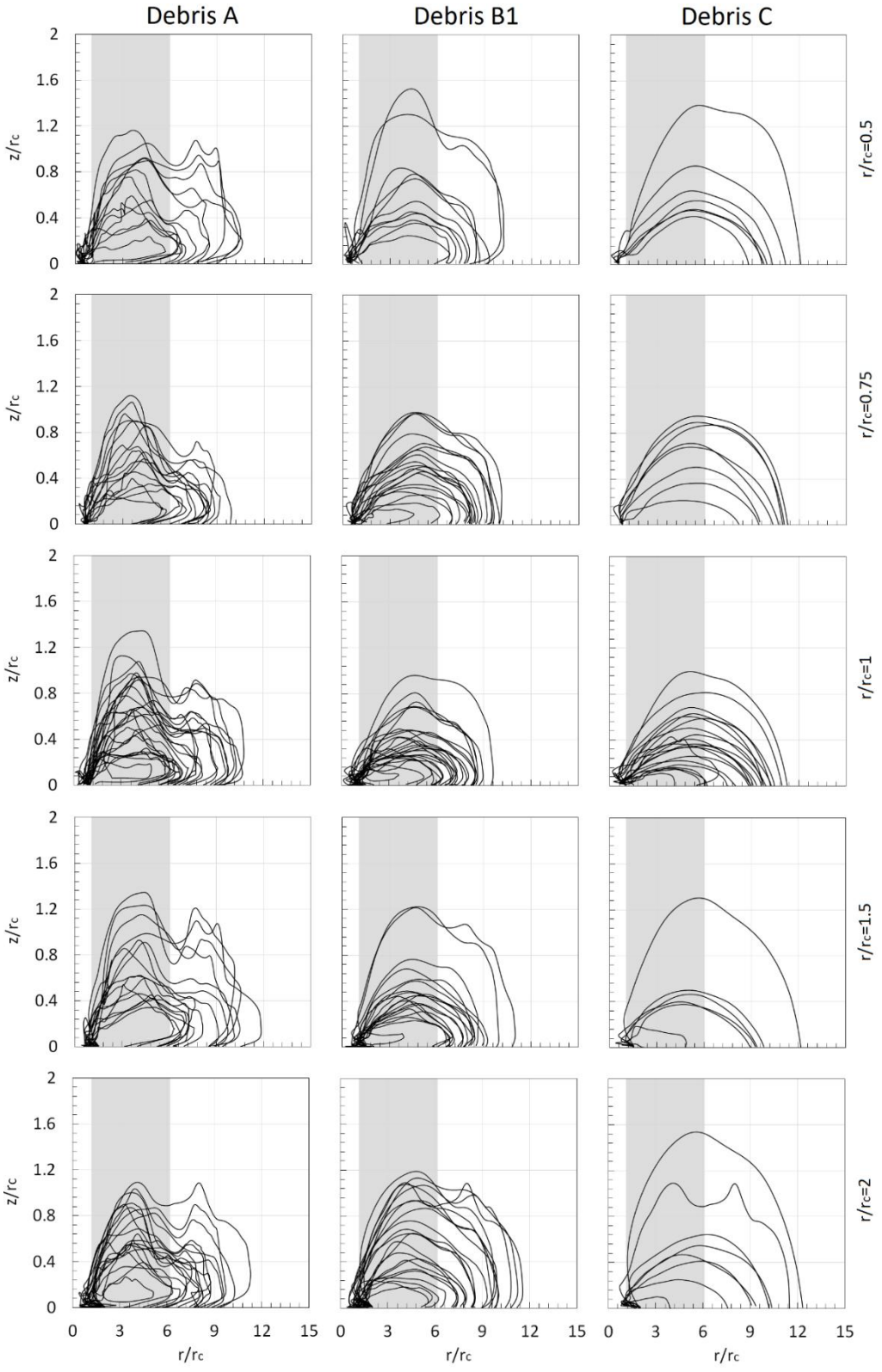

Figure 5.26: Debris flight altitude against radial distance for debris group A, B1 and C.

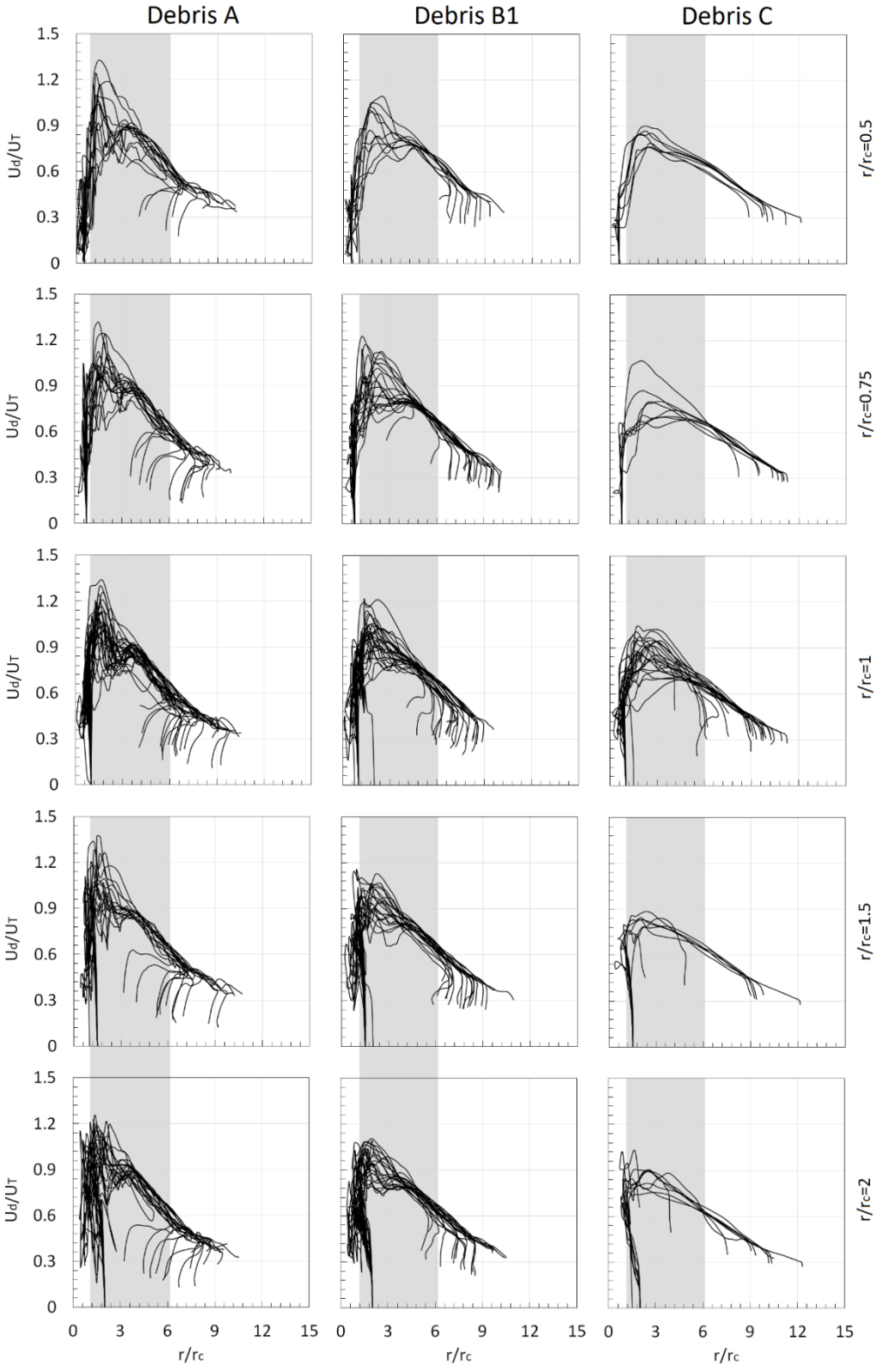

Figure 5.27: Debris velocity against radial distance for debris group A, B1 and C.

5.2.3. Summary relating to variations in Tachikawa number

In order to investigate impact of varying Tachikawa number on the behaviour of wind-borne debris in tornado-like flow fields, a series of numerical simulations were carried out with debris group A, B1 and C corresponding to the Tachikawa number of K =2.5, 1.2 and 0.6 respectively. Debris were released in the tornado-like vortex with S =0.3 and S =0.69, where the correlation of Tachikawa number and debris flight behaviour were investigated and the process of debris initialisation were discussed. The following can be noted:

- Debris with high values of Tachikawa number (K =2.5) have the highest percentage of wind-borne debris in both vortices simulated.
- When K =2.5 (the lighter particles) the debris were observed to have significantly longer trajectories (approximately t_d/t_r =5.5 and 9) for the tornado-like vortex with S =0.3 and S =0.69 respectively. Further analysis of the flight trajectory indicated that these low mass debris has the tendency to circulate around the outer premise of the vortex walls (between r/r_c =5 to 8), and are then drawn towards the centre before impacting on the ground surface due to the radial inflow, resulting in the clustered impact locations close to the vortex structure.
- Debris with low values of Tachikawa number (K =0.6) have the lowest flight altitude and shortest flight duration and (in general) parabolic-like trajectories were observed – the debris were ejected out of the vortex and away from the centre which resulted a higher range of impact distances. The flight duration and altitude of debris with K =0.6 in tornado-like flow fields were found to be somewhat proportional to the impact range.

- The radial distance of highest damage potential of tornado-like vortices are within the vortex wall regions at r/r_c =2 to 3 for vortex with S =0.3 and at r/r_c =1.5 to 2.5 for vortex with S =0.69, as all wind-borne debris obtains the highest velocity magnitude at that radial distance.
- The investigation of debris initialisation demonstrated that debris of all values of Tachikawa number that were positioned around vortex core radius (r/r_c =1) has the highest possibility of becoming wind-borne, whereas debris positioned at the centre region (r/r_c =0 and 0.25) and positions further away (r/r_c >2) were less likely to be initialized. This is due to the presence of high vertical velocities around r/r_c =1 which appear to be the primary factor of debris flight initiation. Further, the position of initialisation only effects the possibility of debris becoming wind-borne and appears to have no correlation with the flight duration or impact radius.

5.3. The Impact of Varying Wind Fields

In this section, the analysis on the flight behaviour of debris in varying vortex flow fields are presented (although a number of results have been discussed / can be inferred from the data presented in section 5.2). The results for debris flight in the tornado-like vortex with S =0.3 and S =0.69 (as presented in section 5.2) are compared and the wind-borne behaviour and impact properties of debris group A, B1 and C are analysed.

5.3.1. Debris flight behaviour

Table 5.1 shows the key debris flight initiation statistics corresponding to both the vortices simulated. In general, the overall number of debris initialised by both of the vortices are not too dissimilar (273 vs. 257) and the distribution per debris group also

show similar differences (maximum difference ~12%). This is surprising given the differences in flow patterns identified in section 4.4, i.e., S=0.3 is identified to resemble the vortex break down stage, where the core is further away from the ground surface, resulting in a greater region of radial inflow between the vortex and the ground surface, whilst the vortex with S=0.69 is identified to resemble the vortex touch down stage, where the vortex core is observed to occur very close to ground surface. Notwithstanding these differences, both of the vortices have a region of positive vertical velocity that surrounds the vortex core. As noted above, it is likely that the positive vertical velocity component (in conjunction with the local pressure field) is the primary driving mechanism which initiates particle flight (over the range of debris examined).

Table 5.1: The total number of wind-borne debris for debris group A, B1 and C that were initialised by the vortex with S=0.3 and S=0.69

Swirl ratio, S	0.3	0.69
Debris A	118	104
Debris B1	99	101
Debris C	56	52
Total	273	257

Figure 5.28 shows the correlation between the maximum debris flight altitude and the impact radius for all three debris groups. Debris group A shows the greatest difference in flight behaviour due to the varying flow fields; the impact radius for debris group A in the vortex with S=0.3 are observed to be clustered around the average radial distance of 3.17, while the vortex with S=0.69 shows greater average impact range of 6.87. Due to the varying magnitudes of the radial inflow for the vortices (details of the effects of radial inflow discussed in Figure 5.31). On the contrary, debris group B1 and C shows similar

range of distribution and resembles a parabolic relationship between maximum flight altitude and impact radius, with the asymptotic behaviour after the radial distance of approximately r/r_c <8 and 10 for debris group B1 and C respectively. The average impact radius of debris group B1 in the vortex with S=0.3 and S=0.69 are 7.34 and 8.05 respectively, and the average impact radius of debris group C in the vortex with S=0.3 and S=0.69 are 9.6 and 9.81 respectively. The average maximum flight altitude of debris group A in the vortex with S = 0.3 are 2.01, significantly greater than debris in the vortex with S=0.69 with the average maximum flight altitude of 0.69. Considerable differences are observed for debris group B1 and C, where the average maximum flight altitude of debris group B1 in the vortex with S=0.3 and S=0.69 are 1.19 and 0.54 respectively, and the average maximum flight altitude of debris group C in the vortex with S=0.3 and S=0.69 are 1.03 and 0.51 respectively.

The correlation between the flight duration and the impact radius for debris group A, B1 and C are shown in Figure 5.28. Similarly, debris group A shows the greatest difference where the mean flight duration of debris group A in the vortex with S=0.3 are 9.07, notably higher than debris in the vortex with S=0.69 with the mean flight duration of 5.46. Some difference are observed for debris group B1 and C, where the mean flight duration of debris group B1 in the vortex with S=0.3 and S=0.69 are 6.08 and 3.51 respectively, and the mean flight duration of debris group C in the vortex with S=0.3 and S=0.69 are 4.44 and 2.79 respectively. The details of all the flight properties for debris group A, B1 and C in the vortex with S=0.3 and S=0.69 are listed in Table 5.2.

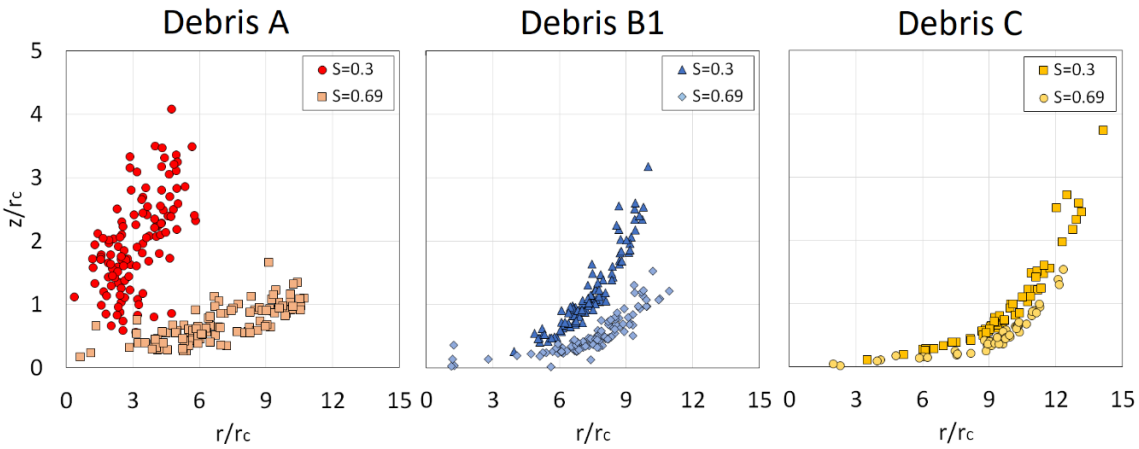

Figure 5.28: The distribution of maximum debris flight altitude against impact radius of debris group A, B1 and C.

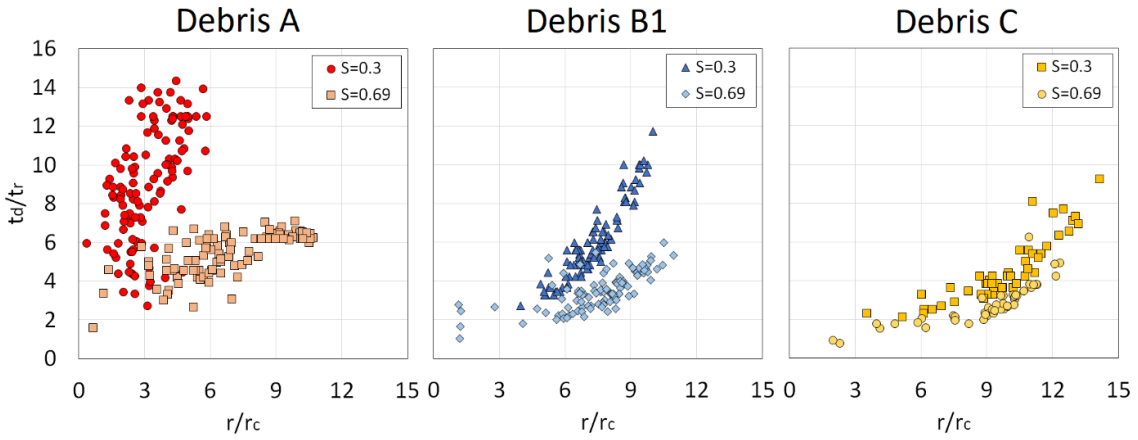

Figure 5.29: The distribution of flight duration against impact radius of debris group A, B1 and C based on the location of debris initialisation.

Generally, it can be observed that the maximum flight altitude and flight duration of all three debris groups are greater in the vortex with S=0.3 in comparison with the vortex with S=0.69. This is not unexpected as the flight behaviour of debris group A (K =2.5) are primarily dominated by the aerodynamic force, while debris group C (K =0.6) is dominated by its inertia; as a result, debris group A are significantly affected by the varying characteristics of the vortex flow field and shows the greatest difference.

Table 5.2: Details of debris flight properties for debris group A, B1 and C in the vortex with S=0.3 and S=0.69.

Swirl ratio, S		Radial distance, r/r_c 0.3	0.69
Impact radius	Debris A	3.17	6.87
	Debris B1	7.34	8.05
	Debris C	9.60	9.81
Maximum altitude	Debris A	2.01	0.69
	Debris B1	1.19	0.54
	Debris C	1.03	0.51
Flight duration	Debris A	9.07	5.46
	Debris B1	6.08	3.51
	Debris C	4.44	2.79

Figure 5.30 (a), (b) and (c) shows the debris flight altitude of all three debris groups, against the radial distance from the centre at the release position of r/r_c =1, while Figure 5.30 (d) illustrates the distribution of vertical velocity profiles at the elevation of z/r_c=0.75, 1, 2 and 3. In both of the vortex flow fields, all three debris groups are observed to gain flight altitude within the vortex wall region due to the presence of high updraft flow around the radial distance of approximately r/r_c=2.5 for vortex with S=0.3 and r/r_c=1.6 for vortex with S=0.69; the flight altitude of all wind-borne debris continues to increase while travelling radially outwards. However, the sudden decrease in vertical velocity for both of the vortices from the radial distance of r/r_c>2.5 for S=0.3 and r/r_c>2 for S=0.69 resulted in the lack of updraft flow required for debris to stay aloft, thus all debris descends back towards the ground surface. In the vortex with S=0.3, debris group A has the tendency to circulate around the outer premise of the vortex walls (between r/r_c =5 to 8) with the decrease in altitude, while in the vortex with S=0.69, debris group

A are observed to travel further outwards around the distance of r/r_c =6 due to the recirculation ring. As the velocity magnitude of the recirculation ring are low, it has very minor effects to the overall the trajectories of debris group B1 and C. Overall, the flight altitude of all three debris groups are significantly greater in the vortex with S=0.3 in comparison with the vortex with S=0.69 due to the higher vertical velocity of the vortex with S=0.3.

The debris flight altitude of debris group A against the radial distance from the centre at the release position of r/r_c =1 are shown in Figure 5.31 (a) while the distribution of radial velocity corresponding to the radial distance of r/r_c=1, 2, 3, 4 and 6 are outlined in Figure 5.31 (b). Further evaluation on the trajectories of debris group A are conducted as a vast majority of debris show a decrease in radial distance towards the end of the flight duration, where debris are observed to be drawn towards the vortex centre before impacting on the ground surface, thereby providing an insight to the flight behaviour of debris in relation to the flow characteristics of the different tornado-like vortices. The individual profiles of radial velocities are separated by a radial offset of U_r/U_T=0.4, 0.6, 1.2, 2 for the profile r/r_c=2, 3, 4 and 6 respectively, in order to correspond to the radial distance of debris flight trajectory in Figure 5.31 (a).

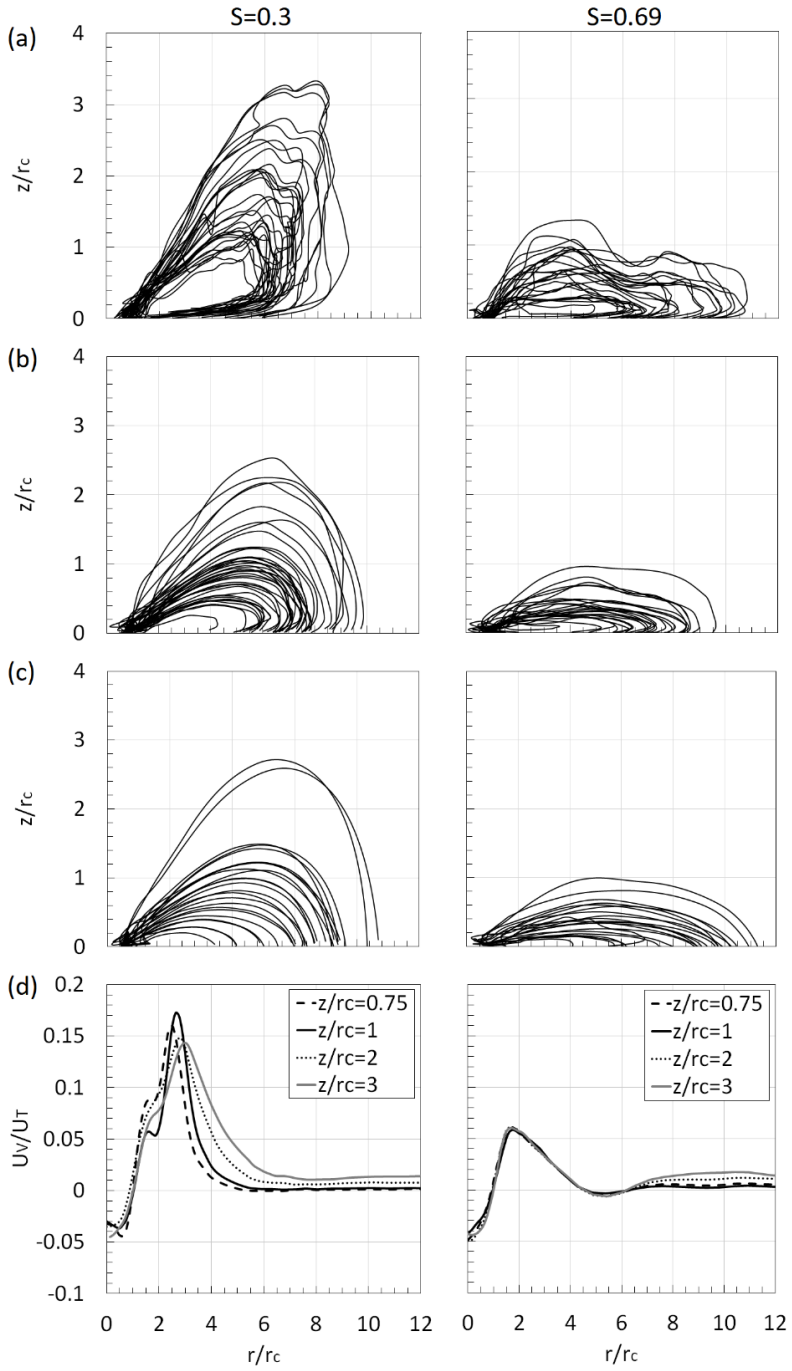

Figure 5.30: Debris flight altitude against radial distance at the position of r/r_c=1 for debris group (a) A (b) B1 (c) C and (d) Normalised vertical velocity profiles at different elevations.

In both of the vortex flow fields, debris show an initial minor reduction in radial distance once initialised due to the region of inflow at the radial distance of r/r_c=1 with the height

of approximately r/r_c=0.3 for vortex with S=0.3 and approximately r/r_c=0.16 for vortex with S=0.69; then all debris are observed to travel radially outwards with the increase in flight altitude due to the outflow.

In the vortex of S=0.3, debris are observed to be ejected outwards due to the regions of high magnitudes of radial outflow at the radial distance of r/r_c=1 to 3 at the elevation of z/r_c>0.3. From the radial distance of r/r_c <4 onwards, the magnitude of radial outflow decreases drastically, as a result debris are observed to retain a consistent radial distance from the centre (between r/r_c =5 to 8), indicating the circulation trajectory around the vortex. Debris are then drawn towards the centre before impacting on the ground surface due to the region of radial inflow with the height of approximately r/r_c=0.3, resulting in the clustered impact location close to the vortex. In the vortex of S=0.69, as the region of inflow are comparably lower, with the height of approximately r/r_c=0.16, debris are closer to the ground surface before being drawn towards the centre, resulting in the impact range that are further from the centre in comparison with the vortex with S=0.3.

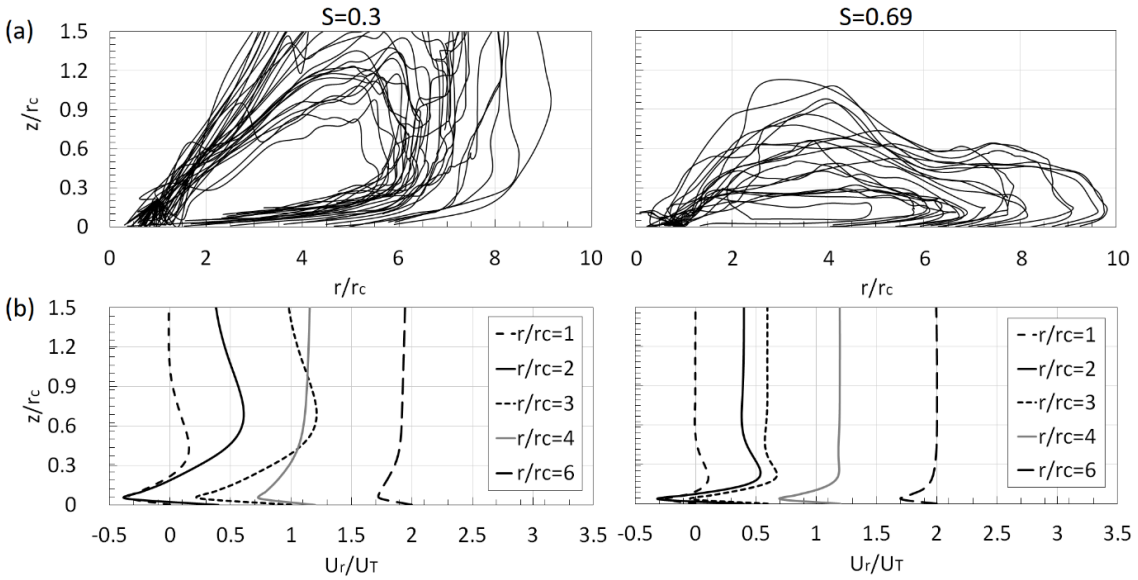

Figure 5.31: (a) Debris flight altitude against radial distance for debris group A at the position of r/r_c=1 (b) Vertical profiles of normalised radial velocity at different radial distances.

5.3.2. Debris impact properties

The correlation between the maximum debris velocity and the impact radius for debris group A, B1 and C are shown in Figure 5.32. In both of the vortex flow fields, the low mass debris group A shows greater wind-borne velocity compared to the high mass debris group C. Debris generally travel with greater velocity in the vortex with S=0.69 than in the vortex with S=0.3; this is due to the higher overall tangential velocity of the vortex with S=0.69. The average maximum velocity for debris group A, B1 and C in the vortex with S=0.3 are 0.93, 0.85 and 0.72 respectively, while the average maximum velocity for debris group A, B1 and C in the vortex with S=0.69 are 1.07, 0.96 and 0.85 respectively. As previously discussed, the mean impact range for debris group A, B1 and C in the vortex with S=0.3 are 3.17, 7.34 and 9.6, and the mean impact range for debris group A, B1 and C in the vortex with S=0.69 are 6.87, 8.05 and 9.81 respectively. Consequently, the impact range of debris are not correlated with the velocity of debris flight; however,

debris with higher values of Tachikawa number has the tendency to travel with greater velocity.

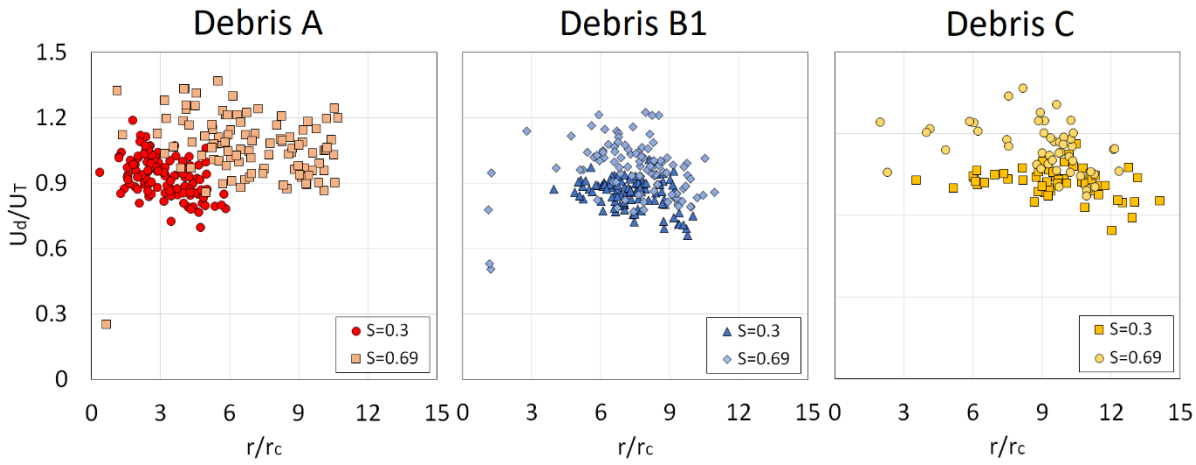

Figure 5.32: Maximum debris velocity against radial distance for debris group A, B1 and C.

Figure 5.33 (a) shows the distribution of impact velocity of debris group A, B1 and C in the tornado-like vortex with S =0.3 and S =0.69, while Figure 5.33 (b) shows the distribution of tangential velocity profiles at the elevation where the maximum tangential velocity (U_T) occurs, z/r_c=0.3 for vortex with S=0.3 and z/r_c=0.15 for vortex with S=0.69. The distribution of tangential velocity is represented in black solid lines while red solid lines represents the mean impact velocity of all wind-borne debris, calculated based on the velocity magnitude of each individual debris at the respective impact location. Although all three debris groups have different range of impact velocities, the trend of impact velocity distribution closely resembles the tangential velocity profiles of the vortices in both of the vortex flow fields. Subsequently, debris impact velocity appears to be dependent of the local flow field regardless on the mass of the debris. This is significant as the maximum tangential velocity of tornado-like vortices generally occurs

near the ground surface, as a result debris have high damage potential around the radial distance of r/r_c =1 to 3 as debris show high magnitudes of velocity.

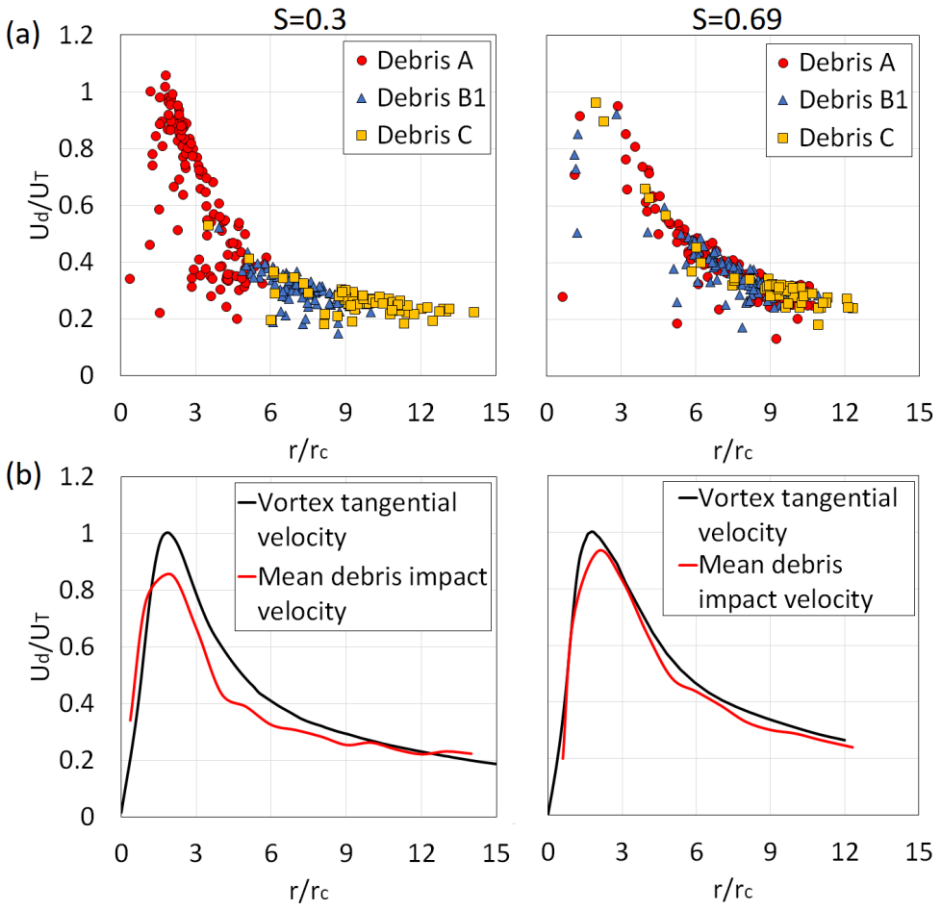

Figure 5.33: (a) The distribution of impact velocity of debris group A, B1 and C (b) Horizontal profiles of normalised tangential velocity.

5.3.3. Asymptotic analysis for debris flight elevation

As discussed in previous sections (section 5.2.1, 5.2.2 and 5.3.1), it was observed that debris group C with greatest mass has the lowest flight altitude; with the decrease in debris mass (consequently decrease in K and increase in Φ), debris flight altitude increases but the radial distance of the flight altitude appears to reach an asymptotic range (Figure 5.10 and Figure 5.21). The debris flight trajectories by Baker and Sterling (2017) suggested

that for flying debris, the trajectories of the debris approaches an asymptotic limit for large times, which can be predicted using an analytical solution, where the increase in Φ results in the increase in flight altitude but a stagnation in radial distance from the vortex centre. However, while the analytical solution describes the equilibrium state of debris flight, it is evident that the numerically simulated debris impacts on the ground and does not stay in an equilibrium. Therefore, in this section, an analysis on the numerically simulated debris trajectory in the tornado-like vortices with S = 0.3 and 0.69 are conducted in order to examine if the analytical asymptotic solutions are applicable in predicting the maximum flight altitude and radial distance of debris flight.

The analytical expression describing debris approaching an asymptotic limit for a large duration of time is expressed in the radial ($r_{Baker\ \&\ Sterling}$) and vertical direction ($z_{Baker\ \&\ Sterling}$) as:

$$r_{Baker\ \&\ Sterling} = 0.518 \left(\frac{S_{Baker\ \&\ Sterling}{}^2}{\Phi}\right) z_{Baker\ \&\ Sterling}^2 \ln\left(z_{Baker\ \&\ Sterling}^2\right)^2 \quad [5.1]$$

$$z_{Baker\ \&\ Sterling}^{\frac{11}{5}} \ln\left(z_{Baker\ \&\ Sterling}^2\right)^{\frac{9}{5}} = 3.36 \left(\frac{\Phi}{S_{Baker\ \&\ Sterling}{}^2}\right)\left(\frac{\Phi}{\Psi}\right)^{\frac{1}{5}} \quad [5.2]$$

where Φ is the buoyancy parameter and Ψ is the inverse tornado Froude number, defined as:

$$\Phi = \frac{0.5\ \rho_a d_d\ r_{rmax}}{m_d} C_D \quad [5.3]$$

$$\Psi = \frac{g\ r_{rmax}}{U_{rmax}^2} \quad [5.4]$$

where ρ_a is the density of the air, d_d is the diameter of the debris (see Table 3.5), r_{rmax} is the radius where the maximum radial velocity occurs, m_d is the mass of the debris, C_D is the drag coefficient of debris, and g is the acceleration due to gravity and U_{rmax} is the maximum radial velocity. In order to ensure that the definitions are consistent with current numerical study, the swirl ratio corresponding to $S_{Baker\ \&\ Sterling}$ = 1.29 and 1.35 are utilised for the calculation (as noted in section 4.4.4), and the properties of the three debris groups are employed for the calculation of buoyancy parameter, Φ. The maximum radial velocity (U_{rmax}) and the radius where the maximum velocity occurs (r_{rmax}) obtained from the numerical simulation for the vortex with $S_{Baker\ \&\ Sterling}$ = 1.29 and 1.35 (S = 0.3 and 0.69) are used for the calculation of Ψ. Details of the obtained parameters are listed in Table 5.3. It should be pointed out that the value of Ψ is considerably low for both of the vortices, indicating that the location of maximum radial velocity from the numerical simulation occurs close to the vortex centre.

Figure 5.34 shows the boundary between the parameter range for debris flight and for debris falling to the ground. Based on the parameter range considered in this study, all debris groups falls within the region of "falling debris", which corresponds to the "falling" behaviour of debris as reported in section 5.2. According to Baker and Sterling (2017), this is due to centrifugal force dominating the trajectories of the debris, resulting in debris being ejected outwards and falling to the ground instead of reaching an equilibrium trajectory around the vortex. However, the findings in this study suggests that debris are being ejected outwards due to the combination of radial outflow and vertical velocities, opposed to centrifugal forces. According to the trajectories of debris as presented in Figure 5.30 and Figure 5.31, it can be observed that debris once initiated, gains elevation

while rapidly travelling outwards due to the regions of high magnitudes of radial outflow, resulting in the behaviour of debris being ejected out of the vortex as observed.

Table 5.3: Parameters obtained for debris group A, B1 and C

	$S_{Baker\ \&\ Sterling}$ = 1.29		$S_{Baker\ \&\ Sterling}$ = 1.35	
	Φ	Ψ	Φ	Ψ
Debris A	1.22		3.84	
Debris B1	0.61	0.04	1.92	0.025
Debris C	0.31		0.96	

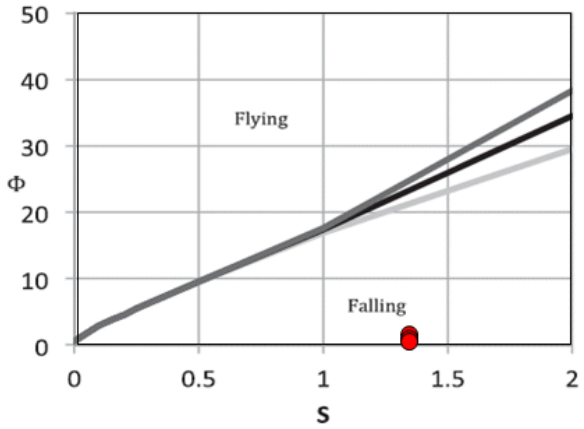

Figure 5.34: Flying and falling debris from numerical simulation in comparison with the parameter range calculated by Baker and Sterling (2017)

Figure 5.35 shows the distribution of maximum flight altitude against the radius in which the maximum flight altitude occurs for debris group A, B1 and C from the numerical simulation, and the calculated asymptotic solutions. It should be noted that in the Baker and Sterling (2017) paper, the velocities and lengths are normalised using the reference radial velocity and the radius at which the reference velocity occurs. However, in order to ensure an adequate comparison, the calculated asymptotic solutions are further adjusted and normalised using the radius of the vortex core (r_c) of both the vortex with $S_{Baker\ \&\ Sterling}$ = 1.29 and 1.35 (S = 0.3 and 0.69). For the vortex with $S_{Baker\ \&\ Sterling}$

= 1.29 (S = 0.3), the radial distance of the asymptotic limit of all three debris groups occurs close to the vortex centre, while the numerical simulation predicted the distribution of maximum flight altitude to occur further from the vortex centre. However, both the analytical solutions and numerical results predicted a similar range of flight altitude. For the vortex with $S_{Baker\ \&\ Sterling}$ = 1.35 (S = 0.69), the asymptotic limit of all three debris groups occurs at a significantly greater radial distance and flight altitude in comparison with the numerical results. The averaged maximum flight altitude and the radius of the maximum flight altitude of the debris flight are listed in Table 5.4 and Table 5.5.

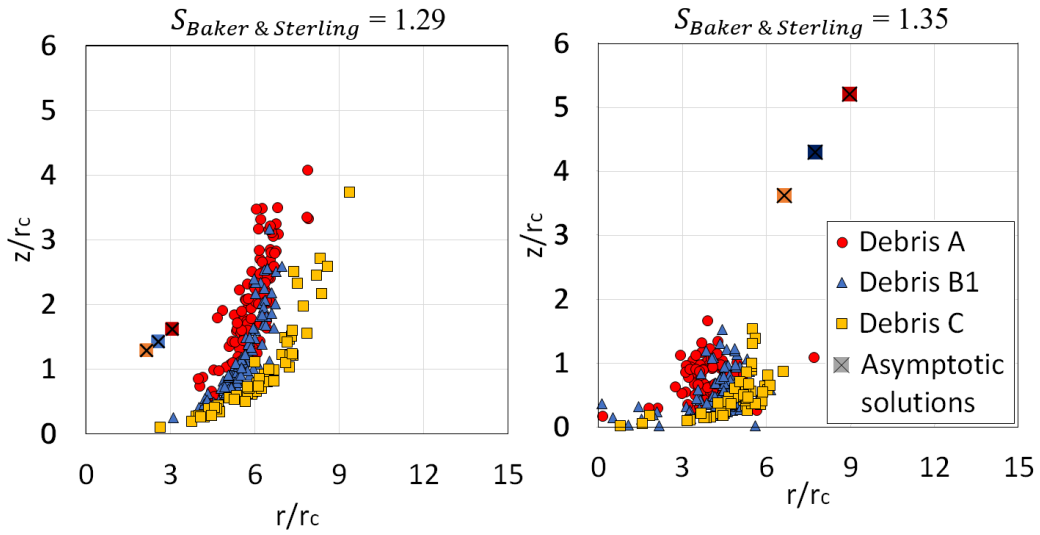

Figure 5.35: The radial distance from the centre of the maximum debris flight altitude for debris group A, B1 and C in comparison with the calculated asymptotic solutions.

Table 5.4: Asymptotic solutions and Flight properties of debris in the vortex with $S_{Baker\ \&\ Sterling}$ = 1.29.

	Baker and Sterling (2017)		CFD	
	z/r_c	r/r_c	z/r_c	r/r_c
Debris A	1.63	3.08	2.01	5.88
Debris B1	1.43	2.59	1.19	5.44
Debris C	1.29	2.61	1.03	6.12

Table 5.5: Asymptotic solutions and Flight properties of debris in the vortex with $S_{Baker\ \&\ Sterling}$ = 1.35.

	Baker and Sterling (2017)		CFD	
	z/r_c	r/r_c	z/r_c	r/r_c
Debris A	5.2	8.97	0.69	4.011
Debris B1	4.28	7.76	0.54	4.2
Debris C	3.61	6.64	0.51	4.88

Figure 5.36 shows the comparison of the average debris flight altitude for all three debris groups in the vortex with $S_{Baker\ \&\ Sterling}$ = 1.29 in comparison with the asymptotic solutions. It can be observed that the maximum flight altitude of debris appears to show a similar range and trend with the analytical solutions.

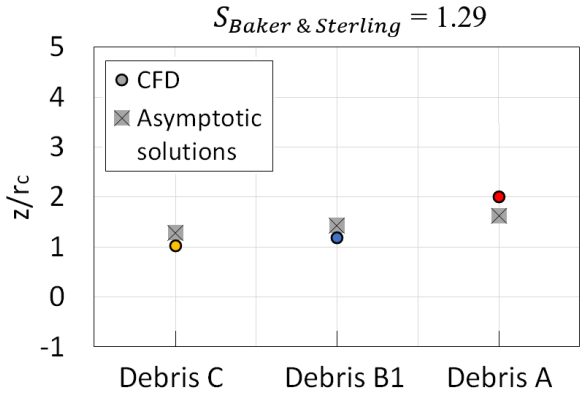

Figure 5.36: comparison of the average debris flight altitude in comparison with the asymptotic solutions for debris groups A, B1 and C.

Overall, for debris flight in the vortex with $S_{Baker\ \&\ Sterling}$ = 1.29, the distribution of maximum flight altitude of debris resembles an asymptotic expansion with the decrease in debris mass and shows a similar altitude range and trend with the analytical solutions. Whilst the analytical solution describes the equilibrium state of debris flight, these steady state solutions appears to be applicable in predicting the maximum flight altitude of debris flight in the vortex with $S_{Baker\ \&\ Sterling}$ = 1.29. With that being said, considerable differences are observed where the radial distance predicted by the analytical solutions are considerably closer to the vortex centre in comparison. These differences can perhaps be attributed to the vortex flow field of the single celled vortex used for the derivation of the analytical solutions; for the Baker and Sterling vortex model, updraft flows are present at the centre of the vortex, while according to the numerical study (as presented in chapter 4), updraft flow occurs around the radial distance of r/r_c=1, as a result, debris obtains flight altitude somewhat further away from the vortex centre thereby resulting in the difference in the radial distance. On the contrary, for debris flight in the vortex with $S_{Baker\ \&\ Sterling}$ = 1.35, the analytical solutions did not predict the trend of maximum flight altitude as shown in the numerical results. This is expected as according to the

results (as presented in chapter 4), the vortex with $S_{Baker\ \&\ Sterling}$ = 1.35 (S = 0.69) resembles the vortex touch down stage; while still considered a one-celled vortex, the flow structure is in a transition stage where the cell breaks down into a two celled vortex.

5.3.4. Summary relating to the flow field comparisons

In order to investigate impact of debris varying vortex flow fields on the debris wind-borne behaviour, an in-depth comparison on the results from the numerical simulations with debris group A, B1 and C in the tornado-like vortex with S =0.3 and S =0.69 was conducted. The flight behaviour of debris in correlation with the vortex wind-field were discussed and the impact properties were investigated. The following summaries can be made:

- The total number of wind-borne debris initialised in both vorticies was similar and it was concluded debris initialisation is governed largely by the vertical velocity component.
- The flight altitude of debris is found to be correlated with the updraft flows of the vortex, as all wind-borne debris gains flight altitude around the regions with the presence of high updraft flow.
- The difference in vortex characteristics demonstrated the effects of the flow field on the flight behaviour of debris groups with different values of Tachikawa number. As the debris group A (K =2.5) are primarily dominated by the aerodynamic force, the flight behaviour shows the greatest difference in comparison to the other two groups.
- The impact velocity of debris appears to be dependent of the local flow field regardless on the Tachikawa number. The trend of impact velocity distribution

closely resembles the tangential velocity profiles of the vortices in both of the vortex flow fields. Consequently, debris have high damage potential particularly around the radial distance of r/r_c =1 to 3 for both of the vortices as debris have high magnitudes of velocity.

6. Discussions and Recommendations for Future Work

"Physics is really nothing more than a search for ultimate simplicity, but so far all we have is a kind of elegant messiness"

Bill Bryson (2003)

THE DANGERS OF tornadoes and the associated flying debris have been an issue that has been long recognised for some time (Chapter 1). Work on modelling tornadoes using analytical models, laboratory scaled experiments and numerical simulation have been reported (Chapter 2) and CFD techniques have been shown to be an invaluable method in this regard; the studies on debris flight in atmospheric boundary layers has shown that compact type debris are well defined and can be accurately represented by the mathematical equations (section 2.3). Whilst the flow fields of tornadoes and debris flight under different wind conditions have been investigated comprehensively, the study on tornado-induced debris are surprisingly sparse.

The aim of this research is to characterise tornado-like flow fields and evaluate the wind-borne behaviour of compact debris within those tornado flows. The analysis on the flow

patterns and vortex structures of different types of tornado-like vortices were presented in chapter 4 and the investigation on flight behaviour and impact properties of debris with varying Tachikawa number were reported in chapter 5. The tornado-like vortex flow fields were generated using Large-eddy simulation, and compared with experimental results (section 4.2) and analytical vortex models (section 4.3). The numerically simulated debris motion in tornado-like flow fields were compared with the experimental results (section 5.1), the impact of Tachikawa number on debris flight were investigated (section 5.2), and the flight behaviour of debris in different tornado-like vortices were reported (section 5.3). The key findings of current work undertaken are discussed in section 6.1, and the recommendations for future work are presented in section 6.2.

6.1. Discussions

Objective 1: The analysis on the numerically simulated tornado-like vortices.

The investigation on the impact of grid resolution demonstrated that the extra fine mesh was able to provide consistent and adequate results for the generation of both of the tornado-like vortices, as the refinement of grid resolution from coarse mesh to fine mesh shows the collapse of results, but only minor changes in the flow field from fine and extra fine mesh (Figure 4.1 & Figure 4.3).

The comparison of numerical results with experimental measurements and analytical vortex models has highlighted that both numerically and physically generated tornado-like vortices corresponds well and shows similar flow patterns and characteristics, while the analytical vortex models can only represent parts of the tornado-flow field. The overall characteristics of the vortices with S = 0.3 and S = 0.69 shows similar trend of velocity distribution at the near ground region and higher elevation in comparison with

the experimental measurements. However, while the numerically generated vortices clearly indicates downward flow at the vortex centre, this flow pattern was not observed in the experimental results (Figure 4.7 & Figure 4.11). This is perhaps due to the lack of fine scaled data around this region, consequently making further comparisons around the vortex core region difficult. Relevant information can be found in section 4.2 & 4.3.

The comparison with analytical models showed that none of the presented analytical models can be used to fully represent the entire three-dimensional flow field tornado-like vortices due to the steady state assumptions for all the analytical vortex models. However, the Burger-Rott and Baker and Sterling vortex models, although simple, are able to represent some parts of the tornado-flow field such as the tangential velocity and pressure distribution relatively well (Figure 4.13, Figure 4.14, Figure 4.15 and Figure 4.16). Relevant information can be found in section 4.3

Objective 2: Characterising the flow structure and features of the tornado-like vortices

The analysis on flow structure and characteristics of two tornado-like vortices corresponding S=0.3 and 0.69 showed that the flow structure of both of the vortices consists of two main features; a core that is situated at the centre of the vortex and the vortex wall that surrounds the core and gives an outline to the structure of the vortex (Figure 4.18). The core primarily consists of downwards flow while the vortex wall consists of updraft flows and high magnitudes of tangential velocity. The flow pattern for the vortex with S = 0.3 was identified to resemble vortex break down stage (as defined by Lugt (1989)), where the vortex core is situated at an elevation from the ground surface and a turbulence region between the core and the ground surface can be observed (Figure

4.24). While the magnitude of tangential velocity of the vortex with S = 0.3 are generally lower (Table 4.1), the updraft flows were considerably greater in comparison with the vortex with S = 0.69 (Figure 4.20 & Figure 4.21). Contrastingly, the flow pattern for the vortex with S = 0.69 was identified as the vortex touch down stage (as defined by Lugt (1989)), where the vortex core is observed to occur very close to ground surface (somewhat touching the ground surface) thus resulting in a smaller turbulence region between the core and the ground surface (Figure 4.24), and the magnitude of tangential velocity is greater, and the core and vortex walls are larger (Table 4.1). Relevant information can be found in section 4.4.1 and 4.4.2. Additionally, the investigation on the spatial displacement of the vortex centre showed that the wandering motion only has an average displacement of approximately r/r_c =0.02, with the maximum displacement less than r/r_c =0.2 for both of the vortices; this low overall displacement in vortex centre showed that the wandering motion will not have significant effects on the debris initialisation process. Relevant information can be found in section 4.4.3.

Objective 3: The evaluation on the flight characteristics of different debris groups under various tornado wind fields

The flight behaviour and impact properties of debris with varying values of Tachikawa number in the tornado-like vortex with S = 0.3 and S = 0.69 were conducted. In both of the simulated vortices, it was found that debris group A with high values of Tachikawa number (K = 2.5) have the highest percentage of wind-borne debris and have significantly longer trajectories (Table 5.1, Figure 5.8 and Figure 5.19). The flight trajectory indicated that these low mass debris circulates around the outer premise of the vortex walls and are

then drawn towards the centre before impact due to the radial inflow; as a result, debris group A has the shortest impact range (Figure 5.14, Figure 5.15, Figure 5.25 and Figure 5.26). On the contrary, debris group C with low values of Tachikawa number (K = 0.6) have the shortest flight duration and lowest flight altitude (Figure 5.12 & Figure 5.23). Generally, these high mass debris have parabolic-like trajectories as debris were ejected away from the centre, resulting in the higher impact range. The flight duration and altitude of debris group C were found to be somewhat proportional to the impact range(Figure 5.12, Figure 5.13, Figure 5.23 & Figure 5.24). Overall, the region of highest damage potential of tornado-like vortices generally occurs within the vortex wall regions (r/r_c = 1.5 to 3) as all wind-borne debris obtains the highest velocity magnitude at that radial distance (Figure 5.16 and Figure 5.27). The investigation of debris initialisation demonstrated that presence of high vertical velocities appears to be the primary factor of debris flight initiation (Figure 5.7 and Figure 5.18), while the position of initialisation only effects the possibility of debris becoming wind-borne and have no correlation with the wind-borne behaviour. Relevant information can be found in section 5.2.1 and 5.2.2.

The flight behaviour of debris in varying vortex flow fields showed that the total number of wind-borne debris initialised in both vorticies were similar as debris initialisation is governed predominantly by the vertical velocity component (Table 5.1). Further, the flight altitude of debris is found to be correlated with the updraft flows of the vortex where all wind-borne debris gains flight altitude around the regions with the presence of high updraft flow (Figure 5.30). As debris group A (K = 2.5) are dominated primarily by the aerodynamic force, the flight trajectories were dependent on the local flow field thus showing the greatest difference due to the varying vortex flow patterns. Last but not least, the trend of impact velocity distribution of all wind-borne debris appears to resemble the

velocity distribution of the local flow field for both of the vortices (Figure 5.33). Relevant information can be found in section 5.3.

6.2. Recommendations for Future Work

The findings presented in this research has characterised tornado-like flow fields and provided an in-depth evaluation on flying behaviour of debris in tornadic flows. The method of numerically simulating debris motion developed in this research has shown good potential for the further investigation of debris flight in tornadoes. However, the challenges associated with this research as well as the limitations of computational fluid dynamics should also be acknowledged. Additionally, further questions needs to be addressed in future studies in order to better understand the interactions between debris and tornadoes in a general scope.

In this research, the flow structure and characteristics of two stationary tornado-like vortices with the swirl ratio of S =0.3 and 0.69 corresponding to the vortex breakdown stage and vortex touchdown stage respectively were simulated, while other stages such as the single-celled, multi-celled stages were not considered. This is due to the available experimental data, which allows the flow field of the numerically generated vortices to be validated. However, in order to accurately reproduce the physical simulator, guide vanes were included during the numerical process, which increased the overall cell number and computational time, as well as restricting the generation of vortices at different swirl ratio within the created computational domain. As presented in section 4.4, it is evident that the flow fields of the vortices varies with the increase in swirl ratio, while the impact of varying vortex flow field on debris wind-borne behaviour differs

significantly (section 5.2). Additionally, as discussed in section 5.2.1 and 5.2.2, the ignorance of the translation effects of the tornadoes result in a relatively low number of debris being initialised. Therefore, the modelling of numerical simulator without the inclusion of guide vanes could potentially allow for the simulation of vortex translation as well as the generation of wider range of swirl ratio.

Furthermore, all debris considered in this study were assumed to be spherical compact debris as compact debris were very well defined and the trajectories and velocities can be predicted by only considering the aerodynamic and gravitational force. However, compact debris may not realistically represent the wind-borne objects observed in the environment. Other debris types such as rod-type and sheet type debris have different physical geometry and aerodynamic effects. Therefore, the flight behaviour of varying types of debris in a tornado-like wind field should be examined in the future. This work has also shown the significant difference in flight behaviour of debris with varying values of Tachikawa number (section 5.3). Debris with lower values of Tachikawa number are dominated by inertia, while debris with higher values of Tachikawa number are primarily dominated by the aerodynamic force and are highly dependent on the flow patterns of the tornado. Consequently, further simulation of debris with a wider range of Tachikawa number may provide a better understand between tornado and debris in a more general scope.

It is also worth pointing out that the current simulation of debris motion is calculated on top of the simulated flow field (at recorded time steps). While this method provides a good prediction of the statistical distribution of debris flight, the effects of continuous changing local flow field has been assumed to be negligible which may not be the case in reality. This can perhaps be observed in the study on debris impact velocity (section 5.3.2),

where the distribution of debris impact velocity closely resembles the mean flow field of the vortex close to the ground; this behaviour may be an artefact of the numerical process as the motion of debris were calculated according to the recorded flow field. Moreover, while forces such as lift generated by the rotation of the debris as well as the centrifugal forces were ignored due to the low magnitude in comparison with the drag and gravitational forces, the inclusion of these forces, although difficult to quantify, may lead to some differences in the overall trajectories as observed in the comparison between numerical and physical simulation (section 5.1.3). As a result, further research on the development of numerical method of computing real-time debris motion on the changing flow field is required. Additionally, the incorporation of other forces such as the centrifugal forces as well as the lift generated by debris rotation should also be investigated in the future. Nevertheless, the numerical simulation is consistent with the physical data and able to capture the entire flight duration from initialization to the impact on the ground, thereby providing a better understanding of the impact distribution and extend the results of the physical simulation. Relevant information can be found in section 3.5, 5.1.1 and 5.1.3.

Whilst every effort has been made to accurately reproduce the physical simulator, there will inevitably be minor differences introduced due to the numerical process; accurately specifying inflow boundary conditions is crucial for LES, yet fraught potentially with difficulties as very specific initial conditions on turbulence is required to reproduce identical inflows, e.g., turbulence intensity, stochastically varying turbulent length scales, and power spectrums of turbulent etc. The effects of SGS modelling are also considered to be a potential source of uncertainty since SGS motions inevitably require unrealistically fine cells at all regions, even locations far away from the vortex structure.

However, in what was presented, the overall predicted velocity field matches that given by the physical results, and is within the range of experimental uncertainty, therefore, it is assumed that the effects of these differences are neglectable and considered suitable for the analysis of this work. Relevant information can be found in section 3.3, 4.1, 4.2 and 4.5.

One of the most challenging aspects of tornado geometric scaling is that, to date, no uniform method exists to determine the scales of laboratory tornado-like vortex simulations to the naturally occurring tornadoes. For that reason, the size of the debris employed in this study relative to full scale tornadoes remains unsolved. A suggested approach is to correlate the numerically obtained velocity field to the available Doppler radar measurements, which will allow all the numerically simulated vortices that are supposed resemble the same full-scale tornado flow field to be compared. In the aspects of wind engineering, the few meters from the ground surfaces of the tornado flow field are of the most interest, as our built environment and civil structures are exposed to this boundary layer region. By doing so, the analysed debris can be scaled to the size with respect to the full-scale tornadoes and the impact forces of these wind-borne debris can be studied.

Reference

[1]. *Afgan, I., 2007. Large Eddy Simulation of Flow over Cylindrical Bodies using Unstructured Finite Volume Meshes (Unpublished doctoral thesis). University of Manchester, UK.*

[2]. *Alexander, C.R., Wurman, J., 2005. The 30 May 1998 Spencer, South Dakota, storm. Part I: the structural evolution and environment of the tornadoes, Amer. Meteor. Soc., 133, 72-96.*

[3]. *ANSYS, CFX, 2013. Ver. 15.0. ANSYS Inc., Southpointe. p, 275.*

[4]. *Ashley, W.S., 2007. Spatial and Temporal Analysis of Tornado Fatalities in the United States: 1880–2005. Weather and Forecasting. 22, 1214-1228.*

[5]. *Bailey, J.R., 1984. Wall Barrier Resistance to the Impact of Tornado Missiles (Unpublished Master's Thesis). Department of Civil Engineering, Texas Tech University, Lubbock, TX.*

[6]. *Baker, C. and Sterling, M., 2019. Are Tornado Vortex Generators fit for purpose?. Journal of Wind Engineering and Industrial Aerodynamics. 190, 287 292*

[7]. *Baker, C.J., 2007. The debris flight equations. J. Wind Eng. Ind. Aerodyn. 95 (5), 329-353.*

[8]. *Baker, C.J., Sterling, M., 2017. Modelling wind fields and debris flight in tornadoes. J. Wind Eng. Ind. Aerodyn. 168, 312-321.*

[9]. *Baker, C.J., Sterling, M., 2018. A conceptual model for wind and debris impact loading of structures due to tornadoes. J. Wind Eng. Ind. Aerodyn. 175, 283-291.*

[10]. *Baker, C.J., Sterling, M., 2018. The calculation of train stability in tornado winds. J. Wind Eng. Ind. Aerodyn. 176, 158-165.*

[11]. *Baker, C. J, Sterling, M and Jesson M, 2020. The lodging of crops by tornadoes. Journal of Theoretical Biology. https://doi.org/10.1016/j.jtbi.2020.110309.*

[12]. *Batterson, J.W., Maicke, B.A., Majdalani, J., 2007. Advancements in Theoretical Models of Confined Vortex Flow fields. Defence Technical Information Center, University of Tennessee Space Institute, Tullahoma, TN 37388.*

[13]. *Bech, J., Gayà, M., Aran, M., Figuerola, F., Amaro, J., Arús, J., 2009. Tornado damage analysis of a forest area using site survey observations, radar data and a simple analytical vortex model. Atmospheric Research. 93, 118–130.*

[14]. *Bloor, M.I.G., Ingham, D.B., 1987. The flow in industrial cyclones. J. Wind Eng. Ind. Aerodyn. 178, 507-519.*

[15]. *Bourriez, F., 2020. Tornados and Windborne Debris: An experimental and Numerical approach. (Unpublished doctoral thesis). University of Birmingham, UK.*

[16]. *Bourriez, F., Sterling, M., Baker, C.J., 2017. Physically modelling windborne debris in tornado-like flow. In: 9th Asia-Pacific Conference on Wind Engineering, Auckland, New Zealand, vol. 2017.*

[17]. *Brown, R.A., Wood, V.T., 2004. Comparisons of Doppler velocity tornadic vortex signatures with signatures from model vortices. In: 22nd Conference on Severe Local Storms, Anonymous Hyannis, MA.*

[18]. *Bryson, B., 2003. A short history of nearly everything. Abridged. New York: Random House, Inc.*

[19]. *Burgers, J.M., 1948. A Mathematical Model Illustrating the Theory of Turbulence. Advances in Applied Mechanics. 1, 171-199.*

[20]. *Church, C. R., Snow, J. T. and Agee, E. M., 1977. Tornado Vortex Simulation at Purdue University, Bulletin of the American Meteorological Society. 58(9), 900-909. doi: 10.1175/1520-0477(1977)0582.0.CO;2.*

[21]. *Church, C.R., Snow, J.T. Agee, E.M., 1977. Tornado vortex simulation at Purdue University. Bulletin of the American Meteorological Society, 58, 900-909.*

[22]. *Church, C.R., Snow, J.T., Baker, G.L., Agee, E.M., 1979. Characteristics of Tornado-Like Vortices as a Function of Swirl Ratio: A Laboratory Investigation. J. Atmos. Sci. 36, 1755-1776.*

[23]. *Cleland, J.D. (2001) Laboratory Measurements of Velocity Pro-Files in Simulated Tornado-Like Vortices. The Journal of Undergraduate Research in Physics, 18: 2*

[24]. *Courant, R., Friedrichs, K., Lewy, H., 1928. Über die partiellen Differenzengleichungen der mathematischen Physik, Math. Ann. 100 (1), 32-74 (in German).*

[25]. *Darrow, M., 2019. Day 4-8 Severe Weather Outlook Issued on Feb 28, 2019, Norman, Oklahoma: Storm Prediction Center. Retrieved from https://www.spc.noaa.gov/products/exper/day4-8/archive/2019/day4-8_20190228.html.*

[26]. *English, E.C., Holmes, J.D., 2005. Non-dimensional solutions for trajectories of wind-driven compact objects. In: Proceedings of The Fourth European and African Conference on Wind Engineering.*

[27]. *Ferziger, J.H., 1993. A Computational Fluid Dynamicist's View of CWE. Computational Wind Engineering. 1, 879-880.*

[28]. *Fujita, T.T., 1971. Proposed Characterization of Tornadoes and Hurricanes by Area and Intensity (Vol. 91). University of Chicago: Research Project.*

[29]. *Fujita, T.T.,1989. The Teton-Yellowstone Tornado of 21 July 1987. Monthly Weather Review. 117 (9), 1913-1940.*

[30]. *Gairola, A., Bitsuamlak, G., 2019. Numerical Tornado Modelling for Common Interpretation of Experimental Simulator. J. Wind Eng. Ind. Aerodyn. 186, 32-48.*

[31]. *Germano, M., Piomelli, U., Moin, P., Cabot, W., 1991. A dynamic subgrid-scale eddy viscosity model. Phys. Fluids A. 3 (7), 1760-1765.*

[32]. *Giaiotti, D.B. Stel, F., 2006. The Rankine vortex model (Doctoral thesis on Environmental Fluid Mechanics-ICTP). University of Trieste, Italy.*

[33]. *Gillmeier, S., 2019. An Investigation Concerning the Simulation of Tornado-like Vortices. (Unpublished doctoral thesis). University of Birmingham, United Kingdom.*

[34]. *Gillmeier, S., Hemida, H., Sterling, M., 2016. An analysis of the influence of a tornado generators geometry on the flow field. In: 8th International Colloquium on Bluff Body Aerodynamics and Applications June 711.*

[35]. *Gillmeier, S., Sterling, M., Baker, C.J. and Hemida, H., 2017. A reflection on analytical tornado-like vortex flow field models. In: International Workshop on Physical Modelling of Flow and Dispersion Phenomena Dynamics of Urban and Coastal Atmosphere.*

[36]. *Grazulis, T.P., 1993. A 110-year perspective of significant tornadoes. In: C. Church et al. (Eds.), The Tornado: its structure, dynamics, prediction, and hazard. 467–474.*

[37]. *Haan, F. L., Balaramudu, V. K. and Sarkar, P. P., 2010. Tornado-Induced Wind Loads on a Low-Rise Building. Journal of Structural Engineering. 136 (1), 106-116. doi: 10.1061/(ASCE)ST.1943-541X.0000093.*

[38]. *Haan, F. L., Sarkar, P. P. and Gallus, W. A., 2008. Design, construction and performance of a large tornado simulator for wind engineering applications. 30, 1146-1159.*

[39]. *Haan, F.L., Sarkar, P.P., Kopp, G.A., Stedman, D.A., 2017. Critical wind speeds for tornado-induced vehicle movements. J. Wind Eng. Ind. Aerodyn. 168, 1-8.*

[40]. *Hangan, H., Kim, J.D., 2006. Numerical simulation of Tornado Vortices. In: 4th International Symposium on Computational Wind Engineering, Yokohama.*

[41]. *Hangan, H., Kim, J.D., 2008. Swirl ratio effects on tornado vortices in relation to the Fujita scale. Wind Struct. 11, 291-302.*

[42]. *Harms, Associate Writer Nicole, 2019. Why Are Tornadoes So Terrifying? February 17. Retrieved from https://www.thoughtco.com/tornado-safety-overview-3444293.*

[43]. *Heisenberg, W., 1996. Galileo. Retrieved from https://galileo.phys.virginia.edu/classes/usem/Origin/notes/05/heisenberg.html.*

[44]. *Historical Records and Trends, National Centers for Environmental Information, 2015. Retrieved from https://www.ncdc.noaa.gov/climate-information/extreme-events/us-tornado-climatology/trends.*

[45]. *Holdeman, J.T., 2010. A Hermite finite element method for incompressible fluid flow. Int. J. Numer. Meth. Fluids, 64 (4), 376-408.*

[46]. *Holmes, J.D., 2004. Trajectories of spheres in strong winds with application to wind-borne debris. J Wind Eng. Ind. Aerodyn. 92, 9-22.*

[47]. *Holmes, J.D., 2010. Windborne debris and damage risk models: a review. Journal of Wind and Structures. 13 (2), 95-108*

[48]. *Holmes, J.D., Baker, C.J., Tamura, Y, 2006. Tachikawa number: A proposal. J Wind Eng. Ind. Aerodyn. 94, 41–47.*

[49]. *Holmes, J.D., English, E.C., Letchford, C., 2004. Aerodynamic forces and moments on cubes and flat plates, with applications to wind-borne debris. In: Summary Papers of the 5th International Colloquium on Bluff Body Aerodynamics and Applications. 103-106.*

[50]. *Holmes., J.D., 2010. Wind borne debris and damage risk models: A review. Wind Struct. 13-2, 95–108.*

[51]. *Hu, H., Yang, Z., Sarkar, P. and Haan, F., 2011. Characterization of the wind loads and flow fields around a gable-roof building model in tornado-like winds. Experiments in Fluids. 51(3), 835.*

[52]. *Huo, S., Hemida, H., Sterling, M., 2020. Numerical study of debris flight in a tornado-like vortex. Journal of fluid and structures. 99, 103134.*

[53]. *Huschke, R.E.,1959. Glossary of Meteorology. Boston, MA: American Meteororology Society.*

[54]. *ICEM, C., 2012. ver. 14.0. ANSYS Inc., Southpointe, 275.*

[55]. *Ishihara, T., Liu, Z., 2014. Numerical study on dynamics of a tornado-like vortex with touching down by using the LES turbulence model. Wind Struct. 19 (1), 89-111.*

[56]. *Ishihara, T., Oh, S., Tokuyama, Y., 2011. Numerical study on flow fields of tornado-like vortices using the LES turbulence model. J. Wind Eng. Ind. Aerodyn. 99, 239-248.*

[57]. *Jischke, M.C., Parang, M., 1974. Properties of simulated tornado-like vortices. J. Atmos. Sci. 31, 506-512.*

[58]. *Kilty, K.T. 2005. Steady-state tornado vortex models to the Rankine combined vortex. Available from: http://www.kilty.com/pdfs/models.pdf. [Accessed 28 December 2018]*

[59]. *Kosiba, K., Wurman, J., 2010. The Three-Dimensional Axisymmetric Wind Field Structure of the Spencer, South Dakota, 1998 Tornado. J. Atmos. Sci. 67, 3074-3083.*

[60]. *Kosiba, K., Wurman, J., 2013. The Three-Dimensional Structure and Evolution of a Tornado Boundary Layer. Weather and Forecasting. 28, 1552-1561.*

[61]. *Kosiba, K.A., Robinson, P., Chan, P.W., Wurman, J., 2014. Wind Field of a Non mesocyclone Anti cyclonic Tornado Crossing the Hong Kong International Airport. Advances in Meteorology, 1-7.*

[62]. *Kuai, L., Haan, F.L., Gallus, W.A. Sarkar, P.P., 2008. CFD simulations of the flow field of a laboratory-simulated tornado for parameter sensitivity studies and comparison with field measurements. Wind Struct. 11, 1-22.*

[63]. *Kuo, H.L., 1971. Axisymmetric Flows in the Boundary Layer of a Maintained Vortex. J. Atmos. Sci. 28, 20-41.*

[64]. *Lee, A.J.H., 1974. A general study of tornado-generated missiles. Nuclear Engineering and Design,.30, 418-433.*

[65]. *Lee, J., Samaras, T., Young, C.R., 2004. Pressure measurements at the ground in an F-4 tornado. In: 22nd Conference on Severe Local Storms, Anonymous Hyannis, MA.*

[66]. *Lee, W.-C. and Wurman, J., 2005. Diagnosed Three-Dimensional Axisymmetric structure of the Mulhall Tornado on 3 May 1999. Journal of the Atmospheric Sciences. 62(7), 2373-2393. doi: 10.1175/JAS3489.1.*

[67]. *Lee, W.C., Wurman, J., 2005. Diagnosed three-dimensional axisymmetric structure of the Mulhall tornado on 3 May 1999. J. Atmos. Sci. 62, 2373-2394.*

[68]. *Lewellen, D.C., Lewellen, W.S., 2007. Near-surface intensification of tornado vortices. J. Atmos. Sci. 64, 2176–2194.*

[69]. *Lewellen, D.C., Lewellen, W.S., Sykes, R.I., 1997. Large-eddy simulation of a tornado's interaction with the surface. J. Atmos. Sci. 54, 581–605.*

[70]. *Lewellen, D.C., Lewellen, W.S., Xia, J., 2000. The influence of a local swirl ratio on tornado intensification near the surface. J. Atmos. Sci. 57, 527–544.*

[71]. *Lewellen, W.S., 1962. A Solution of Three-Dimensional Vortex Flows with Strong Circulation. J. Fluid Mechanics, 14, 420.*

[72]. *Lilly, D. K., 1967. The representation of small-scale turbulence in numerical simulation experiments. In: Proc. IBM scientific computing symposium on environmental sciences. Yorktown Heights N. Y. 195.*

[73]. *Lin, N, Vanmarcke, E., 2010. Windborne debris risk analysis - Part I. Introduction and methodology. Wind Struct.13 (2) 191-206.*

[74]. *Lin, N., Holms J.D., Letchford, C.W., 2007. Trajectory of windborne debris and applications to impact testing, J. Structural Eng. ASCE, 133 (2), 274-282.*

[75]. *Liu, Z, Ishihara, T., 2015. Numerical study of turbulent flow fields and the similarity of tornado vortices using large eddy simulations. J. Wind Eng. Ind. Aerodyn. 145, 42-60.*

[76]. *Liu, Z., Cao, S., Liu, H., Hua, X., Ishihara, T., 2020. Effects of Reynolds number in the Range from 1.6x103 to 1.6x106 on the Flow Fields in Tornado-like Vorices by LES: A systematical Study. J. Wind Eng. Ind. Aerodyn. 196, 104-128.*

[77]. *Liu, Z., Liu, H., Cao, S, 2018. Numerical study of the Structure and Dynamic of a Tornado at the Sub-critical Breakdown Stage. J. Wind Eng. Ind. Aerodyn. 177, 306-326.*

[78]. *Lugt, H., 1989. Vortex breakdown in atmospheric columnar vortices. Bulletin of the American Meteorological Society. 70, 1526-1537.*

[79]. *Maas, H.G., Gruen, A., Papantomiou, D., 1993. Particle tracking Velocimetry in three-dimensional flows, Part I. Exp. Fluid. 15:133-46.*

[80]. *Malik, N.A., Dracos, T., Papantomiou, D., 1993. Particle tracking Velocimetry in three-dimensional flows. Part II. Exp, Fluid, 15, 279-94.*

[81]. *Mark-Paul Gosselaar quote., 2013. Idle Hearts. Retrieved from https://www.idlehearts.com/141951/but-the-hardest-thing-is-trying-to-get-dialogue-out-in-all-of-that.*

[82]. *Marshall, T.P., Robinson, S., 2006. The Birmingham, U.K. tornado: 28 July 2005. In: 23rd Conference on Severe Local Storms, November.*

[83]. *Maruyama, T., 2009. A Numerically Generated Tornado-like Vortex by Large Eddy Simulation. In: Proceedings of Seventh Asia-Pacific Conference on Wind Engineering, Taipei, Taiwan. 349-352.*

[84]. *McDonald, J.R. Kiesling, E.W., 1988. Impact resistance of wood and wood products to simulated tornado missiles. In: Proc. International Conference on Timber Engineering, Seattle, WA, September 19-22.*

[85]. *McDonald, J.R., 1976. Tornado-generated missiles and their effects. In: Proc. Symposium on Tornadoes, Texas Tech University, Lubbock, Texas, June 22-24, 1976.*

[86]. *McDonald, J.R., 1990. Impact resistance of common building materials to tornado missiles. J. Wind Eng. Ind. Aerodyn. 36, 717-742.*

[87]. *McDonald, J.R., 1999. Windborne debris impacts on metal wall panels and their implications. In: Wind Engineering into the 21st Century, Larsen, Larose & Livesey (eds), Balkema, Rotterdam.*

[88]. *Minor, J.E., 1994. Windborne debris and the building envelope. J. Wind Eng. Ind. Aerodyn. 53, 207-227.*

[89]. *Minor., J.E., 1994. Wind borne debris and the building envelope. J. Wind Eng. Ind. Aerodyn. 53, 207–227.*

[90]. *Mishra, A.R., James, D.L., Lethcford, C.W., 2008. Physical simulation of a single-celled tornado-like vortex, Part A: flow field characterization. J. Wind Eng. Ind. Aerodyn. 96, 1234–1257.*

[91]. *Mitsuta, Y., Monji, N., 1984. Development of a laboratory simulator for small scale atmospheric vortices. Nat. Disaster Sci. 6, 43-54.*

[92]. *Montry, G., 2012. High Performance Computing for Engineering Applications. Retrieved from https://www.slideserve.com/dixie/me964-high-performance-computing-for-engineering-applications.*

[93]. *Nasir, Z., Bitsuamlak, G., 2016. Computational Modelling of Hill Effects on Tornado-like Vortex. Resilient Infrastructure, London.*

[94]. *Natarajan, D., 2011. Numerical Simulation of Tornado-like Vortices. (Unpublished doctoral thesis). University of Western Ontario, Canada.*

[95]. *NOAA., 2012. National Oceanic and Atmospheric Administration. Retrieved from www.noaa.gov.*

[96]. *Nolan, D.S., Farrell, B.F., 1999. The structure and dynamics of tornado-like vortices. J. Wind Eng. Ind. Aerodyn. 56, 2908-2936.*

[97]. *Nolan, D.S., Farrell, B.F., 1999. The structure and dynamics of tornado-like vortices. J. Atmos. Sci. 56, 2908-2936.*

[98]. *OpenFOAM, 2019. OpenFOAM: User guide version 7. Retrieved from http://foam.sourceforge.net/docs/Guides-a4/OpenFOAMUserGuide-A4.pdf*

[99]. *Pan, Y.W., 2013. CFD Numerical simulation of tornado wind field and wind loads on structures. IN: Harbin, China: Harbin Institute of Technology. 18-25.*

[100]. *Phuc, P.V., Nozu, T., Nozawa, K., Kikuchi, H., 2012. A Numerical Study of the Effects of Moving Tornado-Like Vortex on a Cube. In: The Seventh International Colloquium on Bluff Body Aerodynamics and Applications, Shanghai, China.*

[101]. *Piomelli, U., 2001. Large-eddy and direct simulation of turbulent flows. In: 9th conférence annuelle de la société Canadienne de CFD, Kitchener, Ontario, Canada.*

[102]. *Piomelli, U., Balaras, E., 2002. Wall-layer models for large-eddy simulations. Annu. Rev. Fluid Mech., 34. 349-374.*

[103]. *Putnam, A., 1961. Integrable form of droplet drag coefficient. ARS Jnl. 31, 1467.*

[104]. *Ramseyer, C., Floyd, R. Holliday, L., 2017. Performance of Enhanced Residential Building Code Requirements during the March 25, 2015, Moore Tornado. Journal of Performance of Constructed Facilities, 31, (5).*

[105]. *Rankine, W.J.M., 1882. A Manual of Applied Physics. 10th ed. Charles Griff and Co. 663.*

[106]. *Redmann, G.H, Radbill, J.R., Marte, J.E., Degarabedian, P., Fendell, F.E., 1976. Wind field and trajectory models for tornado propelled objects. Electrical Power Research Institute, Technical Report 1, Palo Alto, CA.*

[107]. *Refan, M. and Hangan, H., 2016. Characterization of tornado-like flow fields in a new model scale wind testing chamber, Journal of Wind Engineering and Industrial Aerodynamics. 151, 107-121.*

[108]. *Refan, M. and Hangan, H., 2018. Near surface experimental exploration of tornado vortices, Journal of Wind Engineering & Industrial Aerodynamics. 175 (June 2017), 120-135.*

[109]. *Refan, M., 2014. Physical simulation of tornado-like vortices. Electronic Thesis and Dissertation Repository. (Unpublished doctoral thesis). The University of Western Ontario.*

[110]. *Refan, M., Hangan, H. and Wurman, J., 2014. Reproducing tornadoes in laboratory using proper scaling, Journal of Wind Engineering and Industrial Aerodynamics. 135, 136-148.*

[111]. *Refan, M., Hangan, H., Wurman, J., 2014. Reproducing tornadoes in laboratory using proper scaling. J. Wind Eng. Ind. Aerodyn. 135, 136-148.*

[112]. *Richards, P.J., Williams, N., Laing, B., McCarty, M., Pond, M., 2008. Numerical calculation of the three-dimensional motion of wind-borne debris. J. Wind Eng. Ind. Aerodyn. 96, 2188-2202.*

[113]. *Rott, N., 1958. On the viscous core of a line vortex. Zeitschrift für angewandte Mathematik und Physik ZAMP. 9, 543-553.*

[114]. *Rotunno, R., 1977. Numerical simulation of a laboratory vortex. J. Atmos. Sci. 34, 1942-1956.*

[115]. *Sarkar PP, Haan FL, Gallus WA, Kuai L, W. J., 2005. Velocity measurements in a laboratory tornado simulator and their comparison with numerical and full scale data, in Proceedings of the 37th US-Japan panel on wind and seismic joint meeting, Tsukuba, Japan, May 16-18.*

[116]. *Sassa, K., Takemura, S. Yamashita, K., 2009. The behaviour of wind-borne debris accompanied by a traveling tornado. In: Seventh Asia-Pacific Conf. on Wind Eng., Taipei, Taiwan.*

[117]. *Simiu, E., Cordes, M., 1976. Tornado borne missile speeds. NBSIR 76-1050, National Bureau of Standards.*

[118]. *Smagorinsky, J., 1963. General circulation experiments with the primitive equations I. the basic experiment. Mon. Weather Rev. 91 (3), 99-164.*

[119]. *Smagorinsky, J., 1963. General circulation experiments with the primitive equations. The basic experiment. Monthly weather review. 91, 99.*

[120]. *Stokes, G.G., 1842. On the steady motion of incompressible fluids. Transactions of the Cambridge Philosophical Society. 7, 439–453.*

[121]. *Sullivan, R.D., 1959. A Two-Cell Vortex Solution of the Navier-Stokes Equations. Journal of the Aerospace Sciences. 26, 767-768.*

[122]. *Tachikawa, M., 1983. Trajectories of flat plates in uniform flow with application to wind-generated missiles. J. Wind Eng. Ind. Aerodyn. 14, 443-453.*

[123]. *Tang, Z., Feng, C., Wu, L., Zuo, D. and James, D. L., 2018. Characteristics of Tornado-Like Vortices Simulated in a Large-Scale Ward-Type Simulator. Boundary-Layer Meteorology. 166(2), 327-350.*

[124]. *Tang, Z., Feng, C., Wu, L., Zuo, D., James, D.L., 2017. Characteristics of Tornado-Like Vortices Simulated in a Large-Scale Ward-Type Simulator. Boundary-Layer Meteorology. 1-24.*

[125]. *Tari, P.H., Gurka, R., Hangan, H., 2010. Experimental investigation of tornado-like vortex dynamics with swirl ratio: the mean and turbulent flow fields. J. Wind Eng. Ind. Aerodyn. 98, 936-944.*

[126]. *Tornado generator - University of Birmingham. (n.d.) Retrieved from https://www.birmingham.ac.uk/research/activity/engineering/power-infrastructure/facilities/tornado-generator.aspx.*

[127]. *Twisdale, L.A., Dunn, W.L., Davis, T.L., 1979. Tornado missile transport analysis. Nuclear Engineering and Design. 51, 295-308.*

[128]. *U.S. Tornado Climatology, National Centers for Environmental Information (NCEI), 2010. Retrieved from https://www.ncdc.noaa.gov/climate-information/extreme-events/us-tornado-climatology.*

[129]. *Wang, K., Letchford, C.W., 2003. Flying debris behaviour. In: 11th International Conference on Wind Engineering, Lubbock, Texas Proceedings. 2, 1663-1670.*

[130]. *Ward, N.B., 1972. The exploration of certain features of tornado dynamics using a laboratory model. J. Atmos. Sci. 29, 1194-1204.*

[131]. *Watkins, S., Mousley, P.D., Hooper, J.D., 2002. Measurement of fluctuating flows using multi-hole probes. In: Proceedings of the 9th International*

Congress of Sound and Vibration, Orlando, Florida, USA, 8-11 July, International Institute of Acoustics and Vibration.

[132]. *Western University Department of Communications and Public Affairs, 2020. Western News - Western experts talk tornadoes: predicting, mapping, protecting people and property. Retrieved from: https://news.westernu.ca/2020/05/western-experts-talk-tornadoes-predicting-mapping-protecting-people-and-property/.*

[133]. *Wills, J.A.B., Lee, B.E., Wyatt, T.A., 2002. A model of wind-borne debris damage. J. Wind Eng. Ind. Aerodyn. 90, 555-565.*

[134]. *Winn, W.P., Hunyady, S.J., Aulich, G.D., 1999. Pressure at the ground in a large tornado. Journal of Geophysical Research: Atmospheres. 104, 22067-22082.*

[135]. *Wurman, J. and Alexander, C. R., 2005. The 30 May 1998 Spencer, South Dakota, Storm. Part II: Comparison of Observed Damage and Radar-Derived Winds in the Tornadoes. Monthly Weather Review, 133(1), 97-119. doi:10.1175/MWR-2856.1.*

[136]. *Wurman, J., 2000. Fine-scale radar observations of the Dimmitt, Texas (2 June 1995), tornado. Monthly Weather Review. 128, 2135–2164.*

[137]. *Wurman, J., 2002. The multiple vortex structure of a tornado. Wea. Forecasting. 17, 473-505.*

[138]. *Wurman, J., Alexander, C.R., 2005. The 30 May 1998 Spencer, South Dakota, Storm. Part II: Comparison of Observed Damage and Radar-Derived Winds in the Tornadoes. AMS Monthly Weather Review, 133, 97-118.*

[139]. *Wurman, J., Kosiba, K., Robinson, P., 2013. In Situ, Doppler Radar, and Video Observations of the Interior Structure of a Tornado and the Wind–Damage Relationship. Bulletin of the American Meteorological Society, 94, 835-846.*

[140]. *Wurman, J., Straka, J. M., Rasmussen, E.N., 1996. Fine-scale Doppler radar observations of tornadoes. Science. 272 (21), 1774-1777.*

[141]. *Xu, Z., Hangan, H., 2009. An Inviscid Solution for Modelling of Tornadolike Vortices. Journal of Applied Mechanics. 76, 031011-031011-031015.*

[142]. *Yang, Z., 2015. Large-eddy simulation: Pass, Present and the future. Chinese Journal of Aeronautics, 28 (1), 11-24.*

[143]. *Yuan, F., Yan, G., Honerkamp, R., Isaac, K., Zhao, M., Mao, X., 2019. Numerical Simulation of Laboratory Tornado Simulator That Can Produce Translating Tornado-like Wind Flow. J. Wind Eng. Ind. Aerodyn. 190, 200-217.*

[144]. Alexander, R., Wurman, J., 2008. Updated mobile radar climatology of supercell tornado structures and dynamics. 24th Conf. on Severe Local Storms, Savannah, GA, Amer. Meteor. Soc.', p. 19.4.

[145]. Wurman, J., Kosiba, K., Robinson, P., 2013. Doppler Radar, and Video Observations of the Interior Structure of a Tornado and the Wind-Damage Relationship. Bulletin of the American Meteorological Society. 94 (6), 835-846.

[146]. Kosiba, A., Wurman, J., 2013. The Three-Dimensional Structure and Evolution of a Tornado Boundary Layer', Weather and Forecasting. 28(6), 1552-1561.

[147]. Wurman, J., Alexander, C., Robinson, P., Richardson, Y., 2007. Low-Level Winds in Tornadoes and Potential Catastrophic Tornado Impacts in Urban Areas. Bulletin of the American Meteorological Society. 88(1), 31-46.

[148]. Winn, P., Hunyady, J., Aulich, D., 1999. Pressure at the ground in a large tornado. Journal of Geophysical Research Atmospheres. 104 (D18), 22067-22082.

[149]. Lee, J., Samaras, M., 2004. Pressure measurements at the ground in an F-4 tornado. Preprints, 22nd Conf. on Severe Local Storms, Hyannis, MA, Amer. Meteor. Soc., p. 15.3.

[150]. Karstens, D., Samaras, M., Lee, D., Gallus, A., Finley, A., 2010. Near-Ground Pressure and Wind Measurements in Tornadoes, Monthly Weather Review. 138(7), 2570-2588.

[151]. NOAA, 2019. TORUS: Targeted Observations by Radars and UAS of Supercells. [Last Accessed: 2/11/2020]. URL: https://www.nssl.noaa.gov/projects/torus/

Appendices

A. Debris release positions

In this section, data pertaining to the results reported in Chapter 5 are presented. The trajectories of the debris initialised from the positions of r/r_c =0, 0.25, 2.5 and 3 are excluded from the primary figures due to the infrequent occurrence of debris initialisation and are presented as separate figures.

The results from the series of numerical simulations with debris group B1, B2 and B3 with identical Tachikawa number (K =1.2) are conducted chapter 5, section 5.1.2. Figure A.1 illustrates the plan view of debris trajectories for debris group B1, B2 and at the positions of r/r_c =0.25 and 2.5, while no debris were initialised at the positions of r/r_c =0 and 3. It can be observed that only 3 individual debris were initialised at r/r_c =0.25 and 2.5 for debris group B1 and r/r_c =0.25 for debris group B2.

Chapter 5, section 5.1.2 presents the results for debris flight in the tornado-like vortex with S =0.3 with debris group A, B1 and C. The debris trajectories for all three debris groups at the position of r/r_c =2.5 is illustrated, where no debris were initialised at the positions of r/r_c =0, 0.25 and 3. At the position of r/r_c =2.5, the plan view of debris trajectories are shown in Figure A.2, the side view of trajectories are shown in Figure A.3, the flight duration of debris against radial distance are shown in Figure A.4, the flight

altitude of debris against radial distance are shown in Figure A.5 and the debris velocity against radial distance for debris group A, B1 and C are shown in Figure A.6. It can be observed that only 1 individual debris were initialised at r/r_c = 2.5 for debris group A.

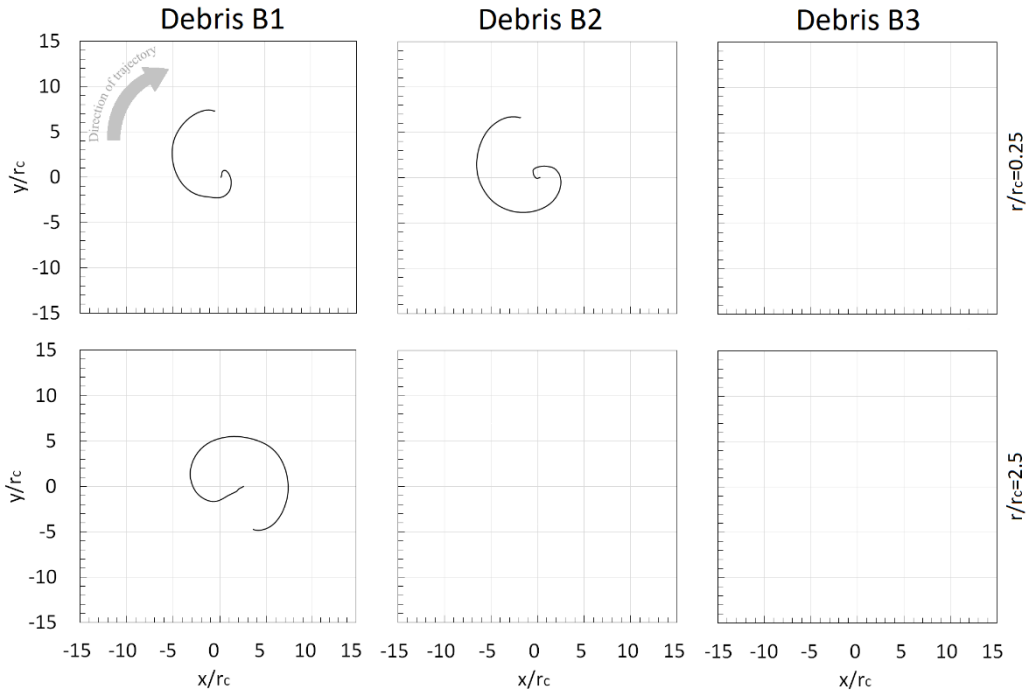

Figure A.1: Plan view of trajectories at different positions for debris A, B1 and C. The grey arrow denotes the direction of debris trajectory for all debris groups.

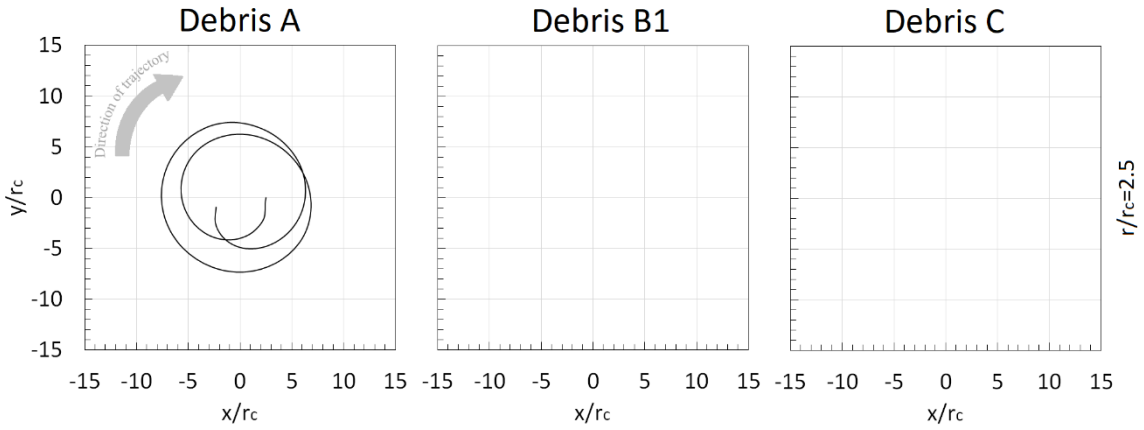

Figure A.2: Plan view of trajectories at different positions for debris A, B1 and C. The grey arrow denotes the direction of debris trajectory for all debris groups.

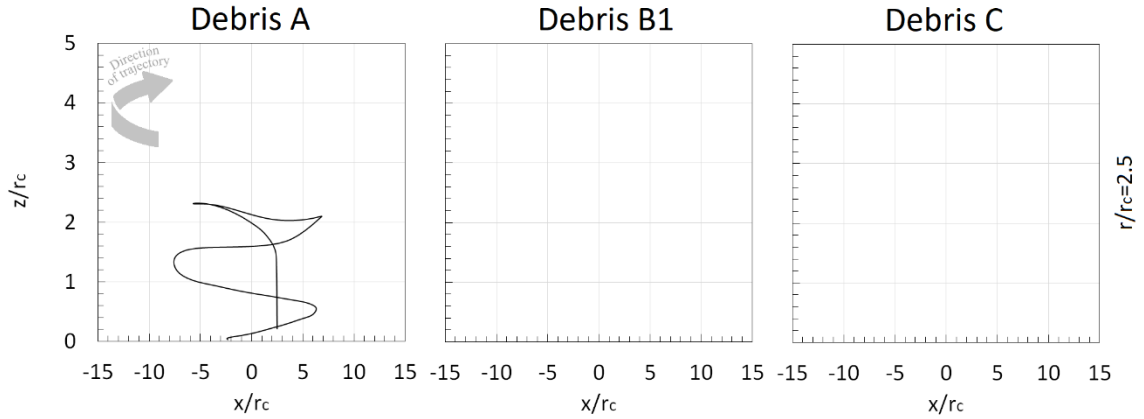

Figure A.3: Side view of trajectories at different positions for debris A, B1 and C. The grey arrow denotes the direction of debris trajectory for all debris groups.

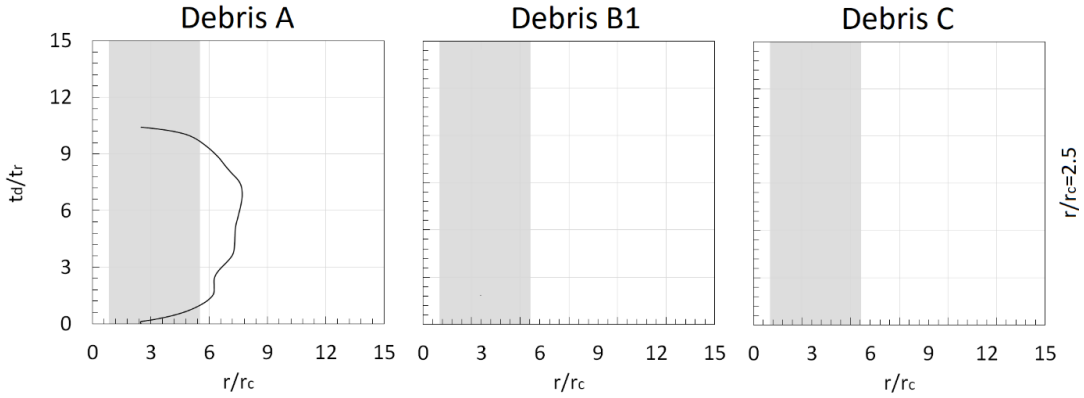

Figure A.4: Debris flight duration against radial distance for debris group A, B1 and C.

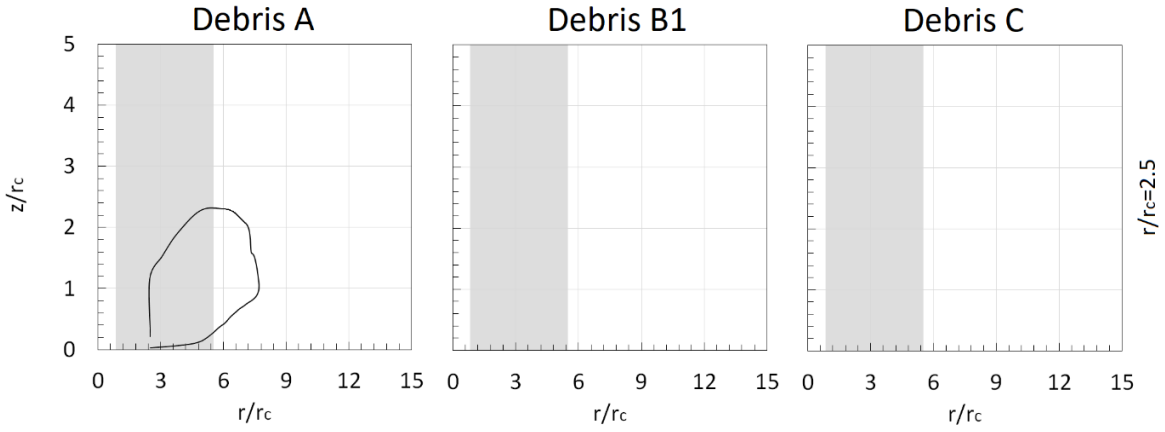

Figure A.5: Debris flight altitude against radial distance for debris group A, B1 and C.

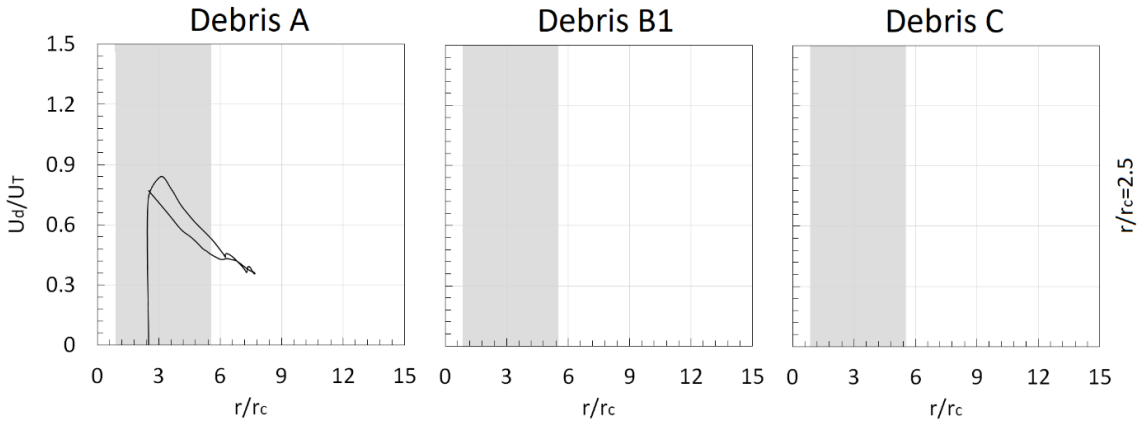

Figure A.6: Debris velocity against radial distance for debris group A, B1 and C.

Chapter 5, section 5.2.2 presents the results for debris flight in the tornado-like vortex with S =0.69. The debris trajectories for all three debris groups at the position of r/r_c =0.25 & 2.5 is illustrated, and no debris were initialised at the positions of r/r_c =0 & 3. At the position of r/r_c =0.25 & 2.5, the plan view of debris trajectories are shown in Figure A.7, the side view of trajectories are shown in Figure A.8, debris flight duration against radial distance are shown in Figure A.9, debris flight altitude against radial distance are shown in Figure A.10, and the debris velocity against radial distance are

shown in Figure A.11. Only 1 debris was initialised at r/r_c = 0.25, and 2 and 1 individual debris at the location of r/r_c = 2.5 for debris group A and B1 respectively.

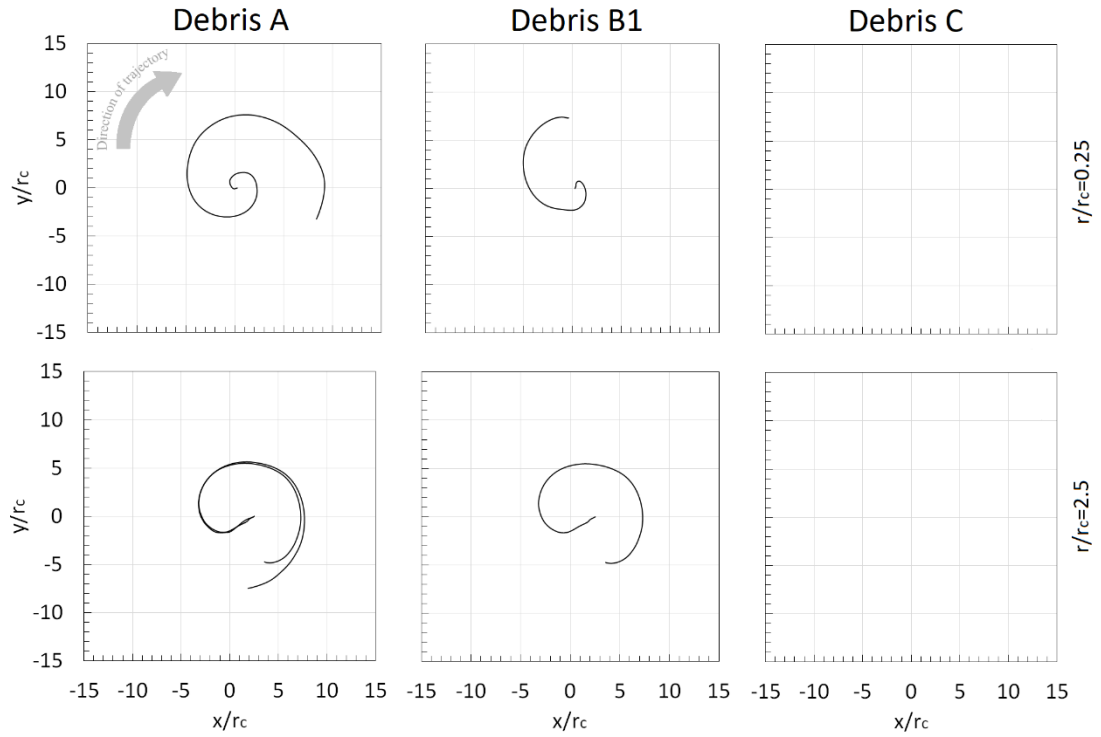

Figure A.7: Plan view of trajectories at different positions for debris A, B1 and C. The grey arrow denotes the direction of debris trajectory for all debris groups.

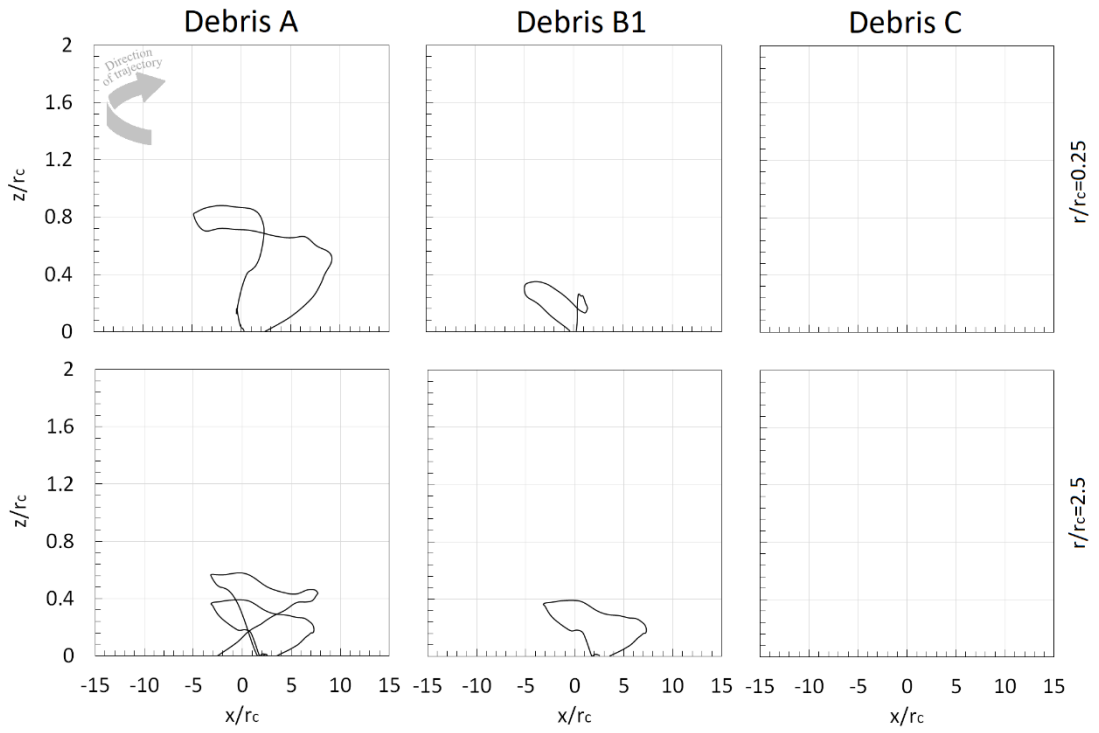

Figure A.8: Side view of trajectories at different positions for debris A, B1 and C. The grey arrow denotes the direction of debris trajectory for all debris groups.

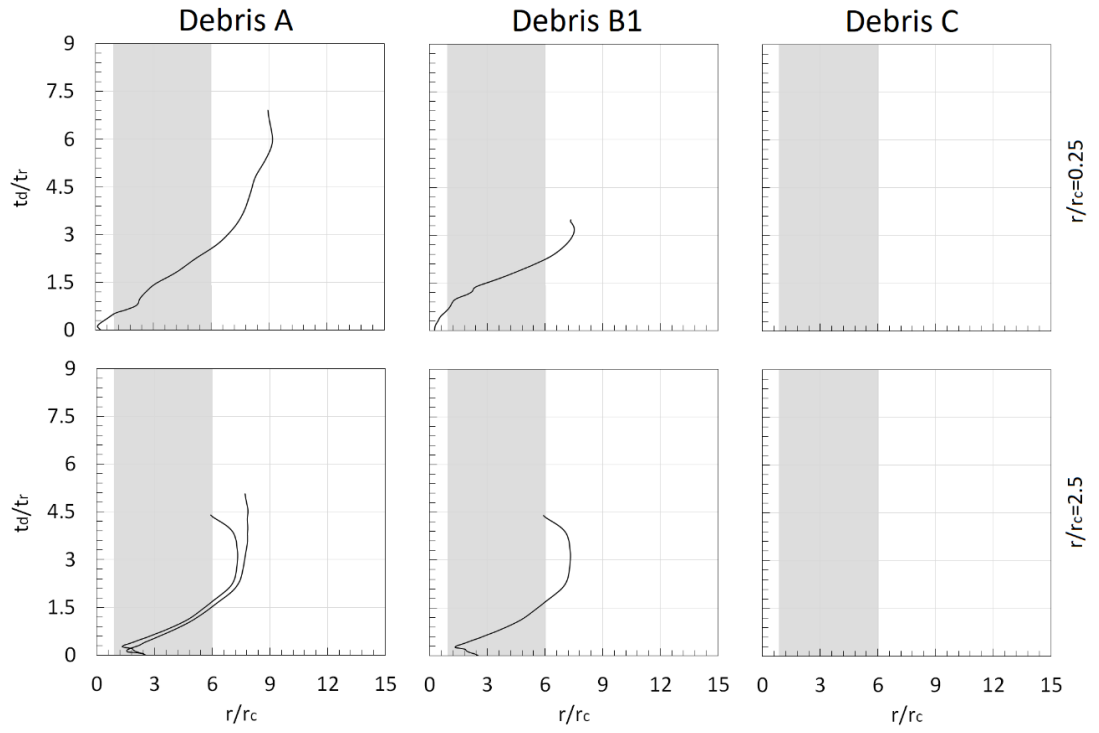

Figure A.9: Debris flight duration against radial distance for debris group A, B1 and C.

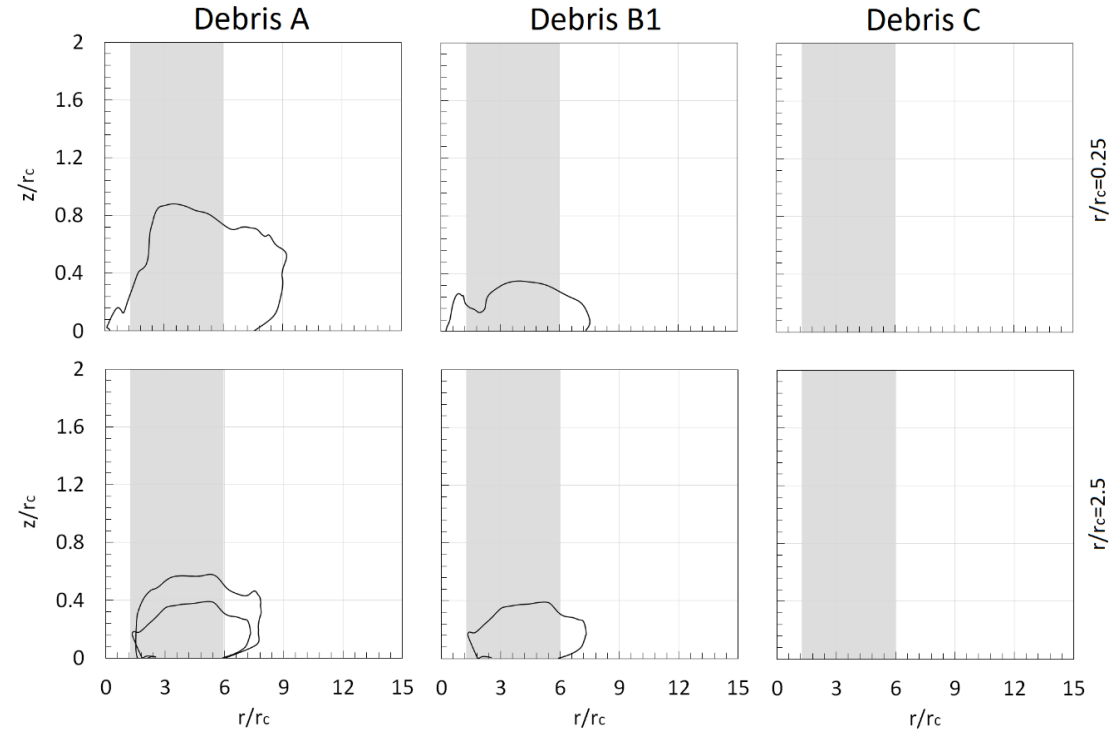

Figure A.10: Debris flight altitude against radial distance for debris group A, B1 and C.

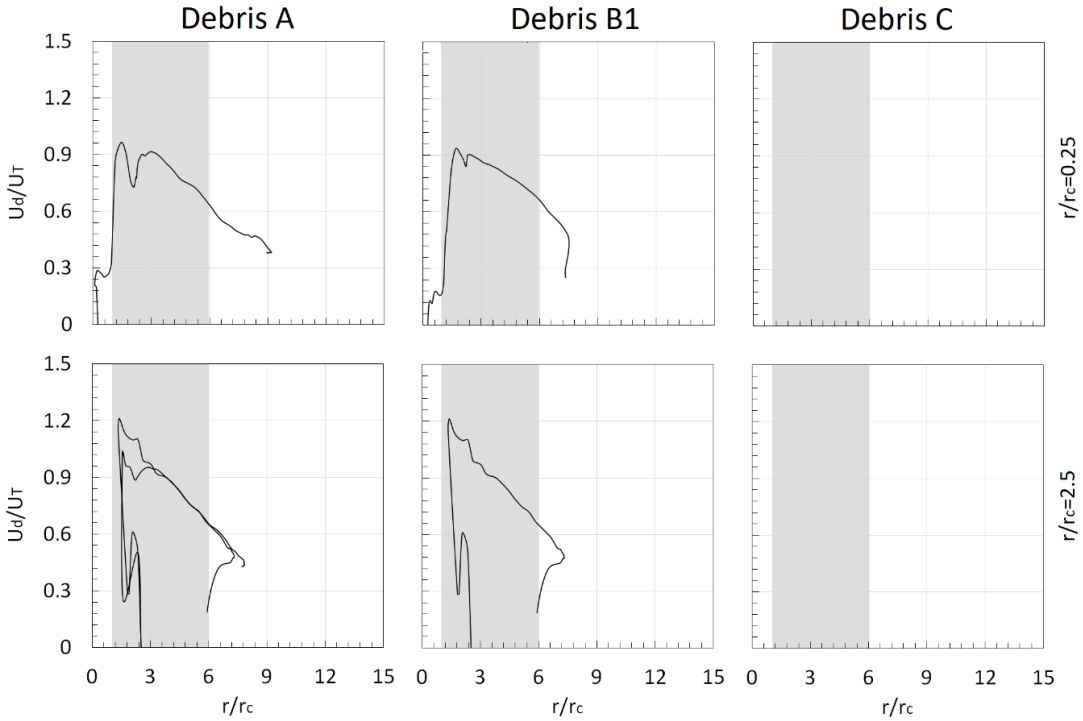

Figure A.11: Debris velocity against radial distance for debris group A, B1 and C.